Science and Risk-Based Development of Ion Exchange Chromatography

MECHANISTIC MODELING AND ADVANCED STATISTICS

Zur Erlangung des akademischen Grades eines
DOKTORS DER INGENIEURWISSENSCHAFTEN (DR.-ING.)

von der KIT-Fakultät für Chemieingenieurwesen und Verfahrenstechnik des
Karlsruher Instituts für Technologie (KIT)
genehmigte

DISSERTATION

von
Till Briskot, M.Sc.
aus Wuppertal

Acknowledgments

This thesis would not have been completed without the presence and support of several people. I would like to express my deepest gratitude to the following people.

First and foremost, I would like to thank my academic supervisor Prof. Dr. Jürgen Hubbuch for supporting, motivating, and inspiring me far beyond my time as a PhD student. Thank you for introducing me to the field of downstream processing and for your dedication and perseverance in giving students like me the opportunity to pursue a PhD in an industrial environment.

I also want to thank Prof. Dr.-Ing. Hermann Nirschl for taking the time to review this thesis as a co-referee, for his interest in my work, and for the good discussions of my results.

Moreover, I would like to thank Tobias Hahn, Thiemo Huuk, and Terese Baumann for giving me the opportunity to conduct my PhD thesis at GoSilico. With great discussions, their openness, their support in attending conferences, as well as their organization of industry collaborations, they have contributed significantly to this work. Tobias, thank you for your constant interest and trust in my work as well as the many creative freedoms you gave me over the past years. Thank you, Thiemo, for your great support throughout my entire scientific career, your introduction of the "holy grail of biotechnology", and your ingenious design of "figure-tables". It is always fun working with you. Please stay as you are. Teresa, thank you for creating and maintaining a great working atmosphere at GoSilico, for your trust, and for all the great summer and company events. I would also like to thank the whole team at Gosilico for being great colleagues and making time in the office always fun.

This thesis would not have been possible without the presence of outstanding industrial collaborations. They have greatly supported the thesis by providing experimental data, technical exchange, and constructive criticism. I want to give my special thanks to Ferdinand Stueckler, Jan Griesbach, Stefan Hepbildikler, Felix Wittkopp, Katharina Doninger, Chris Williams, and Jessica Yang form Roche/Genentech for supporting my thesis from the beginning. Furthermore, I want to thank Gang Wang, Simon Kluters, Joey Studts, Peter Schwan, Isabell Hagemann, Klaus Kaiser, Anja Trapp, and Gunnar Malmquist for their great support.

Finally, I want to thank my parents, brother, and grandparents for believing in me and for supporting me throughout my whole life. Thank you for not filing a missing person's report in case I did not call for a few weeks.

"Happiness is equal to work minus resistance."

- Wolfgang Ostwald

Zusammenfassung

Die in dieser Doktorarbeit vorgestellten Erkenntnisse tragen zur computergestützten Modellierung der Ionenaustauschchromatographie (*ion exchange chromatography*, IEX *chromatography*) bei. In Kombination mit anderen Chromatographieverfahren spielt die IEX-Chromatographie eine wesentliche Rolle bei der Aufreinigung biopharmazeutischer Proteine, sowohl in der Proteinanalytik als auch in der industriellen Produktion. Da sie einen großen Einfluss auf die endgültige Reinheit und Qualität eines biopharmazeutischen Produktes haben, unterliegen die Entwicklung und der Betrieb von Chromatographieschritten strengen regulatorischen Anforderungen. Selbst kleinste Änderungen im Herstellungsprozess können sich negativ auf die Qualität des Endproduktes auswirken und die Patientensicherheit gefährden. Um sicherzustellen, dass das Endprodukt durchgängig vorgegebene Qualitätsmerkmale erfüllt, verlangen Aufsichtsbehörden wie die U.S. Food and Drug Administration und die Europäische Arzneimittelagentur daher ein fundiertes Verständnis des Produktes und dessen Herstellungsprozesses, so wie es die *Quality by Design* (QbD) Initiative vorgibt. Im Gegensatz zur Gewährleistung der Produktsicherheit allein durch "Qualität durch Prüfung" (*'Quality by Testing'*), strebt QbD eine Qualitätssicherung an, bei der sämtliche Quellen für Produkt- und Prozessvariabilität identifiziert, Beziehungen zwischen Prozess- und Produktvariabilität verstanden und geeignete Prozesskontrollstrategien entwickelt sind. Zudem sollte die Prozessentwicklung gemäß QbD auf wissenschaftlichen und risikobasierten Ansätzen beruhen.

Angetrieben durch die QbD-Initiative hat die mechanistische Prozessmodellierung in den letzten Jahren zunehmend an Aufmerksamkeit gewonnen. Indem sie einen Prozess und die ihm zugrundeliegenden biologischen, chemischen und physikalischen Mechanismen auf der Basis von Naturgesetzen beschreiben, liefern mechanistische Modelle ein fundiertes wissenschaftliches Prozessverständnis und sind in der Lage, die Prozessentwicklung auf der Grundlage wissenschaftlicher Prinzipien zu unterstützen, so wie es von QbD angestrebt wird. Im Falle der Chromatographie bestehen diese mechanistischen Modelle meist aus einem System von Kontinuitätsgleichungen, die die Migration von Proteinen und anderen gelösten Stoffen innerhalb einer Chromatographiesäule beschreiben. Diese Kontinuitätsgleichungen berücksichtigen verschiedene Massentransfermechanismen, wie zum Beispiel Konvektion und Diffusion. Sie sind mit einem Adsorptionsmodell gekoppelt, das Wechselwirkungen zwischen den Proteinen und dem Chromatographiemedium berücksichtigt. Obwohl es bereits mehrere mechanistische Modelle für IEX-Prozesse gibt, finden sie in der Industrie jedoch bislang nur selten konsequent Anwendung. Die Zurückhaltung der Industrie bei der Verwendung mechanistischer Modelle lässt sich häufig auf zwei Faktoren zurückführen: 1) Defizite der bestehenden Modelle bei der Beschreibung des realen Prozessverhaltens und 2) mangelndes Vertrauen in mechanistische Modelle aufgrund des Fehlens geeigneter Ansätze zur Bewertung von Modellunsicherheit und Modellrisiko.

Das Ziel dieser Arbeit bestand darin, beide Probleme anzugehen und somit zu einer breiteren Anwendung mechanistischer Modelle für die Entwicklung von IEX-Prozessen beizutragen. Die Arbeit besteht dabei aus vier Veröffentlichungen. In der ersten Veröffentlichung (Kapitel 3) wurde ein statistischer Ansatz für die Kalibrierung und Unsicherheitsbewertung von mechanistischen Chromatographiemodellen vorgestellt. In vorhergehenden Arbeiten beschränkte sich die Unsicherheitsbewertung von Chromatographiemodellen allein auf Modellparameter. Es wurde kaum analysiert, wie sich die Unsicherheit in den Modellparametern auf Modellvorhersagen auswirkt. Darüber hinaus wird die Parameterunsicherheit eines mechanistischen Modells in der Regel mit Hilfe von Konfidenzintervallen einzelner Parameter sowie anhand der Parameterkovarianz unter Verwendung der Fisher-Informationsmatrix (FIM) bewertet. Es ist bekannt, dass eine auf der FIM basierenden Berechnung für komplexe Modelle ungenau sein kann, da sie nur eine untere Grenze für die Parameterunsicherheit liefert und nur für symmetrische Konfidenzintervalle gültig ist. Die Defizite bestehender Ansätze wurden in dieser Arbeit mit Hilfe von *approximate Bayesian inference* unter Einsatz von Monte-Carlo-Techniken wie Markov Chain Monte Carlo gelöst. Auf Grundlage des Gesetzes der großen Zahlen liefern diese Techniken eine Approximation multivariater posterior Parameter- und posterior Vorhersageverteilungen eines Modells. Im Gegensatz zu vorhergehenden Ansätzen, die auf der FIM basieren, liefert der vorgeschlagene Ansatz keine untere Grenze für die Modellunsicherheit. Darüber hinaus ist der Ansatz nicht auf symmetrische Unsicherheitsintervalle beschränkt und liefert eine systematische Bewertung der prädiktiven Modellunsicherheit. Mit Hilfe des statistischen Ansatzes wurde gezeigt, dass mechanistische Chromatographiemodelle trotz erheblicher Unsicherheiten in einigen Modellparametern genaue Vorhersagen jenseits des beobachteten Prozessbereiches treffen können. Das gewonnene Verständnis von Unsicherheiten in Modellsimulationen trägt dazu bei, das Vertrauen in die Vorhersagefähigkeit eines mechanistischen Chromatographiemodells zu erhöhen.

Defizite bestehender Modelle bei der Beschreibung des realen Prozessverhaltens sind die häufigsten Gründe dafür, dass mechanistische Modelle nicht für die Prozessentwicklung eingesetzt werden können. Im Falle der IEX-Chromatographie spielt die Genauigkeit des Adsorptionsmodells eine entscheidende Rolle, da die Migration von Proteinen durch eine Chromatographiesäule unter industriellen Prozessbedingungen insbesondere durch die Thermodynamik beschrieben wird. In den letzten drei Jahrzehnten war das sogenannte *steric mass action* (SMA) Modell das verbreitetste Modell zur Beschreibung der Proteinadsorption in IEX-Prozessen. Im Rahmen des SMA-Modells wird die Adsorption von Proteinen an geladene IEX-Medien als eine stöchiometrische Reaktion dargestellt, bei der ein Protein eine stöchiometrische Anzahl an Adsorber-Gegenionen reversibel verdrängt. Die Proteinadsorption wird dabei physikalisch durch die Anzahl der verfügbaren Gegenionen auf der Adsorberoberfläche begrenzt. Trotz der weiten Verbreitung des SMA-Modells hat sich gezeigt, dass es das reale Prozessverhalten nur unter bestimmten Bedingungen abbilden kann. Insbesondere für industrielle IEX-Prozesse, bei denen die Chromatographiesäule mit einer großen Menge an Protein nahe ihrer dynamischen Bindungskapazität beladen wird, wurde festgestellt, dass das SMA-Modell das beobachtete Prozessverhalten nicht mehr ausreichend abbilden kann. Aufgrund dieser Limitierungen des SMA-Modells und anderer existierender Modelle, ist der Hauptteil dieser Arbeit der Entwicklung eines alternativen Adsorptionsmodells gewidmet. Analog zum SMA-Modell und anderen Adsorptionsmodellen versucht das entwickelte Modell eine Balance zwischen mechanistischer Beschreibung und Empirie herzustellen. Ziel war es dabei, eine mathematische Formulierung zu liefern, die computertechnisch einfach zu lösen und somit in der industriellen

Praxis breit anwendbar ist. Im Gegensatz zum SMA-Modell basiert das entwickelte *colloidal particle adsorption* (CPA) Modell nicht auf einer vereinfachten stöchiometrischen Beschreibung der Proteinadsorption, sondern auf einem strengeren physikalischen Ansatz auf der Grundlage der Kolloidwissenschaft. Im Rahmen des CPA-Modells werden Proteine als kolloidale Partikel mit einer perfekten sphärischen Form und homogener Oberflächenladungsdichte idealisiert. Unter Verwendung der linearisierten Poisson-Boltzmann-Gleichung berücksichtigt das Modell elektrostatische Wechselwirkungen zwischen geladenen Proteinen und geladenen IEX-Medien als die dominierende Kraft für die Adsorption. Nichtlineares Adsorptionsverhalten wird durch die Simulation sterischer und elektrostatischer Wechselwirkungen zwischen adsorbierten Proteinen berücksichtigt. Im Gegensatz zu stöchiometrischen Modellen, bei denen die verfügbaren Gegenionen der limitierende Faktor für die Proteinadsorption sind, berücksichtigt das CPA-Modell die tatsächliche Oberfläche eines IEX-Mediums als den physikalisch begrenzenden Faktor für die Proteinadsorption.

Das CPA-Modell wurde im Laufe von drei aufeinander aufbauenden Veröffentlichungen entwickelt. In er ersten Veröffentlichung dieser Reihe (Kapitel 4) wurde das Modell für den Grenzfall des linearen Adsorptionsbereichs eingeführt und zur Simulation von Verteilungskoeffizienten mehrerer Proteine in Abhängigkeit von dem pH-Wert und der Ionenstärke angewendet. Da Protein-Protein-Wechselwirkungen im linearen Adsorptionsbereich vernachlässigt werden können, beschränkte sich das Modell in diesem Stadium auf die Beschreibung der elektrostatischen Wechselwirkungen zwischen einem einzelnen Protein und dem geladenen IEX-Medium. Molekulare Strukturinformationen basierend auf bekannten Proteinprimärstrukturen wurden verwendet, um die Oberflächenladungsdichte der analysierten Proteine abzuschätzen und elektrostatische Wechselwirkungen zwischen Protein und Adsorber in Abhängigkeit von dem pH-Wert und der Ionenstärke zu simulieren. Es wurde gezeigt, dass das Modell in der Lage ist, Verteilungskoeffizienten über einen weiten Bereich von pH-Werten und Ionenstärken zu beschreiben und zuverlässige Extrapolationen über den beobachteten pH-Bereich hinaus durchzuführen. Durch die Berücksichtigung von Unterschieden in der molekularen Struktur eines monoklonalen Antikörpers (*monoclonal antibody*, mAb) und dessen posttranslationalen Modifikationen war das Modell auch in der Lage, das Adsorptionsverhalten von Antikörper-Ladungsvarianten vorherzusagen. Die Menge und das Verhältnis von Protein-Ladungsvarianten ist ein gängiges Qualitätsmerkmal von biopharmazeutischen Arzneimitteln. Ladungsvarianten können bei der Proteinaufreinigung eine Herausforderung darstellen, da sie sich in ihrer Struktur nur geringfügig vom intakten Protein unterscheiden und und somit ähnliche physikochemische Eigenschaften aufweisen.

In der zweiten Veröffentlichung (Kapitel 5) wurde das CPA-Modell auf den nichtlinearen Adsorptionsbereich ausgeweitet und zur Simulation von Adsorptionsisothermen eines mAbs über einen weiten Bereich von Ionenstärke und pH-Wert angewendet. Ein detaillierter Vergleich des CPA-Modells mit dem traditionellen SMA-Modell zeigte vergleichbare Modellergebnisse im linearen Adsorptionsbereich, allerdings erhebliche Unterschiede im nichtlinearen Adsorptionsbereich. Gemessene Adsorptionsisothermen wurden im Allgemeinen besser durch das CPA-Modell beschrieben. Die in dieser Arbeit vorgestellten Ergebnisse bestätigen, dass die Vereinfachungen und Annahmen im SMA-Modell nur in bestimmten Regimen gültig sind und nicht alle Experimente angemessen beschreiben. Die Ergebnisse deuten auch darauf hin, dass nichtlineare Adsorptionseffekte durch das SMA-Modell erheblich überschätzt werden können und im Allgemeinen durch das CPA-Modell besser wiedergegeben werden. Angesichts der besseren Beschreibung der experimentellen

Isothermen durch das CPA-Modell stellt Letzteres eine Verbesserung des SMA-Modells dar und trägt zu einem besseren Verständnis der Proteinadsorption bei.

Nach Entwicklung des CPA-Modells unter Gleichgewichtsbedingungen wurde in der letzten Veröffentlichung (Kapitel 6) eine kinetische Herleitung des Adsorptionsmodells vorgestellt, die eine Geschwindigkeitsgleichung für die Adsorption und Desorption von Proteinen liefert. In Kombination mit einem Massentransportmodell wurde die kinetische Form des CPA-Modells schließlich zur Simulation der Proteinretention in der präparativen IEX-Chromatographie verwendet. Um die allgemeine Anwendbarkeit des CPA-Modells zu demonstrieren, umfasste die Studie mehrere industrielle Prozesse mit verschiedenen mAbs und IEX-Medien. Die Proteinelution wurde durch eine lineare oder stufenweise Variation der Ionenstärke und/oder des pH-Wertes der mobilen Phase kontrolliert. Trotz des breiten Spektrums an Prozessbedingungen wurde das Elutionsverhalten in allen Fällen zufriedenstellend durch das CPA-Modell beschrieben. Insbesondere hat sich gezeigt, dass das Modell auch komplexes Elutionsverhalten von Proteinen beschreiben kann, welches in der Vergangenheit nicht durch das SMA-Modell beschrieben werden konnte.

Zusammenfassend lässt sich sagen, dass diese Arbeit wertvolle Verbesserungen bei der computergestützten Modellierung von IEX-Prozessen in zwei Aspekten liefert. Erstens wurden Unzulänglichkeiten bestehender Theorien bei der Beschreibung von präparativen IEX-Prozessen durch die Einführung des CPA-Modells überwunden. Zweitens wurde zur Erhöhung der Glaubwürdigkeit mechanistischer Modelle ein statistischer Ansatz eingeführt, der eine detaillierte Bewertung der Unsicherheiten in Modellparametern und Modellvorhersagen ermöglicht. Die in dieser Arbeit entwickelten Ansätze und Theorien tragen zu einer vielfältigeren Anwendung mechanistischer Modelle bei, um die Prozessentwicklung der IEX-Chromatographie auf wissenschaftliche, aber auch risikobasierte Weise zu unterstützen, so wie es von QbD befürwortet wird.

Abstract

The work presented in this thesis contributes to the computational modeling of ion exchange (IEX) chromatography. In combination with other types of chromatography, IEX chromatography plays an essential role in the purification of biopharmaceutical proteins in both protein analysis and industrial manufacturing. Since chromatography processes have a major impact on the final purity and quality of a biopharmaceutical product, the development and operation of these processes are subject to strict regulatory requirements. Even small changes in the process during manufacturing can negatively affect the quality of the final product and compromise patient safety. Thus, to ensure that the final product consistently meets specified quality attributes, regulatory agencies like the U.S. Food and Drug Administration and the European Medicines Agency require a sound understanding of the product and its manufacturing process, as emphasized by the Quality by Design (QbD) initiative. In contrast to ensuring product safety through 'Quality by Testing' alone, QbD aims for quality assurance by identifying all sources of product and process variability, understanding the relationship between process and product variability, and developing appropriate process control strategies. According to QbD, process development should further be informed by science and risk-based approaches.

Driven by the QbD initiative, mechanistic process modeling has attracted increased attention in recent years. By describing a process and its underlying biological, chemical, or physical mechanisms based on natural laws, mechanistic models provide sound scientific process understanding and are able to support process development based on scientific rationale, as emphasized by QbD. In case of chromatography, these mechanistic models mostly consist of a system of continuity equations that describe the migration of proteins and co-solutes within a chromatography column. These continuity equations account for different mass transfer mechanisms including convection and diffusion. They are coupled with an adsorption model that considers interactions between proteins and the chromatography medium. Despite the existence of mechanistic models for IEX processes, their application in industry remains sparse. The reluctance of the industry to use mechanistic models can often be attributed to two factors: 1) Shortcomings of existing mechanistic models in describing real process behavior and 2) a lack of confidence in mechanistic models due to the absence of appropriate approaches to assess model uncertainty and risk.

The goal of this work was to address both issues and thus contribute to a more widespread application of mechanistic models for the development of IEX processes. The thesis consists of four publications. In the first publication (Chapter 3), a statistical framework for the calibration and uncertainty assessment of mechanistic chromatography model was introduced. In previous works, uncertainty assessment of chromatography models was limited to model parameters alone. It was hardly analyzed how the uncertainty in model

parameters propagates to model predictions. Additionally, parameter uncertainty of a mechanistic model is commonly assessed by means of single parameter confidence intervals and parameter covariance using the Fisher information matrix (FIM). It is known that an approximation based on the FIM can be inaccurate for complex models, as it only provides a lower bound for the parameter uncertainty and is only valid for symmetric confidence intervals. The shortcomings of existing approaches were resolved in this thesis by performing approximate Bayesian inference using Monte Carlo techniques like Markov Chain Monte Carlo. Based on the law of large numbers, these techniques provide an approximation of the joint parameter posterior distribution and posterior predictive distribution of a model. In contrast to previous approaches based on the FIM, the proposed approach does not only provide a lower bound for the model uncertainty. Moreover, the approach is not limited to symmetric uncertainty intervals and provides a systematic assessment of the predictive model uncertainty. Using the statistical approach, it was demonstrated that, despite significant uncertainty in some model parameters, mechanistic chromatography models can make accurate predictions beyond observed process conditions. By providing a detailed understanding of the uncertainties in model simulations, the proposed statistical framework helps to increase confidence in the predictive capability of a model.

Shortcomings of existing models in describing real process behavior are probably the most common reasons that prevent mechanistic models from being used for process development. In case of IEX chromatography, the accuracy of the adsorption model plays an essential role, as protein migration through a chromatography column under industrial process conditions is largely described by thermodynamics. For the past three decades, the so-called steric mass action (SMA) model has been the most widely used model to describe protein adsorption in IEX processes. Within the framework of the SMA model, protein adsorption onto charged IEX media is described as a stoichiometric reaction in which a protein reversibly displaces a stoichiometric number of adsorber counter-ions. Protein adsorption is thereby physically limited by the number of available counter-ions on the adsorber surface. Despite its widespread use, it has been shown that the SMA model reproduces real process behavior only under certain limited conditions. Especially for industrial IEX processes, where the chromatography column is loaded with a large amount of protein close to its dynamic binding capacity, it was found that the SMA model can no longer describe the observed process behavior. Motivated by these limitations of the SMA model and other existing models, the main part of this work is devoted to the development of an alternative adsorption model. Similar to the SMA model and other adsorption models, the developed model seeks to balance a mechanistic description and empiricism to provide a mathematical description that is computationally simple to solve and thus widely applicable to industrial practice. In contrast to the SMA model, the developed colloidal particle adsorption (CPA) model is not based on a simplified stoichiometric description of protein adsorption but on a more rigorous physical approach using colloid science. Within the framework of the CPA model, proteins are idealized as colloidal particles with a perfect spherical shape and homogeneous surface charge density. Using the linearized Poisson-Boltzmann equation, the model considers electrostatic double-layer interactions between charged proteins and charged IEX media as the dominant force for adsorption. Nonlinear adsorption behavior is considered by simulating steric and electrostatic interactions between adsorbed proteins. In contrast to stoichiometric models, for which the available counter-ions are the limiting factor of protein adsorption, the CPA model respects the actual surface area of an IEX medium as the physically limiting factor for protein adsorption.

The CPA model was developed over the course of three consecutive publications. In the first publication of this series (Chapter 4), the model was introduced for the limiting case of the linear adsorption range and applied to simulate partitioning coefficients of multiple proteins as a function of the pH value and ionic strength. Since protein-protein interactions can be neglected in the linear adsorption range, the model at this stage was limited to a description of electrostatic interactions between a single protein and the charged IEX medium. Molecular structural information based on known protein primary structures was used to estimate the surface charge density of the analyzed proteins and to simulate electrostatic protein-adsorber interactions as a function of the pH value and ionic strength. The model was shown to be able to describe partitioning coefficients over a wide range of pH and ionic strength and to make reliable extrapolations beyond the observed pH range. By considering molecular structural differences between a monoclonal antibody (mAb) and its post-translational modifications, the model was also able to predict the adsorption behavior of antibody charge variants. The amount and ratio of protein charge variants is a common quality attribute of biopharmaceutical drugs. Charge variants can pose a challenge in downstream processing as they differ only slightly in structure from the intact protein and therefore show similar physicochemical properties.

In the second publication (Chapter 5), the CPA model was extended to the nonlinear adsorption range and applied to simulate adsorption isotherms of a mAb over a wide range of ionic strength and pH. A detailed comparison of the CPA model with the traditional SMA model showed comparable model results in the linear adsorption range but considerable differences in the nonlinear adsorption range. Measured adsorption isotherms were in general better described by the CPA model. The results presented in this work confirm that the simplifications and assumptions in the SMA model are only valid in certain regimes and do not adequately describe all experiments. The results also suggest that nonlinear adsorption effects can be overestimated considerably by the SMA model and are in general better reproduced by the CPA model. Given the better description of the experimental isotherms by the CPA model, the latter provides an improvement to the SMA model and helps to better understand protein adsorption.

After developing the CPA model under equilibrium conditions, the final publication (Chapter 6) introduces a kinetic derivation of the adsorption model providing a rate equation for protein adsorption and desorption. Combined with a transport model, the kinetic form of the CPA model was finally used to simulate protein retention in preparative IEX chromatography. To demonstrate the general applicability of the CPA model, the study included multiple industrial processes using different mAbs and IEX media. The protein elution was controlled by a linear or stepwise variation of the ionic strength and/or the pH value of the mobile phase. Despite the wide range of process conditions, the elution behavior was adequately described by the CPA model in all cases. Most significantly, the model has been shown to be able to describe even complex protein elution behavior that could not be described by the SMA model in the past.

In summary, this thesis provides valuable improvements in the computational modeling of IEX chromatography in two areas. Firstly, limitations of existing theories in describing preparative IEX processes were overcome by introducing the CPA model. Secondly, to enhance the credibility of mechanistic models, a statistical framework has been introduced that enables a detailed assessment of uncertainties in model parameters and model predictions. The approaches and theories developed in this thesis contribute to a broader

use of mechanistic models to support process development of IEX chromatography in a
scientific but also risk-based manner, as advocated by QbD.

Contents

CHAPTER 1

Introduction

To treat a broad spectrum of diseases and conditions, pharmaceutical companies own an extensive drug portfolio or pipeline of drug candidates that, for practical reasons, are divided into two main categories: small molecules (synthetics) and large molecules (biologics) [31]. While the majority of drugs currently on the market are still synthetics, biologics represent the fastest growing segment in the pharmaceutical industry [115]. In recent years, recombinant proteins such as monoclonal antibodies have been among the most important representatives of large molecules [85; 178; 179]. Due to their high specificity and potency compared to small molecules, recombinant proteins have revolutionized the treatment of many diseases including cancer, metabolic disorders, and other rare diseases [93; 112; 179].

Despite the advantages of recombinant proteins, their size and complexity often pose substantial manufacturing challenges [132]. While most small molecule drugs are manufactured through chemical synthesis, pharmaceutical proteins cannot be synthesized in this way and need to be expressed in living cells. The host cell is genetically modified to produce the desired protein which can then be harvested from the so-called cell culture fluid. As the cell produces not exclusively the active pharmaceutical ingredient, the harvested cell culture fluid contains not only the desired protein, but also other components such as DNA and other host cell proteins [107; 156]. In addition to these process-related impurities, there are also product-related impurities caused by aggregation, fragmentation, and post-translational modifications of the actual desired recombinant protein [94; 106; 175]. To assure safety of the drug product, the protein of interest must be purified and isolated from these potentially harmful impurities. Typically, a series of multiple consecutive purification steps is required to isolate the desired protein and to meet the high regulatory requirements for product purity. This series of purification steps is also referred to as downstream process.

Over the past decades, preparative liquid chromatography has been the workhorse of almost every biopharmaceutical downstream process [35; 73; 85]. In general, liquid chromatography is a separation technique in which molecules are separated by their distribution between two phases; a solid stationary phase and a liquid mobile phase that flows through the stationary phase. Due to differences in physicochemical properties, the different molecules to be separated require different times to travel through the stationary phase.

These properties include, inter alia, the molecule size, charge, hydrophobicity, and/or its affinity to a particular ligand. Most downstream processes contain at least two orthogonal chromatography steps. The focus of this thesis lies on ion exchange (IEX) chromatography, in which molecules are mostly separated due to differences in their net charge. This chromatography method is frequently used for the purification of recombinant proteins due to its robustness, selectivity, and mild operating conditions [61].

Every downstream process used to commercially manufacture a biopharmaceutical product must meet certain technical, economic, and regulatory requirements. The objective of process development is to ensure that the final process meets all requirements and ensures product safety. Today's development workflows rely heavily on empiricism, using experience and knowledge from previous projects as well as extensive and expensive experimental studies to achieve development goals [25; 117; 141; 160]. However, given the steady growth and diversification of pharmaceutical pipelines, as well as increasing regulatory and economic constraints [41; 42], there is a growing interest in adopting new and more efficient development workflows. In this context, computer-aided process development using mechanistic process models has gained increasing interest in recent years [73; 117; 141; 160]. Mechanistic or first-principle models are based on a fundamental understanding of the underlying physical phenomena of a process. Once generated, these models can be used to digitally replicate the actual process. The digital evidence provided by the mechanistic model about the behavior of a process can be used to augment or even replace empirical evidence, reducing development time and costs.

In the following sections, an introduction to protein liquid chromatography is given along with a brief review of biopharmaceutical process development. Subsequently, the theory and mathematical description of protein chromatography is reviewed. The last section addresses the description of protein systems and their properties from the perspective of colloid science.

1.1   Introduction to Liquid Chromatography

This section introduces the basic concepts of liquid column chromatography. The general structure of a liquid chromatography column is schematically shown in Fig. 1.1. In most applications, the column contains a packed bed of spherical adsorber particles with a mobile phase flowing through the void volume between the adsorber particles or beads. In the context of this thesis, the mobile phase consists of an aqueous buffer that is applied from the top of the column at a constant flow rate. Depending on the intended use of the chromatography column, the size of the adsorber beads can range from a few micrometers in analytical chromatography to ~ 100 μm in preparative applications [89]. The adsorber bead itself is commonly characterized by a high particle porosity ε_p, typically in the range of 50 to 90 % [152]. This provides a high specific surface area required for preparative applications. The functionalization of the adsorber surface defines the mode of chromatography and thus the underlying separation principle. In IEX chromatography, the surface is functionalized by ligands that contain at least one ionizable functional group. Depending on the charge of the functional groups, we distinguish between positively charged anion exchangers and negatively charged cation exchangers.
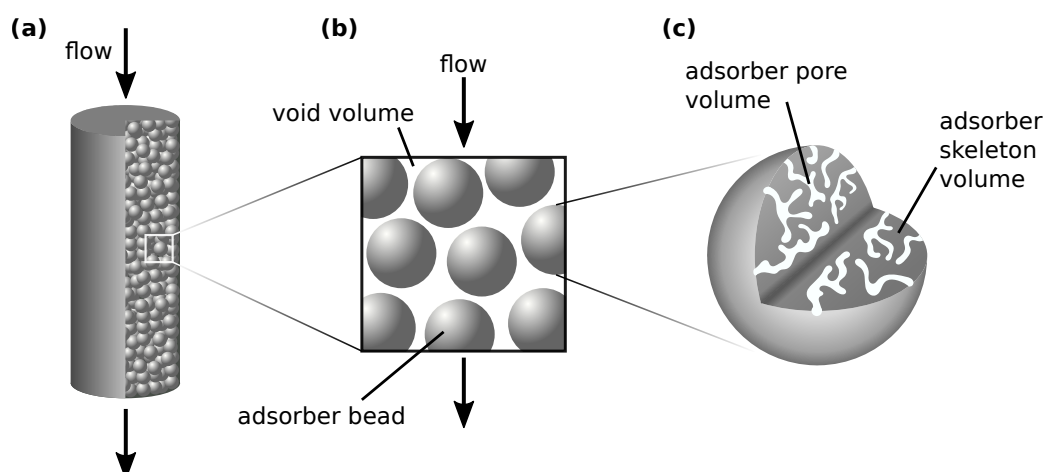
Figure 1.1: Schematic of a chromatography column containing a packed bed of porous adsorber particles. Figure is adapted from [152].

The migration of proteins and other solutes through the packed bed is governed by several transport phenomena summarized schematically in Fig. 1.2. Inside the void volume of the packed bed, mass transport is mostly defined by convection and axial dispersion. The latter describes the backmixing that occurs during the flow through the packed bed. It is caused by several effects, including eddy diffusion, molecular diffusion, and an uneven flow distribution at the column wall and at the particle surface [68; 152]. Once transported towards an individual adsorber particle, solutes can pass the stagnant boundary layer by diffusion and enter the pore system of the adsorber bead. As the liquid phase inside the pore system is stagnant, solutes inside the adsorber bead are transported solely by diffusion, before they finally adsorb on the surface of the stationary phase. The velocity at which a protein migrates through the column is strongly determined by its interaction with the adsorber surface. In IEX chromatography, the interaction is in general strongly dependent on how a solute is charged relative to the adsorber surface. While oppositely charged solutes are retained and can spend a long time adsorbed on the adsorber surface, equally charged solutes are not attracted and migrate almost unhindered through the column. As solutes differ in their net charge, surface charge density, or surface charge distribution, they migrate through the column at different velocities, resulting in a separation of the applied mixture.

In IEX chromatography, the interaction between solutes and the adsorber is commonly regulated by the pH and/or the ionic strength of the mobile phase. By changing both modifiers in a controlled manner during the process, the separation efficiency can be optimized and the desired protein can be isolated with high purity. Depending on how the composition of the mobile phase is selected and manipulated, several modes of operation are distinguished, as depicted schematically by the chromatograms in Fig. 1.3. A chromatogram as shown in Fig. 1.3 summarizes essentially the result of a chromatography run. It shows process readouts measured at the outlet of the column as a function of the process time or volume of mobile phase applied to the column. In this case, the schematics show the total protein concentration (black) and the modifier concentration (red). In general, it is distinguished between bind-and-elute mode and flow-through mode. In the former, the
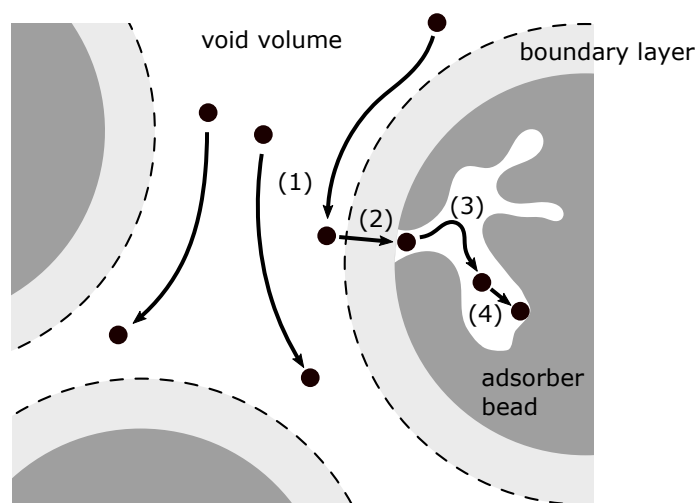
Figure 1.2: Mass transfer phenomena inside a chromatography column including convection and dispersion inside the column void volume (1), diffusion of solute molecules through the stagnant boundary layer (2), pore diffusion (3), and adsorption kinetics (4). Figure is adapted from [152].

composition of the mobile phase is initially chosen so that, ideally, only the product and a few impurities are bound to the adsorber surface. After loading the column, the protein of interest is eluted and separated from remaining impurities by changing the composition of the mobile phase (e.g. by increasing the ionic strength). Thereby, the composition of the mobile phase is often changed in a linear or step-wise manner, as shown in Fig. 1.3(a) and Fig. 1.3(b), respectively. In flow-through mode, on the other hand, the properties of the mobile phase and adsorber are chosen so that the protein of interest hardly binds to the adsorber surface and passes the column almost unhindered during the loading phase. Ideally, only impurities are retained and can be removed during the regeneration of the chromatography column.
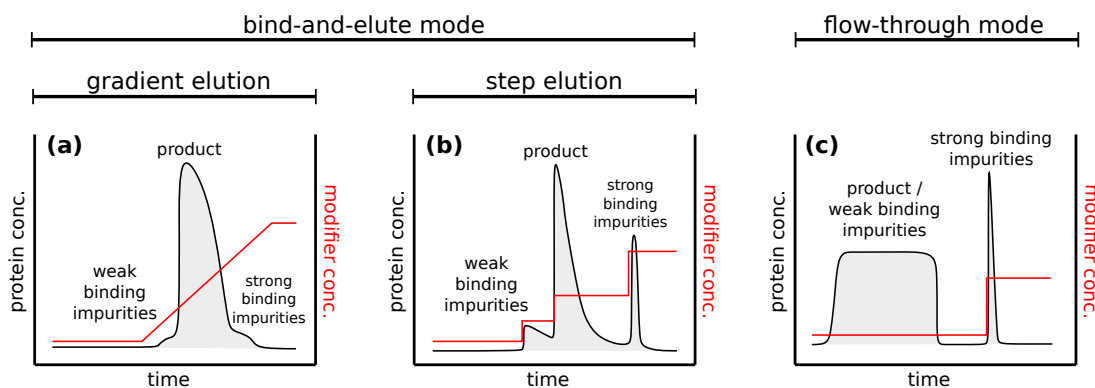
Figure 1.3: Modes of operation commonly used in preparative chromatography. (a) gradient elution, (b) step elution, (c) flow-through operations.

1.2 Development of Chromatography Processes

As mentioned earlier, every process step, downstream process, or pharmaceutical manu-
facturing process in general must meet a set of basic requirements, including economic
and especially regulatory requirements [85]. To ensure consistent manufacturing of an
efficacious product that is safe for patients, regulatory agencies such as the U.S. Food
and Drug Administration (FDA) and the European Medicines Agency (EMA) impose
stringent requirements on the design and validation of manufacturing processes, as out-
lined by the Quality by Design (QbD) initiative. The QbD initiative strives for holistic,
science-based, and risk-based development approaches, where product quality is ensured
not only through testing, but rather through sound product and process understanding
and process control [83]. The term process understanding means first and foremost a deep
understanding of how process changes or deviations, whether intended or not, affect the
quality of the product [72; 133; 192].

Today, process understanding is generated largely in an empirical fashion through a series
of development steps. Manufacturing processes are usually characterized by a large number
of process parameters that are optimized during the process design phase. In chromatog-
raphy, these process parameters can include, among others, the type of adsorber system,
modifier concentrations, and the amount of protein loaded onto the column. The optimized
process meets, inter alia, requirements in terms of product quality, as well as technical and
economic requirements. From a regulatory or QbD perspective, not all of these optimized
process parameters are critical. Only those process parameters whose variability has a
significant impact on product quality are considered critical and must be monitored and
controlled later on [83]. The goal of an initial risk-ranking and filtering (RFF) is to iden-
tify potential critical process parameters (pCPPs) and distinguish them from non-critical
process parameters. As many steps in process development, the classification of process
parameters into non-critical and potentially critical is a risk-based approach relying on
project-specific empirical knowledge gained during the process design phase, prior knowl-
edge from previous comparable projects, and small dedicated experimental studies in small
scale [72; 83]. Following the RFF, the identified pCPPs are analyzed in more detail as part
of a comprehensive process characterization and validation study. These studies encom-
pass elaborated experimental studies where process parameters are varied in a systematic
and statistically designed manner to analyze the interactive effects of all pCPPs on the
quality of the product. The generated understanding of the process behavior is used to
determine critical process parameters (CPPs) and their acceptable variability that will
ensure a consistent product quality [72]. Since performing experimental studies at the
manufacturing scale is not feasible, experiments for process optimization and characteri-
zation are performed predominantly on qualified scale-down models, i.e. miniaturized but
representative versions of the actual commercial manufacturing system. Although RRF
and scale-down models help to streamline experimental studies, the experimental effort to
derive profound process understanding empirically is still large.

Driven by the QbD initiative and economic constraints, there is a growing interest across
the biopharmaceutical industry to augment or even replace empirically derived process
understanding with scientific understanding in form of mechanistic process models [73;
117; 141]. Mechanistic models are based on first principles and capture the behavior of a
system by describing the underlying physical effects in terms of mathematical equations.

Thus, they provide a systematic way to organize the physical or scientific understanding of the process, as emphasized by QbD. Experiments usually performed on small-scale systems or the commercial system itself can be reproduced *in silico*, i.e. by computer simulations. Once calibrated, mechanistic models can be applied at all stages of development to optimize the process, streamline experiments, scale-up, and ultimately producing a comprehensive process understanding [27; 141]. While the application of mechanistic models is highly desirable in terms of process understanding, it requires knowledge and especially a mathematical formulation of the underlying effects. The application is therefore limited to operating units such as chromatography, for which theories exist.

1.3   Modeling of Chromatography

The schematic in Fig. 1.2 shows that chromatography is a process that involves an intricate combination of different physical effects, including fluid dynamics, mass transfer phenomena, and thermodynamics of adsorption [68]. In the following sections, we recall most of these phenomena and their mathematical description. First, we will focus on thermodynamics of adsorption and present the model commonly used to describe the interaction between proteins and IEX adsorbers. Second, we review chromatography models describing mass transfer effects inside the column void volume and the adsorber bead.

1.3.1   Protein Adsorption

The adsorption of proteins and other solutes onto the adsorber surface is described through adsorption isotherms. Considering a protein i, an isotherm describes the functional relationship between the concentration of the protein in the liquid phase c_i and the concentration of adsorbed protein per adsorber skeleton volume q_i at equilibrium and constant absolute temperature T.

1.3.1.1   Stoichiometric Displacement Model

In IEX chromatography of proteins, the mathematical description of the adsorption isotherm is mostly based on the stoichiometric displacement model (SDM) initially proposed by Boardman and Partridge [13] in 1953 and further developed by Regnier and et al. [44; 98; 144]. According to the SDM, the adsorption of a protein P_i onto the adsorber surface is accompanied by a reversible and stoichiometric displacement of counter-ions S bound to the adsorber surface. Under the assumption of counter-ions with charge $|z_{\pm}| = 1$, the reversible exchange can be described by the stoichiometric reaction

$$P_i^{\nu_i} + \nu_i LS_{ads} \rightleftharpoons L_{\nu_i}P_{i,ads}^{\nu_i} + \nu_i S, \qquad (1.1)$$

where the subscript ads indicates the adsorbed state, L denotes a ligand (functional group) on the adsorber surface, and ν_i represents the number of counter-ions displaced by the i-th protein. The equilibrium constant $k_{eq,i}$ for Eq. (1.1) can be written as

$$k_{eq,i} = \frac{\gamma_{L_{\nu_i}P_{i,ads}^{\nu_i}} q_i}{\gamma_{P_i^{\nu_i}} c_i} \left(\frac{\gamma_S c_S}{\gamma_{LS_{ads}} \bar{q}_S} \right)^{\nu_i}, \qquad (1.2)$$
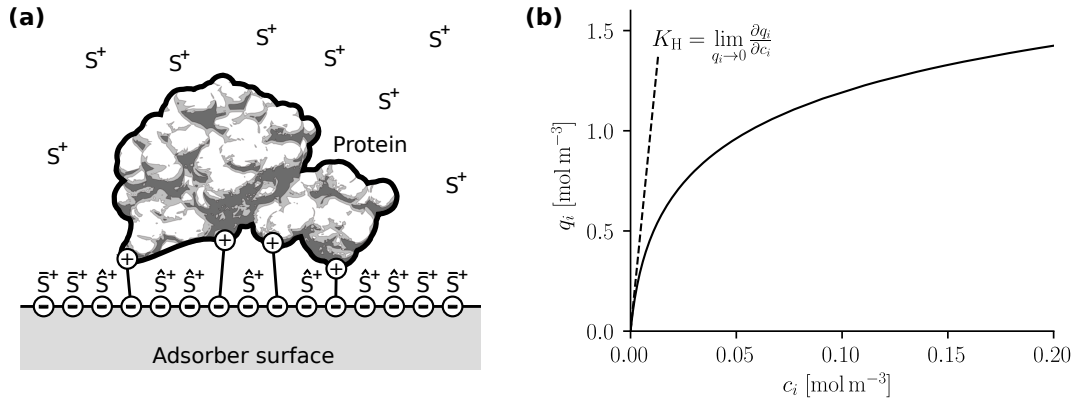
Figure 1.4: Protein adsorption on a cation exchange adsorber according to the SMA model. (a) Schematic representation of the protein-ligand complex $L_{\nu_i}P^{\nu_i}_{i,\text{ads}}$. The number of ligands involved in the complex is indicated by the characteristic charge ν_i of the protein i. Given the steric size of the protein, some of the ligands are sterically shielded. Counter-ions bound to sterically shielded adsorber ligand ($\hat{S}^+$) cannot be replaced by other proteins. The figure is adapted from [22]. (b) Adsorption isotherm according to the SMA model for $c_S = 50 \text{ mol m}^{-3}$, $\Lambda_{\text{IEX}} = 700 \text{ mol m}^{-3}$, $k_{\text{eq}} = 1 \times 10^{-6}$, $\nu = 7$, and $\sigma = 150$.

where γ represents the activity coefficient, c_S is the counter-ion concentration in the liquid phase, and $\bar{q}_S$ denotes the counter-ion concentration per adsorber skeleton volume available for exchange.

1.3.1.2 Steric Mass Action Model

According to the steric mass action (SMA) model introduced by Brooks and Cramer [22], not all counter-ions bound to the adsorber surface can be replaced by proteins in the liquid phase. Given the steric size of macromolecules like proteins, some of the ligands are sterically shielded, as schematically shown in Fig. 1.4(a). Counter-ions bound to sterically shielded adsorber ligands, $\hat{S}^+$, cannot be replaced by other proteins. Considering the total ionic capacity of the adsorber Λ_{IEX} and n different proteins, $\bar{q}_S$ is defined by the electroneutrality condition

$$\bar{q}_s = \Lambda_{\text{IEX}} - \sum_{i=1}^{n}(\nu_i + \sigma_i)q_i, \tag{1.3}$$

where σ_i denotes the number of ligands shielded by the i-th protein. Assuming thermodynamically ideal behavior in the liquid and stationary phase ($\gamma = 1$), Eq. (1.2) and Eq. (1.3) lead to the equilibrium relationship

$$\frac{q_i}{c_i} = \underbrace{k_{\text{eq},i}\left(\frac{\Lambda_{\text{IEX}}}{c_S}\right)^{\nu_i}}_{\text{protein-adsorber interaction}} \underbrace{\left(1 - \frac{\sum_j q_j(\nu_j + \sigma_j)}{\Lambda_{\text{IEX}}}\right)^{\nu_i}}_{\text{steric hindrance}}. \tag{1.4}$$

An exemplary isotherm according to Eq. (1.4) is shown in Fig. 1.4(b). For simplicity, the shown isotherm considers only one protein species i. Based on the shape of the isotherm,

adsorption can in general be divided into two ranges: a linear and a nonlinear range. In the limiting case of linear adsorption $q_i \to 0$, the steric hindrance in Eq. (1.4) reduces to unity and Eq. (1.4) is dominated by the first part, the protein-adsorber interaction. This part defines the initial slope of the isotherm and thus the Henry coefficient

$$K_{\mathrm{H},i} = k_{\mathrm{eq},i} \left(\frac{\Lambda_{\mathrm{IEX}}}{c_{\mathrm{S}}} \right)^{\nu_i}. \tag{1.5}$$

It accounts for the interaction between an individual protein i and the adsorber surface as a function of c_{S}. The second part of Eq. (1.4) accounts for steric hindrance at the adsorber surface and leads to a nonlinear adsorption behavior at higher concentrations q_i. It also defines the static binding capacity of the adsorber system, i.e. the maximum amount of protein that can bind to the adsorber surface. For a system containing only one protein, the static binding capacity is defined by the SMA model as $q_{\mathrm{max},i} = \Lambda_{\mathrm{IEX}}(\nu_i + \sigma_i)^{-1}$. We will discuss the SMA model and its underlying assumptions in more detail in Chapter 5.

1.3.2 Transport Models

To describe the migration of proteins and other solutes within a chromatography column, several mathematical models have been introduced in the past. These models are based on assumptions about the predominant physical effects in the real system and therefore allow for specific simplifications in the mathematical description. In general, it is assumed that the column is radially homogeneous. This means that all variables like the concentration of the i-th solute in the void fraction $c_{\mathrm{v},i}$ are only a function of the process time t and the axial column position $x \in [0, L_{\mathrm{c}}]$, where L_{c} is the length of the column. Furthermore, the packed bed shown in Fig. 1.1(a) is considered to be homogeneous in x and consists of perfect spherical adsorber particles with constant radius r_{p}. Thus, the void fraction ε_{v} and the particle porosity ε_{p} are constant and not a function of x. The system is isothermal and perfused by an incompressible and inert mobile phase with constant viscosity and linear velocity u. Depending on additional simplifications made, we distinguish between several model types, which are reviewed in the following. For the sake of brevity, the review is limited to a small number of models commonly used in model-based process development and in this thesis. For a more detailed summary, it is referred to the text books by Guiochon [68] and Schmidt-Traub [152].

1.3.2.1 General Rate Models

The most detailed models used in modeling chromatography processes are classified as general rate models (GRMs). They account explicitly for all physical effects described earlier in both the column void volume and the adsorber particle. According to the GRM, mass transfer inside the column void volume shown in Fig. 1.1(b) can be described by the continuity equation

$$\frac{\partial c_{\mathrm{v},i}}{\partial t}(x,t) = \overbrace{\left[-\frac{1 - \varepsilon_{\mathrm{v}}}{\varepsilon_{\mathrm{v}}} \frac{3}{r_{\mathrm{p}}} k_{\mathrm{film},i} \left(c_{\mathrm{v},i}(x,t) - c_{\mathrm{p},i}(x,r_{\mathrm{p}},t) \right) \right]}^{\text{Film mass transfer}}$$
$$\underbrace{\left[-\frac{u}{\varepsilon_{\mathrm{v}}} \frac{\partial c_{\mathrm{v},i}}{\partial x}(x,t) \right]}_{\text{Convection}} + \underbrace{\left[D_{\mathrm{ax}} \frac{\partial^2 c_{\mathrm{v},i}}{\partial x^2}(x,t) \right]}_{\text{Axial dispersion}}, \tag{1.6}$$

where $k_{\mathrm{film},i}$ is the film mass transfer coefficient, D_{ax} is the axial dispersion coefficient, and $c_{\mathrm{p},i}(r_{\mathrm{p}})$ is the concentration at the particle surface. As highlighted, Eq. (1.6) describes the local temporal change in $c_{\mathrm{v},i}$ due to convection, film mass transfer, and axial dispersion. It is assumed that axial dispersion in the liquid phase can be defined in analogy to Fick's laws of diffusion. The axial dispersion coefficient D_{ax} is considered to be independent of the concentration and the type of solute. Due to the simplification of a homogeneous packed bed, both $k_{\mathrm{film},i}$ and D_{ax} are constants. However, it is important to note that both are affected by u. The mathematical formulation of mass transfer in the column void volume is completed with Danckwerts' boundary conditions of dispersive systems at the column inlet

$$\left.\frac{\partial c_{\mathrm{v},i}}{\partial x}\right|_{x=0,t} = \frac{u}{\varepsilon_{\mathrm{v}} D_{\mathrm{ax}}} \left(c_{\mathrm{v},i}(x=0,t) - c_{\mathrm{inlet},i}(t) \right) \tag{1.7}$$

and the column outlet

$$\left.\frac{\partial c_{\mathrm{v},i}}{\partial x}\right|_{x=L_{\mathrm{c}},t} = 0, \tag{1.8}$$

where $c_{\mathrm{inlet},i}$ is the concentration of the i-th solute at the column inlet.

Inside the adsorber particle, the liquid phase is assumed to be stagnant and mass transfer is driven only by diffusion according to Fick's laws. Given the assumption of perfect spherical adsorber particles, the concentration inside the adsorber pore system is only a function of the radial position r. According to the GRM proposed by Gu et al. [62; 63], mass transfer inside the adsorber particle can be described by the continuity equation

$$\frac{\partial c_{\mathrm{p},i}}{\partial t}(x,r,t) = \frac{1}{r^2} \frac{\partial}{\partial r} \left(r^2 D_{\mathrm{pore},i} \frac{\partial c_{\mathrm{p},i}}{\partial r}(x,r,t) \right) - \frac{1-\varepsilon_{\mathrm{p}}}{\varepsilon_{\mathrm{p}}} \frac{\partial q_i}{\partial t}(x,r,t), \tag{1.9}$$

where ε_{p} is the particle porosity and $D_{\mathrm{pore},i}$ denotes the pore diffusion coefficient of the i-th component. For reasons of symmetry, the concentration gradient at the center of the adsorber particle vanishes,

$$\left.\frac{\partial c_{\mathrm{p},i}}{\partial r}\right|_{x,r=0,t} = 0. \tag{1.10}$$

At $r = r_{\mathrm{p}}$, the concentration gradient is defined by the boundary condition

$$\left.\frac{\partial c_{\mathrm{p},i}}{\partial r}\right|_{x,r=r_{\mathrm{p}},t} = \frac{k_{\mathrm{film},i}}{\varepsilon_{\mathrm{p}} D_{\mathrm{pore},i}} \left(c_{\mathrm{v},i}(x,t) - c_{\mathrm{p},i}(x,r=r_{\mathrm{p}},t) \right) \tag{1.11}$$

linking the mass balance for the void volume and adsorber pore volume.

1.3.2.2 Transport Dispersive Model

By simplifying the previously described GRM, several other model classes can be derived. One of the most widely used chromatography models is the transport dispersive model (TDM). The TDM assumes that mass transfer resistance is dominated by the external mass transfer resistance due to the stagnant boundary layer. By neglecting mass transfer resistance inside the adsorber bead ($D_{\mathrm{p},i} \to \infty$), no concentration distribution inside the adsorber particle is considered. Thus, the continuity equation inside the adsorber bead simplifies to

$$\frac{\partial c_{\mathrm{p},i}}{\partial t}(x,t) = k_{\mathrm{eff},i} \frac{3}{\varepsilon_{\mathrm{p}} r_{\mathrm{p}}} \left(c_{\mathrm{v},i}(x,t) - c_{\mathrm{p},i}(x,t) \right) - \frac{1-\varepsilon_{\mathrm{p}}}{\varepsilon_{\mathrm{p}}} \frac{\partial q_i}{\partial t}(x,t), \tag{1.12}$$

where $k_{\text{eff},i}$ denotes the effective mass transfer coefficient. Given the assumption $D_{\text{p},i} \to \infty$, $k_{\text{eff},i}$ is a lumped parameter that accounts for both external and internal mass transfer resistance. Mass transfer inside the column void volume is still described by Eq. (1.6) as in the GRM. However, the film diffusion coefficient $k_{\text{film},i}$ in the linear driving force model has to be replaced by $k_{\text{eff},i}$.

1.3.2.3 Ideal Column Model

The ideal column model represents the simplest transport model described first by Wicke [181], Wilson [183], and DeVault [39]. By assuming $D_{\text{ax}} \to 0$, $D_{\text{pore},i} \to \infty$, and $k_{\text{film},i} \to \infty$, it neglects the influence of axial dispersion and all mass transfer resistances. Thus, the ideal model accounts only for convective transport in the mobile phase and thermodynamics. Introducing the total column porosity $\varepsilon_{\text{t}} = \varepsilon_{\text{v}} + (1 - \varepsilon_{\text{v}})\varepsilon_{\text{p}}$, the continuity equation simplifies to

$$\frac{\partial c_i}{\partial t}(x,t) = -\frac{u}{\varepsilon_{\text{t}}}\frac{\partial c_i}{\partial x}(x,t) - \frac{1 - \varepsilon_{\text{t}}}{\varepsilon_{\text{t}}}\frac{\partial q_i}{\partial t}(x,t), \tag{1.13}$$

where $c_i = c_{\text{v},i} = c_{\text{p},i}$. The liquid phase and stationary phase are at equilibrium as defined by the adsorption isotherm $q_i(c_i)$. Considering the chain law, Eq. (1.13) can be rewritten to describe the migration velocity

$$w(c_i^+) = \frac{u}{\varepsilon_{\text{t}}}\left(1 + \frac{1 - \varepsilon_{\text{t}}}{\varepsilon_{\text{t}}}\left.\frac{\partial q_i}{\partial c_i}\right|_{c_i = c_i^+}\right)^{-1} \tag{1.14}$$

of an arbitrary concentration c_i^+ inside the chromatography column as a function of the isotherm slope. In the case of linear or analytical chromatography, the condition $q_i \to 0$ holds and Eq. (1.14) simplifies to

$$w(c_i^+) = \frac{u}{\varepsilon_{\text{t}}}\left(1 + \frac{1 - \varepsilon_{\text{t}}}{\varepsilon_{\text{t}}}K_{\text{H},i}\right)^{-1}. \tag{1.15}$$

Even though the ideal model is highly simplified, Eq. (1.14) illustrates the great importance of thermodynamics in preparative chromatography. While in linear or analytical chromatography the migration velocity or retention time in the column is independent of c_i^+ [see Eq. (1.15)], protein migration in preparative chromatography is strongly dependent on the local protein concentration, as described by Eq. (1.14). Thus, the performance of a preparative chromatography process in isolating a protein of interest is largely determined by thermodynamics.

1.3.3 Parameter Estimation

The chromatography models introduced in the previous sections possess a vector of model parameters $\boldsymbol{\theta} = (k_{\text{eff},i}, D_{\text{pore},i}, ...)$ that is usually unknown and has to be inferred from experimental data in order to make the chromatography model predictive. The inference of $\boldsymbol{\theta}$ from experimental data is also referred to as inverse problem. Once $\boldsymbol{\theta}$ is known, the forward problem can be solved: the prediction of an unobserved chromatography run. Preparative experiments with pharmaceutical proteins are very cost-intensive and can only be performed within a limited scope. Thus, experimental data to solve the inverse problem

is often limited. As they can also contain experimental noise, parameter inference rarely leads to a precise point estimate for $\boldsymbol{\theta}$. This section recalls statistical principles that are necessary to perform parameter inference. In this context, the difference between frequentist and Bayesian parameter estimation is briefly discussed.

In chromatography, an experimental observation $\bar{y}$ usually represents a measured state at the column outlet, e.g. the concentration of a protein at the column outlet $\bar{y}(t) = c_{\mathrm{v},i}(L_{\mathrm{c}}, t)$. All measurements can then be visualized as a function of the process time t, as depicted by the chromatograms in Fig. 1.3. For the sake of simplicity, but without loss of generality, we consider in the following only one experiment. In this case, the time series of all experimental observations makes up the experimental data $\mathcal{D} = \{(t_k, \bar{y}(t_k))\}_{k=1}^m$, whereby m denotes the number of data points. Due to experimental noise, all measured data have an inherent uncertainty about their true value. It is common to assume that the model correctly represents the true underlying process and thus defines this true value [12; 116]. In this case $\bar{y}$ can be defined by

$$\bar{y}(t_k) = y(t, \boldsymbol{\theta}) + \varepsilon, \tag{1.16}$$

where $y(t, \boldsymbol{\theta})$ is the true value given by the model and ε represents the experimental error or noise. In this thesis, we consider normally distributed measurement noise. Thus, the uncertainty over $\bar{y}$ is expressed by the normal distribution

$$\bar{y}(t) \sim p(\bar{y} \mid t, \boldsymbol{\theta}) = \mathcal{N}\left(\bar{y} \mid y(t, \boldsymbol{\theta}), \sigma^2\right), \tag{1.17}$$

with $y(t, \boldsymbol{\theta})$ as mean and standard deviation σ. Considering Eq. (1.17) and independent and identically distributed (iid) observations, the likelihood of observing $\mathcal{D}$ given $\boldsymbol{\theta}$ is defined by

$$
\begin{aligned}
p(\mathcal{D} \mid \boldsymbol{\theta}) &\overset{\text{iid}}{=} \prod_{k=1}^m \mathcal{N}\left(\bar{y} \mid y(t_k, \boldsymbol{\theta}), \sigma_k^2\right) \\
&= \prod_{k=1}^m \frac{1}{\sqrt{2\pi\sigma_k^2}} \exp\left(-\frac{1}{2}\left(\frac{\bar{y}(t_k) - y(t_k, \boldsymbol{\theta})}{\sigma_k}\right)^2\right).
\end{aligned} \tag{1.18}
$$

It is a well-known measure for the distance between model prediction and measured data and plays a central role in both classical and Bayesian inference [46]. The way it is used, on the other hand, is fundamentally different in these two statistical approaches. In the classical or frequentist approach, the observed and noisy data $\mathcal{D}$ is considered as a random variable, while $\boldsymbol{\theta}$ is an unknown but fixed parameter. A widely used frequentist single point estimate for $\boldsymbol{\theta}$ is the maximum likelihood estimate (MLE)

$$\hat{\boldsymbol{\theta}}_{\mathrm{MLE}}^{\mathcal{D}} = \arg\max_{\boldsymbol{\theta}} p(\mathcal{D} \mid \boldsymbol{\theta}) = \arg\min_{\boldsymbol{\theta}} \left[-\ln p(\mathcal{D} \mid \boldsymbol{\theta})\right] \tag{1.19}$$

that is obtained by maximizing Eq. (1.18) or minimizing the negative logarithm of Eq. (1.18). Determining the MLE corresponds to choosing the value of $\boldsymbol{\theta}$ for which the probability of the observed data set is maximized. The uncertainty in the estimate can be computed by considering the distribution of possible data sets $\mathcal{D}$. As $\hat{\boldsymbol{\theta}}_{\mathrm{MLE}}^{\mathcal{D}}$ depends on $\mathcal{D}$, it is itself a random variable. Thus, considering multiple experimental data sets provides a sampling distribution that quantifies the uncertainty in $\hat{\boldsymbol{\theta}}_{\mathrm{MLE}}^{\mathcal{D}}$. Note that each sampled set of observations provides only one single estimate. In Bayesian approach, the roles of $\mathcal{D}$ and

$\boldsymbol{\theta}$ are reversed. Here, $\boldsymbol{\theta}$ is treated as a random variable and inference is performed by conditioning on the actual fixed observed data. In Bayesian statistics we can also leverage prior knowledge on $\boldsymbol{\theta}$ according to the Bayes' theorem

$$p(\boldsymbol{\theta} \mid \mathcal{D}) \propto p(\mathcal{D} \mid \boldsymbol{\theta})p(\boldsymbol{\theta}), \tag{1.20}$$

whereby $p(\boldsymbol{\theta} \mid \mathcal{D})$ is the posterior probability that incorporates both the evidence provided by the measured data $p(\mathcal{D} \mid \boldsymbol{\theta})$ [Eq. (1.18)] and the prior $p(\boldsymbol{\theta})$. Once $p(\boldsymbol{\theta} \mid \mathcal{D})$ is estimated, the model can be used to make a prediction for an unobserved measurement $\tilde{y}$. In this case, the posterior predictive distribution for $\tilde{y}$

$$p(\tilde{y} \mid t, \mathcal{D}) = \int_{\boldsymbol{\theta}} p(\tilde{y} \mid t, \boldsymbol{\theta})p(\boldsymbol{\theta} \mid \mathcal{D})d\boldsymbol{\theta} \tag{1.21}$$

can be determined by marginalizing the distribution of $p(\tilde{y} \mid t, \boldsymbol{\theta})$ [Eq. (1.17)] over the posterior distribution $p(\boldsymbol{\theta} \mid \mathcal{D})$. The posterior predictive represents the uncertainty in the predicted value of $\tilde{y}$ due to the uncertainty in $\boldsymbol{\theta}$ and the experimental noise indicated by σ^2 in Eq. (1.17).

1.4 Colloidal Description of Proteins

Looking at proteins from the perspective of colloid science has a long tradition. The term colloid (from ancient greek κόλλα: glue) was introduced in 1861 by the British chemist Thomas Graham. In his research, he discovered that some substances can permeate a fine membrane, while others, such as glue, starch or gelatin, are retained. Based on this property, he referred to the first group of substances as crystalloids and the second group as colloids [58]. Using this principle, Graham was able to isolate both substance classes and introduced a method for separating and purifying colloids known as dialysis. Today, the term colloid is usually applied to a heterogeneous system in which small insoluble particles are dispersed throughout another medium [23; 56; 84]. As illustrated in Fig. 1.5, the dispersed particles are typically in the range from 1 nm to 1 μm [56; 75]. Colloidal systems differ from suspensions as Brownian motion keeps the particles dispersed and prevents them from settling. At the same time, they differ from homogeneous true solutions in that the dispersed particle is significantly larger than the solvent molecule or particle itself (e.g. water). An essential characteristic of colloidal systems is that their behavior is strongly governed by interfacial effects [23]. This characteristic can be attributed to the small size of the dispersed particles and thus to the large interface-to-volume ratio in colloidal systems. Thus, colloid science and interface science are closely related. In the following, important properties of proteins as colloidal particles are summarized. In addition, important surface interactions are described.

1.4.1 Protein Size

Although the aforementioned colloidal range from 1 nm to 1 μm is rather arbitrary and may vary within the literature, the particle size plays a central role in colloidal systems as it determines the interface-to-volume ratio and thus the significance of surface effects. If one wanted to define colloids exclusively by their size, proteins would represent a class of
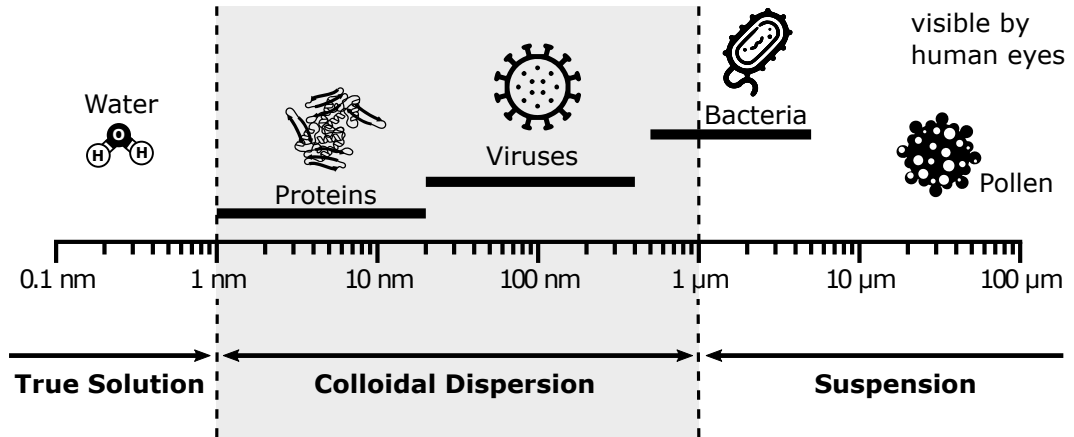
Figure 1.5: Typical length scales of colloidal systems.

very small colloidal particles with a size ranging from approximately 3 to 20 nm. However, given the complex structure of proteins, it is difficult to clearly define the size of a protein based on a single value. A parameter commonly used to determine the size of a protein is its hydrodynamic radius r_h. It is related to the diffusion coefficient of the protein D_0 according to the Stokes-Einstein equation

$$r_h = \frac{k_b T}{6\pi\eta D_0},$$

(1.22)

where k_b is the Boltzmann constant, T denotes the absolute temperature, and η is the dynamic viscosity. Accordingly, r_h represents the radius of a hypothetical spherical colloidal particle that diffuses at the same rate as the actual protein. The simplification of colloidal particles as perfect spheres as in Eq. (1.22) is quite common in colloidal science and is also used in this thesis.

1.4.2 Protein Charge

Most surfaces that are in contact with an electrolyte solution are charged either by the ionization of functional surface groups or the specific adsorption of ions from the bulk phase [23; 84; 171]. In the case of proteins, the surface charge can be attributed primarily to amino acids, the building blocks of any protein. Some amino acids have acidic or basic side chains which, if exposed to the electrolyte solution, define the surface charge. Such "immobile" charges on the surface of a colloidal particle are also referred to as inner or compact layer [171]. Given the amphoteric nature of proteins, the average surface charge density of the inner layer σ_I can be positive or negative, dependent on the pH at the protein surface.

To maintain electroneutrality, the charge of the inner layer is always balanced by an oppositely charged layer of ions. Both the inner layer and the layer of ions surrounding the colloidal particle form an electrostatic double layer that has a decisive influence on the behavior of a colloidal system. One of the most widely used theories to describe the electrostatic double layer is the theory of a diffuse double layer [59]. Due to thermal motion,

ions surrounding the colloidal particle are considered to be spatially inhomogeneously distributed within a diffuse layer surrounding the colloidal particle. Neglecting the finite ion size and considering only electrostatic interactions, the electrochemical potential $\bar{\mu}_i$ of an ion i with charge z_i inside the diffuse layer is given by

$$\bar{\mu}_i = \mu_i^* + k_{\mathrm{b}}T \ln\left(\frac{c_i}{c^+}\right) + ez_i\psi, \tag{1.23}$$

where μ_i^* is a reference potential at infinite dilution, ψ is the electrostatic potential, e is the elementary charge, and c^+ is a reference concentration. At equilibrium, the ion concentration inside the diffuse layer is given by the Boltzmann relation

$$c_i = c_{\infty,i} \exp\left(-z_i \frac{e\psi}{k_{\mathrm{b}}T}\right), \tag{1.24}$$

where $c_{\infty,i}$ represents the concentration of the i-th ion inside the bulk where the electrostatic potential vanishes ($\psi_\infty = 0$). The electrostatic force $F = -ez_i\nabla\psi$ acting on an ion counteracts the concentration gradient and leads to an accumulation of counter-ions and a depletion of co-ions near the surface of the colloidal particle. Considering a spherical protein with radius a and a solution with constant relative permittivity ε, ψ within the diffuse layer follows the Poisson equation

$$\nabla^2\psi(r) = -\frac{e}{\varepsilon\varepsilon_0}\sum_i z_i N_{\mathrm{A}} c_i(r), \tag{1.25}$$

where ε_0 represents the vacuum permittivity, N_{A} is the Avogadro number, and r denotes the radial position. Combining the Boltzmann relation (1.24) with the Poisson equation leads to the Poisson-Boltzmann equation. It is a continuum mean-field approach assuming point-like ions in thermodynamic equilibrium and neglecting ion-ion correlations [23].

The inner and diffuse layer may be considered as two adjacent subsystems that are in constant equilibrium [6]. Electroneutrality requires that the charges of both layers compensate each other. Considering that the electric field vanishes for $r \to \infty$, this equilibrium condition is sufficed by Gauss' law

$$\left.\frac{\partial\psi}{\partial r}\right|_{r=a} = -\frac{\sigma_{\mathrm{I}}}{\varepsilon\varepsilon_0}. \tag{1.26}$$

This boundary condition implies that σ_{I} or the charge of a protein is strongly affected by its electrostatic environment, in particular the electrostatic potential at the protein surface $\psi_0 = \psi(a)$. If the diffuse layer is manipulated, the inner layer has to regulate its charge to maintain electroneutrality, and *vice versa* [171]. Thus, the charge of a protein can vary not only with the pH in the bulk but also with the presence of another charged surface or the ionic strength in the bulk.

1.4.3 Double Layer Forces

If two charged surfaces approach each other, their electrostatic double layers start to overlap and an electrostatic double layer force F_{dl} arises that can be attractive or repulsive. According to the Derjaguin approximation, the force acting between two particles of arbitrary shape can be related to the interaction free energy per unit area w between two

(a)

(b)
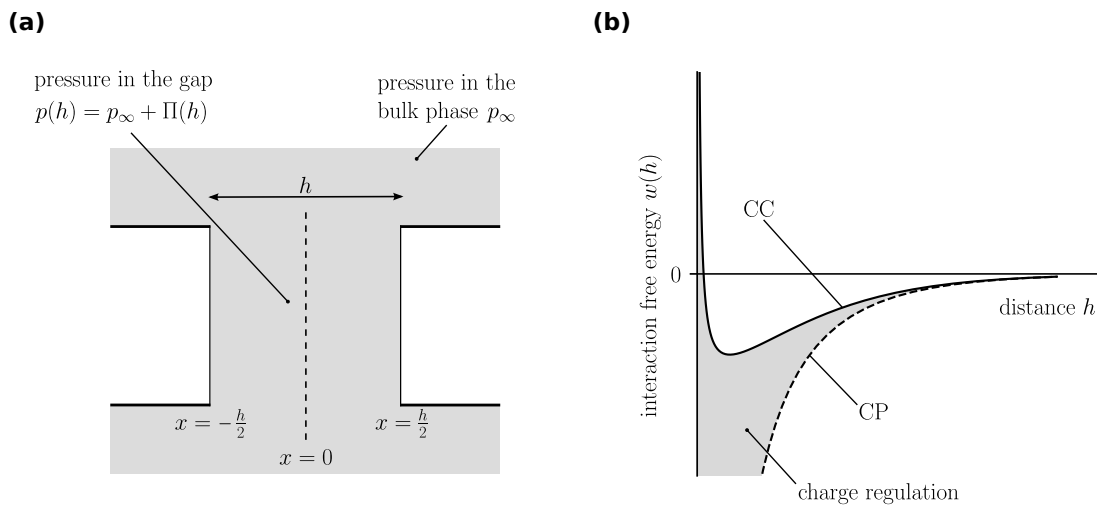
Figure 1.6: Schematic representation of the double layer interactions. (a) The disjoining pressure between two planar surfaces separated by the distance h. The figure is adapted from [23]. (b) Schematic representation of w between two oppositely charged planar surfaces separated by the distance h. The interaction profile is shown for the constant charge (CC) and constant potential (CP) boundary condition. The gray shaded region between both limiting cases indicates the area where the interaction profile is expected to be, considering charge regulation.

planar surfaces of the same surface charge density,

$$F_{\mathrm{dl}}(h) = 2\pi r_{\mathrm{eff}} w(h), \tag{1.27}$$

where h denotes the distance between both planar surfaces and r_{eff} represents the effective radius [148]. Common geometries considered include the interaction between two identical spheres with radius a or the interaction between a sphere and a planar surface. In this case the effective radius is given by $r_{\mathrm{eff}} = a/2$ and $r_{\mathrm{eff}} = a$, respectively. Considering two parallel plates, $w(h)$ in Eq. (1.27) can be derived from the disjoining pressure Π according to

$$w(h) = \int_h^\infty \Pi(h')dh'. \tag{1.28}$$

As schematically shown in Fig. 1.6(a), the disjoining pressure $\Pi(h) = p(h) - p_\infty$ represents the difference between the pressure within the gap between both plates $p(h)$ and the pressure in the bulk phase p_∞. For double layer interactions, Π is given by

$$\Pi = k_{\mathrm{b}}T \sum_i c_{\infty,i} N_{\mathrm{A}} \left(\exp\left(-z_i \frac{e\psi(x)}{k_{\mathrm{b}}T} \right) - 1 \right) - \frac{\varepsilon\varepsilon_0}{2} \left(\frac{\partial\psi}{\partial x} \right)^2, \tag{1.29}$$

where x denotes the position in between both plates, as shown in Fig. 1.6 [23; 84]. It can be noticed that Π is composed of two contributions. The first contribution is always repulsive (positive) and accounts for the osmotic contribution. When two equally charged plates approach each other, the ion concentration in the gap increases with decreasing distance. The osmotic pressure increases and leads to a repulsive force. The second quadratic part is always attractive and represents the electrostatic field energy contribution (Maxwell stress) [23]. While both contribution depend on the position within the gap x, it is

important to note that the sum of both contributions and thus Π is constant throughout the gap. Thus, Π can be evaluated at any x once $\psi(x)$ is known by solving the Poisson-Boltzmann equation. For this, boundary conditions must be defined at the surface of both plates. Often it is assumed that either the surface charge density of the inner layer σ_I or the electrostatic potential at the surface ψ_0 remains unchanged during the approach. This is also referred to as constant charge (CC) or constant potential (CP) boundary condition, respectively. As an example, Fig. 1.6(b) shows schematically w acting between two oppositely charged plates as a function of h. The interaction profile is shown for both boundary conditions, CC and CP. Both boundary conditions represent limiting cases. The gray shaded region between both limiting cases indicates the area where the interaction profile is expected to be, considering the mutual interplay between inner and diffuse layer and the regulation of σ_I and ψ_0 during the approach, as discussed in the previous section.

CHAPTER 2

Research Proposal

As pointed out in Sec. 1.2, downstream process development is a highly regulated environment. Within the QbD framework, regulatory agencies encourage the use of science- and risk-based approaches to generate a sound understanding of the process and ensure the safety and efficacy of the product. Despite these efforts, processes understanding to date is largely based on experiential knowledge and empiricism rather than true scientific knowledge. To meet the goals of QbD, process understanding in the form of mechanistic models can serve as an alternative or addition to empirical evidence. Even though the benefits of a model-based process development approach have been demonstrated by academia, there are still unresolved issues that hinder the systematic application of mechanistic models in the highly regulated environment of biopharmaceutical industry.

The major goal of this research is to solve problems that prevent mechanistic models from being used in a more systematic way in the development of IEX processes. In an industry where risk aversion is the cultural norm, it is particularly important to reduce the intrinsic risk of mechanistic models by (a) developing mechanistic models that represent the real process with as little error as possible, and (b) developing approaches to assess the uncertainty of models to support decision making in process development not only in a science-based manner, but also in a risk-based manner, as encouraged by QbD.

As described in Sec. 1.3.3, every mechanistic model contains model parameters that are often unknown and need to be inferred from experimental data. Thus, even though the model itself is based on first principles, it calls upon statistics for solving the inverse problem. The solution of the inverse problem is rarely an exact solution, but leaves some uncertainty in the model parameters. At the beginning of this work, frequentist approaches already existed to analyze this parameter uncertainty in chromatography models, usually based on confidence intervals as a measure for uncertainty. However, these approaches do not adequately answer the question of how this parameter uncertainty affects model predictions. Having a measure of the predictive uncertainty of a model is important in industrial applications as it is the model predictions that support decision making, not the model parameters themselves. Therefore, one goal of this work is to develop a workflow to assess the predictive uncertainty of mechanistic chromatography models in a systematic and especially quantitative way.

The inference of model parameters relies on the assumption that the model is true and is a perfect representation of reality. In fact, a mechanistic model - like any other model - is always a simplification or approximation of reality, as pointed out in Sec. 1.3. To describe the system in a mathematical way, it is always based on certain assumptions or simplifications. By repeatedly applying the model to new experimental data, it must be ensured that the simplifications made are still valid and that the model structure itself adequately represents the true process behavior. In the case of the adsorption of proteins onto IEX media, the mathematical description is usually based on the assumption that the interaction is defined by a stoichiometric reaction between the protein and adsorber ligands. For the past three decades, the SMA model described in Sec. 1.3.1.2 has been the most widely used stoichiometric adsorption model not only in academia but also in industrial applications. However, with increasing application of the model in industry, it has become apparent that only in limiting cases, the model provides an adequate description of the real process behavior. Discrepancies between simulated and observed process behavior often limit the applicability of mechanistic models, making a purely empirical understanding of the process the only option.

Motivated by the limitations of the SMA model and other adsorption models, the main part of this work is devoted to the development of an alternative adsorption model. In addition to increasing the accuracy of the mechanistic description, the focus is also on the degree of mechanistic abstraction. Simplifications made during the derivation of a model always lead to a certain level of model parameter abstraction. In case of the SMA model, for instance, the charge of a protein is abstracted by a stoichiometric coefficient (see Sec. 1.3.1.2). In this particular case, the degree of abstraction is very high. By describing protein adsorption in IEX chromatography using a colloidal description of proteins, briefly addressed in Sec. 1.4, the aim is to reduce the level of abstraction and provide a more rigorous physical approach to describe protein adsorption.

In summary, this research addresses two important challenges related to mechanistic modeling of IEX chromatography in industrial practice. The findings and resulting approaches could contribute to a better understanding of protein adsorption in IEX chromatography and a more widespread application of mechanistic models in process development.

2.1 Manuscript Overview

This section provides an overview of all publications that constitute this publication-based thesis. All articles are peer-reviewed and published in international, well-established scientific journals and are not used in any other publication-based thesis. The full text of all main contributions follows in Chapters 3 to 6.

Chapter 3: Prediction Uncertainty Assessment of Chromatography Models using Bayesian Inference **21**

T. Briskot, F. Stückler, F. Wittkopp, C. Williams, J. Yang, S. Konrad, K. Doninger, J. Griesbach, M. Bennecke, S. Hepbildikler, J. Hubbuch

Journal of Chromatography A (1587), 2019, p. 101-110

This publication describes a statistical framework for the calibration and uncertainty assessment of mechanistic chromatography models. Using Bayesian inference, the presented framework exploits available experimental data to identify the uncertainties in model parameters. In contrast to previous approaches, the presented framework considers the propagation of these parameter uncertainties to model simulations to provide a quantitative assessment of the predictive performance and reliability of the mechanistic model. The benefit of this uncertainty assessment is demonstrated using the example of a mechanistic model describing the separation of an antibody from its impurities on a strong cation exchanger. Despite significant parameter uncertainty, it is demonstrated that the mechanistic model can perform reliable extrapolations beyond observed process conditions.

Using Bayes theory of probability, the presented framework exploits information provided by experimental data and prior knowledge

Chapter 4: Adsorption of Colloidal Proteins in Ion Exchange Chromatography under Consideration of Charge Regulation **37**

T. Briskot, T. Hahn, T. Huuk, J. Hubbuch

Journal of Chromatography A (1611), 2020, p. 460608

In this publication, a mechanistic model is introduced that describes the adsorption of proteins onto IEX media within the linear adsorption range. In contrast to the traditional stoichiometric description of protein adsorption within the framework of the SMA model, the proposed adsorption model is based on a non-stoichiometric description of electrostatic interactions in IEX chromatography by means of a colloidal descriptions of proteins and the Poisson-Boltzmann equation. The proposed model explicitly accounts for the effect of pH and ionic strength on the adsorption equilibrium. Its capability of describing the adsorption equilibrium is demonstrated by simulating Henry coefficients of multiple proteins on different adsorber systems as a function of ionic strength and pH.

Chapter 5: Protein Adsorption on Ion Exchange Adsorbers: A Comparison of a Stoichiometric and Non-Stoichiometric Modeling Approach

T. Briskot, T. Hahn, T. Huuk, J. Hubbuch

Journal of Chromatography A (1653), 2021, p. 462397

In this study, the theory of the adsorption model presented in Chapter 4 is extended to the nonlinear adsorption range. In addition to the electrostatic interactions between a single protein and the adsorber surface, the developed colloidal particle adsorption (CPA) model accounts for electrostatic and steric interactions between adsorbed proteins. The advantage of the presented model in comparison to the traditional SMA model is demonstrated by simulating adsorption isotherms of a monoclonal antibody over a wide range of ionic strength and pH. It is shown that adsorption isotherms can be reproduced more accurately by the developed CPA model than by the traditional SMA model.

Chapter 6: Analysis of Complex Protein Elution Behavior in Preparative Ion Exchange Processes using a Colloidal Particle Adsorption Model

T. Briskot, T. Hahn, T. Huuk, G. Wang, S. Kluters, J. Studts, F. Wittkopp, J. Winderl, P. Schwan, I. Hagemann, K. Kaiser, A. Trapp, S. M. Stamm, J. Koehn, G. Malmquist, J. Hubbuch

Journal of Chromatography A (1654), 2021, p. 462439

This publication describes a kinetic derivation of the CPA model providing an expression for the rate of adsorption and desorption. Combined with a transport model such as the GRM or TDM, the kinetic for of the CPA model can be used to simulate preparative column chromatography. The general applicability of the model in describing preparative IEX processes is demonstrated using multiple industrial case studies. It is shown that the CPA model is able to describe complex protein elution behavior that could not be described by the traditional SMA model in the past.

Prediction Uncertainty Assessment of Chromatography Models using Bayesian Inference

Till Briskot[1], Ferdinand Stückler[1], Felix Wittkopp[2], Christopher Williams[3], Jessica Yang[3], Susanne Konrad[1], Katharina Doninger[1], Jan Griesbach[1], Moritz Bennecke[1], Stefan Hepbildikler[1], Jürgen Hubbuch[4]

[1] Roche Pharma Technical Development, Roche Diagnostics GmbH, Penzberg, Germany

[2] Roche Pharma Research and Early Development, Roche Innovation Center Munich, Roche Diagnostics GmbH, Penzberg, Germany

[3] Department of Purification Development, Genentech Inc., South San Francisco, USA

[4] Karlsruhe Institute of Technology (KIT), Institute of Process Engineering in Life Sciences, Section IV: Biomolecular Separation Engineering, Karlsruhe, Germany

Abstract

Mechanistic modeling of chromatography has been around in academia for decades and has gained increased support in pharmaceutical companies in recent years. Despite the large number of published successful applications, process development in the pharmaceutical industry today still does not fully benefit from a systematic mechanistic model-based approach. The hesitation on the part of industry to systematically apply mechanistic models can often be attributed to the absence of a general approach for determining if a model is qualified to support decision making in process development.

In this work a Bayesian framework for the calibration and quality assessment of mechanistic chromatography models is introduced. Bayesian Markov Chain Monte Carlo is used to assess parameter uncertainty by generating samples from the parameter posterior distribution. Once the parameter posterior distribution has been estimated, it can be used to propagate the parameter uncertainty to model predictions, allowing a prediction-based uncertainty assessment of the model. The benefit of this uncertainty assessment is demonstrated using the example of a mechanistic model describing the separation of an antibody from its impurities on a strong cation exchanger. The mechanistic model was calibrated at moderate column load density and used to make extrapolations at high load conditions. Using the Bayesian framework, it could be shown that despite significant parameter uncertainty, the model can extrapolate beyond observed process conditions with high accuracy and is qualified to support process development.

Keywords: *Ion exchange chromatography; Monoclonal antibody; Mechanistic modeling; Parameter estimation; Markov Chain Monte Carlo; Prediction uncertainty*

3.1 Introduction

Preparative chromatography is still the primary workhorse in the purification of high quality biopharmaceutical products [160]. In the development of chromatography processes, mechanistic models play an increasingly important role. The possible applications of mechanistic models go far beyond the plain optimization of these processes [71; 80; 97; 100; 118; 122–124; 155]. They provide a way to perform process control [100; 165], root-cause investigation [18], process scale-up [53; 111; 123], and *in silico* process robustness studies [14; 30; 37; 86–88; 92; 180]. Despite numerous successful applications in academia and increased support for mechanistic modeling in pharmaceutical companies [77; 92; 180], many decisions made in process development today still do not fully benefit from a systematic mechanistic model-based approach. One possible explanation for this restraint is the lack of confidence in mechanistic models because of the absence of a general approach to assess model uncertainty. Due to the complexity of pharmaceutical products and processes and the highly regulated nature of the industry, decision making is always a science- and risk-based procedure [81–83]. Mechanistic models can only deliver their full potential in identifying and reducing these risks if we understand the intrinsic risks of the models itself.

Mechanistic process models represent the current state of knowledge of a process and its underlying physical principles in a mathematical manner. Due to the complexity of most real-world processes, they are generally based on explicitly formulated assumptions and hypotheses. In this way, a mechanistic model is always a simplification of reality. By repeatedly validating the model with new experimental data, it can be ensured that model assumptions are valid and accurately represent the real process. Like statistical models, mechanistic models contain parameters and thus call upon statistics to get high confidence in these unknown model parameters. The estimation of these parameters belongs to the class of so called inverse problems. Parameters which are difficult to assess or cannot be measured directly are estimated by fitting the model to experimental data. The limited amount of experimental data and the uncertainty in the data can lead to large parameter uncertainties or even parameter non-identifiability [134], resulting in uncertainty in model predictions. The computation of parameter uncertainty in mechanistic chromatography models is usually based on a frequentist point of view using the Fisher information matrix (FIM) to approximate the single parameter confidence intervals and parameter covariance [18; 78]. Using the FIM has some important limitations, especially for nonlinear models. It will only give a lower bound for the uncertainty, and uses symmetric confidence intervals [91]. Uncertainty analysis for mechanistic models in systems biology showed that a Fisher information based approach can lead to misleading results for the parameter uncertainty [51; 91]. Another frequentist approach for the analysis of parameter uncertainty is bootstrapping. The bootstrap is a Monte Carlo technique that uses data resampling and parameter estimation using the resampled data to determine parameter confidence intervals. Borg et al. [15; 16] and Zhang et al. [194] used the parametric bootstrap to investigate the impact of measurement errors in process inputs and process outputs on model parameter uncertainty, respectively. For both approaches, the bootstrap and FIM, large parameter uncertainties have been reported in the past, but it was hardly analyzed how this parameter uncertainty affects the predictive power of the mechanistic model.

In other research areas like climate research [47] cosmology [172], and systems biology [173; 174], Bayesian inference has been used to assess prediction uncertainty of models.

In systems biology, it has been concluded that a sole inspection of parameter uncertainty is insufficient for evaluating the prediction uncertainty of a model [173; 174], making a prediction-based uncertainty assessment inevitable.

Inspired by the aforementioned contributions this work introduces an approach to assess the prediction uncertainty of arbitrary chromatography models using Bayesian inference. Usage and benefit of the approach will be illustrated by applying it to a cation exchange chromatography process of an industrial antibody. A mechanistic model was calibrated at moderate column load density and used to predict the separation of the antibody from its impurities at high load densities taking into account the model uncertainty. Such a model-based approach is especially attractive for early-stage process development, as it can help to reduce development time and feedstock consumption significantly. The application of the Bayesian approach to this case study allowed for a prediction-based uncertainty assessment of the model, increasing the confidence in the mechanistic model on the part of the decision makers.

3.2   Theory

3.2.1   Transport Dispersive Model

In conformity with previous works [78; 80; 124], a column-wide mass balance equation according to the transport dispersive model (TDM) is used to describe the migration of solutes through the packed bed of length L_c [m] and average adsorber particle diameter d_p [m]. In the TDM, the temporal change of the solute bulk concentration $c_{\mathrm{b},i}$ [mol m^{-3}] in the interstitial volume is described by the differential equation [152]

$$
\begin{aligned}
\frac{\partial c_{\mathrm{b},i}}{\partial t}(x,t) = & -\frac{1-\varepsilon}{\varepsilon}\frac{6}{d_\mathrm{p}}k_{\mathrm{eff},i}\left(c_{\mathrm{b},i}(x,t) - c_{\mathrm{p},i}(x,t)\right) \\
& -u_{\mathrm{int}}(t)\frac{\partial c_{\mathrm{b},i}}{\partial x}(x,t) + D_{\mathrm{ax}}\frac{\partial^2 c_{\mathrm{b},i}}{\partial x^2},
\end{aligned}
\tag{3.1}
$$

where t [s] is the time, x [m] is the axial position, u_{int} [m s^{-1}] is the interstitial velocity, D_{ax} [m^2 s^{-1}] represents the axial dispersion coefficient, and ε [$-$] denotes the interstitial bed porosity. The accumulation term in Eq. (3.1) is defined by the linear driving force model, with the component specific effective film diffusion coefficient $k_{\mathrm{eff},i}$ [m s^{-1}] and solute concentration $c_{\mathrm{p},i}$ [mol m^{-3}] on the adsorber surface. The solute concentration $c_{\mathrm{p},i}$ is assumed to be identical to the constant concentration inside the particle pore system. Intra-particle and extra-particle mass transfer resistance is lumped together in $k_{\mathrm{eff},i}$. Equation (3.1) is completed with Danckwerts' boundary conditions of dispersive systems at the column inlet

$$
\frac{\partial c_{\mathrm{b},i}}{\partial x}(x=0,t) = \frac{u_{\mathrm{int}}(t)}{D_{\mathrm{ax}}}\left(c_{\mathrm{b},i}(x=0,t) - c_{\mathrm{inlet},i}(t)\right)
\tag{3.2}
$$

and the column outlet

$$
\frac{\partial c_{\mathrm{b},i}}{\partial x}(x=L_\mathrm{c},t) = 0.
\tag{3.3}
$$

The mass balance in the adsorber pore system can be described by the differential equation

$$
\varepsilon_\mathrm{p}\frac{\partial c_{\mathrm{p},i}}{\partial t}(x,t) + (1-\varepsilon_\mathrm{p})\frac{\partial q_i}{\partial t}(x,t) = k_{\mathrm{eff},i}\frac{6}{d_\mathrm{p}}\left(c_{\mathrm{b},i}(x,t) - c_{\mathrm{p},i}(x,t)\right),
\tag{3.4}
$$

where q_i [mol m^{-3}] denotes the adsorbed solute concentration per adsorber skeleton volume and ε_{p} [−] represents the particle porosity.

3.2.2 Generalized Ion Exchange Isotherm

According to the stoichiometric displacement model [176], the interaction mechanism in ion exchange chromatography is primarily based on an exchange of counter-ions bound to charged ligands on the adsorber surface with charged proteins in the mobile phase, and *vice versa*. The stoichiometric exchange of a monovalent salt S from the stationary phase by n different proteins P$_i$, $i \in [1, n]$, can be described by the stoichiometric expression

$$P_i^{\nu_i} + \nu_i LS_{\mathrm{ads}} \rightleftharpoons L_{\nu_i} P_{i,\mathrm{ads}}^{\nu_i} + \nu_i S, \tag{3.5}$$
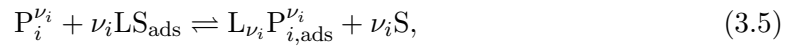
whereby ν_i [−] represents the characteristic charge of the i-th protein, L is the ligand, and the subscript ads depicts the adsorbed state. Due to the size of proteins, some of the ligands on the adsorber surface are sterically shielded by adsorbed protein molecules. Counter-ions bound to these shielded ligands cannot be replaced by protein molecules in the mobile phase. To account for this steric shielding effect Brooks and Cramer introduced a steric shielding parameter σ_i [−] [22]. To comply with the law of electroneutrality, the sum of the charges of the counter-ions and the interacting charges on the proteins must be equal to the ionic capacity of the ion-exchanger

$$\Lambda_{\mathrm{IEX}} = \bar{q}_{\mathrm{s}} + \sum_{i=1}^{n} \left(\nu_i + \sigma_i \right) q_i, \tag{3.6}$$

where $\bar{q}_{\mathrm{s}}$ [mol m^{-3}] represents the bound salt concentration per adsorber skeleton volume available for exchange [22]. It must be mentioned that Eq. (3.6) is only strictly valid for strong cation exchangers, as used in this work [125; 184].

If we assume that the salt in both states and proteins associated with the ligands behave thermodynamically ideal, the adsorption/desorption rate of the i-th protein is described by the rate equation

$$r_i = \frac{\partial q_i}{\partial t} = k_{\mathrm{ads},i} \bar{q}_{\mathrm{s}}^{\nu_i} \gamma_i c_{\mathrm{p},i} - k_{\mathrm{des},i} q_i c_{\mathrm{p,s}}^{\nu_i}, \tag{3.7}$$

where γ_i [−] is the activity coefficient of the i-th protein in solution and $k_{\mathrm{ads},i}$ [s^{-1} (mol^{-1} m^3)$^{\nu_i}$] and $k_{\mathrm{des},i}$ [s^{-1} (mol^{-1} m^3)$^{\nu_i}$] are the reaction rate constants of adsorption and desorption, respectively. The original steric mass action (SMA) isotherm by Brooks and Cramer was derived assuming a constant activity coefficient for the protein in the mobile phase ($\gamma_i = 1$) [22]. According to Huuk et al. [78], this simplification is no longer valid for high load densities. To get an expression for the activity coefficient it is convenient to introduce the rational activity coefficient $\gamma_i^* = \gamma_i (\gamma_i^\infty)^{-1}$ with $\gamma_i^\infty = \lim_{c_i \to 0} \gamma_i$ [−] as the activity coefficient of the i-th protein at infinite dilution. Mollerup used the van der Waals equation of state to get the expression

$$\ln \gamma_i^* = k_{\mathrm{s},i} c_{\mathrm{p,s}} + \sum_{j=1}^{n} k_{\mathrm{p},ij} c_{\mathrm{p},j}, \tag{3.8}$$

with $k_{\mathrm{s},i}$ [mol^{-1} m^3] and $k_{\mathrm{p},ij}$ [mol^{-1} m^3] as constants [113].

Using the Eq. (3.6) for the available salt concentration $\bar{q}_s$ in Eq. (3.7) as well as the rational activity coefficient, we get the final rate equation

$$\frac{\partial q_i}{\partial t} = k_{\text{ads},i}\gamma_i^\infty \left(\Lambda_{\text{IEX}} - \sum_{j=1}^n \left(\nu_j + \sigma_j\right) q_j \right)^{\nu_i} \gamma_i^* c_{\text{p},i} - k_{\text{des},i} q_i c_{\text{p,s}}^{\nu_i}. \tag{3.9}$$

Instead of the rate constants $k_{\text{ads},i}$ and $k_{\text{des},i}$ we will hereinafter use the equilibrium constant $k_{\text{eq},i} = \gamma_i^\infty k_{\text{ads},i} k_{\text{des},i}^{-1}$ $[-]$ and the kinetic constant $k_{\text{kin},i} = k_{\text{des},i}^{-1}$ $[\text{s} \, (\text{mol m}^{-3})^{\nu_i}]$ as the reciprocal value of $k_{\text{des},i}$.

3.2.3   Inverse Problem Formulation

To estimate the model parameters $\boldsymbol{\Theta} = (k_{\text{eff},1}, k_{\text{kin},1}, ...)$ by inverse modeling, experimental data is collected in several experiments at discrete time points t_k at the column outlet. In the following we denote the measured molar concentration of the i-th component at the column outlet as $\bar{y}_i(t_k)$ $[\text{mol m}^{-3}]$ and summarize all component concentrations at time point t_k in the vector $\bar{\boldsymbol{y}}(t_k) = (\bar{y}_1(t_k), ..., \bar{y}_n(t_k))$. Under the assumption of additive normally distributed and isotropic measurement noise, the measurement is given by $\bar{y}_i(t_k) = y_i(t_k; \boldsymbol{\Theta}) + \varepsilon_{i,k}$ where $y_i(t_k; \boldsymbol{\Theta})$ $[\text{mol m}^{-3}]$ indicates the true model and $\varepsilon_{i,k} \sim \mathcal{N}(0, \sigma_{i,k}^2)$ $[\text{mol m}^{-3}]$ represents the normally distributed measurement noise with zero mean and variance $\sigma_{i,k}^2$ $[(\text{mol m}^{-3})^2]$. Under these conditions, the likelihood of the measured data $\mathcal{D} = \{(t_k, \bar{\boldsymbol{y}}(t_k))\}_{k=1}^m$ is given by

$$P\left(\mathcal{D} \mid \boldsymbol{\Theta}\right) = \prod_{i=1}^n \prod_{k=1}^m \frac{1}{\sqrt{2\pi\sigma_{i,k}^2}} \exp\left(-\frac{1}{2} \left(\frac{\bar{y}_i(t_k) - y_i(t_k; \boldsymbol{\Theta})}{\sigma_{i,k}} \right)^2 \right), \tag{3.10}$$

where n and m represent the number of components and number of observed time points, respectively. The likelihood is a well-known measure for the distance between model prediction and data [46]. To get an expression for $\sigma_{i,k}$ in Eq. (3.10), a parameterized function

$$\sigma_{i,k} = s_{\text{a},i} + s_{\text{b},i} y_i(t_k; \boldsymbol{\Theta}), \tag{3.11}$$

can be used, where $s_{\text{a},i}$ $[\text{mol m}^{-3}]$ and $s_{\text{b},i}$ $[-]$ represent the absolute and relative noise, respectively [135; 182].

Parameter estimation is commonly performed from a frequentist viewpoint. In frequentist statistics the parameters are considered as fixed but unknown and the experimental data $\mathcal{D}$ as random samples from the true model [116]. The maximum likelihood estimate of the parameters

$$\hat{\boldsymbol{\Theta}}^{\mathcal{D}} = \underset{\boldsymbol{\Theta}}{\arg\max} \, P\left(\mathcal{D} \mid \boldsymbol{\Theta}\right) = \underset{\boldsymbol{\Theta}}{\arg\min} \left[-\ln P\left(\mathcal{D} \mid \boldsymbol{\Theta}\right)\right], \tag{3.12}$$

is obtained by maximizing the likelihood [Eq. (3.10)] or by minimizing the negative logarithm of the likelihood. In contrast to frequentist inference, from a Bayesian viewpoint the solution of the inverse problem with fixed $\mathcal{D}$ encompasses various possible parameter values that have been chosen from some probability distribution. In this way, Bayesian inference attaches a notion of probability to the parameter values [174]. Before performing any experiment, the Bayesian assigns a prior probability distribution $P(\boldsymbol{\Theta})$ to the parameters that captures the knowledge of $\boldsymbol{\Theta}$ before observing $\mathcal{D}$. If the empirical evidence

about the parameters is limited or not available at all, non-informative uniform priors can be used. These priors are called non-informative as they do not favor certain parameter values. According to the Bayes' theorem, the prior probability is converted into a posterior probability

$$P\left(\boldsymbol{\Theta} \mid \mathcal{D}\right) = \frac{P\left(\mathcal{D} \mid \boldsymbol{\Theta}\right) P(\boldsymbol{\Theta})}{P(\mathcal{D})} \tag{3.13}$$

by incorporating the evidence provided by the measured data $P\left(\mathcal{D} \mid \boldsymbol{\Theta}\right)$ [Eq. (3.10)]. The denominator in Eq. (3.13) is the normalization constant, which ensures that the posterior distribution on the left-hand side is a valid probability density that integrates to one. Due to the high dimensionality of practical models it is usually not possible to calculate this normalization constant analytically [12]. This problem can be circumvented by using stochastic methods like Markov Chain Monte Carlo (MCMC), since they only need the non-normalized numerator of Eq. (3.13). The basic idea behind MCMC is to construct a Markov chain [12; 116] that generates a stochastic walk in the model parameter space and whose stationary distribution is $P\left(\boldsymbol{\Theta} \mid \mathcal{D}\right)$. Over time, MCMC draws representative parameter samples from $P\left(\boldsymbol{\Theta} \mid \mathcal{D}\right)$ that summarizes everything known about $\boldsymbol{\Theta}$ [116], i.e. prior knowledge and experimental evidence. The "width" of $P\left(\boldsymbol{\Theta} \mid \mathcal{D}\right)$ can be used as a measure of confidence in $\boldsymbol{\Theta}$, indicating how certain $\boldsymbol{\Theta}$ is given the measured data $\mathcal{D}$.

3.3   Material and Methods

3.3.1   Buffer System, Adsorber, and Protein

For all experiments described below, 50 mM sodium acetate (pH 5.0) was used as equilibration buffer. Product elution was performed using a high salt buffer consisting of 50 mM sodium acetate (pH 5.0) and sodium sulfate ranging from 150 to 200 mM, depending on the experiment. All chromatography runs were conducted with a ECO$^{\mathrm{PLUS}}$ column (YMC Europe, Dinslaken, Germany) packed with the strong cation exchanger Poros XS (Applied Biosystems, Foster City, California, USA). The resin beads are comprised of an almost incompressible cross-linked poly[styrene divinylbenzene] backbone with an average particle diameter of 50 μm. The resin bed volume and height were 16 ml and 205 mm, respectively. A human IgG1 monoclonal antibody (mAb) with a molecular weight of approximately 150 kDa was used. The feed material for all chromatography runs consisted of Protein A pools with a total protein concentration of approximately 4 mg mL^{-1} and an average product purity of 98.5% according to size exclusion chromatography. Antibody charge heterogeneity was determined by analytical cation exchange chromatography (CEX). According to the elution order in the analytical chromatogram, four major protein variants (Pro1- Pro4) were identified. The average proportion of the four protein variants in the feed stock was 43.9%, 16.1%, 38.2%, and 1.8%, respectively.

3.3.2   Instruments

All experiments were performed on an ÄKTAexplorer equipped with a pump module P900, UV monitor UV900, a conductivity cell pH/C 900, as well as a fraction collector Frac-950 (all GE Healthcare, Little Chalfont, Buckinghamshire, UK).

3.3.3   Software

The ÄKTAexplorer was operated with the control software UNICORN 5.20 (GE Healthcare, Little Chalfont, Buckinghamshire, UK). The system of partial differential equations described earlier were numerically solved by using ChromX (GoSilico GmbH, Karlsruhe, Germany) [69] with a Python 3.6.2 interface. For all simulations, the variable time-stepping scheme IDAS was used for discretization in time. The initial time step was set to 0.2 s. Discretization in space was performed with 50 equidistant axial cells using a linear Streamline-Upwind Petrov-Galerkin (SUPG) ansatz. Simulation accuracy was verified by regularly repeating simulations with a finer axial discretization of 100 equidistant axial cells and a fractional step θ-scheme with a constant time step of 0.1 s. The Python packages SciPy and emcee were used to solve the inverse problem and perform MCMC, respectively.

3.3.4   System and Column Characterization

Extra column parameters describing the residence time distribution in the system peripheral were determined by conducting tracer pulse injections using 1% (v/v) acetone in equilibration buffer and high salt buffer. Column porosities and the axial dispersion coefficient were determined from pulse injection experiments using high salt buffer as pore-penetrating, non-adsorbing tracer and 10 mg mL^{-1} dextran with an average molecular weight of 2000 kDa as non-pore penetrating, non-interacting tracer. All experiments were performed in triplicates. The axial dispersion coefficient was determined by fitting the TDM [Eq. (3.1)] to the dextran peaks using the software ChromX. The mass transfer term in Eq. (3.1) was neglected, since dextran is non-pore penetrating. The ionic capacity of Poros XS was determined by acid-base titration according to [79]. The capacity value was not determined specifically for the packed column but was taken from an in-house database.

3.3.5   Column Experiments

For model calibration, three bind-and-elute experiments comprising of one linear gradient experiment and two step elution experiments were used. All experiments were performed at a constant flow rate of 2.6 mL min^{-1} and a column load density of 30 mg mL^{-1}. For the linear gradient experiment, 120 mL of feed material was injected on the equilibrated column. After a post-loading wash step over 5 CV of equilibration buffer, elution was performed by increasing the salt concentration linearly to 200 mM over 30 CV. For each step elution experiment, the column was first equilibrated with 5 CV of equilibration buffer. Subsequently, 120 mL load was injected. After a post-loading wash step over 5 CV of equilibration buffer, the salt concentration was increased to 150 mM and 180 mM, respectively. In all experiments, 8 mL fractions were collected at the column outlet and analyzed by analytical CEX to determine the molar protein concentration.

For model validation, a third step elution experiment was performed at a load density of 80 mg mL^{-1}. The equilibrated column was loaded with 315 mL feed material and washed with equilibration buffer over 5 CV. For product elution, the salt concentration was increased to 150 mM. After the UV trace at 280 nm exceeded 100 mAU, the column effluent was pooled. The collection of the column effluent was stopped once the declining UV trace fell below 420 mAU. The collected product pool was analyzed by analytical CEX.

3.3.6 Markov Chain Monte Carlo

First, the maximum likelihood estimate [Eq. (3.12)] for the three calibration experiments was determined using simulated annealing and sequential least squares programming (SLSQP) as global and local optimizer, respectively. Simulated annealing was used to explore a wide range of the parameter space and find the global optimum. The result of simulated annealing was further refined with the local optimizer. The measurement noise parameters $s_{a,i}$ and $s_{b,i}$ were assumed to result from uncertainties in the concentration determination and analytical CEX. Both parameters were derived *a priori* from internal analytical method validation reports. The analytical methods were developed specifically for the antibody system being studied in this work. The method validation reports ensure that these analytical methods are suited for the quantitative evaluation of the analytes and contain method characteristics like method sensitivity, accuracy, and precision [48]. To generate samples from the parameter posterior distribution, the Goodman & Weare [55] affine invariant ensemble sampler was used for MCMC as implemented in the emcee Python package [49]. An ensemble MCMC algorithm is a Markov Chain that operates an ensemble of walkers in parallel. Fifty walkers were initialized around the maximum likelihood estimate and evolved over 5000 steps per walker. For all model parameters, a non-informative uniform prior in logarithmic parameter space was used. The convergence of MCMC was assessed by visual inspection of the likelihood and parameter traces of the walkers. Once the Markov chain reached the region of highest posterior density, samples were acquired from the parameter posterior distribution.

3.3.7 Model Prediction and Extrapolation

After model calibration at a load density of 30 mg mL^{-1}, the mechanistic model was used to investigate the effect of the load density on the impurity pattern in the product pool for a 150 mM salt step elution process. The process conditions were identical to those of the 150 mM salt step elution experiment used for model calibration. Only the load volume was adjusted to increase the load density stepwise from 30 mg mL^{-1} up to 110 mg mL^{-1}. For each load density, a product pool was taken and analyzed *in silico* using a UV-based pooling criterion of 100 mAU and 420 mAU for the pooling start point and end point, respectively. The pooling criterion was defined based on previous experiments. The transformation from molar protein concentration to UV absorption was performed according to the Lambert-Beer law using the theoretical extinction coefficient of the mAb. To assess the propagation of parameter uncertainty to model prediction, 500 parameter sets were drawn randomly from the parameter posterior distribution. Model predictions were performed for each of the drawn parameter sets. To verify the model predictions at high load density, the predictions at 80 mg mL^{-1} were compared to experimental results.

3.4 Results and Discussion

3.4.1 System and Column Characterization

The system dead volume of 2.01 mL was determined from tracer pulse injections without a column attached to the ÄKTA system. All experimental data from the system were

Table 3.1: Results from the system and column characterization.

Parameter	Unit	Value
System dead volume	[mL]	2.010
Column volume V_c	[mL]	16
Column length L_c	[mm]	205
Void fraction ε	[−]	0.407
Bead porosity ε_p	[−]	0.637
Axial dispersion D_{ax}	[mm^2 s^{-1}]	0.671
Ionic capacity Λ_{IEX}	[M]	0.673

corrected with respect to the measured dead volume. The void fraction, bead porosity, and axial dispersion coefficient were determined from tracer pulse experiments with column attached to the system. Since the external system dead volume was almost one order of magnitude smaller than the column volume, axial dispersion due to extra-column and intra-column effects were summarized in one single axial dispersion coefficient D_{ax} [130]. As dextran peaks showed a noticeable tailing, only the non-diffusive peak front was used for the estimation of D_{ax}. It is safe to assume that this diffusion behavior is caused by the polydispersity of dextran [129]. The ionic capacity was taken from an in-house database. All results are summarized in Table 3.1.

3.4.2 Markov Chain Monte Carlo

To assess the propagation of parameter uncertainty to model predictions, MCMC was first used to acquire samples from the parameter posterior probability distribution. For high dimensional parameter spaces, MCMC can take impractically long to converge if we initialize the walkers at random guesses. To reduce this burn-in phase, the walkers were initialized around the maximum likelihood estimate [Eq. (3.12)] found by global and local optimizers. The protein parameters $k_{p,ij}$ in Eq. (3.8) were neglected since Huuk et al. observed almost no impact of the parameter on the model output for a mAb on Poros 50HS and a load density of 90 mg mL^{-1} [78]. The measurement noise parameters $s_{a,i}$ and $s_{b,i}$ quoted at the top of Table 3.2 were estimated *a priori* from internal method validation reports. They result from the propagation of uncertainties in the concentration determination and analytical CEX.

Starting around the maximum likelihood estimate, the chains were evolved over 5000 steps for each chain. For parameters that are by definition non-negative, non-informative uniform priors in logarithmic parameter space were used. This applies for all model parameters, except $k_{s,i}$. Since the $k_{s,i}$ values of the maximum likelihood estimate were negative for all proteins, the parameter space for MCMC was restricted to negative $k_{s,i}$ values, allowing a log-scale for all model parameters. As mentioned earlier, the uniform priors do not favor certain parameter values but ensure that the parameters attain no physically unrealistic values. The convergence of MCMC was assessed by visual inspection of the likelihood and parameter traces of the chains. As shown in Fig. A.1 in the appendix, the chains converged and reached the region of highest posterior density after 3000 steps. Parameter samples taken during this burn-in-phase were discarded to avoid assigning too much weight to improbable samples. To get a sufficient approximation of the parameter posterior distribution, the chains were run for an additional 2000 steps leading to 100,000 representative samples from the posterior distribution.

Table 3.2: Model parameters estimated by MCMC. Quoted model parameters are the medians of the parameter posterior distribution. Parameter uncertainty is expressed by the 95% credible interval. The absolute noise parameter s_a and relative noise parameter s_b were estimated *a priori* from internal method validation reports.

Parameter	Pro1	Pro2	Pro3	Pro4
$s_{a,i}$ [M]	$4.43e-7$	$2.36e-7$	$3.30e-7$	$1.51e-8$
$s_{b,i}$ $[-]$	0.041	0.047	0.033	0.033
$\log\left(k_{\mathrm{eff},i} \cdot 1\,\mathrm{s\,mm}^{-1}\right)$ $[-]$	$-3.22\,^{+0.05}_{-0.04}$	$-3.03\,^{+0.06}_{-0.07}$	$-2.71\,^{+0.07}_{-0.06}$	$-2.52\,^{+0.09}_{-0.06}$
$\log\left(k_{\mathrm{kin},i} \cdot 1\,\mathrm{s}^{-1}\,\mathrm{M}^{-\nu_i}\right)$ $[-]$	$-3.26\,^{+0.17}_{-0.18}$	$-6.21\,^{+0.25}_{-0.26}$	$-6.30\,^{+0.18}_{-0.21}$	$-7.79\,^{+1.06}_{-0.55}$
$\log\left(k_{\mathrm{eq},i}\right)$ $[-]$	$0.38\,^{+0.19}_{-0.18}$	$-2.36\,^{+0.33}_{-0.21}$	$-2.62\,^{+0.19}_{-0.21}$	$-2.71\,^{+0.23}_{-0.21}$
ν_i $[-]$	$6.60\,^{+0.19}_{-0.23}$	$10.24\,^{+0.25}_{-0.30}$	$10.52\,^{+0.20}_{-0.21}$	$11.18\,^{+0.32}_{-0.40}$
σ_i $[-]$	$158.56\,^{+6.29}_{-6.46}$	$156.93\,^{+13.74}_{-17.34}$	$102.52\,^{+5.52}_{-5.03}$	$136.86\,^{+31.06}_{-44.36}$
$k_{s,i}$ $[\mathrm{M}^{-1}]$	$-30.38\,^{+1.41}_{-1.39}$	$-13.72\,^{+1.41}_{-2.37}$	$-8.39\,^{+1.32}_{-1.05}$	$-7.37\,^{+0.80}_{-0.96}$
$k_{p,ij}$ $[\mathrm{M}^{-1}]$	-	-	-	-

The computation time required was several days on a personal computer. However, since MCMC allows efficient parallelization, the computation time can be reduced significantly if the simulations are performed on a computer cluster. Figure A.2 in the appendix shows the resulting histograms of marginal parameter distributions as well as the joint parameter distributions. It is important to note that further samples would lead to a better resolution of the posterior distribution but would also increase the computational effort. Table 3.2 quotes marginalized parameter values and uncertainties for all model parameters. The depicted model parameters are medians of the marginal parameter distributions. Parameter uncertainty is expressed by the 95% credible interval. The estimated effective film diffusion coefficient increases from Pro1 to Pro4, indicating a change in the hydrodynamic radius from Pro1 to Pro4. The characteristic charge and k_{eq} values of Pro2, Pro3, and Pro4 are very similar, indicating similar interaction characteristics. The k_s values are negative for all proteins which has also been reported in [78] for a mAb on Poros 50HS. The results summarized in Table 3.2 indicate substantial uncertainty in the parameter estimates, especially for k_{kin} and k_{eq}. As described by Eq. (3.9), the effect of the shielding parameter σ is only visible in the non-linear region of the isotherm where protein molecules start to compete for binding sites on the adsorber surface. Despite the moderate load density of $30\,\mathrm{mg\,mL}^{-1}$, the remaining uncertainty in the shielding parameter is relatively low. Only Pro4 shows significant uncertainty in σ. It is safe to assume that the injected amount of this component was not sufficient to estimate σ reliably.

In process modeling, more attention should be paid to the predictive uncertainty of the model than on interpreting the model parameters and their uncertainty. Using the generated MCMC samples, the parameter uncertainty contained in the posterior parameter distribution can be propagated accurately and easily to predictions of the mechanistic model. Given samples of the parameter posterior distribution, predictions can be made by solving the model for each of the parameter sets. The distribution of such predictions is referred to as the predictive posterior distribution and reflects the prediction uncertainty of the model. Figure 3.1 shows the experimental fraction data used for Bayesian parameter estimation, along with the predictive posterior distribution of the model. Solid lines indicate the median of the predictive posterior distribution. The transparent areas
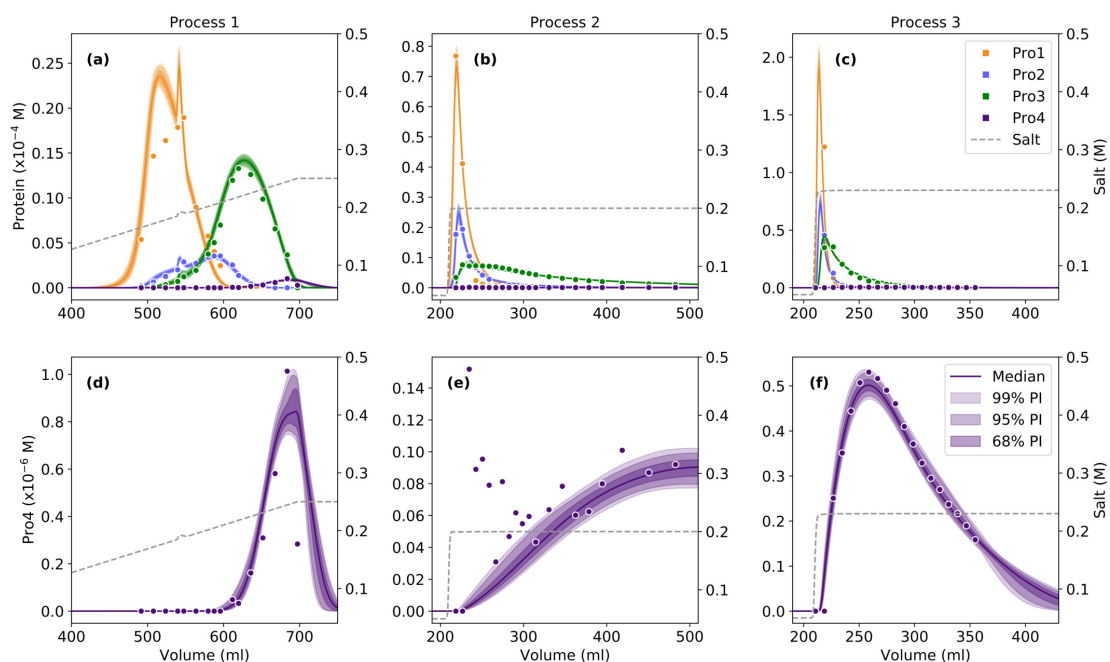
Figure 3.1: Propagation of parameter uncertainty to model predictions. (a)-(c) Comparison of experimental fraction data (dots) and model predictions (lines). The salt concentration is indicated by gray dashed lines. Solid colored lines indicate the median of the predictive posterior distribution. The transparent areas indicate the 99%, 95%, and 68% prediction intervals (PIs). (d)-(f) For the sake of clarity, experimental data and model predictions for Pro4 are also shown separately. It is important to note that the upper limits of the y-axes differ among the experiments.

indicate the 99%, 95%, and 68% prediction intervals (PIs), respectively. It is important to note that the upper limits of the y-axes in Fig. 3.1 differ among the experiments. In very good accordance with the experimental data, the mechanistic model describes the elution behavior of Pro2 and Pro3. Deviations from the experimental data can be observed for Pro1 at the peak maximum in Fig. 3.1(a) and at the peak tailing in Fig. 3.1(b). The sharp increase in the predicted protein concentration at about 550 mL of the linear gradient was caused by an unintended jump in the ionic strength and could also be observed in the UV trace of the ÄKTA system. The reason for the jump in the ionic strength was not investigated further. The predictive posterior distribution for the calibration runs reveals spots where the uncertainty has the largest impact on the model. The spots of greatest uncertainty are mainly concentrated close to the peak maximum of Pro1 and Pro2 under step elution conditions, as shown in Fig. 3.2. The large prediction uncertainty at these spots can be ascribed to the steep elution profile of both components, which complicates the exact localization of their peak maxima. Finer fractions close to the peak maximum of Pro1 and Pro2 would reduce this uncertainty as they would provide more detailed data. For the sake of clarity, the good agreement between experimental data and model predictions for the lowest concentrated component Pro4 is also shown separately in Fig. 3.1(d)-(f). The low concentration of Pro4 close to the analytical detection limit increases the risk of experimental outliers as shown in Fig. 3.1(e). These potential outliers were not removed prior to model calibration and are also an explanation for the significant parameter uncertainty for Pro4. A spot of large uncertainty for Pro4 can be observed in
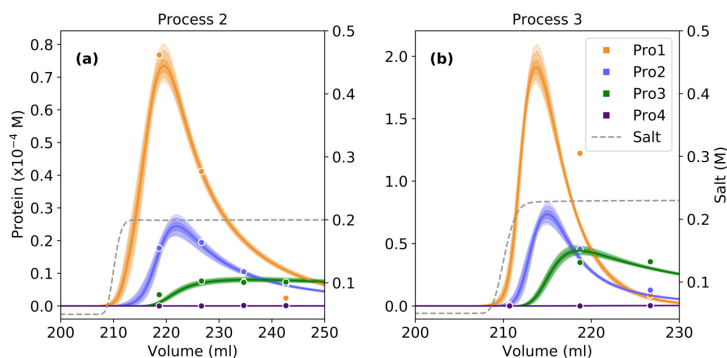
Figure 3.2: Elution front of process 2 and 3 shown in Fig. 3.1. Comparison of experimental fraction data (dots) and model predictions (lines). The salt concentration is indicated by gray dashed lines. Solid colored lines indicate the median of the predictive posterior distribution. The transparent areas indicate the 99%, 95%, and 68% prediction intervals (PIs).

Fig. 3.1(f) in the range of 350 to 450 mL. Additional fractions in this range are also likely to reduce the uncertainty for this component.

3.4.3 Model Prediction and Extrapolation

A major advantage of mechanistic models over purely empirical models is the ability to extrapolate beyond observed process conditions. In process modeling, this capability is often used for *in silico* process optimization, process scale-up, and root-cause-investigation. It is, however, only possible if the model parameters are perfectly known. Uncertainty in the model parameters can restrict this ability considerably. To assess the model's ability to extrapolate, the load density of the 150 mM salt step elution process shown in Fig. 3.1(b) and Fig. 3.1(e) was increased *in silico* from 30 $mg\,mL^{-1}$ up to 110 $mg\,mL^{-1}$. For each load density, product pools were taken and analyzed model-based using a pooling criterion of 100 mAU and 420 mAU for the pooling start point and end point, respectively. The predictive posterior distribution for protein recovery is shown in Fig. 3.3(a). It is important to note that the upper limits of the y-axes in Fig. 3.3 differ among the proteins. The percent recovery is shown since it enables a component-specific assessment of the prediction uncertainty. The predicted protein purity shown in Fig. 3.3(b), which is often used as a measure of product quality, is not suitable for such an assessment as it depends on the protein sum signal. For Pro1, the load density has almost no effect on protein recovery. The steady decline in Pro1 recovery from a load density of approximately 90 $mg\,mL^{-1}$ can be ascribed to an increasing breakthrough of Pro1 during the loading phase. Pro3 shows a significant increase in recovery, which leads to a significant decline in the pool purity for Pro1 and Pro2. It is interesting to see that even though the mechanistic model was calibrated at a moderate load density of 30 $mg\,mL^{-1}$ and contains significant parameter uncertainty, the prediction uncertainty for Pro1 to Pro3 increases only slightly from 30 $mg\,mL^{-1}$ to 110 $mg\,mL^{-1}$. Only for Pro4, a significant increase in the prediction uncertainty can be observed when increasing the load density beyond the observed process conditions at 30 $mg\,mL^{-1}$, as shown in Fig. 3.3(a). This indicates, that the model predictions for Pro4 at load densities beyond 40 $mg\,mL^{-1}$ should be used with caution.
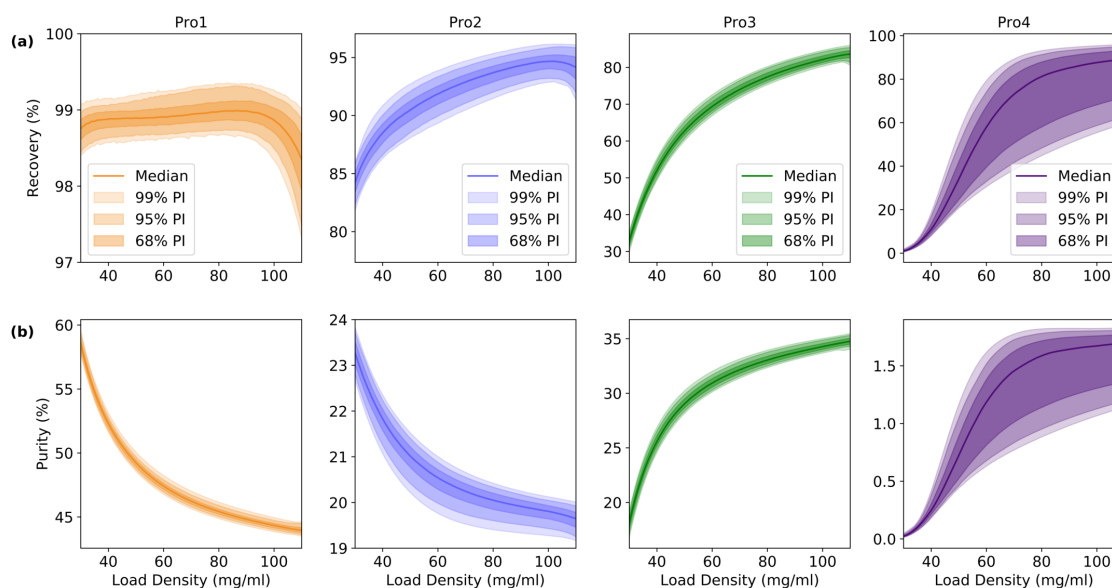
Figure 3.3: Predicted effect of load density on protein recovery (a) and protein purity (b) in the product pool. Solid colored lines indicate the median of the predictive posterior distribution. The transparent areas indicate the 68%, 95%, and 99% prediction intervals (PIs). It is important to note that the upper limits of the y-axes differ among the proteins.

To validate the model's predictions at high load conditions, *in silico* data at a load density of 80 mg mL^{-1} were verified experimentally. The load density of 80 mg mL^{-1} was chosen due to the decline in Pro1 recovery from a load density of 90 mg mL^{-1}, as shown in Fig. 3.3(a). The experimental results as well as the model predictions are quoted in Table 3.3. As expected, model predictions for Pro1 to Pro3 are in good agreement with experimental data. Taking into account the high parameter uncertainty and the considerable extrapolation, the prediction uncertainty is fairly low. For all three components, the experimental data are within the 95% PI, indicating that the parameter uncertainty is propagated correctly to model predictions. As already suggested, the prediction for Pro4 disagrees with the experimental data. The measured Pro4 content in the product pool is slightly outside the 95% PI which is not surprising considering the measured content well below 1%, the experimental noise in Fig. 3.1(e), and the significant model uncertainty regarding Pro4 shown in Fig. 3.3(a). The results quoted in Table 3.3 show that the mechanistic model can perform reliable extrapolations at 80 mg mL^{-1} with a prediction uncertainty below 1%. The model prediction for Pro4 deviates slightly from experimental data but is greater than the experimental value. In a risk-based assessment of the model quality this deviation may be tolerated since Pro4 has to be depleted and the model is

Table 3.3: Predicted and measured pool composition at a load density of 80 mg/ml. Quoted model predictions are the medians of the predictive posterior distribution. The quoted prediction uncertainty represents the 95% prediction interval.

	Pro1 [%]	Pro2 [%]	Pro3 [%]	Pro4 [%]
Model prediction	$45.4^{+0.5}_{-0.4}$	$20.1^{+0.3}_{-0.5}$	$33.0^{+0.7}_{-0.6}$	$1.6^{+0.2}_{-0.7}$
Measurement	45.5	20.4	33.6	0.5

therefore on the "safe side".

3.5 Conclusion

We introduced a Bayesian framework for the calibration and prediction uncertainty assessment of mechanistic chromatography models using the example of a CEX step to separate an industrial antibody from its impurities. A mechanistic model was calibrated at moderate column load density and used to make extrapolations at high load conditions. Due to the small amount of experimental data for model calibration and noise in the experimental data, estimated model parameters showed substantial uncertainty. Taking into account this parameter uncertainty, the model's ability to extrapolate was verified experimentally. Despite the significant parameter uncertainty, the mechanistic model could perform reliable extrapolations at high load densities with a prediction uncertainty below 1%.

The advantage of the presented Bayesian framework is founded in the propagation of information provided by experimental data and prior assumptions from general physical knowledge and previous models to the posterior distribution of model predictions. The concept of using both prior knowledge and experimental evidence is a concept firmly anchored in the traditional development of chromatography processes but has sparsely been used in the course of the modeling of such processes. The Bayesian prior used in this study was a very weak prior, that does not favor any parameter sets but ensures that parameters attain no physically unrealistic values. The more mechanistic models are calibrated and the more empirical evidence about the model parameters is available, the more informative priors can be formulated and converted into the parameter posterior distribution using experimental data. Once the parameter posterior distribution has been estimated, parameter uncertainty can be easily propagated to model predictions allowing a prediction-based uncertainty assessment of the model. Having a measure for the prediction uncertainty is crucial for a model-based decision making in process development, since model predictions can only be verified after the decision has been made. Knowing the predictive limits of the mechanistic model not only increases the modelers confidence in the mechanistic model but increases also the confidence on the part of the decision makers and authorities. This will help to develop more robust and efficient processes for biopharmaceutical products.

Acknowledgements

Adsorption of Colloidal Proteins in Ion Exchange Chromatography under Consideration of Charge Regulation

Till Briskot[1,2], Tobias Hahn[1], Thiemo Huuk[1], Jürgen Hubbuch[2]

[1] GoSilico GmbH, Karlsruhe, Germany
[2] Karlsruhe Institute of Technology (KIT), Institute of Process Engineering in Life Sciences, Section IV: Biomolecular Separation Engineering, Karlsruhe, Germany

Abstract

Mechanistic modeling of protein adsorption has gained increasing importance in the development of ion exchange (IEX) chromatography processes. The most common adsorption models use a stoichiometric representation of the adsorption process based on the law of mass action. Despite the importance of these models in model-based development, the stoichiometric representation of the adsorption process is not accurate for the description of long-range electrostatic interactions in IEX chromatography, limiting the application and mechanistic extension of these models.

In this work an adsorption model is introduced describing the non-stoichiometric electrostatic interaction in IEX chromatography based on the linear Poisson-Boltzmann equation and a simplified colloidal representation of the protein. In contrast to most recent non-stoichiometric models, the introduced model accounts for charge regulation during the adsorption process. Its capability of describing the adsorption equilibrium is demonstrated by simulating partitioning coefficients of multiple proteins on different adsorber systems as a function of ionic strength and pH. Despite model simplifications the physical meaning and predictive value of the model could be preserved. By transferring model parameters of a monoclonal antibody (mAb) from one adsorber system to another, it could be demonstrated that protein parameters are theoretically not only valid on a specific adsorber system but freely transferable to other adsorbers. The predictive value of the mechanistic model on the new adsorber system was highlighted by predicting the elution behavior of charge variants of the mAb.

Keywords: *Mechanistic modeling; Charge regulation; Resin transfer; Monoclonal antibody; Charge variants*

4.1 Introduction

Ion exchange (IEX) chromatography still remains one of the most frequently used polishing steps in the purification of recombinant proteins due to its moderate cost, high selectivity under mild operating conditions, and its capability to deplete both, process-related impurities and product-related impurities [57; 156]. For the development of IEX processes, mechanistic modeling has gained increasing importance in recent years. Efficient modeling of these processes requires knowledge of the full adsorption isotherm that describes how specific resin properties, buffer conditions, and other process parameters affect protein adsorption.

The mechanistic description of protein adsorption in IEX chromatography was introduced by Boardman and Partridge [13] and further developed by Regnier and co-workers [44; 98; 144]. It is based on a stoichiometric exchange of counter-ions bound to the adsorber surface with charged proteins in the mobile phase, and *vice versa*. This initial stoichiometric displacement model applies to the linear adsorption range of proteins. It was extended to the nonlinear adsorption range by the introduction of the steric mass action (SMA) model by Brooks and Cramer [22], which has been the most widely used adsorption model for IEX chromatography ever since, both in academia [14; 71; 80; 87; 88; 97; 123; 124] and industry [21; 77; 92; 180]. Mechanistic models like the SMA model have contributed greatly to the understanding of protein chromatography and are still expedient for the fundamental research on chromatography. However, the stoichiometric description of the adsorption process according to the law of mass action implies short-range interactions between the protein and the adsorber surface and is therefore not an accurate representation for the long-range electrostatic interactions determining the retention of proteins in IEX chromatography [161–163]. The simplified representation of the adsorption process can hamper the mechanistic extension of stoichiometric models and limits their application to a specific adsorber system. Extensions of the SMA model trying to explicitly account for pH-dependent protein adsorption, are therefore mostly performed on a purely empirical bases [77; 92; 114], making the models valid only within a small pH range. More mechanistically driven pH-dependent SMA extensions have been introduced by Shen and Frey [153; 154] and Frech and co-workers [96; 97; 151]. However, due to the high degree of mechanistic abstraction, these model are only valid within a narrow pH range around the isoelectric point of a protein or contain a large number of model parameters which cannot be determined *a priori* but have to be determined by inverse modeling.

The theoretical limitations of stoichiometric models to describe the electrostatic interactions between charged proteins and the charged adsorber surface as a function of ionic strength and pH has prompted the development of non-stoichiometric adsorption models. These models are based on a more fundamental description of the electrostatic interactions in IEX chromatography using an idealized colloidal representation of the protein and analytical solutions of the linear Poisson-Boltzmann equation. Models using a more complex representation of the protein [142; 191] or solutions of the nonlinear Poisson-Boltzmann equation [52] are only available through cumbersome numerical computations, which make them of limiting practical use for model-based process development. Analytical expressions are only available for the linear Poisson-Boltzmann equation and a simplified geometrical representation of the protein. Ståhlberg et al. [163; 164] and Guélat et al. [64–67] used analytical expressions of the linearized Poisson-Boltzmann equation to calculate the interaction energy between the protein and the adsorber surface. Oberholzer and Lenhoff

[119; 120] used a solution of the based on the linear superposition approximation. All these analytical expressions assume that the charge of the protein remains constant during the adsorption process. This assumption has been questioned as the charge of the protein is affected by the local electrostatic environment [74; 109; 153; 154; 162]. As the protein approaches the adsorber surface, the local electrostatic environment changes, which can induce a regulation of the protein charge [6; 24; 171]. The non-stoichiometric model proposed by Ståhlberg and Jönssen [162] considers protein charge regulation but does not explicitly describe protein adsorption over a wide pH range.

This work introduces a mechanistic adsorption model which is based on a description of the non-stoichiometric electrostatic interactions in IEX chromatography. The model explicitly accounts for the effect of pH and ionic strength on the adsorption of a protein with known primary sequence similar to [64–67], but considers charge regulation during the adsorption process. The model's capability of describing adsorption equilibria is illustrated by simulating partitioning coefficients of multiple proteins on different adsorber systems as a function of pH and ionic strength. Finally, the transferability of model parameters from one adsorber system to another as well as the application of the model for product-related impurities are discussed.

4.2 Theory

4.2.1 Charge Regulation

We consider an isolated protein i and adsorber A which are immersed in an electrolyte solution with relative permittivity ε [−] and ionic strength I_m [mol m^{-3}]. The protein is considered to be a perfect sphere with radius a_i [m] which is characterized by its uniform surface charge density $\sigma_{\mathrm{I},i}$ [C m^{-2}] or electric surface potential $\psi_{0,i}$ [V]. The adsorber is considered to be a plane surface with uniform charge density $\sigma_{\mathrm{I,A}}$ and surface potential $\psi_{0,\mathrm{A}}$. Charges localized on the surface of the protein and adsorber are hereinafter referred to as the inner layer which is indicated by the subscript I. They originate from ionizable surface groups or the specific adsorption of ions from solution [67; 84]. The ionization of the j-th surface group R on the amphoteric surface of a protein is governed by the dissociation reaction

$$-\mathrm{RH}^{\zeta_j} \rightleftharpoons -\mathrm{R}^{(\zeta_j-1)} + \mathrm{H}^+ \tag{4.1}$$

whereby $\zeta_j \in [0, 1]$ represents the charge of the protonated acidic ($\zeta_j = 0$) or basic ($\zeta_j = 1$) site in units of elementary charge. The ionizable side chains include the imidazole moiety of histidine (His), the carboxyl groups of aspartic acid (Asp) and glutamic acid (Glu), the hydroxyl group of tyrosine (Tyr), the amino group of lysine (Lys), as well as the guanidino group of arginine (Arg). In conformity with previous works [64], it is assumed that the thiol group of cysteine does not contribute to the protein charge as it predominantly forms disulfide bridges in proteins. Neglecting ion specific binding, $\sigma_{\mathrm{I},i}$ can be written as

$$\sigma_{\mathrm{I},i}(\psi_{0,i}) = e N_\mathrm{A} \sum_j \Gamma_{j,i}\Bigg((\zeta_j - 1)\left[1 + \frac{c_{\mathrm{b,H^+}}}{K_{j,i}} \exp\left(-\frac{e\psi_{0,i}}{k_\mathrm{b}T}\right)\right]^{-1}$$
$$+ \zeta_j \left[1 + \frac{K_{j,i}}{c_{\mathrm{b,H^+}}} \exp\left(\frac{e\psi_{0,i}}{k_\mathrm{b}T}\right)\right]^{-1}\Bigg), \tag{4.2}$$

where e [C] represents the elementary charge, N_A [mol^{-1}] is the Avogadro number, $\Gamma_{j,i}$ [$\text{mol}\,\text{m}^{-2}$] is the surface density of the j-th ionizable residue, $K_{j,i}$ [M] is the dissociation constant of the functional group, k_b [$\text{J}\,\text{K}^{-1}$] is the Boltzmann constant, c_{b,H^+} [M] is the proton concentration in the bulk phase, and T [K] denotes the absolute temperature [171]. In the case of a cation exchanger the adsorber surface is solely covered by an acidic ligand L with surface density Γ_L. Its surface charge density is given by

$$\sigma_{I,A}(\psi_{0,A}) = -eN_A\Gamma_L \left[1 + \frac{c_{b,H^+}}{K_L}\exp\left(-\frac{e\psi_{0,A}}{k_b T}\right)\right]^{-1}. \tag{4.3}$$

In contrast to previous non-stoichiometric adsorption models [64–67], the dissociation reaction in Eq. (4.2) and Eq. (5.15) is determined by the proton concentration at the charged surface c_{0,H^+} and not by the bulk concentration itself. Both are related by the Boltzmann relation

$$c_{0,H^+} = c_{b,H^+}\exp\left(-\frac{e\psi_0}{k_b T}\right). \tag{4.4}$$

If we assume that all amino acids with ionizable side chains are located on the surface of the protein, $\Gamma_{j,i}$ in Eq. (4.2) is related to the number of amino acids $N_{j,i}$ [−] in the primary protein structure according to

$$\Gamma_{j,i} = \frac{N_{j,i}}{4\pi a_i^2 N_A}. \tag{4.5}$$

As the number of ionizable side chains in a protein is too large to calculate the ionization state individually, Eq. (4.2) considers an average ionization state for each type of side chain using a mean $\text{p}K_{j,i} = -\log(K_{j,i} \cdot 1\text{M}^{-1})$ [−] value. As a first approximation, one may use the intrinsic $\text{p}K$ values of the amino acids, as proposed by Guélat et al. [64–67]. However, due to charge-charge interactions, hydrogen-bonding, and burial of the ionizable side chains, $\text{p}K$ values of ionizable residues in proteins can deviate significantly from intrinsic values [17; 60; 126]. Alterations in the $\text{p}K$ value of histidine imidazole moieties are particularly important as they strongly determine the protein charge profile within the process-relevant pH range in cation exchange chromatography. The $\text{p}K$ of an individual imidazole moiety depends on whether the side chain is fully accessible or buried within the protein. Measured $\text{p}K$ values of buried imidazole moieties show a higher variability and are often higher than those of fully accessible side chains [45]. To take this variation into account, histidine side chains in a protein are divided into two groups with an average $\text{p}K$ value of $\text{p}K_{\text{His}1,i}$ and $\text{p}K_{\text{His}2,i}$, respectively.

In some cases, it is convenient to approximate Eq. (4.2) or Eq. (5.15) linearly around a reference potential ψ^*, as schematically shown in Fig. 4.1(a) for the inner charge of the protein. The charge potential-relationship is then given by

$$\sigma_I(\psi_0) = \sigma_I(\psi^*) - C_I(\psi^*)(\psi_0 - \psi^*), \tag{4.6}$$

where $\sigma_I(\psi^*)$ and

$$C_I(\psi^*) = -\left.\frac{\partial\sigma_I}{\partial\psi_0}\right|_{\psi_0=\psi^*} \tag{4.7}$$

[$\text{C}\,\text{m}^{-2}\,\text{V}^{-1}$] are the surface charge density and capacitance of the inner layer at ψ^*, respectively [24].

The charge density of the inner layer is balanced by an equal but oppositely charged diffuse layer D of spatial inhomogeneous distributed ions [84]. Neglecting the curvature of the

　　　　　　　　　　　　　　　　　　　　(b)
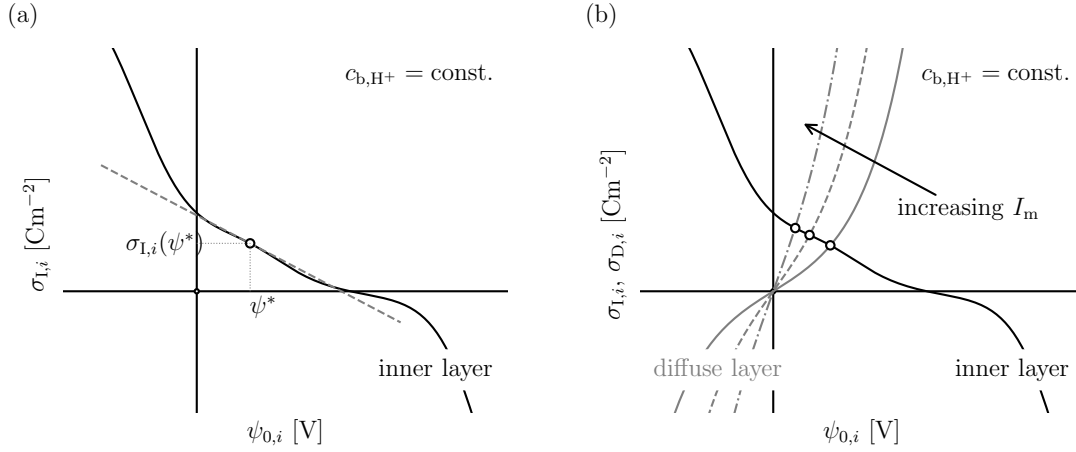
Figure 4.1: Schematic representation of the charge-potential relationship at a constant bulk pH. (a) Charge-potential relationship of the inner layer (solid black line) according to Eq. (4.2). The dashed gray line represents a linear approximation of the relationship around the reference potential ψ^* according to Eq. (4.6). (b) Charge-Potential relationship of the inner layer (solid black line) according to Eq. (4.2) and diffuse layer (gray lines) according to Eq. (4.8) at varying ionic strengths. Intercepts of both relationships are indicated by open circles. They define $\sigma_{I,i}$ and $\psi_{0,i}$ for a given ionic strength and pH in the bulk phase.

protein surface and considering a 1:1 electrolyte, the charge density compensated by the diffuse layer σ_D is given by the Grahame equation

$$\sigma_D = 2\varepsilon\varepsilon_0\kappa\frac{k_bT}{e}\sinh\left(\frac{e\psi_D}{2k_bT}\right), \tag{4.8}$$

where ψ_D denotes the electric potential at the origin of the diffuse layer, ε_0 [C V^{-1} m^{-1}] is the vacuum permittivity, and

$$\kappa = \sqrt{\frac{2e^2 I_m N_A}{k_b T \varepsilon\varepsilon_0}} \tag{4.9}$$

[m^{-1}] corresponds to the reciprocal Debye length. The Grahame equation derives from the nonlinear Poisson-Boltzmann equation. For the linear Poisson-Boltzmann equation (Debye-Hückel theory), Eq. (4.8) simplifies to

$$\sigma_D = \varepsilon\varepsilon_0\kappa\psi_D. \tag{4.10}$$

According to the Gouy-Chapman theory the diffuse layer potential is identical to the surface potential, namely $\psi_D = \psi_0$ [84; 171]. The charge-potential relationship of the diffuse layer [Eq. (4.8)] is schematically shown in Fig. 4.1(b). The inner and diffuse layer can be considered as two adjacent subsystems, each described by its charge-potential relationship [6]. The intercept of both relationships satisfies the equilibrium condition $\sigma_I = \sigma_D$ and defines σ_I and ψ_0 for a given ionic strength and pH in the bulk phase [6; 24; 171]. If the diffuse layer or electrostatic environment is manipulated, the inner layer has to regulate its charge density in order to satisfy electroneutrality, and *vice versa* (see Fig. 4.1(b)). This effect is referred to as charge regulation [6; 24; 171]. Depending on

whether Eq. (4.2) or Eq. (4.6) is used for σ_I, one distinguishes between full regulation and constant regulation [171].

4.2.2 Double Layer Forces

Both, the charged protein and the charged adsorber surface are surrounded by a diffuse layer. If the protein approaches the adsorber surface, the overlap of both diffuse layers gives rise to a double layer interaction defined by an attractive Maxwell stress and a repulsive osmotic pressure [121; 127]. These interactions are commonly described in the mean-field approximation using the nonlinear or linear Poisson-Boltzmann equation [177]. Solutions of the nonlinear Poisson-Boltzmann equation are only available through cumbersome numerical computations which makes them of limiting practical use for model-based process development. Analytical expressions are only available for the linear Poisson-Boltzmann equation. Ståhlberg et al. [163; 164] and Guélat et al. [64–67] used an analytical expression of the linearized Poisson-Boltzmann equation derived by Parsegian and Gingell [127] to calculate the interaction energy between the protein and the adsorber surface within the Derjaguin limit. Oberholzer and Lenhoff [119; 120] used a solution of the Poisson-Boltzmann equation based on the linear superposition approximation. These analytical expressions were derived assuming that the charge density of the interacting surfaces remains constant during the adsorption process [127]. This assumption has been questioned as the penetration of the diffuse layer of the protein into the diffuse layer of the adsorber induces a change in their surface potentials, leading to a regulation of the surface charge as described earlier in Fig. 4.1 [74; 162]. A simplified analytical solution of the linear Poisson-Boltzmann equation which accounts for charge regulation was introduced by Carnie and Chan [24]. Under the assumption of constant regulation for the inner layer [Eq. (4.6)] and diffuse layer [Eq. (4.10)], the interaction free energy per unit area w_i [J m^{-2}] between the protein and the adsorber at distance z [m] is given by

$$
\begin{aligned}
w_i(z) =& \varepsilon\varepsilon_0\kappa \frac{2\psi_{0,A}\psi_{0,i}\exp\left(-\kappa z\right)}{1-(2p_i-1)(2p_A-1)\exp\left(-2\kappa z\right)} \\
&+ \varepsilon\varepsilon_0\kappa \frac{\left[(2p_i-1)\psi_{0,A}^2+(2p_A-1)\psi_{0,i}^2\right]\exp\left(-2\kappa z\right)}{1-(2p_i-1)(2p_A-1)\exp\left(-2\kappa z\right)},
\end{aligned}
\tag{4.11}
$$

whereby

$$
p = \lim_{z\to\infty} p(z) = \frac{C_D}{C_D+C_I}
\tag{4.12}
$$

[−] is the regulation parameter of the isolated surface ($z\to\infty$) with the diffuse layer capacitance $C_D = \partial\sigma_D/\partial\psi_D$ [5; 6]. This parameter characterizes how the surface charge density changes upon approach. If the charge density of the protein and adsorber remains constant upon approach ($p_A = p_i = 1$), Eq. (5.19) simplifies to the expression of Parsegian and Gingell used in [67; 163; 164].

In conformity with previous models [64–67], the Derjaguin approximation [84]

$$
u_i(z) = 2\pi a_i \int_z^\infty w_i(z)dz.
\tag{4.13}
$$

is used to derive the interaction free energy u_i [J] between protein and adsorber. A closed-form expression of Eq. (5.18) with Eq. (5.19) for $w_i(z)$ can be found in [24]. The Derjaguin
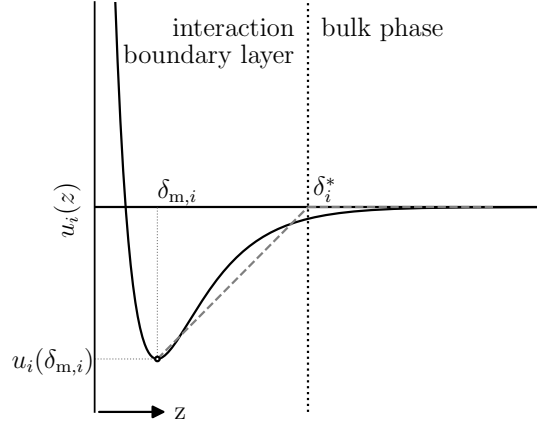
Figure 4.2: Schematic representation of the interaction boundary layer. The interaction free energy between protein and adsorber (black continuous line) is only relevant within a boundary layer at the adsorber surface. The interaction profile inside the interaction boundary layer is approximated by an idealized energy profile (dashed gray line).

approximation is accurate only for large κa_i when the diffuse layers are thin relative to the colloid size [11]. This Derjaguin limit is commonly not fulfilled for small colloids like proteins. Alternatives like the surface element integration [10] have shown to provide more accurate predictions than Eq. (5.18). However, as these approaches do not provide an analytical solution for u_i, they have not been further investigated.

4.2.3 Adsorption Isotherm

We consider the interaction profile $u_i(z)$ between protein and adsorber schematically shown in Fig. 4.2. Due to the finite extent of the diffuse layer, interactions between colloid and adsorber surface are only relevant inside a boundary layer with thickness δ_i^* [m] referred to as interaction boundary layer [146; 147; 159]. If the interaction energy between colloid and adsorber [Eq. (5.18)] has a minimum at

$$\delta_{\mathrm{m},i} = \arg\min_z u_i(z), \tag{4.14}$$

as shown in Fig. 4.2, a particle flux may be formed that accumulates protein inside the interaction boundary layer. The surface density of protein bound to the adsorber q_i [$\mathrm{mol\,m^{-2}}$] can then be defined by

$$q_i = c(\delta_i^*)K_i = c(\delta_i^*) \int_{\delta_{\mathrm{m},i}}^{\delta_i^*} \exp\left(-\frac{u_i(z)}{k_{\mathrm{b}}T}\right) dz, \tag{4.15}$$

whereby $c(\delta_i^*)$ corresponds to the colloid concentration in the bulk phase and K_i [m] is the partitioning coefficient. For a steep increase in u_i for $z < \delta_{\mathrm{m},i}$, Eq. (6.5) introduces little error but leaves δ_i^* as additional parameter to be specified. To get a closed-form expression for K_i in Eq. (6.5) we consider an idealized energy profile as shown in Fig. 4.2.

Table 4.1: Functionalization and ligand density of the adsorber systems used.

Resin	Functional group	Γ_{L} [μmol m^{-2}]	pK_{L} [$-$]
Fractogel EMD SE HiCap	sulfoisobutyl	5.64 [64; 67]	2.3 [89]
YMC BioPro SP (10 μm)	sulfopropyl	1.90 [64; 67]	2.3 [89]
YMC BioPro SP (5 μm)	sulfopropyl	1.22 [64]	2.3 [89]

Under these idealized conditions, the potential profile within $z = [\delta_{\mathrm{m},i}, \delta_i^*]$ is given by

$$u_i(z) = u_i(\delta_{\mathrm{m},i}) \frac{\delta_i^* - z}{\delta_i^* - \delta_{\mathrm{m},i}} \tag{4.16}$$

and K_i can be expressed as

$$K_i = k_{\mathrm{eq},i}^* \frac{k_{\mathrm{b}} T}{u_i(\delta_{\mathrm{m},i})} \left(1 - \exp\left(-\frac{u_i(\delta_{\mathrm{m},i})}{k_{\mathrm{b}} T} \right) \right), \tag{4.17}$$

whereby $k_{\mathrm{eq},i}^* = (\delta_i^* - \delta_{\mathrm{m},i})$ [m] is a model parameter to be specified.

4.3 Materials and Methods

4.3.1 Buffer System, Adsorber, and Protein

The data analyzed in this study were obtained from the literature [64; 67] aiming to describe the partitioning coefficient [Eq. (4.17)] of different proteins as a function of buffer pH and ionic strength. For the sake of clarity, important information from [67] and [64] are quoted below.

For all isocratic experiments, 20 mM sodium phosphate (pH > 5.5) and 20 mM sodium acetate (pH ≤ 5.5) were used as buffer system. The ionic strength of the buffer system was adjusted using sodium chloride. Experiments were performed on the strong cation exchange resin Fractogel EMD SE HiCap (Merck KGaA, Darmstadt, Germany) and two strong YMC BioPro SP resins (both YMC Europe GmbH, Dinslaken, Germany). The resin beads of Fractogel EMD SE HiCap and YMC BioPro SP are comprised of an almost incompressible methacrylate backbone with an average particle diameter of 40-90 μm, 10 μm, and 5 μm, respectively. The adsorber surface of Fractogel EMD SE HiCap is grafted with polymeric tentacles functionalized with sulfoisobutyl. YMC BioPro SP is functionalized with sulfopropyl. Ligand densities and pK_{L} values of the functional groups for Fractogel EMD SE HiCap and both YMC BioPro SP resins are summarized in Table 4.1.

Partitioning coefficients of lysozyme (Chicken) and three monoclonal antibodies (mAbs) were investigated. The three mAbs included Bevacizumab, Trastuzumab (both Roche, Basel, Switzerland), and an anonymized mAb1 (Merck Serono S.A., Fenil-sur-Corsier, Switzerland). Lysozyme has a theoretical molecular weight of 14.3 kDa and consists of a single polypeptide chain with 129 amino acids. The third monoclonal antibody (mAb1) contained six charge variants according to analytical cation exchange chromatography [64; 66]. They were denoted according to their elution order with respect to most abundant variant (P). The weak adsorbing isoforms (W1, W2, and W3) were ascribed to the

Table 4.2: Number of ionizable groups for lysozyme (Lys), Bevacizumab (BmAb), Trastuzumab (TmAb), and mAb1 isoforms. The primary sequence of Lys was taken from the RCSB PDB data bank (PDB ID: 1GXV) [136]. The number of ionizable groups for the mAbs were taken from [64].

Protein	N_{Lys}	N_{Arg}	N_{His}	N_{Glu}	N_{Asp}	N_{Tyr}	N_{Nterm}	N_{Cterm}
Lys	6	11	1	2	7	3	1	1
TmAb	90	40	26	60	58	62	4	4
BmAb	88	32	28	60	52	62	4	4
mAb1(P)	86	36	26	66	54	60	4	4
mAb1(S1)	87	36	26	66	54	60	4	4
mAb1(S2)	88	36	26	66	54	60	4	4
mAb1(W1)	86	36	26	66	56	60	4	4
mAb1(W2)	86	36	26	66	55	60	4	4
mAb1(W3)	86	36	26	66	55	60	4	4

deamidation of neutrally charged asparagine (Asn) residues to negatively charged aspartate. In W2 and W3, a single Asn deamidation occured at two different sites. In W1, two deamidation sites were transformed. The strong adsorbing isoforms S1 and S2 were ascribed to C-terminal lysine truncation [64; 66]. The number of ionizable groups of all proteins are summarized in Table 4.2.

4.3.2 Software

All calculations were performed in MATLAB R2018a (The MathWorks, Natick, Massachusetts, USA). Parameter estimation was performed using the nonlinear least-squares solver *lsqcurvefit* in MATLAB. Parameter confidence intervals were estimated using the MATLAB function *nlparci*.

4.3.3 Parameter Estimation

Model parameters were taken from the literature or determined by fitting the model to experimental data. The model was calibrated on Fractogel EMD SE HiCap for lysozyme and mAb1 and on YMC BioPro SP (5 μm) for Bevacizumab and Trastuzumab.

The average pK values of the ionizable groups used in Eq. (4.2) are summarized in Table 4.3. Except for Arg, they represent average values of a total of 541 experimental pK values from 78 proteins [60; 126]. Due to missing information in [60; 126], the mean pK value of the Arg side chains was taken from the null model [17]. The mean pK values of the histidine imidazole moieties were further refined using experimental data. For each antibody, two imidazole groups were considered with a mean pK value of p$K_{\text{His1,i}}$ and p$K_{\text{His2,i}}$, respectively. Without further information about the ternary structure of the antibodies, the ratio of the two imidazole groups was arbitrarily set to 50/50. Only for lysozyme, a single pK_{His} was considered as the primary sequence of lysozyme contains only one imidazole side chain. Other unknown model parameters were the protein size a_i used in Eq. (4.5) and Eq. (5.18), as well as $k_{\text{eq},i}^*$ used in Eq. (4.17). Unlike previous studies [64–66], $\delta_{\text{m},i}$ [Eq. (5.1)] between protein and adsorber surface was not assumed to be a constant model parameter, but was determined for each condition using the predicted

Table 4.3: Average pK values used in this study. Except for Arg, they represent average values of a total of 541 experimental pK values from 78 proteins [60; 126]. The average pK value of Arg side chains was taken from the null model [17].

Ionizable group	Average pK
Lys	10.59
Arg	12.00
His	6.55
Glu	4.18
Asp	3.53
Tyr	10.26
N terminus	7.66
C terminus	3.30

interaction profile $u_i(z)$. Parameter estimation was performed using experimental data at a pH between 4.0 and 6.5. Experiments at pH 7.0 were used for model validation. In all cases, dielectric decrement was neglected and a relative permittivity of pure water $\varepsilon = 78.4$ at 298 K was assumed.

4.3.4 Resin Transfer

After determination of the model parameters of mAb1 on Fractogel EMD SE HiCap, the mechanistic model was used to describe partitioning coefficients on YMC BioPro SP (10 μm) keeping the estimated protein parameters a_{mAb1}, p$K_{\text{His1,mAb1}}$, and p$K_{\text{His2,mAb1}}$ constant. The adsorber dependent parameter $k^*_{\text{eq,mAb1}}$ was redetermined by using retention data on YMC BioPro SP at pH 5.4. Model validation was performed at pH 4.9, 5.9, and 6.5.

4.3.5 Protein Isoforms

After determination of the protein parameters a_{mAb1}, p$K_{\text{His1,mAb1}}$, and p$K_{\text{His2,mAb1}}$ on Fractogel EMD SE HiCap and $k^*_{\text{eq,mAb1}}$ on YMC BioPro SP (10 μm), the model was used to predict partitioning coefficients of mAb1 isoforms on YMC BioPro SP (10 μm). All model parameters were kept constant. Only the number of amino acid side chains was adjusted according to Table 4.2.

4.4 Results and Discussion

4.4.1 Parameter Estimation

The protein is characterized by its idealized size, the number of ionizable amino acid side chains as well as their pK values. The average pK values of the imidazole side chains as well as a_i and $k^*_{\text{eq,}i}$ were determined using measured partitioning coefficients at varying ionic strength and pH. The ionic strength was adjusted using sodium chloride which justifies the assumption of a 1:1 electrolyte. Table 4.4 summarizes parameter values and uncertainties

Table 4.4: Estimated model parameters of lysozyme and mAb1 on Fractogel EMD SE HiCap and TmAb and BmAb on YMC BioPro SP (5μm). Parameter uncertainty is expressed by the 95% confidence interval.

Parameter	Unit	Lys	mAb1	TmAb	BmAb
Resin		Fractogel	Fractogel	YMC	YMC
a_i	nm	0.96 ± 0.03	3.64 ± 0.40	2.81 ± 0.08	2.85 ± 0.30
$\mathrm{p}K_{\mathrm{His1},i}$	–	5.67 ± 0.15	7.68 ± 2.95	7.38 ± 0.26	7.49 ± 0.51
$\mathrm{p}K_{\mathrm{His2},i}$	–	–	6.29 ± 0.12	5.61 ± 0.31	6.00 ± 0.22
$\log\left(k_{\mathrm{eq},i}^* \cdot 1\mathrm{m}^{-1}\right)$	–	-10.53 ± 0.16	-10.36 ± 0.99	-12.97 ± 0.51	-12.25 ± 0.42

for all proteins. Parameter uncertainty is expressed by the 95% confidence interval. As expected, the colloid radius of lysozyme is significantly lower than those of the three mAbs. However, the determined radius of 0.96 nm deviates considerably from the experimental Stokes radius of 1.83 nm [108]. The determined antibody radii are also not in agreement with an average Stokes radius of 5.77 nm for mAbs, as reported in the literature [103]. The discrepancy between a_i and the Stokes radius can most likely be attributed to the different assumptions made. While the Stokes radius corresponds to a fictitious hard sphere that diffuses at the same rate as the protein, a_i corresponds to a fictitious sphere that shows similar electrostatic properties as the protein assuming a uniform surface charge density. Both assumptions, the consideration of a spherical colloid and the uniform charge distribution, are significant simplifications that lead to an abstraction of a_i. A perfect sphere may be an appropriate representation of globular proteins but is inaccurate for complex proteins like mAbs. Even the body of lysozyme is known to be a prolate ellipsoid rather than a sphere [99]. It has also been shown that charge heterogeneity on the protein plays a significant role in chromatographic separation of similarly charged proteins, both experimentally [28; 105] and computationally [43; 50]. However, computational studies accounting in detail for the protein shape and charge distribution also suggest that model calculations can be quite robust to model idealizations, if the protein and the adsorber surface are oppositely charged [4]. Since this condition is fulfilled in the experimental study, the structural idealizations in the model are reasonable.

Determined average $\mathrm{p}K$ values of the imidazole side chains, on the other hand, are within the distribution of experimental $\mathrm{p}K$ values reported in the literature [60; 126]. Due to charge-charge interactions, hydrogen-bonding, and burial of the imidazole side chains, parameter estimates deviate significantly from the intrinsic $\mathrm{p}K$ value of 6.06. The determined $\mathrm{p}K$ value of His-15 in lysozyme is also in good agreement with values reported in the literature [17; 101].

The adsorber-dependent $k_{\mathrm{eq},i}^*$ is a measure for the thickness of the interaction boundary layer. As the interaction between protein and adsorber arises from an overlap of their diffuse layers, $k_{\mathrm{eq},i}^*$ depends on the extension of both diffuse layers. However, due to the higher absolute charge density on the surface of strong cation exchangers in relation to the protein surface, the thickness of the interaction boundary layer is expected to be mainly determined by the diffuse layer of the adsorber. Therefore, $k_{\mathrm{eq},i}^*$ values of proteins on the same adsorber, such as lysozyme and mAb1 or Trastuzumab and Bevacizumab, are very similar. Parameter values of Trastuzumab and Bevacizumab on YMC BioPro SP (5 μm) are lower than parameter values of lysozyme and mAb1 on Fractogel EMD SE HiCap, as the interaction boundary layer thickness increases with increasing charge density on the adsorber surface.
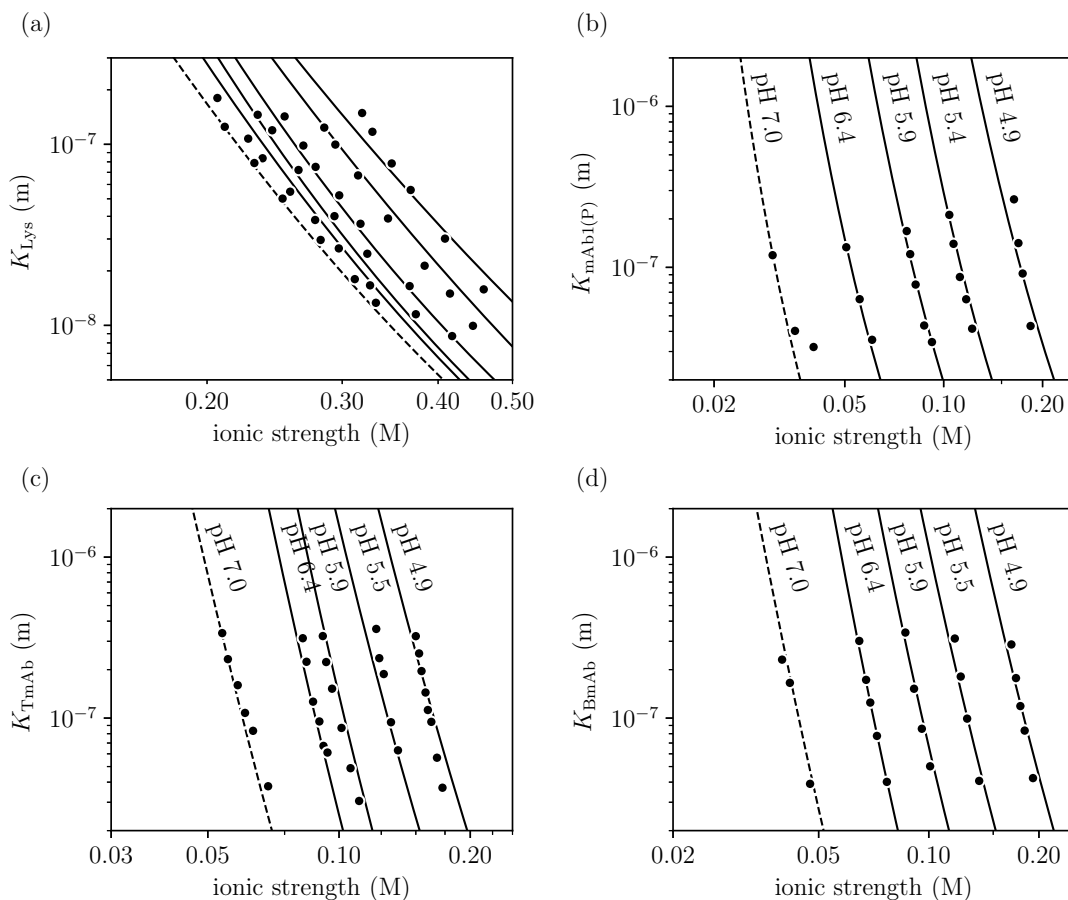
Figure 4.3: Comparison of experimental (dots) and simulated (lines) partitioning coefficients of (a) lysozyme and (b) mAb1 on Fractogel EMD SE HiCap, as well as (c) Trastuzumab and (d) Bevacizumab on YMC BioPro SP (5 μm). Solid black lines indicate the model fit. Dashed black lines represent model extrapolations at pH 7.0. Partitioning coefficients of lysozyme were measured at pH 4.4, 4.9, 5.4, 5.9, 6.4, and 6.8 (from right to left).

Figure 4.3 shows experimental partitioning coefficients along with model predictions. Experimental data at a pH between 4.0 and 6.5 were used for model calibration. Solid black lines represent the model fit. Experiments at pH 7.0 were used for model validation. Model extrapolations for this pH are indicated as dashed black lines. In very good agreement with the experimental data, the mechanistic model describes the elution behavior of all four proteins as a function of pH and ionic strength. Slight deviations from the experimental data can be observed for lysozyme and the mAbs at pH 4.9. These deviations may be explained by the model simplifications as described above. The Derjaguin approximation in Eq. (5.18) can also explain deviations between model results and experimental data. As described earlier, this expression is only correct within the Derjaguin limit $\kappa a_i \gg 1$, which is fulfilled for small colloids like proteins only at high salt concentrations. To keep the model simple, $k_{eq,i}^*$ is also considered to be independent of the buffer pH and ionic strength. However, as the pH and ionic strength affect the thickness of the interaction boundary layer they should also affect $k_{eq,i}^*$. For strong ion exchange resins, as used in this study, the effect of pH and ionic strength on $k_{eq,i}^*$ is expected to be small. However, in the case of weak ion exchange resins, this assumption is no longer justified since the adsorber

surface charge density can vary with the pH. Deviations at pH 4.9 and below may also be due to an increasing protonation of Glu and Asp. Instead of protein-specific parameter values, empirical pK values were used for the carboxyl groups of Asp and Glu which could lead to deviations at low pH values. Model predictions at pH 7.0, on the other hand, are in very good agreement with experimental data. These data were used for model validation, as model results in [64] showed a significant underestimation of protein adsorption for this pH value, especially for mAb1 whose isoelectric point (pI $\sim$ 7.8) is close to pH 7.0. The deviations between experimental data and model results were generally explained by a nonuniform charge distribution on the protein surface, which can lead to a change in the binding orientation [64]. The effect of charge regulation, on the other hand, was not taken into consideration. Other research groups [153; 162] have postulated that the effect of charge regulation is particularly relevant at pH values close to the isoelectric point of the protein, as the relative change in protein charge upon adsorption is largest under these conditions. This would explain the underestimation of mAb1 adsorption at pH 7.0 in [64], as the applied non-stoichiometric model considered a constant protein charge. A change in the binding orientation due to a nonuniform charge distribution cannot be ruled out. However, the good agreement with experimental data at pH 7.0 demonstrates that the proposed mechanistic model is capable of describing protein adsorption at high pH values assuming a uniform but regulated surface charge density.

4.4.2 Resin Transfer

An advantage of the proposed non-stoichiometric adsorption model over traditional stoichiometric models is that protein parameters are not defined in relation to adsorber properties and are therefore theoretically valid for different adsorber systems. Differences in the adsorber properties are taken into account by the ligand density and the pK value of the ligand. Variations in the surface morphology are not considered, as the model approximates the adsorber surface as a flat surface and assumes a uniform charge distribution. The extent of the ligands on the adsorber surface and the associated surface roughness is thereby neglected. This assumption represents a considerable simplification, especially for tentacular resins like Fractogel EMD SE HiCap. The morphology of the grafted polyelectrolyte layer is reported to be dependent on the ionic strength, which can affect the structural [9] and functional [8] properties of the adsorber system. In order to assess whether the model can sufficiently reflect differences in adsorber properties, the mechanistic model of mAb1 was transferred from Fractogel EMD SE HiCap to YMC BioPro SP (10 μm). Only $k_{\mathrm{eq,mAb1}}^*$ is expected to change due to the difference in surface ligand density. Therefore, $k_{\mathrm{eq,mAb1}}^*$ was redetermined for the YMC resin using experimental data at pH 5.4. The determined parameter value $\log(k_{\mathrm{eq,mAb1}}^* \cdot 1\mathrm{m}^{-1}) = -11.20 \pm 0.04$ lies between determined parameter values on Fractogel EMD SE HiCap and YMC BioPro SP (5 μm). This is expected, since the ligand density of YMC BioPro SP (10 μm) is between that of Fractogel EMD SE HiCap and YMC BioPro SP (5 μm), as shown in Table 4.1. Measured partitioning coefficients along with model predictions are shown in Fig. 4.4. Lines indicate model predictions for the YMC resin. They show very good agreement with experimental data at pH 5.4 used to redetermine $k_{\mathrm{eq,mAb1}}^*$. Model predictions at pH 4.9, 5.9, and 6.5 deviate from experimental data. However, trends in the adsoption behavior of mAb1 on the YMC resin are correctly reflected by the mechanistic model, although the majority of the model parameters were determined on Fractogel EMD SE HiCap. Other
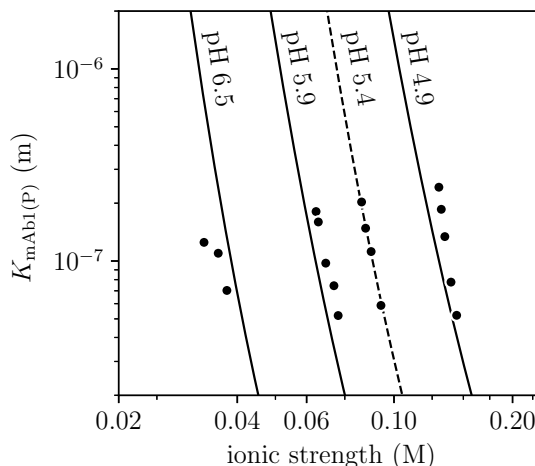
Figure 4.4: Comparison of experimental (dots) and simulated (lines) partitioning coefficients mAb1 on YMC BioPro SP (10 μm). The dashed line indicates the model fit used to redetermine $k^*_{\text{eq,mAb1}}$. Solid lines represent model extrapolations.

than described for previous non-stoichiometric models [66; 67], protein parameters of the proposed adsorption model are therefore theoretically not only valid on a specific IEX adsorber system, but freely transferable to other adsorber systems.

4.4.3 Protein Isoforms

Efficient process modeling requires not only the description of the protein of interest but also of important impurities. Antibody isoforms are product-related impurities that often pose a difficult separation problem due to the similar physicochemical properties to the main component. Depending on the post-translational modification (PTM), they differ only slightly in the number of amino acids. Figure 4.5 shows measured partitioning coefficients of five mAb1 charge variants on YMC BioPro SP (10 μm) at varying ionic strength and pH. Experimental data were taken from [66]. The charge variants were ascribed to C-terminal lysine truncation and Asn deamidation. It is important to note that the weak binding isoforms W1 and W2 are shown together in Fig. 4.5(b), as both isoforms are characterized by a single Asn deamidation at different sites. Solid black lines in Fig. 4.5 represent predicted partitioning coefficients of the isoforms using the mechanistic model of mAb1 on the YMC resin. For comparison, dashed gray lines indicate model predictions for the main component also shown in Fig. 4.4. For the charge variants, only the number of ionizable side chains was adjusted in the model according to the PTM. As the protein conformation is generally not affected by C-terminal lysine truncation and Asn deamidation [169; 193], a_{mAb1} was assumed to be not affected by the PTM and kept constant. The same applies to $k^*_{\text{eq,mAb1}}$, which should be determined mainly by the adsorber properties. Futhermore, it was assumed that the change in the number of ionizable amino acids does not affect the average pK values used in Eq. (4.2). As can be seen, despite minor changes in the primary sequence of mAb1, the charge variants show significantly different affinity to YMC BioPro SP (10 μm). The binding behavior predicted by the model corresponds very well with experimental data considering the high degree of model extrapolation. It
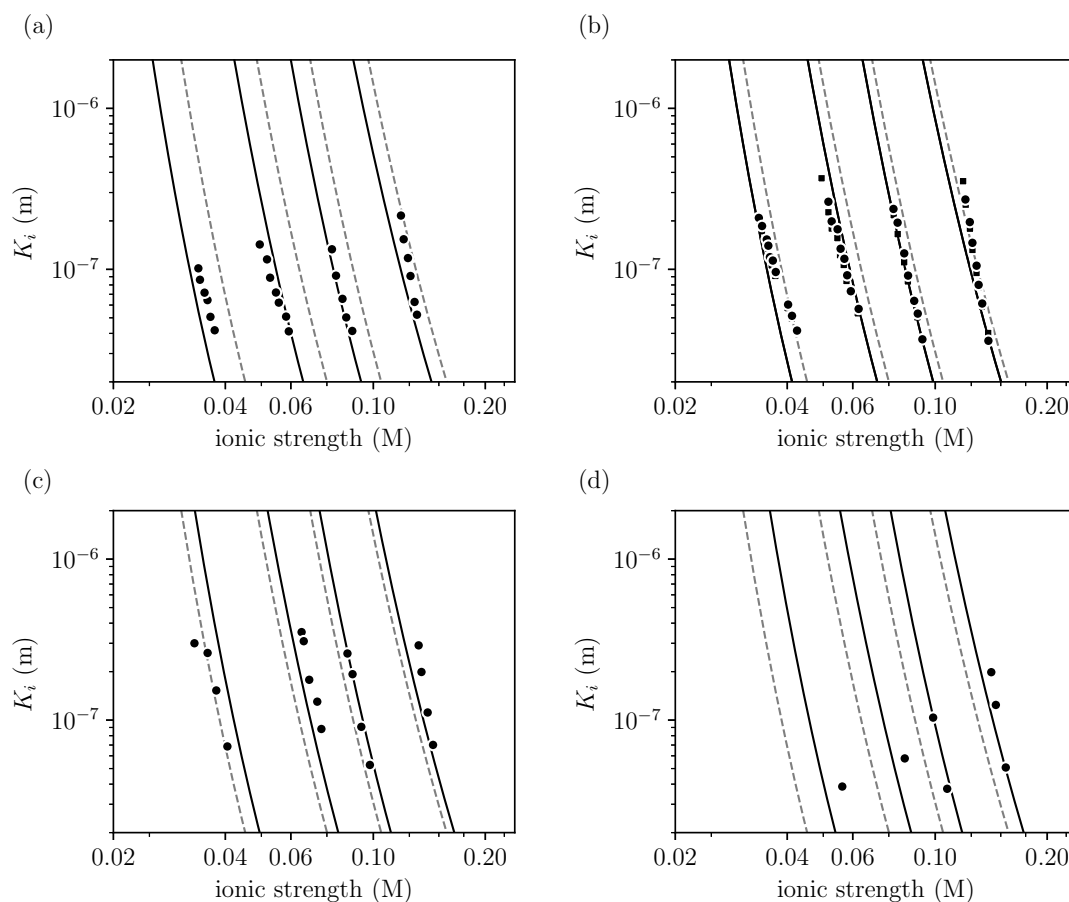
Figure 4.5: Comparison of experimental (markers) and predicted (lines) partitioning coefficients of mAb1 isoforms on YMC BioPro SP (10 μm). Dashed gray lines represent model predictions for mAb1(P) also shown in Fig. 4.4. Solid black lines indicate model predictions for the charge variants (a) W1, (b) W2/W3, (c) S1, and (d) S2.

is important to note that differences between the two weak binding charge variants W2 and W3 cannot be resolved by the mechanistic model, since it assumes a uniform surface charge density and neglects the location of specific amino acids. However, experimental data for W2 and W3 in Fig. 4.5(b) show no significant difference, indicating that the location of the deamidation site has no significant influence in this particular case.

4.5   Conclusion

We introduced a mechanistic adsorption model which is based on a fundamental description of the non-stoichiometric electrostatic interactions in IEX chromatography using the linear Poisson-Boltzmann equation and a colloidal representation of the protein. The model explicitly accounts for the effect of pH and ionic strength on protein adsorption. Unlike most recent colloidal models, the proposed model does not assume a constant surface charge density, but takes into account charge regulation of the protein and the adsorber system during the adsorption process. Usage and benefit of the proposed model was demonstrated by modeling the adsorption behavior of lysozyme and three mAbs on

different adsorber systems. Model results were in all cases in very good agreement with experimental data. A model validation beyond observed pH conditions demonstrated that the consideration of charge regulation can improve model quality at higher pH values close to the protein pI in relation to previous non-stoichiometric models. To demonstrate that protein parameters are theoretically not only valid on a specific adsorber sytem but freely transferable to other adsorber systems, protein parameters of mAb1 were transferred from Fractogel EMD SE HiCap to YMC BioPro SP (10 μm). Only one adsorber-dependent model parameter had to be redetermined to extrapolate elution behavior of mAb1 on the YMC resin. The recalibrated model was also able to accurately predict the elution behavior of five mAb1 charge variants on the YMC resin solely based on differences in the protein primary structure.

The proposed mechanistic model is based on several simplifications to keep it computationally simple and applicable for model-based chromatography process development. These simplifications include, *inter alia*, the use of the linear Poisson-Boltzmann equation within the Derjaguin limit, a homogeneous surface charge density, and a spherical protein shape. It is important to note that some of the assumptions made are justified only for the investigated linear adsorption range. Despite these simplifications, the physical meaning and predictive value of the model could be preserved. Estimated model parameters exhibit only a low degree of abstraction, which simplifies model calibration and supports the use of homology models in model calibration. As most of the protein properties are derived directly from the primary structure of the protein, the model can be used to simulate the separation of well-characterized product-related impurities like charge variants and low molecular weight species.

Protein Adsorption on Ion Exchange Adsorbers: A Comparison of a Stoichiometric and Non-Stoichiometric Modeling Approach

Till Briskot[1,2], Tobias Hahn[1], Thiemo Huuk[1], Jürgen Hubbuch[2]

[1] GoSilico GmbH, Karlsruhe, Germany
[2] Karlsruhe Institute of Technology (KIT), Institute of Process Engineering in Life Sciences, Section IV: Biomolecular Separation Engineering, Karlsruhe, Germany

Abstract

For mechanistic modeling of ion exchange (IEX) processes, a profound understanding of the adsorption mechanism is important. While the description of protein adsorption in IEX processes has been dominated by stoichiometric models like the steric mass action (SMA) model, discrepancies between experimental data and model results suggest that the conceptually simple stoichiometric description of protein adsorption provides not always an accurate representation of nonlinear adsorption behavior.

In this work an alternative colloidal particle adsorption (CPA) model is introduced. Based on the colloidal nature of proteins, the CPA model provides a non-stoichiometric description of electrostatic interactions within IEX columns. Steric hindrance at the adsorber surface is considered by hard-body interactions between proteins using the scaled-particle theory. The model's capability of describing nonlinear protein adsorption is demonstrated by simulating adsorption isotherms of a monoclonal antibody (mAb) over a wide range of ionic strength and pH. A comparison of the CPA model with the SMA model shows comparable model results in the linear adsorption range, but significant differences in the nonlinear adsorption range due to the different mechanistic interpretation of steric hindrance in both models. The results suggest that nonlinear adsorption effects can be overestimated by the stoichiometric formalism of the SMA model and are generally better reproduced by the CPA model.

Keywords: *Protein purification; Mechanistic modeling; Colloidal particle adsorption model; Steric mass action model; Adsorption isotherm; Scaled particle theory*

5.1 Introduction

For the last three decades, chromatography has been a pillar of commercial downstream processes [157]. Ion exchange (IEX) chromatography in particular is frequently used for the purification of recombinant proteins due to its robustness, selectivity, and mild operating conditions [61]. For the development of IEX processes, mechanistic process models have become increasingly important in recent years. By providing a digital replicate of the real-world process, mechanistic models can help to support process optimization [71; 80; 118; 123; 124], process scale-up [7; 53; 111], and process robustness studies [14; 30; 88; 92; 180] in a resource-efficient manner. As they rely on a description of the underlying physical effects, a sound understanding of the protein retention mechanism in IEX processes is important for a systematic application of mechanistic models.

In the past, the modeling of protein retention in IEX processes has been dominated by stoichiometric adsorption models relying on the work of Boardman and Partridge [13] and Regnier and co-workers [44; 98; 144]. The interaction between a protein and the adsorber is thereby ascribed to a reversible stoichiometric displacement of counter-ions bound to the adsorber surface by charged proteins within the mobile phase. Based on the mass action law, this model explicitly accounts for the effect of the ionic strength on protein adsorption. While the initial stoichiometric displacement model was limited to the linear adsorption range, where only protein-adsorber interactions are relevant, it has been extended to the nonlinear adsorption range with the introduction of the steric mass action (SMA) model by Brooks and Cramer [22]. Within the framework of the SMA model, nonlinear adsorption behavior up to adsorber saturation is attributed to a reduction of available adsorber counter-ions due to adsorbed proteins. Counter-ions of the adsorber are thereby either displaced from the surface by a protein or sterically shielded due to its size. Thus, the model does not consider the surface of the adsorber as the sterically limiting factor for adsorption, but its ionic capacity. Although stoichiometric adsorption models like the SMA model provide a conceptually simple description of protein adsorption, their ability to reflect electrostatic interactions between proteins and adsorbers has often been questioned [161–163]. Reported deficiencies of the SMA model in describing experimental adsorption isotherms [32; 34; 188] and chromatography elution profiles [40; 78] indicate that nonlinear effects may be inadequately reflected by the stoichiometric interpretation of protein adsorption.

In addition to the stoichiometric adsorption models, a further class of non-stoichiometric adsorption models has been developed. Given the colloidal nature of proteins, these models provide a more fundamental description of electrostatic interactions in IEX chromatography based on the Poisson-Boltzmann equation. Since most of these models are limited to a mechanistic description of electrostatic interactions between proteins and the adsorber surface, they are often only valid for the linear adsorption range [19; 64; 67; 143; 163; 164]. Only a small number of models have been proposed that also cover the nonlinear adsorption range [65; 119; 188]. In the model initially proposed by Oberholzer et al. [119], nonlinear adsorption behavior is attributed to lateral interactions among adsorbed proteins giving rise to a change in the internal energy as well as the surface pressure. Although this model describes experimental data reasonably well, model parameters were often determined individually for each pH and ionic strength [187; 188], which can make model calibration cumbersome. A related model was introduced by Guélat et al. in which electrostatic protein-adsorber interactions are described as a function of pH and ionic strength

using the DLVO theory. The model was used to describe the elution behavior of antibody charge variants in the linear and nonlinear adsorption regime based on molecular information. Using statistical thermodynamics, the model accounts for surface coverage effects and electrostatic protein-protein interactions.

This work introduces a colloidal particle adsorption (CPA) model describing protein adsorption within the linear and nonlinear adsorption range as a function of ionic strength and pH. Nonlinear adsorption behavior is described by a combination of steric surface blocking effects and electrostatic interactions between adsorbed proteins. Steric effects are accounted for by using a two-dimensional scaled-particle theory according to [104; 138; 139]. Electrostatic protein-protein interactions are estimated assuming a two-dimensional Yukawa lattice. Similar to the SMA model and other adsorption models, the CPA model seeks to balance a mechanistic description and minor empiricism to provide a mathematical description of the isotherm over a wide range of pH and ionic strength. To address the question of how the CPA model differs from the traditional stoichiometric formalism of the SMA model, both model approaches are analyzed and compared in detail. After model calibration and comparison in the linear adsorption range, both models are extended and discussed in the nonlinear adsorption range using adsorption isotherms of a monoclonal antibody.

5.2 Theory

In this section, an adsorption theory of proteins on IEX resins in the linear and nonlinear adsorption regime is developed. First, the equilibrium equation of the CPA model is derived that accounts for electrostatic interactions between proteins and the IEX adsorber as well as electrostatic and steric interactions between adsorbed proteins. The individual interaction effects are described in more detail in Sec. 5.2.2 - Sec. 5.2.4. In Sec. 5.2.5, the stoichiometric adsorption theory based on the SMA model is briefly summarized.

5.2.1 Colloidal Particle Adsorption Model

We consider a system at constant temperature T=298.15 K where the adsorber A and proteins i are immersed in an electrolyte solution with relative permittivity $\varepsilon = 78.3$ and ionic strength I_m [mol m^{-3}]. Proteins in the system are represented as perfect hard spheres with radius a_i [m] and net charge Z_i [$-$]. Depending on the pH in the system and the pI of the protein, Z_i can be positive or negative. The adsorber surface is considered to be solid and planar. The interaction free energy $u_{\mathrm{A},i}$ [J] between a single protein and the adsorber surface separated by the distance z [m] is considered to be dominated by electrostatic interactions. In this case, $u_{\mathrm{A},i}(z)$ follows a function schematically shown in Fig. 5.1 that is characterized by a distinct minimum at

$$\delta_{\mathrm{m},i} = \arg\min_z u_{\mathrm{A},i}(z). \tag{5.1}$$

Due to the finite range of electrostatic interactions, $u_{\mathrm{A},i}$ is only relevant inside a boundary layer with thickness δ_i^* [m] referred to as interaction boundary layer [146; 147; 159]. Proteins inside this boundary layer are considered to be adsorbed to the adsorber surface,
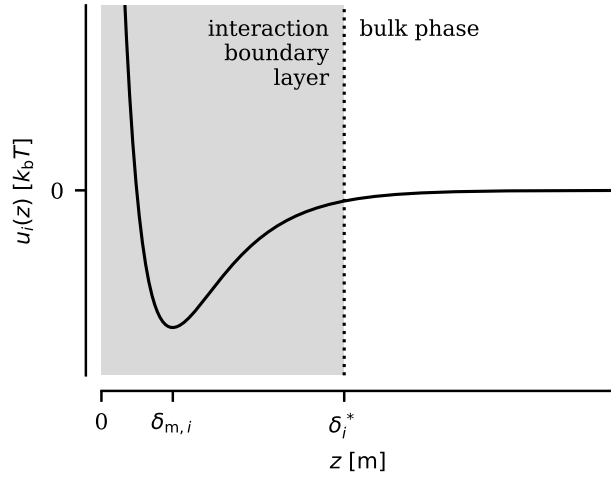
Figure 5.1: Schematic representation of the interaction profile between a single protein and the adsorber surface separated by the distance z. Electrostatic interactions between the protein and the adsorber surface are only relevant within an interaction boundary layer. Proteins within the boundary layer are considered to be adsorbed to the adsorber surface.

while proteins outside the boundary layer are not affected by the charged adsorber surface. In this case the surface density of protein bound to the adsorber surface q_i [mol m^{-2}] may be defined by

$$q_i = \int_{\delta_{\mathrm{m},i}}^{\delta_i^*} c_i(z)dz, \qquad (5.2)$$

where c_i [mol m^{-3}] represents the concentration of the i-th colloid. This definition produces little error if $u_{\mathrm{A},i}(z)$ is dominated by repulsive forces for $z < \delta_{\mathrm{m},i}$ as shown in Fig. 5.1. It is often more convenient to relate the amount of adsorbed protein not to the adsorber surface but to the skeleton volume of the adsorber $q_{\mathrm{v},i}$ [mol m^{-3}]. According to $q_{\mathrm{v},i} = A_{\mathrm{s},i}q_i$, both definitions are related by the specific adsorber surface per skeleton volume $A_{\mathrm{s},i}$ [m^{-1}] accessible by the colloid.

Inside the interaction boundary layer, the electrochemical potential $\bar{\mu}_i$ [J] of a colloid can be defined by

$$\bar{\mu}_i(z) = \mu_i^* + k_{\mathrm{b}}T \ln\left(\frac{c_i(z)}{c^+}\right) + \mu_i^{\mathrm{ex}}(z) + u_i(z), \qquad (5.3)$$

where μ_i^* is the reference potential at infinite dilution, k_{b} [J K^{-1}] is the Boltzmann constant, c^+ is a reference concentration to make the term inside the logarithm dimensionless, μ_i^{ex} represents the excess chemical potential, and u_i is the interaction free energy accounting for $u_{\mathrm{A},i}$ and electrostatic protein-protein interactions $u_{\mathrm{lat},i}$. For simplicity and in accordance with previous studies [65; 119; 120; 188], u_i is defined by the superposition of both contributions, namely $u_i = u_{\mathrm{A},i} + u_{\mathrm{lat},i}$. While u_i accounts for electrostatic contributions within the boundary layer, the excess property μ_i^{ex} represents the reversible work of introducing a protein into the boundary layer while avoiding any steric overlaps with other adsorbed proteins.

If we neglect protein-protein interactions outside the interaction boundary layer and as-

sume $\mu_i^{\text{ex}} = 0$ and $c_i = c_{\text{b},i}$ for $z > \delta_i^*$, $\bar{\mu}_i$ in the bulk phase simplifies to

$$\bar{\mu}_{\text{b},i} = \mu_i^* + k_{\text{b}}T \ln \left(\frac{c_{\text{b},i}}{c^+} \right). \tag{5.4}$$

Using Eq. (5.3), Eq. (5.4), and the equilibrium condition $\bar{\mu}_i(z) = \bar{\mu}_{\text{b},i}$, $c_i(z)$ in Eq. (5.2) can be related to $c_{\text{b},i}$ using the Boltzmann expression

$$c_i(z) = c_{\text{b},i} \exp \left(-\frac{\mu_i^{\text{ex}}(z) + u_{\text{A},i}(z) + u_{\text{lat},i}(z)}{k_{\text{b}}T} \right). \tag{5.5}$$

The interaction profile shown in Fig. 5.1 and Eq. (5.5) suggest that accumulation of colloids inside the boundary layer occurs mainly at the minimum $\delta_{\text{m},i}$ and results in the formation of a monolayer of colloids close to the adsorber surface. The contribution of μ_i^{ex} and $u_{\text{lat},i}$ is therefore considered to be independent of z and only a function of the arrangement of proteins in the adsorption layer. Under this assumption, $q_{\text{v},i}$ can be defined by

$$q_{\text{v},i} = c_{\text{b},i} A_{\text{s},i} \exp \left(-\frac{\mu_i^{\text{ex}}(\Theta)}{k_{\text{b}}T} \right) \exp \left(-\frac{u_{\text{lat},i}(\Theta)}{k_{\text{b}}T} \right)$$
$$\cdot \int_{\delta_{\text{m},i}}^{\delta_i^*} \exp \left(-\frac{u_{\text{A},i}(z)}{k_{\text{b}}T} \right) dz, \tag{5.6}$$

where

$$\Theta = \pi N_{\text{A}} \sum_i a_i^2 q_i = \pi N_{\text{A}} \sum_i a_i^2 \frac{q_{\text{v},i}}{A_{\text{s},i}} \tag{5.7}$$

represents the surface coverage with N_{A} [mol^{-1}] being the Avogadro number. Since μ_i^{ex} accounts for steric hindrance between adsorbed proteins, the expression

$$B_i(\Theta) = \exp \left(-\frac{\mu_i^{\text{ex}}}{k_{\text{b}}T} \right) \tag{5.8}$$

is often referred to as blocking or available surface function (ASF) [3; 167]. For the limiting case $\Theta \to 0$, Eq. (5.6) reduces to

$$q_{\text{v},i} = c_{\text{b},i} K_{\text{H},i} = c_{\text{b},i} A_{\text{s},i} \int_{\delta_{\text{m},i}}^{\delta_i^*} \exp \left(-\frac{u_{\text{A},i}(z)}{k_{\text{b}}T} \right) dz \tag{5.9}$$

that we used in [19] as an expression for the Henry coefficient K_{H} [−]. As described in [19], Eq. (5.9) can be further simplified to

$$q_{\text{v},i} = c_{\text{b},i} K_{\text{H},i} = c_{\text{b},i} A_{\text{s},i} (\delta_i^* - \delta_{\text{m},i}) \frac{k_{\text{b}}T}{u_{\text{A},i}(\delta_{\text{m},i})}$$
$$\cdot \left(1 - \exp \left(-\frac{u_{\text{A},i}(\delta_{\text{m},i})}{k_{\text{b}}T} \right) \right) \tag{5.10}$$

using a linear approximation of $u_{\text{A},i}(z)$ within $z \in [\delta_{\text{m},i}, \delta_i^*]$.

Inserting Eq. (5.10) in Eq. (5.6) finally yields

$$q_{\text{v},i} = c_{\text{b},i} K_{\text{H},i} B_i(\Theta) \exp \left(-\frac{u_{\text{lat},i}(\Theta)}{k_{\text{b}}T} \right) \tag{5.11}$$

which describes protein adsorption in the linear and nonlinear adsorption regime. In

contrast to previous works [119; 188], this expression does not only attribute the decrease in the partition coefficient with increasing Θ to electrostatic protein-protein interactions, but also takes into account steric hindrance using $B_i(\Theta)$. While Eq. (5.11) provides a simple expression for the partitioning coefficient, it leaves $\Delta_i = A_{s,i}(\delta_i^* - \delta_{m,i})$ as a model parameter that needs to be determined based on experimental data. It also requires functional descriptions of $u_{A,i}(\delta_{m,i})$, $u_{lat,i}(\Theta)$, and $B_i(\Theta)$ that are derived in the following sections.

5.2.2 Protein-Adsorber Interaction

Given the superposition approximation used in Sec. 5.2.1, $u_{A,i}(\delta_{m,i})$ accounts for the interaction between a single protein i and the adsorber surface. Thus, it is a function of the pH and I_m, but independent of Θ.

Both the adsorber and proteins in the system are surrounded by an electric double layer consisting of a diffuse layer D of mobile ions from the solution and a compact inner layer I that is formed by immobile surface charges. The inner layer is characterized by the surface charge density σ_I [C m^{-2}] and electrostatic surface potential ψ_0 [V]. Both are related by the charge-potential relationship $\sigma_I(\psi_0)$. To comply with electroneutrality, σ_I is balanced by the equal but oppositely charged diffuse layer. Neglecting the curvature of the surface and considering a 1:1 electrolyte, the charge density compensated by the diffuse layer σ_D is given by the Grahame equation

$$\sigma_D(\psi_D) = 2\varepsilon\varepsilon_0\kappa\frac{k_bT}{e}\sinh\left(\frac{e\psi_D}{2k_bT}\right), \tag{5.12}$$

whereby

$$\kappa = \sqrt{\frac{2e^2 I_m N_A}{k_b T \varepsilon\varepsilon_0}} \tag{5.13}$$

represents the inverse Debye length, e [C] is the elementary charge, ε_0 [C V^{-1} m^{-1}] denotes the vacuum permittivity, and ψ_D is the electrostatic potential at the origin of the diffuse layer. The influence of the ionic strength on $\sigma_D(\psi_D)$ is taken into account via κ. Within the Gouy-Chapman theory, $\psi_D = \psi_0$ is identical to the surface potential [6; 24; 171].

In the case of the adsorber surface, $\sigma_{I,A}(\psi_{0,A})$ is governed by the ionization of ligands L according to the dissociation reaction

$$\text{LH}^{\zeta_L} \rightleftharpoons \text{L}^{\zeta_L-1} + \text{H}^+, \tag{5.14}$$

whereby ζ_L represents the charge of the fully protonated ligand. Neglecting the specific adsorption of ions from the bulk phase, $\sigma_{I,A}$ is only a function of the pH at the adsorber surface pH$_0$ and can be defined by

$$\sigma_{I,A} = eN_A\Gamma_L\left[\zeta_L - \left(1 + 10^{pK_L - pH_0}\right)^{-1}\right], \tag{5.15}$$

whereby Γ_L [mol m^{-2}] is the surface density of the ligand which is characterized by pK_L [−]. The surface pH relates to the bulk pH according to the Boltzmann relation

$$\text{pH}_0 = \text{pH} + \frac{1}{\ln(10)}\frac{e\psi_0}{k_bT}. \tag{5.16}$$

Combining Eq. (5.15) and Eq. (5.16) defines $\sigma_{I,A}(\psi_{0,A})$ for the adsorber at a constant bulk pH. Since Eq. (5.14) considers only the protonation of the ligand but neglects other ion-specific interactions, $\sigma_{I,A}(\psi_{0,A})$ is only a function of the pH. Given the expression for $\sigma_{I,A}(\psi_{0,A})$, Eq. (5.12) and the general neutrality condition

$$\sigma_I(\psi_0) = \sigma_D(\psi_0) \tag{5.17}$$

provide $\sigma_{I,A} = \sigma_{I,A}(\text{pH}, I_m)$ and $\psi_{0,A} = \psi_{0,A}(\text{pH}, I_m)$ for a given pH and I_m. It is important to note that Eq. (5.15) applies to both anion exchangers (e.g. $\zeta_L = 1$) and cation exchangers (e.g. $\zeta_L = 0$). Strong and weak ion exchangers are distinguished via pK_L.

For proteins with known amino acid sequence, a similar charge-potential relationship can be derived assuming that all ionizable amino acid side chains are located on the surface of the protein [19]. However, in practice, the protein primary sequence is often not known. Therefore, in the following, the characteristic protein net charge $Z_i(\text{pH}) = 4\pi a_i^2 e^{-1} \sigma_{I,i}(\text{pH})$ is considered as a model parameter that is only a function of the pH and must be determined by fitting the model to experimental data. Given $Z_i(\text{pH})$ or $\sigma_{I,i}(\text{pH})$, $\psi_{0,i} = \psi_{0,i}(\text{pH}, I_m)$ can again be determined using the neutrality condition Eq. (5.17) and Eq. (5.12).

If the protein approaches the adsorber surface, its diffuse layer starts to overlap with the diffuse layer of the adsorber which gives rise to a double layer interaction defined by an attractive Maxwell stress and a repulsive osmotic pressure [121; 127]. Within the Derjaguin limit $\kappa a_i \gg 1$, $u_{A,i}(z)$ can be derived from the Derjaguin approximation [84]. According to

$$u_{A,i}(z) = 2\pi a_i \int_z^\infty w_{A,i}(z) dz, \tag{5.18}$$

it relates the interaction free energy per unit area $w_{A,i}$ [J m^{-2}] between two flat plates with surface charge density $\sigma_{I,i}$ and $\sigma_{I,A}$ to $u_{A,i}$ between the spherical protein and the flat adsorber surface. Under the assumption that $\sigma_{I,i}$ and $\sigma_{I,A}$ remain constant during the adsorption process, $w_{A,i}$ in Eq. (5.18) can be defined by the expression

$$
\begin{aligned}
w_i(z) = & \varepsilon \varepsilon_0 \kappa \frac{2\psi_{0,A}\psi_{0,i}}{\exp(\kappa z) - \exp(-\kappa z)} \\
& + \varepsilon \varepsilon_0 \kappa \frac{\left(\psi_{0,A}^2 + \psi_{0,i}^2\right)\exp(-\kappa z)}{\exp(\kappa z) - \exp(-\kappa z)}
\end{aligned}
\tag{5.19}
$$

derived by Parsegian and Gingell [127]. A closed-form expression of Eq. (5.18) with Eq. (5.19) for $w_{A,i}(z)$ can be found in [24]. It is important to note that Eq. (5.19) is based on the linear Poisson-Boltzmann equation. Thus, it is only accurate for low to moderate surface potentials $(e\psi_0(k_b T)^{-1} \ll 1)$.

5.2.3 Protein-Protein Interaction

As described earlier, adsorbed proteins are assumed to be located predominantly at $\delta_{m,i}$ forming a monolayer of colloids close to the adsorber surface. In the following, the adsorption layer is considered to contain n different protein species varying in size and charge. The lateral interaction within the adsorption layer is a complex function that does not only

(a)

(b)
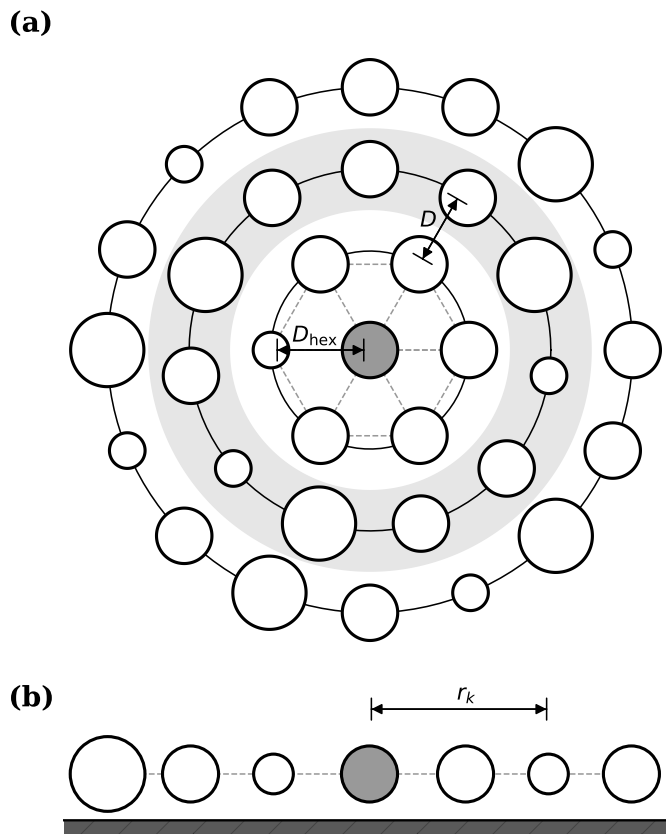
Figure 5.2: Schematic representation of the considered protein arrangement within the two-dimensional adsorption layer. (a) Top view: protein centers are assumed to be arranged on evenly spaced concentric circles. (b) Side view: protein centers are arranged equidistantly to the adsorber surface.

depend on Θ but also on the spatial distribution of proteins. To simplify the calculation of $u_{\text{lat},i}$, it is often assumed that proteins within the adsorption layer are arranged according to ordered crystal-like structures [65; 90; 119; 137; 188]. In this work, the idealized arrangement according to Fig. 5.2 is considered that has been used previously to calculate the Madelung energy in two-dimensional ionic crystals [128]. Considering a protein of interest indicated in gray, neighboring proteins are assumed to be arranged on evenly spaced concentric circles and equidistantly to the adsorber surface.

In accordance with previous works [65; 119; 120; 188], the lateral interaction energy between the protein of interest and all other adsorbed proteins is calculated assuming pairwise additive of two-body interactions. In this case, $u_{\text{lat},i}$ can be approximated by

$$u_{\text{lat},i} \approx \sum_{j=1}^{n} \sum_{k=1}^{\infty} n_{k,j} u_{i,j}(r_k), \qquad (5.20)$$

where $u_{i,j}$ represents a electrostatic two-body interaction, r_k is the center-to-center distance between the protein of interest and proteins on the k-th concentric circle, and $n_{k,j}$ denotes the number of protein j on the k-th circle. At low salt concentrations where electrostatic protein-protein interactions are relevant, $u_{i,j}$ in Eq. (5.20) can be described by

the Yukawa potential

$$u_{i,j}(r_k) = \beta_{i,j} \frac{\exp(-\kappa r_k)}{r_k} \tag{5.21}$$

whereby

$$\beta_{i,j} = Z_{\text{lat},i} Z_{\text{lat},j} \frac{e^2}{4\pi\varepsilon\varepsilon_0} \frac{\exp(\kappa(a_i + a_j))}{(1+\kappa a_i)(1+\kappa a_j)} \tag{5.22}$$

is defined by the characteristic lateral charge Z_{lat} of both proteins [54]. Due to the heterogeneity of charges on protein surfaces and different theoretical approaches, $Z_{\text{lat},i}$ in Eq. (5.22) can differ from Z_i used to calculate $u_{\text{A},i}$. Given the Yukawa lattice that follows Fig. 5.2, Eq. (5.20), and Eq. (5.21), $u_{\text{lat},i}$ can be expressed by the closed-form expression

$$u_{\text{lat},i} = 3\sqrt{3} D_{\text{hex}} N_{\text{A}} \frac{\exp(-\kappa D_{\text{hex}})}{1 - \exp\left(-\frac{3\sqrt{3}}{2\pi}\kappa D_{\text{hex}}\right)} \sum_{j=1}^{n} q_j \beta_{i,j}, \tag{5.23}$$

whereby D_{hex} is defined by the maximum packing density of a hexagonal lattice

$$\Theta_{\text{hex}} = \frac{\pi}{4} D_{\text{hex}}^2 N_{\text{A}} \sum_{i=1}^{n} q_i = \frac{\sqrt{3}\pi}{6}. \tag{5.24}$$

A detailed derivation of Eq. (5.23) can be found in the supplementary material.

Like previous colloidal adsorption models [65], Eq. (5.23) accounts for electrostatic interactions between a protein of interest and all surrounding proteins in the adsorption layer. Unlike [65], however, Eq. (5.23) does not assume that $u_{\text{lat},i}$ is the same for all protein species. Depending on the size and charge, proteins can experience different lateral interactions. It is important to note that for electrostatic interactions, previous studies have shown that the pairwise additivity of two-body interactions in Eq. (5.20) produces little error for the limiting case $\kappa r_k \gg 1$, but may be inaccurate if the interparticle spacing within the adsorption plane is smaller then the Debye length [137].

5.2.4 Available Surface Function

The ASF in Eq. (5.11) accounts for the reversible work required to introduce an adsorbing protein into the multi-component adsorption layer without any steric overlaps with other adsorbed proteins [139]. In contrast to Sec. 5.2.3, proteins are thereby considered to interact according to the pair-potential

$$u_{i,j} = \begin{cases} \infty & \text{for } r_{i,j} \leq a_i + a_j \\ 0 & \text{for } r_{i,j} > a_i + a_j. \end{cases} \tag{5.25}$$

In the following $B_i(\Theta)$ is determined by means of the scaled-particle theory [104; 138; 139]. For the limiting case where the adsorbing protein i may be considered as a point particle, μ_i^{ex} can be defined by

$$\mu_i^{\text{ex}} = -k_{\text{b}} T \ln(1 - \Theta) \tag{5.26}$$

as described in close detail by [104]. This yields to the widely used Langmuirian ASF

$$B_i(\Theta) = B(\Theta) = 1 - \Theta. \tag{5.27}$$

Since the Langmuirian ASF neglects the finite size of proteins, Eq. (5.27) is only a function of Θ, but not a_i. According to Widom [185], $B_i(\Theta)$ can also be considered as the probability that an adsorbing protein encounters a free area on the adsorber surface that is not occupied by other adsorbed proteins. Thus, according to the Langmuirian ASF, all proteins have the same probability of encountering a free adsorption site, regardless of their size. Equation (5.27) therefore produces a large error for large colloids adsorbing on a continuous surface [2; 3].

The core assumption on which the scaled particle theory is based, is that the work for an adsorbing protein with finite radius can be approximated by a Taylor series up to second order around the reference point of a point particle [Eq. (5.26)] [104]. Using the two-dimensional scaled particle theory where proteins are considered as hard discs, $B_i(\Theta)$ is defined by [168]

$$B_i(\Theta) = (1 - \Theta) \exp \left(-\frac{\pi a_i^2 \sum_j q_j N_{\mathrm{A}} + 2\pi a_i \sum_j a_j q_j N_{\mathrm{A}}}{1 - \Theta} \right.$$
$$\left. -\frac{\pi a_i^2 \left(\sum_j a_j q_j N_{\mathrm{A}} \right)^2}{(1 - \Theta)^2} \right). \tag{5.28}$$

Due to the Taylor series approximation, Eq. (5.28) still contains the Langmuirian part. In contrast to the Langmuirian ASF and previous adsorption models [65], Eq. (5.28) explicitly considers the size of the adsorbing protein. According to Eq. (5.28), large colloids have a lower probability of hitting an unoccupied region on the adsorber surface and therefore experience greater steric hindrance than smaller colloids.

5.2.5 Steric Mass Action Model

According to the SMA model, protein adsorption in IEX chromatography is based on a stoichiometric exchange of counter-ions bound to charged adsorber ligands L with charged proteins in the mobile phase, and *vice versa*. The exchange of monovalent counter-ions S with a protein P, can be described by the stoichiometric expression

$$P_i^{\tilde{\nu}_i} + \tilde{\nu}_i \mathrm{LS_{ads}} \rightleftharpoons \mathrm{L}_{\tilde{\nu}_i} \mathrm{P}_{i,\mathrm{ads}} + \tilde{\nu}_i \mathrm{S}^+, \tag{5.29}$$
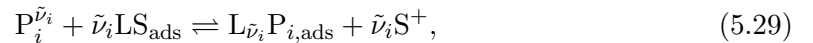
where $\tilde{\nu}_i$ [$-$] represents the characteristic charge of the i-th protein in the SMA model and the subscript ads depicts the adsorbed state. In the following, all model parameters or functions related to the SMA model are indicated with a tilde. According to the SMA model, not all counter-ions bound to the surface can be replaced by protein molecules in the mobile phase [22]. Due to the steric extend of proteins, some of the adsorber ligands are sterically shielded by adsorbed protein molecules. As described in more detail in [22], the equilibrium state is defined by

$$q_{\mathrm{v},i} = c_{\mathrm{b},i} \tilde{k}_{\mathrm{eq},i} \left(\frac{\Lambda_{\mathrm{IEX}} - \sum_i q_{\mathrm{v},i} (\tilde{\nu}_i + \tilde{\sigma}_i)}{c_{\mathrm{b},\mathrm{S}}} \right)^{\tilde{\nu}_i}, \tag{5.30}$$

where $\tilde{k}_{\mathrm{eq},i}$ is the equilibrium coefficient, Λ_{IEX} denotes the ionic capacity of the adsorber system, $c_{\mathrm{b},\mathrm{S}}$ is the counter-ion concentration in the bulk phase, and $\tilde{\sigma}_i$ is the number of

ligands shielded by the i-th protein. In reference to Eq. (5.11) in the CPA model, Eq. (5.30) can be rewritten to

$$q_{\mathrm{v},i} = c_{\mathrm{b},i} \tilde{K}_{\mathrm{H},i} \tilde{B}_i(q_{\mathrm{v}}), \tag{5.31}$$

whereby the Henry coefficient is given by $\tilde{K}_{\mathrm{H},i} = \tilde{k}_{\mathrm{eq},i} \Lambda_{\mathrm{IEX}}^{\tilde{\nu}_i} c_{\mathrm{b,S}}^{-\tilde{\nu}_i}$ and $\tilde{B}_i(q_{\mathrm{v}})$ is defined by

$$\tilde{B}_i(q_{\mathrm{v}}) = \left(1 - \frac{\sum_i q_{\mathrm{v},i}(\tilde{\nu}_i + \tilde{\sigma}_i)}{\Lambda_{\mathrm{IEX}}} \right)^{\tilde{\nu}_i}. \tag{5.32}$$

The latter accounts for steric hindrance at the adsorber surface within the framework of the SMA model. Following $B_i(\Theta)$ [Eq. (5.28)] in the CPA model, $\tilde{B}_i(q_{\mathrm{v}})$ is in the following referred to as the ASF according to the SMA model.

5.3 Materials and Methods

The data analyzed in this study were obtained from the literature [32] aiming to describe the adsorption of a mAb with molecular weight $M_{\mathrm{w}} \approx 150$ kDa on the strong cation exchanger Poros XS as a function of buffer pH and ionic strength.

5.3.1 System Characterization

According to the manufacturer, the backbone of Poros XS is comprised of cross-linked poly[styrene divinylbenzene] functionalized with sulphopropyl groups. With reference to [89], the properties of the functional groups used in Eq. (5.15) are given by $\zeta_{\mathrm{L}} = 0$ and $\mathrm{p}K_{\mathrm{L}} = 2.3$. Due to a missing characterization of the adsorber system in [32], the ionic capacity $\Lambda_{\mathrm{IEX}} = 0.86$ M of Poros XS was adopted from [166]. Using inverse size exclusion chromatography (SEC) data also reported in [166], $A_{\mathrm{s},i}$ used in Eq. (5.7) was characterized as described by DePhillips and Lenhoff [38]. Accordingly, for a protein with radius a_i, $A_{\mathrm{s},i}$ can be defined by

$$A_{\mathrm{s},i}(a_i) = \frac{\varepsilon_{\mathrm{p}}}{1 - \varepsilon_{\mathrm{p}}} \frac{\int_{a_i}^{\infty} 2(r - a_i) r^{-2} f(r) dr}{\int_0^{\infty} f(r) dr}, \tag{5.33}$$

where $f(r)$ denotes the pore size distribution. The limiting case $A_{\mathrm{s},0} = \lim_{a_i \to 0} A_{\mathrm{s},i}(a_i)$ defines the total accessible surface area per adsorber skeleton volume $A_{\mathrm{s},0}$. In agreement with previous studies [9; 38; 190], $f(r)$ in Eq. (5.33) was assumed to follow a log-normal distribution

$$f(r) = \frac{1}{r} \exp \left(-\frac{1}{2} \left(\frac{\ln(r/r_{\mathrm{p}})}{s_{\mathrm{p}}} \right)^2 \right) \tag{5.34}$$

with the distribution parameters r_{p} and s_{p}. As described in [38], both parameters can be related to the SEC distribution coefficient K_{D} according to

$$K_{\mathrm{D}}(a_{\mathrm{h}}) = \frac{\int_{a_{\mathrm{h}}}^{\infty} f(r) \left(1 - \frac{a_{\mathrm{h}}}{r} \right)^2 dr}{\int_0^{\infty} f(r) dr}. \tag{5.35}$$

Using the experimental K_{D} values reported in [166], least squares fitting of Eq. (5.35) allowed a determination of r_{p} and s_{p}, and $A_{\mathrm{s},0}$. Based on $A_{\mathrm{s},0}$, the ligand surface density was derived from Λ_{IEX} according to $\Gamma_{\mathrm{L}} = \Lambda_{\mathrm{IEX}} A_{\mathrm{s},0}^{-1}$.

5.3.2 Linear Gradient Experiments

The CPA and SMA model were calibrated using linear salt gradient experiments at very low protein load density. Experimental data were generated at pH 5.5, 6.0, 6.5, and 7.0 and with varying normalized gradient slope $G_{\mathrm{H}} = \varepsilon(I_{\mathrm{m,B}} - I_{\mathrm{m,A}})V_{\mathrm{c}}V_{\mathrm{g}}^{-1}$, whereby $V_{\mathrm{c}} = 1.96$ mL denotes the column volume, $\varepsilon = 0.35$ is the void fraction, V_{g} is the duration of the gradient in volume, and $I_{\mathrm{m,A}}$ and $I_{\mathrm{m,B}}$ represent the ionic strength at the beginning and end of the gradient, respectively. A detailed description of the experiments can be found in [32].

In alignment with previous works [32; 150; 189], model parameters were determined using the measured ionic strength at the peak maximum as reference value. The simulated ionic strength at peak maximum was calculated by solving the ideal mass balance equation

$$\frac{\partial c_i}{\partial t}(x,t) = -\frac{1-\varepsilon_{\mathrm{t}}}{\varepsilon_{\mathrm{t}}}\frac{\partial q_{\mathrm{v},i}}{\partial t}(x,t) - \frac{u_0}{\varepsilon_{\mathrm{t}}}\frac{\partial c_i}{\partial x}(x,t) \tag{5.36}$$

described in [68; 152], where t [s] is the time, x [m] is the axial column position, $\varepsilon_{\mathrm{t}} = 0.76$ represents the total column porosity, and $u_0 = 150$ cm h^{-1} denotes the linear velocity. This column model is highly simplified, but is sufficient for the determination of the ionic strength at peak maximum and thus equilibrium parameters. The temporal change of $q_{\mathrm{v},i}$ was described using the solid film linear driving force model [68; 152]

$$\frac{\partial q_{\mathrm{v},i}}{\partial t}(x,t) = k_{\mathrm{app},i}\left(q_{\mathrm{v},i}^*(c_i) - q_{\mathrm{v},i}(x,t)\right), \tag{5.37}$$

where $k_{\mathrm{app},i}$ [s^{-1}] is the lumped mass transfer coefficient, and $q_{\mathrm{v},i}^*$ is the equilibrium solid concentration given c_i according to the CPA model [Eq. (5.11)] or SMA model [Eq. (5.31)]. The system of partial differential equations were numerically solved by using ChromX (GoSilico GmbH, Karlsruhe, Germany). For all simulations, the variable time-stepping scheme IDAS was used for discretization in time. Discretization in space was performed with 200 equidistant axial cells using a linear Streamline-Upwind Petrov-Galerkin (SUPG) ansatz.

For the CPA model, the radius of the mAb was estimated to be $a_i = 5.5$ nm based on literature data [26; 29; 103]. Following reported titration curves for antibodies [64], the characteristic protein charge within the investigated pH range was approximated by the quadratic function

$$\begin{aligned} Z_i(\mathrm{pH}) = &Z_i(\mathrm{pH_{ref}}) + Z_{1,i}(\mathrm{pH} - \mathrm{pH_{ref}}) \\ &+ Z_{2,i}(\mathrm{pH} - \mathrm{pH_{ref}})^2, \end{aligned} \tag{5.38}$$

where $\mathrm{pH_{ref}} = 6.25$ represents a reference pH and $Z_i(\mathrm{pH_{ref}})$, $Z_{1,i}$, and $Z_{2,i}$ are empirical parameters determined by model fitting. As derived empirically in the supplementary material, the pH dependence of Δ_i can be described by

$$\begin{aligned} \log_{10}\left(\Delta_i(\mathrm{pH})\right) = &\log_{10}\left(\Delta_i(\mathrm{pH_{ref}})\right) \\ &+ \Delta_{1,i}\left(|\sigma_{\mathrm{I},i}(\mathrm{pH})| - |\sigma_{\mathrm{I},i}(\mathrm{pH_{ref}})|\right) \end{aligned} \tag{5.39}$$

where $\Delta_i(\mathrm{pH_{ref}})$ and $\Delta_{1,i}$ are fitting parameters and $\sigma_{\mathrm{I},i} = eZ_i(4\pi a_i^2)^{-1}$. In case of the SMA model, the pH was not directly considered in the model. Instead, the SMA parameters $\tilde{\nu}_i$ and $\tilde{k}_{\mathrm{eq},i}$ were determined independently for each investigated pH value.

5.3.3   Batch Adsorption Experiments

The calibrated CPA model and SMA models were extended to the nonlinear adsorption range and compared using adsorption isotherms of the mAb at varying ionic strength and pH. For the CPA model, the adsorber surface accessible by the mAb $A_{\text{s},i}(a_i = 5.5 \text{ nm})$ was derived *a priori* from Eq. (5.33). To allow a direct comparison of the SMA and CPA model with respect to the ASF, lateral electrostatic interactions between adsorbed proteins were neglected by setting $Z_{\text{lat},i} = 0$. Experimental adsorption data were used for model validation. In case of the SMA model, $\tilde{\sigma}_i$ was determined for each investigated pH by fitting the SMA model to experimental adsorption data keeping $\tilde{\nu}_i$ and $\tilde{k}_{\text{eq},i}$ fixed.

5.4   Results and Discussion

5.4.1   Model Parameters

Both the CPA model and SMA model contain model parameters that can be determined either *a priori* using literature data or by fitting the model to experimental data. In the case of the SMA model, the adsorber system is thereby defined by the system parameter Λ_{IEX}. It can be determined by a combination of tracer pulse injections and acid-base titration. For the CPA model, an additional characterization of the adsorbent system by iSEC is required to determine $A_{\text{s},0}$ and thus Γ_{L}. Compared to the SMA model, this requires about five additional pulse injections with tracer substances that differ significantly in size and thus pore accessibility. The pK_{L} of the ligand can usually be taken from the literature and does not require an experimental determination. It allows an explicit distinction between strong and weak ion exchanges in the CPA model.

In the linear adsorption regime and constant pH, the Henry coefficient is defined by additional protein-specific model parameters in both models. These include a_i, Δ_i, and Z_i in the CPA model and $\tilde{k}_{\text{eq},i}$ and $\tilde{\nu}_i$ in the SMA model. The radius of a protein a_i can often be derived empirically from its molecular weight and thus usually requires no experimental effort. Following the approach described by Yamamoto [189], the SMA parameters $\tilde{k}_{\text{eq},i}$ and $\tilde{\nu}_i$ are often determined using linear gradient elution experiments with varying gradient length and low protein load density. The same experiments can be used to determine Δ_i, and Z_i in the CPA model. However, given the mathematical complexity of the CPA model, both parameters cannot be derived analytically from the normalized gradient slope and the ionic strength at protein elution, as in the case of the SMA model.

In the case of the SMA model, the extension of the model to the nonlinear adsorption region is performed by introducing the shielding parameter $\tilde{\sigma}_i$. The parameter can be determined using batch adsorption data or chromatography data at high load density. For the CPA model, $A_{\text{s},i}$ can be estimated based on iSEC data using Eq. (5.33) and further refined using data in the nonlinear adsorption regime. As the CPA model parameter $Z_{\text{lat},i}$ accounts for electrostatic protein-protein interactions, it can be accurately determined only at high protein load density and low ionic strength.

Table 5.1: System parameters of Poros XS

System parameter	Unit	Value
Pore size distribution parameter r_p	[nm]	11.46
Pore size distribution parameter s_p	[−]	0.01
Total accessible surface area $A_{\mathrm{s},0}$	[nm^{-1}]	0.46[‡]
Theoretical surface area accessible by the mAb $A_{\mathrm{s},i}(5.5\text{ nm})$	[nm^{-1}]	0.24[‡]
Ionic capacity Λ_IEX	[M]	0.86[§]
Ligand density $\Gamma_\mathrm{L} = \Lambda_\mathrm{IEX} A_{\mathrm{s},0}^{-1}$	[μmol m^{-2}]	1.86
Column length L_c	[mm]	100[†]
Column volume V_c	[mL]	1.96[†]
Void fraction ε	[−]	0.35[†]
Total column porosity ε_t	[−]	0.76[†]

[§] according to Steinebach et al. [166]
[†] according to Creasy et al. [32]
[‡] according to Eq. (5.33)

5.4.2 System Characterization

Estimated parameters of the adsorber system Poros XS are summarized in Table 5.1. The pore size distribution parameters r_p and s_p were determined by fitting Eq. (5.35) to measured K_D values for Poros XS published in [166]. A comparison between the fitted pore model and experimental data can be found in Fig. B.1 in the appendix. Given r_p, s_p, and Eq. (5.33), the theoretical adsorber surface accessible by the mAb $A_{\mathrm{s},i} = 0.24$ nm^{-1} corresponds to approximately 50% of the total adsorber surface $A_{\mathrm{s},0} = 0.46$ nm^{-1}.

5.4.3 Linear Gradient Experiments

To calibrate the CPA and SMA model for the limiting case $\Theta \to 0$, retention data of linear gradient experiments at low protein load density and with varying G_H were used. Markers in Fig 5.3 indicate the measured ionic strength at protein elution as a function of G_H. Black lines represent fitted model curves based on the CPA model (Fig. 5.3(a)) and SMA model (Fig. 5.3(b)). In the case of the CPA model, model curves shown in Fig. 5.3(a) are based on a single model that accounts explicitly for the pH. In case of the SMA model, each pH is described by an individual model. A direct consideration of the pH in the SMA model was not considered as there is no unified approach in the literature to extend the original pH independent model. Both models the CPA and SMA model are able to describe the experimental results adequately. While they show no significant differences with respect to the data shown in Fig. 5.3, they differ significantly in the mechanistic description of the observed behavior. As schematically shown in Fig. 5.4(a), the stoichiometric description of protein adsorption within the framework of the SMA model [Eq. (5.29)] suggests that counter-ions of the adsorber surface are condensed at the adsorber surface. Accompanied by the formation of a reversible protein-ligand complex, they can be displaced from the adsorber surface. For a medium with high relative permittivity like water, this state of adsorbed counter-ions has been questioned in the past as it would result in a significant reduction of the entropy in the system [161]. Within the framework of the CPA model, the system close to the adsorber surface is considered to be much more disordered as schematically shown in Fig. 5.4(b). Given their thermal energy, counter-ions are not expected to be condensed but diffusely distributed around charged surfaces. The
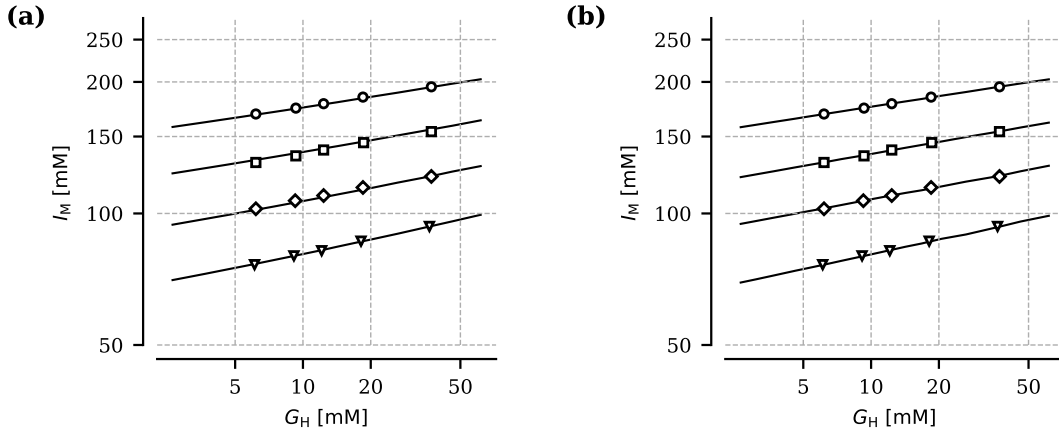
Figure 5.3: Elution salt gradient as a function of the normalized gradient slope for a mAb on Poros XS according to [32]. Experimental data are shown as markers. Continuous lines represent fitted curves based on the CPA model (a) and SMA model (b). Experimental data were generated at pH 5.5 ($\circ$), 6.0 ($\square$), 6.5 ($\diamond$), and 7.0 ($\triangledown$).

adsorption state of a protein is also not defined by a unique and ordered protein-ligand complex. Instead, Eq. (5.5) and Eq. (5.6) in the CPA model propose a more disordered state where adsorbed proteins are distributed within the interaction boundary layer.

The different mechanistic interpretation of protein adsorption has significant impact on the characteristic protein charge Z_i in the CPA model and $\tilde{\nu}_i$ in the SMA model. While the terminology is the same in both models, their physical interpretation is different. In the SMA model, $\tilde{\nu}_i$ describes the number of ligands involved in the formation of the protein-ligand complex as indicated in red in Fig. 5.4(a). As expected from a protein charge, determined model parameters summarized in Table 5.3 show a decrease of $\tilde{\nu}_i$ with increasing pH. However, given the stoichiometric description of the adsorption process in the SMA model, $\tilde{\nu}_i$ is rather abstract in nature and should not be compared with the net charge of a protein. In the CPA model, on the other hand, the characteristic charge Z_i defines the effective charge density or electrostatic potential of the protein surface directed towards the adsorber surface. Thus, in principle, the characteristic charge in the CPA model has a comparable meaning as the net charge of a protein. However, due to a number of assumptions and simplifications in the CPA model, Z_i is also subject to some model abstraction. Considering proteins as perfect spheres with homogeneous surface charge density greatly simplifies the mathematical description of the adsorption equilibrium, but is a considerable simplification for complex proteins such as mAbs. In addition to geometrical simplifications, the description of electrostatic protein-adsorber interactions is based on the linearized Poisson-Boltzmann equation. The accuracy of this description is rather uncertain considering the high surface charge density of the adsorber and the mAb. In the light of these simplifications, the fitting parameter Z_i is also rather abstract in nature. Thus, estimated characteristic charge values shown in Table 5.2 should not be compared with the true net charge of a protein.

5.4.4 Batch Adsorption Experiments

With growing coverage of the adsorber surface, interactions between proteins become increasingly important causing a nonlinearity in the adsorption behavior. In both models

Table 5.2: CPA parameters of the mAb on Poros XS determined using linear salt gradient experiments at low protein density. The calibrated model describes the adsorption as a function of the ionic strength and the pH. Parameter uncertainty is indicated by the 95% confidence interval.

Parameter	Unit	Value
$Z_i(\text{pH}_{\text{ref}})$	$[-]$	63.32 ± 0.75
$Z_{1,i}$	$[-]$	-26.23 ± 0.67
$Z_{2,i}$	$[-]$	4.07 ± 0.29
$\log_{10}(\Delta_i(\text{pH}_{\text{ref}}))$	$[-]$	-3.61 ± 0.19
$\Delta_{1,i}$	$[\text{m}^2\,\text{C}^{-1}]$	-94.11 ± 4.13

the SMA and CPA model, protein-protein interactions are mostly ascribed to steric or hard body interactions that are mathematically described by the ASF $B_i(\Theta)$ in the CPA model or $\tilde{B}_i(q_v)$ in the SMA model. Similar to the protein-adsorber interaction discussed in Fig. 5.4, both modeling approaches deviate considerably in the mechanistic interpretation of steric effects. While according to $B_i(\Theta)$ protein adsorption is physically limited by the accessible surface area of the adsorber system, $\tilde{B}_i(q_v)$ defines the ionic capacity of the adsorber system as the limiting factor. Within the stoichiometric framework of the SMA model, steric effects are described by a shielding of adsorber ligands by adsorbed proteins, as schematically shown in Fig. 5.5(a). The number of ligands shielded by a single protein is defined by the SMA parameter $\tilde{\sigma}_i$. For a sphere with radius 5.5 nm, the expected value would be $\tilde{\sigma}_i = 107$ using the ligand surface density of Poros XS in Table 5.1. According to Eq. (5.30), the shielding of ligands is mathematically associated with a decrease in the protein-adsorber interaction. With increasing coverage of the adsorber surface, adsorbed proteins face only a fictitious reduced ligand density, resulting in a lower affinity to the adsorber surface. As a consequence, the characteristic charge of the protein $\tilde{\nu}_i$ enters Eq. (5.32) as an exponent and has a significant effect on $\tilde{B}_i(q_v)$. Proteins with a high characteristic charge are more affected by the described steric effects as they are more sensitive to a change in Λ_{IEX}. A theoretical shortcoming of the stoichiometric description of steric effects in the SMA model is that $\tilde{\sigma}_i$ depends physically on the ligand density. It is therefore only valid for a specific Λ_{IEX} and is expected to increase with an increase in Λ_{IEX}.

Unlike the SMA model, the CPA model treats the ionic capacity or ligand density of the
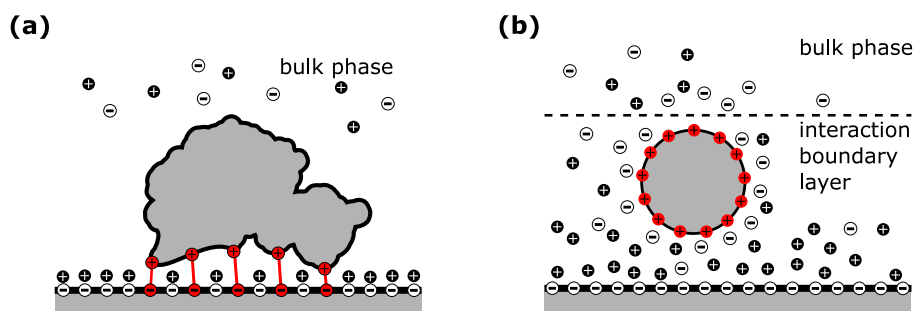
Figure 5.4: Mechanistic interpretation of the characteristic protein charge in the SMA model (a) and CPA model (b). In the SMA model, ν_i defines the number of adsorber ligands forming the protein-ligand complex. In the CPA model, Z_i defines the effective surface charge density or electrostatic surface potential of a perfect sphere.
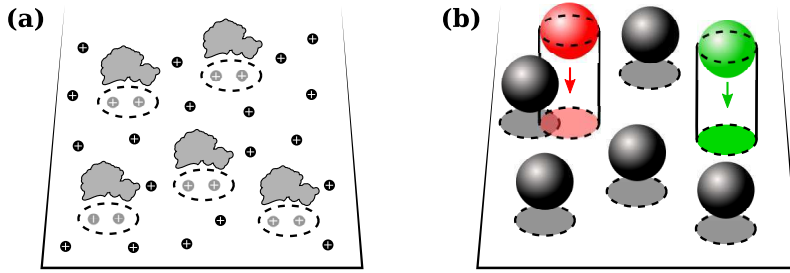
Figure 5.5: Mechanistic interpretation of the available surface function according to the SMA model (a) and CPA model (b).

adsorber system as a constant and defines the accessible surface area as the physically limiting factor. According to Widom [185], $B_i(\Theta)$ can be considered as a measure for the probability of inserting a protein into the given configuration of adsorbed proteins so that no overlap occurs. As schematically shown in Fig. 5.5(b) for the CPA model, a protein can only adsorb if it encounters an unoccupied area on the adsorber surface. With growing coverage of the adsorber surface, there is an increased probability of encountering an occupied region on the adsorber surface that prevents a protein from adsorbing, regardless of its affinity. In contrast to the SMA model, $B_i(\Theta)$ is not affected by the characteristic charge of a protein as it only accounts for hard-body interactions. Given a configuration of adsorbed protein defined by Θ, smaller proteins have a higher probability of encountering an unoccupied area than large proteins. Electrostatic protein-protein interactions induced by the surface charge density of proteins are considered independently in the CPA model by $u_{\text{lat},i}$. These soft-body interactions are not explicitly considered by the SMA model. A fundamental difference to the SMA model is that the protein-adsorber interaction is independent of the surface coverage according to the superposition in Eq. (5.3). As indicated in Fig. 5.5(b), every adsorbed protein faces the bare adsorber surface with constant ligand density. While the superposition approximation is justified for low values in Θ, it is important to note that this assumption can lose its justification at very high surface coverage where the distance between adsorbed proteins is small. The reason for this is that proteins change the electrostatic environment close to the adsorber surface and therefore affect the double layer of the adsorber surface locally. With decreasing distance between adsorbed proteins, the protein-adsorber interaction becomes more and more a multi-body problem which is not taken into consideration.

The superposition approximation in the CPA model is a crucial assumption as it also implies that protein parameters determined in the linear adsorption range are valid over the entire adsorption range $\Theta \in [0, \Theta_{\text{max}}]$. To validate this assumption and compare both adsorption models in the nonlinear adsorption range, both models were used to describe experimental batch adsorption data of the mAb shown as markers in Fig. 5.6. Using the theoretical accessible surface area $A_{\text{s},i} = 0.24 \text{ nm}^{-1}$ in Table 5.1 and assuming $Z_{\text{lat},i} = 0$, the CPA model calibrated in the linear adsorption range in Sec. 5.4.3 can already be used to perform extrapolations across the entire adsorption regime. Adsorption isotherms extrapolated by the CPA model are represented by continuous lines on the left side of Fig. 5.6. As a measure of how well experimental data are replicated by the CPA model, the predictive R^2 is shown for each pH. The gray shading indicates the region $\Theta \in [\Theta_{\text{jam}}, \Theta_{\text{hex}}]$ between the maximum surface coverage according to random sequential adsorption $\Theta_{\text{jam}} = 0.547$ [76] and hexagonal close packing $\Theta_{\text{max}} = 0.907$. Although the
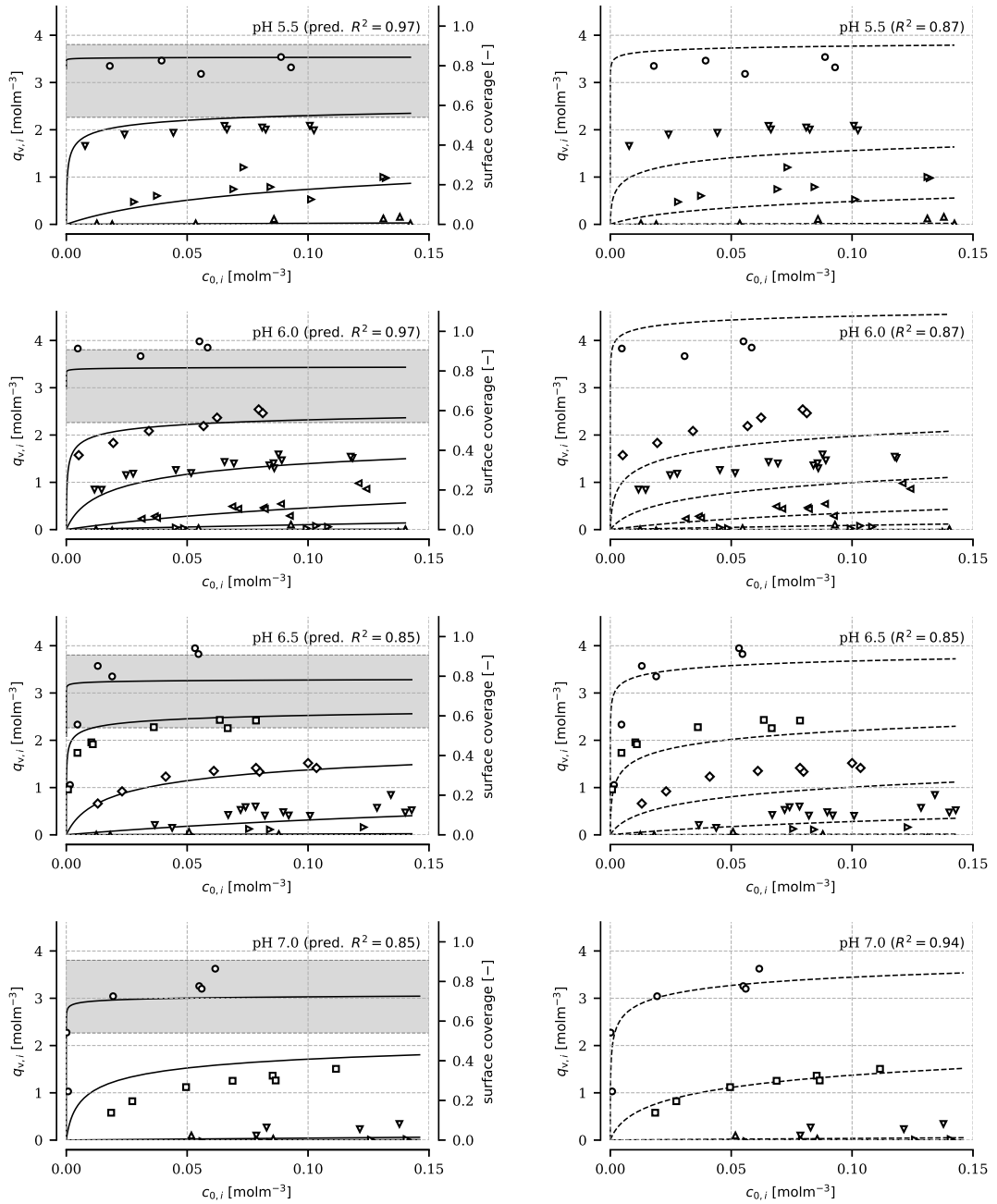
Figure 5.6: Adsorption isotherms of a mAb on Poros XS as a function of pH and ionic strength. Markers represent experimental data according to [32] while lines represent model curves. left: Comparison between experimental data and extrapolated adsorption isotherms based on the CPA model (—). The CPA model was calibrated in the linear adsorption regime using linear gradient experiments shown in Fig. 5.3. As a measure of how well experimental data are replicated by the CPA model, the predictive R^2 is shown for each pH. Gray shading indicates the region between the maximum surface coverage according to random sequential adsorption and hexagonal close packing. right: Comparison between fitted model curves based on the SMA model (---) and experimental data. For each pH, the goodness of fit is indicated by R^2. Protein adsorption was investigated at an ionic strength of 20 mM ($\circ$), 45 mM ($\square$), 70 mM ($\diamond$), 95 mM ($\triangledown$), 120 mM ($\triangleleft$), 145 mM ($\triangleright$), and 220 mM ($\triangle$).

Table 5.3: SMA parameters of the mAb on Poros XS determined using linear salt gradient experiments at low protein density shown in Fig. 5.3 and batch adsorption data shown in Fig. 5.6. Parameter uncertainty is indicated by the 95% confidence interval.

Parameter	Unit	pH 5.5	pH 6.0	pH 6.5	pH 7.0
$\tilde{\nu}_i$ [§]	$[-]$	11.35 ± 0.43	9.89 ± 0.34	9.34 ± 0.32	7.90 ± 0.28
$\log(\tilde{k}_{\mathrm{eq},i})$ [§]	$[-]$	-7.52 ± 0.31	-7.64 ± 0.28	-8.26 ± 0.30	-8.01 ± 0.30
$\tilde{\sigma}_i$ [†]	$[-]$	183.14 ± 18.86	142.07 ± 13.03	163.38 ± 16.40	148.08 ± 14.05

[§] based on retention data shown in Fig. 5.3

[†] based on batch adsorption data shown in Fig. 5.6

CPA model was calibrated in the linear adsorption range and $A_{\mathrm{s},i}$ was estimated *a priori* using inverse SEC data, extrapolated adsorption isotherms are already in good agreement with experimental data. Only experimental data close to or beyond Θ_{max} cannot be reproduced by the CPA model as they would result in a steric overlap between adsorbed proteins. While the neglect of electrostatic protein-protein interactions ($Z_{\mathrm{lat},i} = 0$) might be a simplification for the gray shaded area, it has no affect for conditions $\Theta \lesssim \Theta_{\mathrm{jam}}$ given the large distance between adsorbed proteins and the fact that electrostatic interactions are screened at higher ionic strength. A posterior incorporation of electrostatic protein-protein interactions in the calibrated CPA model was not considered in view of the already good validation results. Furthermore, neglecting $Z_{\mathrm{lat},i}$ allows a direct model comparison with respect to the ASF.

In case of the SMA model, $\tilde{\sigma}_i$ can hardly be estimated *a priori* and needs to be determined by fitting the model to experimental data at high surface coverage. Therefore, dashed lines on the right side of Fig. 5.6 represent fitted model curves based on the SMA model. As in the case of the CPA model, model parameters determined earlier in Sec. 5.4.3 were adopted. Only $\tilde{\sigma}_i$ was determined for each pH. Parameter estimates at pH 5.5, 6.0, 6.5, and 7.0 can again be found in Table 5.3. With values around 150, estimates are larger than the theoretical value of 107 derived earlier, but reasonable compared to values reported in the literature [21; 34; 78]. They do not show a distinct pH dependence. Comparing model curves based on the SMA model with those of the CPA model, significant differences between both models can be observed. Although simulated curves based on the CPA model are extrapolations, they show in general a better agreement with experimental data than fitted curves based on the SMA model, as indicated by the R^2 values in Fig. 5.6. Only in the case of pH 7.0, data based on the SMA model are in better alignment with measurements. Discrepancies between model predictions based on the CPA model and experimental data at pH 7.0 may possibly be attributed to the assumption that only Z_i and Δ_i are pH dependent. The protein radius a_i, on the other hand, is assumed to be constant and not affected by variations in pH. Given the ability of proteins to adjust their conformation and thus their size in response to variations in pH and ionic strength, this represents a simplification that may explain some discrepancies in Fig. 5.6.

As electrostatic protein-protein interactions were neglected in the CPA model ($Z_{\mathrm{lat},i} = 0$) and both models show comparable results in the linear adsorption range (Fig. 5.3), model differences in Fig. 5.6 must be attributed to the different mechanistic interpretation of steric interactions and thus the ASF. A comparison of $B_i(\Theta)$ and $\tilde{B}_i(q_{\mathrm{v}})$ according to the calibrated models is given in Fig. 5.7. As $\tilde{B}_i(q_{\mathrm{v}})$ is a function of $\tilde{\nu}_i$, the profile of $\tilde{B}_i(q_{\mathrm{v}})$ shown in black is inherently affected by the pH. For the available surface function of the CPA model shown in red, a single relationship is shown as $B_i(\Theta)$ is unaffected
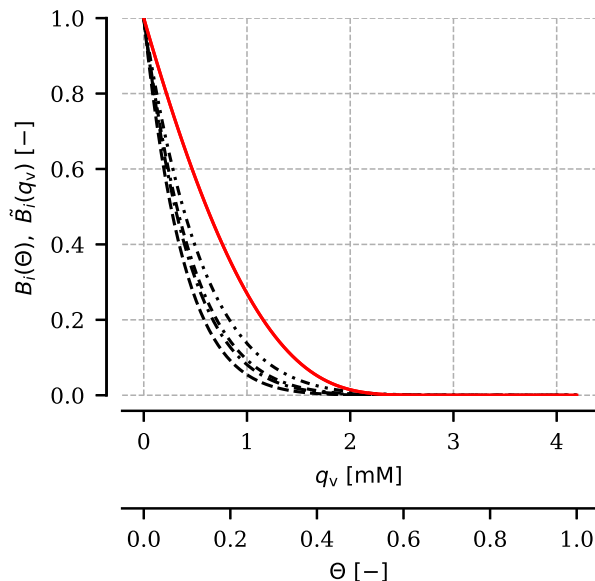
Figure 5.7: Available surface function according to the SMA and CPA model. Black lines represent $\tilde{B}_i(q_v)$ according to the SMA model at pH 5.5 (---), 6.0 (-·-), 6.5 (·---·), and 7.0 (-···-). The red line represents $B_i(\Theta)$ according to the CPA model.

by a change in pH. As can be seen steric effects described by the SMA model are much more pronounced than in case of the CPA model. This can be attributed to the fact that steric effects are described by a reduction in the ionic capacity. As described earlier, this stoichiometric interpretation of steric hindrance implies also a reduction of the protein-adsorber interaction. With decreasing characteristic protein charge, the interaction between the protein and the adsorber becomes less sensitive to a change in Λ_{IEX}. As a consequence, steric effects in the SMA model are less pronounced with increasing pH and $\tilde{B}_i(q_v)$ approaches $B(\Theta)$. It is noticeable that discrepancies between the SMA model and experimental isotherm data shown in Fig. 5.6 increase with decreasing pH. At pH 5.5 where $\tilde{B}_i(q_v)$ deviates strongly from $B_i(\Theta)$, simulated data based on the SMA show a significant overestimation of nonlinear adsorption effects. As the pH increases and $\tilde{B}_i(q_v)$ approaches $B_i(\Theta)$, simulated data based on the SMA model show increasing agreement with experimental data. Results shown in Fig. 5.6 and Fig. 5.7 suggest that the simplified stoichiometric description of steric hindrance in the SMA model can provide an overestimation of nonlinear effects. The good agreement between experimental data and model predictions in case of the CPA model shows that the model can provide in general a better description of steric effects across the entire investigated pH range. Results support further the superposition approximation in the CPA model and show that the majority of model parameters can be determined at the limiting case $\Theta \to 0$ and used afterwards across the entire adsorption range.

5.5 Conclusion

We introduced a colloidal particle adsorption model that describes protein adsorption within the linear and nonlinear adsorption regime. The proposed CPA model is based

on a non-stoichiometric description of electrostatic interactions between proteins and IEX adsorbers combined with steric and electrostatic interactions between adsorbed proteins. It was demonstrated that the majority of model parameters can be determined in the linear adsorption range or estimated *a priori* using inverse SEC. Subsequently, the model can be used to predict adsorption behavior in the nonlinear adsorption regime. If necessary, the model can be extended or refined as soon as experimental data in the nonlinear adsorption regime becomes available. Such a sequential approach is often preferred as it can significantly reduce the amount of material needed to calibrate the mechanistic model.

The introduced model was compared with the SMA model commonly used in academia and industry. By using the formalism of the available surface function for the SMA model, a clear basis for distinguishing the CPA and SMA model in the nonlinear adsorption regime was established. The model comparison showed consistent model results in the linear adsorption regime but significant model differences in the nonlinear adsorption regime in simulating adsorption isotherms and elution profiles under ideal chromatography conditions. Observed model differences could be attributed to the varying interpretation of steric hindrance in both models. Results suggest that the stoichiometric framework of the SMA model leads to an inadequate description of steric effects between adsorbed proteins. Given the overall better description of experimental adsorption isotherms of a mAb over a wide range of pH and ionic strength by the CPA model, it can help to better understand nonlinear protein adsorption.

Analysis of Complex Protein Elution Behavior in Preparative Ion Exchange Processes using a Colloidal Particle Adsorption Model

Till Briskot[1,2], Tobias Hahn[1], Thiemo Huuk[1], Gang Wang[3], Simon Kluters[3], Joey Studts[3], Felix Wittkopp[4], Johannes Winderl[5], Peter Schwan[6], Isabell Hagemann[6], Klaus Kaiser[6], Anja Trapp[7], Serge M. Stamm[7], Jadranka Koehn[7], Gunnar Malmquist[8], Jürgen Hubbuch[2]

[1] GoSilico GmbH, Karlsruhe, Germany
[2] Karlsruhe Institute of Technology (KIT), Institute of Process Engineering in Life Sciences, Section IV: Biomolecular Separation Engineering, Karlsruhe, Germany
[3] Late Stage DSP Development, Boehringer Ingelheim Pharma GmbH & Co. KG, Biberach an der Riß, Germany
[4] Pharma Research and Early Development (pRED), Roche Innovation Center Munich, Roche Diagnostics GmbH, Penzberg, Germany
[5] Roche Pharma Technical Development, Roche Diagnostics GmbH, Penzberg, Germany
[6] Bayer AG, Leverkusen, Germany
[7] Process Science & Innovation, Rentschler Biopharma SE, Laupheim, Germany
[8] R&D, Cytiva, Uppsala, Sweden

Abstract

A fundamental understanding of the protein retention mechanism in preparative ion exchange (IEX) chromatography columns is essential for a model-based process development approach. For the past three decades, the mechanistic description of protein retention has been based predominantly on the steric mass action (SMA) model. In recent years, however, retention profiles of proteins have been reported more frequently for preparative processes that are not consistent with the mechanistic understanding relying on the SMA model.

In this work, complex elution behavior of proteins in preparative IEX processes is analyzed using a colloidal particle adsorption (CPA) model. The CPA model is found to be capable of reproducing elution profiles that cannot be described by the traditional SMA model. According to the CPA model, the reported complex behavior can be ascribed to a strong compression and concentration of the elution front in the lower unsaturated part of the chromatography column. As the unsaturated part of the column decreases with increasing protein load density, exceeding a critical load density can lead to the formation of a shoulder in the peak front. The general applicability of the model in describing preparative IEX processes is demonstrated using several industrial case studies including multiple monoclonal antibodies on different IEX adsorber systems. In this context, the work covers both salt controlled and pH-controlled protein elution.

Keywords: *Protein adsorption; Protein purification; pH gradient; Mechanistic modeling; Steric mass action model; Poisson-Boltzmann*

6.1 Introduction

While the development of chromatography processes for the purification of biopharmaceutical proteins is still predominantly based on an empirical approach, mechanistic process models have gained increasing attention from pharmaceutical companies in recent years [141; 145]. By providing a fundamental understanding of the behavior of a process, mechanistic models can play a decisive role in the optimization [71; 80; 118; 123; 124], characterization [14; 30; 88; 92; 180], and scale-up of chromatography processes [7; 53; 111]. In particular, mechanistic modeling of ion exchange (IEX) chromatography has received considerable attention, as IEX chromatography remains the most widely used chromatography mode and is considered to be mechanistically understood.

Over the past three decades, the mechanistic description of protein retention in IEX processes has been predominantly based on the steric mass action (SMA) isotherm introduced by Brooks and Cramer [22]. By describing the interaction between proteins and IEX resins based on a reversible exchange of adsorber counter-ions by proteins in the mobile phase, the model explicitly accounts for the influence of the ionic strength on protein adsorption. The nonlinear behavior of adsorption at high protein concentrations is described by considering a shielding of counter-ions bound to the adsorber surface due to steric hindrance and repulsive forces between adsorbed proteins [22; 102]. The protein binding capacity of an IEX adsorber is thereby physically constrained by its ionic capacity. Despite its conceptual simple representation of protein adsorption, the model has successfully been used in many cases and is therefore still the most widely used model in both academia [14; 71; 80; 87; 88; 97; 123; 124] and industry [21; 77; 92; 140; 149; 150; 180]. However, with the increasing application of the adsorption model for industrial IEX processes, discrepancies between the model and experimental data have been observed more frequently in recent years [32; 33; 40; 78]. In case of high protein load densities close to the dynamic binding capacity of the column and protein elution based on linear salt gradients, the formation of a shoulder in the front of the elution peak was observed for different proteins and adsorber systems, which could not be interpreted based on the traditional SMA model. Diedrich et al. [40] hypothesized that the observed elution behavior of a monoclonal antibody (mAb) on the polymer-grafted adsorber system Fractogel EMD SO_3^- is caused by the existence of multiple binding configurations. Adsorbed proteins were thereby assumed to be gradually wrapped by the tentacle structures grafted onto the surface of Fractogel EMD SO_3^- [40]. By extending the traditional SMA model to multiple binding configurations, the elution behavior could be described adequately. While the mechanism proposed by Diedrich et al. provides a vivid explanation for the observed behavior on polymer-grafted adsorber systems, it does not provide a distinct explanation for the observation of the same behavior on classical adsorber systems without tentacle structures. Huuk et al. [78] explained the formation of a comparable peak shoulder for a mAb on the adsorber Poros 50 HS by a non-ideal behavior of proteins in the mobile phase. Using an expression for the protein activity coefficient initially introduced by Mollerup [114], the non-ideality was mostly ascribed to interactions between proteins and ions at high salt concentrations. While the proposed extension of the SMA model was able to describe the experimental data, the assumed non-ideal behavior cannot be clearly verified in the linear adsorption range due to the moderate salt concentrations used in IEX processes [19]. Both mechanistic descriptions of the observed elution behavior are based on extensions of the original SMA model and on the assumption that the underlying stoichiometric mechanism of the

adsorption model is valid. An alternative approach of describing complex elution behavior that cannot be described by existing adsorption models like the SMA model was proposed by Creasy et al. [32–34]. Using high-throughput batch isotherm data and a systematic interpolation method, mAb elution profiles could be described at high protein load densities that could not be replicated using the traditional SMA model. However, since the method is based on a statistical approach, the calibration of the model is resource and time consuming, especially in the case of complex industrial multi-component systems.

In a previous study [20], we presented an alternative colloidal particle adsorption (CPA) model that describes nonlinear protein adsorption on charged surfaces as a function of ionic strength and pH. In contrast to the SMA model, the CPA model is not based on a stoichiometric exchange of counter-ions by proteins but on a fundamental description of electrostatic interactions within IEX columns using the colloidal nature of proteins. The maximum protein binding capacity of an adsorber is thereby not limited by its ionic capacity as in the SMA but by the accessible adsorber surface. Nonlinear adsorption behavior is described by considering steric blocking of the adsorber surface and electrostatic interactions between adsorbed proteins. While the CPA model was initially derived under equilibrium conditions to analyze batch adsorption data, the kinetic derivation of the adsorption model in this work provides a mechanistic description of the adsorption and desorption rate that can be used for the simulation of chromatography processes. The general ability of the CPA model in describing complex protein elution behavior is illustrated by applying the model to several preparative chromatography processes of multiple mAbs on adsorber systems differing in ligand structure and backbone.

6.2 Theory

6.2.1 Transport Dispersive Model

We consider a packed bed of length L_c [m] consisting of spherical adsorber beads with an average particle diameter d_p [m] and particle porosity ε_p [−]. The bed is considered to be homogeneous, both in radial and axial direction $x \in [0, L_c]$ [m]. According to the transport dispersive model (TDM), the temporal change of the solute bulk concentration $c_{b,j}$ [mol m^{-3}] in the interstitial volume at time t [s] is described by the column-wide mass balance equation

$$\frac{\partial c_{b,j}}{\partial t}(x,t) = -\frac{1-\varepsilon_v}{\varepsilon_v}\frac{6}{d_p}k_{\text{eff},j}\left(c_{b,j}(x,t) - c_{p,j}(x,t)\right)$$
$$- u_{\text{int}}(t)\frac{\partial c_{b,j}}{\partial x}(x,t) + D_{\text{ax}}\frac{\partial^2 c_{b,j}}{\partial x^2}, \tag{6.1}$$

whereby u_{int} [m s^{-1}] is the interstitial velocity of the mobile phase, D_{ax} [m^2 s^{-1}] denotes the axial dispersion coefficient, ε_v [−] represents the void fraction, $k_{\text{eff},j}$ [m s^{-1}] is the effective mass transfer coefficient, and $c_{p,j}$ [mol m^{-3}] represents the concentration of the j-th solute on the particle surface [152]. The mass balance equation is completed with Danckwerts' boundary conditions of dispersive systems at the column inlet

$$\frac{\partial c_{b,j}}{\partial x}(x=0,t) = \frac{u_{\text{int}}(t)}{D_{\text{ax}}}\left(c_{b,j}(x=0,t) - c_{\text{inlet},j}(t)\right) \tag{6.2}$$

and the column outlet

$$\frac{\partial c_{\mathrm{b},j}}{\partial x}(x = L_{\mathrm{c}}, t) = 0, \tag{6.3}$$

whereby $c_{\mathrm{inlet},j}$ is the concentration of the j-th solute at the inlet of the column [36].

In the TDM, the concentration inside the particle is assumed to be constant and identical to $c_{\mathrm{p},j}$. Under this assumption, $k_{\mathrm{eff},j}$ in the linear driving force model accounts for both internal and external mass transfer resistances. The mass transfer equation inside the adsorber bead simplifies to

$$\begin{aligned}
\frac{\partial c_{\mathrm{p},j}}{\partial t}(x, t) = &\frac{6}{\varepsilon_{\mathrm{p}} d_{\mathrm{p}}} k_{\mathrm{eff},j} \left(c_{\mathrm{b},j}(x,t) - c_{\mathrm{p},j}(x,t)\right) \\
&- \frac{1 - \varepsilon_{\mathrm{p}}}{\varepsilon_{\mathrm{p}}} \frac{\partial q_{\mathrm{v},j}}{\partial t}(x,t),
\end{aligned} \tag{6.4}$$

where $q_{\mathrm{v},j}$ [mol m^{-3}] denotes the adsorbed solute concentration per adsorber skeleton volume [152]. The surface density of protein bound to the adsorber surface $q_j = q_{\mathrm{v},j} A_{\mathrm{s},j}^{-1}$ [mol m^{-2}] is related to $q_{\mathrm{v},j}$ by the specific adsorber surface per skeleton volume accessible by the solute $A_{\mathrm{s},j}$ [m^{-1}].

6.2.2 Adsorption Rate

The mobile phase is considered to be an electrolyte solution at constant temperature $T = 298.15$ K, ionic strength I_{m} [mol m^{-3}], and relative permittivity $\varepsilon = 78.3$. The surface of the adsorber A immersed in the electrolyte solution is considered to be solid and planar. It is characterized by the surface ligand density Γ_{L} [mol m^{-2}] and the surface charge density σ_{A} [C m^{-2}]. A protein i immersed in the electrolyte solution is represented by a perfect sphere with radius a_i [m]. In alignment with [20], two definitions of the surface charge density of the sphere are considered in the following. The surface of the sphere directed towards the adsorber surface is characterized by the surface charge density σ_i or effective net charge $Z_i = 4\pi a_i^2 e^{-1} \sigma_i$ [−], whereby e [C] denotes the elementary charge. The protein surface laterally facing other adsorbed proteins, on the other hand, is defined by $\sigma_{\mathrm{lat},i} = e Z_{\mathrm{lat},i} (4\pi a_i^2)^{-1}$. The interaction free energy $u_{\mathrm{A},i}(z)$ [J] between the i-th protein and the adsorber surface is governed predominantly by electrostatic interactions and is a function of the distance z between the protein and the adsorber surface. Due to the finite range of electrostatic interactions, the protein interacts only within an interaction boundary layer with the adsorber surface [146; 147; 159]. The surface density q_i may therefore be describe by

$$q_i = \int_{\delta_{\mathrm{m},i}}^{\delta_i^*} c_i(z) dz, \tag{6.5}$$

where δ_i^* is the thickness of the boundary layer and $\delta_{\mathrm{m},i} = \arg\min_z u_{\mathrm{A},i}(z)$ denotes the position of the minimum of $u_{\mathrm{A},i}(z)$. Neglecting mass transfer lateral to the adsorber surface, the mass transfer inside the stagnant boundary layer can be described by the one-dimensional continuity equation

$$\frac{\partial c_i(z)}{\partial t} = -\frac{\partial j_i(z)}{\partial z} = \frac{\partial}{\partial z}\left(c_i(z) \frac{D_i(z)}{k_{\mathrm{b}} T} \frac{\partial \bar{\mu}_i(z)}{\partial z}\right), \tag{6.6}$$

where j_i [mol m^{-2}s^{-1}] represents the colloid flux, k_{b} [J K^{-1}] is the Boltzmann constant, D_i [m^2 s^{-1}] is the diffusion coefficient, and $\bar{\mu}_i$ [J] represents the electrochemical

potential [3]. The flux in Eq. (6.6) is considered to be negative if directed towards the adsorber surface. The electrochemical potential within the boundary layer is given by

$$\bar{\mu}_i(z) = \mu_i^* + k_{\mathrm{b}}T \ln\left(\frac{c_i(z)}{c^+}\right) + \Phi(z), \tag{6.7}$$

where μ_i^* is the reference potential at infinite dilution, c^+ is a reference concentration to make the term inside the logarithm dimensionless, and $\Phi = u_{\mathrm{A},i} + u_{\mathrm{lat},i} + \mu_i^{\mathrm{ex}}$ considers $u_{\mathrm{A},i}$, the lateral interaction between adsorbed proteins $u_{\mathrm{lat},i}$, and the excess chemical potential μ_i^{ex} [20]. As described in [20], μ_i^{ex} accounts for steric hindrance between proteins within the boundary layer. Using Eq. (6.7), Eq. (6.6) can be rewritten to

$$\begin{aligned}
\frac{\partial c_i(z)}{\partial t} &= -\frac{\partial j_i(z)}{\partial z} \\
&= \frac{\partial}{\partial z}\left(D_i(z)\frac{\partial c_i(z)}{\partial z} + D_i(z)\frac{c_i(z)}{k_{\mathrm{b}}T}\frac{\partial \Phi(z)}{\partial z}\right).
\end{aligned} \tag{6.8}$$

If we assume that the relaxation time of establishing the quasi stationary transport condition $\partial c_i(z)/\partial t = 0$ through the thin interaction boundary layer is very short, one can treat j as quasi-stationary [1; 3; 146]. In this case j is given by the expression

$$-j_i(z) = -j_i = D_i(z)\left(\frac{\partial c_i(z)}{\partial z} + \frac{c_i(z)}{k_{\mathrm{b}}T}\frac{\partial \Phi(z)}{\partial z}\right) \tag{6.9}$$

which can also be written as

$$-j_i = D_i(z)\exp\left(-\frac{\Phi(z)}{k_{\mathrm{b}}T}\right)\frac{\partial}{\partial z}\exp\left(\frac{\Phi(z)}{k_{\mathrm{b}}T} + \ln\left(c_i(z)\right)\right). \tag{6.10}$$

Integrating Eq. (6.10) within the limits $z \in [\delta_{\mathrm{m},i}, \delta_i^*]$, leads to

$$-j_i = \frac{c_{\mathrm{p},i}\exp\left(\frac{\Phi(\delta_i^*)}{k_{\mathrm{b}}T}\right) - c_i(\delta_{\mathrm{m},i})\exp\left(\frac{\Phi(\delta_{\mathrm{m},i})}{k_{\mathrm{b}}T}\right)}{\int_{\delta_{\mathrm{m},i}}^{\delta_i^*}\frac{1}{D_i(z)}\exp\left(\frac{\Phi(z)}{k_{\mathrm{b}}T}\right)dz} \tag{6.11}$$

with $c_i(\delta_i^*) = c_{\mathrm{p},i}$. Using Eq. (6.5) for q_i and considering ideal protein behavior outside the boundary layer ($\Phi(\delta_i^*) = 0$), Eq.(6.11) can be rewritten to

$$\frac{\partial q_i}{\partial t} = -j_i = k_{\mathrm{kin},i}\left(K_i c_{\mathrm{p},i} - q_i\right) \tag{6.12}$$

or

$$\frac{\partial q_{\mathrm{v},i}}{\partial t} = -A_{\mathrm{s},i}j_i = k_{\mathrm{kin},i}\left(K_{\mathrm{v},i}c_{\mathrm{p},i} - q_{\mathrm{v},i}\right), \tag{6.13}$$

whereby $k_{\mathrm{kin},i}$ [s^{-1}] is a kinetic parameter defined by

$$k_{\mathrm{kin},i} = \frac{1}{\int_{\delta_{\mathrm{m},i}}^{\delta_i^*}\frac{1}{D_i(z)}\exp\left(\frac{\Phi(z)}{k_{\mathrm{b}}T}\right)dz\int_{\delta_{\mathrm{m},i}}^{\delta_i^*}\exp\left(-\frac{\Phi(z)}{k_{\mathrm{b}}T}\right)dz} \tag{6.14}$$

and $K_{\mathrm{v},i}$ [$-$] represents an equilibrium coefficient given by

$$K_{\mathrm{v},i} = A_{\mathrm{s},i}K_i = A_{\mathrm{s},i}\int_{\delta_{\mathrm{m},i}}^{\delta_i^*}\exp\left(-\frac{\Phi(z)}{k_{\mathrm{b}}T}\right)dz. \tag{6.15}$$

As described in more detail in [20], it is assumed that both μ_i^{ex} and $u_{\mathrm{lat},i}$ are not a function of z, but depend only on the composition and configuration of the two-dimensional layer of adsorbed proteins. If we further assume that D_i is constant, Eq. (6.14) and Eq. (6.15) can be simplified to

$$k_{\mathrm{kin},i} = \frac{D_i}{\int_{\delta_{\mathrm{m},i}}^{\delta_i^*} \exp\left(\frac{u_{\mathrm{A},i}(z)}{k_{\mathrm{b}}T}\right) dz \int_{\delta_{\mathrm{m},i}}^{\delta_i^*} \exp\left(-\frac{u_{\mathrm{A},i}(z)}{k_{\mathrm{b}}T}\right) dz} \tag{6.16}$$

and

$$K_{\mathrm{v},i} = A_{\mathrm{s},i} B_i(\Theta) \exp\left(-\frac{u_{\mathrm{lat},i}}{k_{\mathrm{b}}T}\right) \int_{\delta_{\mathrm{m},i}}^{\delta_i^*} \exp\left(-\frac{u_{\mathrm{A},i}(z)}{k_{\mathrm{b}}T}\right) dz, \tag{6.17}$$

whereby $B_i(\Theta) = \exp\left(-\mu_i^{\mathrm{ex}}(k_{\mathrm{b}}T)^{-1}\right)$ represents the available surface function, $\Theta = \pi N_{\mathrm{A}} \sum a_i^2 q_i$ is the surface coverage, and N_{A} denotes the Avogadro number.

To get closed-form expressions for Eq. (6.16) and Eq. (6.17), $u_{\mathrm{A},i}(z)$ is linearized within $z \in [\delta_{\mathrm{m},i}, \delta_i^*]$ as described in [19; 20] leading to

$$k_{\mathrm{kin},i} = k_{\mathrm{kin},i}^* \frac{1}{2} \left(\frac{u_{\mathrm{A},i}(\delta_{\mathrm{m},i})}{k_{\mathrm{b}}T}\right)^2 \frac{1}{\cosh\left(\frac{u_{\mathrm{A},i}(\delta_{\mathrm{m},i})}{k_{\mathrm{b}}T}\right) - 1} \tag{6.18}$$

and

$$\begin{aligned} K_{\mathrm{v},i} = {} & \Delta_i B_i(\Theta) \frac{k_{\mathrm{b}}T}{u_{\mathrm{A},i}(\delta_{\mathrm{m},i})} \\ & \cdot \exp\left(-\frac{u_{\mathrm{lat},i}}{k_{\mathrm{b}}T}\right) \left(1 - \exp\left(-\frac{u_{\mathrm{A},i}(\delta_{\mathrm{m},i})}{k_{\mathrm{b}}T}\right)\right), \end{aligned} \tag{6.19}$$

whereby $\Delta_i = A_{\mathrm{s},i}(\delta_i^* - \delta_{\mathrm{m},i})$ and

$$k_{\mathrm{kin},i}^* = \frac{D_i}{(\delta_i^* - \delta_{\mathrm{m},i})^2} = A_{\mathrm{s},i}^2 \frac{D_i}{\Delta_i^2} \tag{6.20}$$

are fitting parameters. While $k_{\mathrm{kin},i}^*$ defines the rate of adsorption/desorption, the fitting parameter Δ_i is a measure for the thickness of the interaction boundary layer. In the case of $\partial q_{\mathrm{v},i}/\partial t = 0$, Eq. (6.13) leads to $q_{\mathrm{v},i} = K_{\mathrm{v},i} c_{\mathrm{p},i}$ which is identical to the expression previously derived in [20]. For a detailed description of $u_{\mathrm{A},i}(\delta_{\mathrm{m},i})$, $B_i(\Theta)$, and $u_{\mathrm{lat},i}$ in Eq. (6.18) and Eq. (6.19), we refer to [20].

6.2.3   Counter-Ion Release

We assume an electrolyte solution that contains only ions with absolute charge $z_+ = |z_-| = 1$ forming a diffuse layer around a protein of interest and the adsorber surface as schematically shown in Fig. 6.1. At infinite distance between adsorber and protein surface, the charge of the diffuse layer neutralizes the surface charge density of the corresponding inner layer. As the protein approaches the adsorber surface, the oppositely charged diffuse layers start to overlap causing an entropically driven release of counter-ions from the gap between both surfaces into the bulk phase. A detailed mathematical description of the amount of released counter-ions is complex and out of scope of this work. Instead, a simplified model is used where the exchange of counter-ions between bulk phase and diffuse
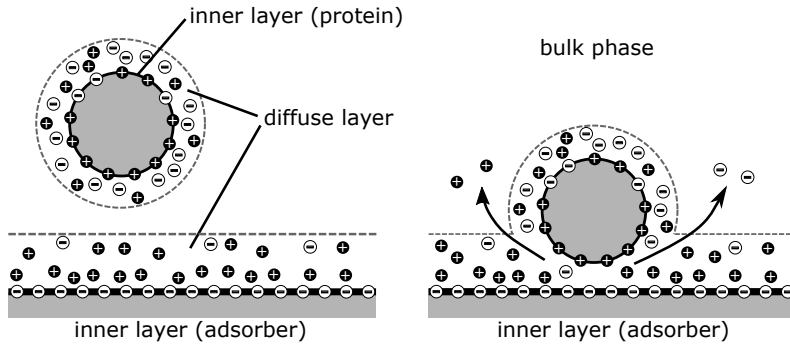
Figure 6.1: Schematic representation of the release of counter-ions upon protein adsorption.

layer upon protein adsorption and desorption is attributed to a mutual neutralization of the inner layers within the gap. The charge compensated by the adsorbed protein

$$z_{c,i} = \frac{\sigma_i}{e} A_i \tag{6.21}$$

is thereby approximated using the projection surface of the protein $A_i = \pi a_i^2$. If we assume that the diffuse layer contains only counter-ions, the amount of adsorbed counter-ions per adsorber surface q_c can be described by the neutrality condition

$$\sigma_A - e N_A \left(\mathrm{sgn}(\sigma_A) q_c - \sum_i z_{c,i} q_i \right) = 0. \tag{6.22}$$

Similar to the neutrality condition used within the framework of the SMA model [22], the algebraic equation (6.22) accounts for the release of adsorber counter-ions during protein adsorption and an update of counter-ions during protein desorption. To comply with overall electroneutrality, the same amount of protein counter-ions are released into the bulk phase as schematically shown in Fig. 6.1.

6.3   Materials and Methods

6.3.1   Proteins and Adsorber Systems

The retention behavior of five mAbs (mAb1-mAb5) with a molecular weight of approximately $M_{w,i} = 150$ kDa was investigated.

All experimental data were generated on the cation exchange resins Poros 50 HS (Thermo Fisher Scientific, Waltham, Massachusetts, USA), the polymer-grafted Capto S ImpAct (Cytiva, Uppsala, Sweden), and the polymer-grafted Fractogel EMD SO_3^- (Merck Millipore, Burlington, Massachusetts, USA). While the backbone of Capto S ImpAct consists of a highly cross-linked agarose base matrix, Poros 50 HS and Fractogel EMD SO_3^- are composed of synthetic methacrylate based polymeric beads. All adsorbers are functionalized with strong cation exchange ligands with a pK value of 2.3 according to [89].

6.3.2 Software

The system of partial differential equations described earlier were numerically solved by using ChromX (GoSilico GmbH, Karlsruhe, Germany). For all simulations, the variable time-stepping scheme IDAS was used for discretization in time. Discretization in space was performed using a linear Streamline-Upwind Petrov-Galerkin (SUPG) ansatz.

6.3.3 Parameter Estimation

As described in [70; 77; 79], the system parameters ε_v and ε_p used in the TDM were determined by tracer pulse injections using a high salt buffer and dextran with a molecular weight of 2000 kDa as pore penetrating and non-pore penetrating tracer, respectively. The dispersion coefficient D_{ax} used in Eq. (6.1) was derived from the column specific height of an equivalent theoretical plate (HETP) measured by the dextran pulse injection [68; 152]. As described in more detail in [20], the ligand surface density $\Gamma_L = \Lambda_{IEX} A_{s,0}^{-1}$ was derived from the ionic capacity Λ_{IEX} and the total accessible surface area per adsorber skeleton volume $A_{s,0}$ of the adsorber systems. The ionic capacity was determined by acid-base titration as described in [79], while $A_{s,0}$ was derived from inverse size exclusion chromatography (iSEC) data following the procedure described by DePhillips and Lenhoff [38]. For all resins, iSEC data were taken from [166]. Due to the lack of iSEC data for Capto S ImpAct, iSEC data for Capto S reported in [166] were used instead.

In addition to column and system parameters, the chromatography model described in Sec. 6.2 contains protein specific parameters that must be determined before the model can be used to simulate the chromatographic behavior of proteins in ion exchange processes. The radius of a protein a_i was estimated from its molecular weight. For all mAbs with $M_{w,i} = 150$ kDa, the radius was considered to be $a_i = 5.5$ nm based on literature data [26; 29; 103]. For product-related and process-related impurities with a molecular weight not equal to 150 kDa, a_i was determined using the empirical correlation

$$a_i = a \log_{10}\left(\frac{M_{w,i}}{1\text{kDa}}\right) + b \tag{6.23}$$

whereby the empirical parameters $a = 5.1$ nm and $b = -5.4$ nm have been determined based on literature data [95; 103; 131]. The remaining protein specific model parameters $k_{eff,i}$, $k_{kin,i}^*$, Z_i, Δ_i, $Z_{lat,i}$, and $A_{s,i}$ were determined by fitting the model to experimental chromatograms. The least squares problem was solved using a combination of global and local optimizers within the ChromX software environment. The accuracy of parameter estimation was examined using the 95% confidence interval determined using the Fisher information matrix [140].

As described in more detail in the following sections, the process behavior of mAb1-mAb3 was studied at constant pH. In the case of mab4 and mAb5, on the other hand, process behavior was analyzed at varying pH conditions. To account for the pH-dependence in case of mAb4 and mAb5, empirical pH-dependencies for Z_i and Δ_i were used, as derived in [20]. The pH-dependence of Z_i was approximated using a general polynomial expression

$$Z_i(\text{pH}) = Z_i(\text{pH}_{ref}) + \sum_{k=1}^{m} Z_{k,i}\left(\text{pH} - \text{pH}_{ref}\right)^k \tag{6.24}$$

around a reference value pH_{ref}, where $Z_i(pH_{ref})$ denotes the protein charge at the reference pH, m is the degree of the polynomial, and $Z_{k,i}$ represent empirical parameters that define the shape of the model titration curve. The selected value for pH_{ref} may vary among the antibodies. Depending on the width of the analyzed pH range, the polynomial expression (6.24) was either of second degree or third degree. In case of a pH variation over more than one pH unit, a third-degree polynomial was used ($m = 3$). For variations smaller than one pH unit, the approximation was reduced to a second-degree polynomial ($m = 2$) to avoid an over-parameterization of the empirical equation. For pH variations over multiple pH units, the pH-dependence of Δ_i used in Eq. (6.19) can be described by the empirical relation

$$
\begin{aligned}
\log_{10}\left(\Delta_i(pH)\right) = {} & \log_{10}\left(\Delta_i(pH_{ref})\right) \\
& + \Delta_{1,i}\left(|\sigma_i(pH)| - |\sigma_i(pH_{ref})|\right)
\end{aligned}
\tag{6.25}
$$

previously derived in [20]. The empirical parameters in Eq. (6.24) and Eq. (B.10) were determined along the other model parameter by least squares fitting, as described above.

6.3.4   mAb1 and mAb2

Experimental data of mAb1 on Poros 50 HS and mAb2 on Fractogel EMD SO_3^- were taken from the literature. The data include salt gradient experiments at constant pH and varying protein load density. For a detailed summary of the experiments, we refer to [78] and [40], respectively. As no antibody isoforms are reported in [78] and [40], only one protein component was considered in the model.

6.3.5   mAb3

Bind-and-elute experiments of mAb3 were performed on Capto S ImpAct packed in a column with $L_c = 97.2$ mm and a bed volume of $V_c = 1.9$ mL. For all experiments, the column was first equilibrated for 5 CV and then loaded to achieve a load density between 61 and 123 $g\,L^{-1}$, depending on the experiment. After a post-loading wash step over 5.5 CV, product elution was performed by a linear increase in the salt concentration of the mobile phase over 10, 25, or 30 CV, depending on the experiment. All experiments were performed at a constant pH and a constant linear velocity of 100 $cm\,h^{-1}$.

Based on analytical data, several product-related and process-related impurities were considered in the chromatography model, including three main charge variants of mAb3, two low-molecular weight (LMW) species with an estimated molecular weight of $M_{w,i} = 75$ kDa, and one high-molecular weight (HMW) species with an estimated molecular weight of $M_{w,i} = 300$ kDa. Considered process-related impurities involved host cell proteins (HCPs) and leached Protein A. For simplicity and due to the lack of analytical information on the number of species present, HCPs were considered as a single protein component in the model. The model parameter $A_{s,i}$ was considered to be the same for all proteins. Due to the similar physicochemical properties of the charge variants, they were assumed to have the same mass transfer resistance $k_{eff,i}$ and steric size $a_i = 5.5$ nm. For the HCPs and leached Protein A, a molecular weight of 150 kDa and 50 kDa was assumed, respectively. For both components, the radius was determined using Eq. (6.23).

6.3.6 mAb4

The strong cation exchanger Capto S ImpAct was prepacked in a column with $L_c = 100$ mm and $V_c = 4.7$ mL. All experiments were performed at a constant linear velocity of $100 \, \mathrm{cm \, h^{-1}}$.

Linear salt gradient experiments at very low column load density were performed by injecting a small protein pulse onto the equilibrated column. After a wash step, the protein was eluted using a linear salt gradient over 20, 40, or 60 CV, depending on the experiment. Experiments were performed at three different relative pH values $\mathrm{pH_{rel}} = \mathrm{pH} - \mathrm{pH_{ref}}$, including -0.3, 0, and +0.3. Four preparative experiments were performed at a constant $\mathrm{pH_{rel}} = 0$. The experiments included two step elution experiments with a protein load density of $20 \, \mathrm{g \, L^{-1}}$ and $93 \, \mathrm{g \, L^{-1}}$ as well as two salt gradient experiments with a gradient length of 20 CV and a protein load density of 20 and $93 \, \mathrm{g \, L^{-1}}$, respectively. Two additional step elution experiments were performed at a protein load density of $45 \, \mathrm{g \, L^{-1}}$. After equilibrating, loading, and washing the column at $\mathrm{pH_{rel}} = 0$, protein elution was performed at increased salt concentration and a relative pH of -0.2 and +0.1, respectively.

Based on analytical data, three main isoforms of mAb4 were considered in the model. Due to similar physicochemical properties, $k_{\mathrm{eff},i}$ and $A_{\mathrm{s},i}$ were considered to be the same for all three isoforms. Given the small investigated pH range and to avoid an over-parameterization of the model, Δ_i was considered to be independent of the pH and $Z_i(\mathrm{pH})$ was approximated by a quadratic function assuming $Z_{3,i} = 0$ in Eq. (6.24).

6.3.7 mAb5

Bind-and-elute experiments with mAb5 were performed on a Poros 50 HS column with $L_c = 100$ mm and $V_c = 5.0$ mL. In four experiments, product elution was performed by a linear or step-wise increase of the ionic strength keeping the pH constant at a reference value $\mathrm{pH_{ref}}$. In four additional experiments, product elution was performed by increasing the pH linearly or step-wise by 3.5 pH units relative to $\mathrm{pH_{ref}}$. For all experiments an adapted multi-component buffer system according to [170] was used. The load density varied between 60 and 130% of the dynamic binding capacity (DBC).

The model was calibrated using two salt elution and two pH elution experiments. The remaining four experiments were used for model validation. Given the change in pH over multiple pH units, a third-degree polynomial equation was used to describe the pH-dependence of Z_i. For Δ_i, the pH-dependence given by Eq. (B.10) was used. The pH and ionic strength during the process was simulated based on the buffer equilibrium, as previously discussed by [32].

6.4 Results and Discussion

The elution profile of five mAb systems on three different CEX adsorber systems was analysed using the chromatography model described in Sec. 6.2. Given the high protein load densities considered in all case studies, the focus was primarily on the influence of the

thermodynamics of adsorption on the shape of the elution profiles. Since thermodynamics has a dominant influence on the overall elution profile in nonlinear chromatography [68], the CPA model was combined with the TDM in this study. For studies that are more focused on mass transfer effects at the particle level, the CPA model can also be combined with more complex mass transfer models.

6.4.1   Parameter Estimation

System parameters of all used chromatography columns based on tracer experiments, acid-base titration, and iSEC are summarized in Table 6.1 along with model parameters for all investigated mAbs. The system parameters were considered constant under all process conditions. Since ε_p of polymer-grafted adsorber systems has been reported to be affected by the ionic strength, this assumption might be a simplification for Capto S ImpAct and Fractogel EMD SO_3^- [9]. Due to the lack of iSEC data for Capto S ImpAct, its ligand surface density was approximated using iSEC data for Capto S. All other parameters were determined specifically for the respective adsorber systems.

Protein specific model parameters summarized in Table 6.1 were determined by fitting the model to experimental chromatograms at varying process conditions. Lumped mass transfer coefficients $k_{\mathrm{eff},i}$ determined for Poros 50 HS are in the range of previous studies [21; 149]. They tend to be larger than those estimated on Capto S ImpAct and Fracto-gel EMD SO_3^-. A possible explanation for this could be the bimodal pore size distribution of Poros 50 HS including large open pores transecting a network of smaller pores [186]. As described in Sec. 6.2.1, $k_{\mathrm{eff},i}$ accounts for both external mass transfer resistance due to film diffusion and internal mass transfer resistance due to pore diffusion. According to the Mackie-Meares correlation [110], the internal mass transfer resistance decreases with increasing ε_p. This would explain why among the native mAbs $k_{\mathrm{eff},i}$ is lowest for mAb2 on Fractogel EMD SO_3^-. It is noticeable that mass transfer coefficients for mAb3 and mAb4 differ significantly from each other. This discrepancy may be due to complex transport effects occurring within polymer-grafted adsorber systems. As all these effects are lumped into one effective mass transfer coefficient, $k_{\mathrm{eff},i}$ may become rather empirical in nature and thus difficult to interpret.

Within the framework of the CPA model, proteins are primarily characterized by their size a_i and effective charge Z_i. It is important to note that the charge values for the individual mAb systems in Table 6.1 relate to different reference pH values. A quantitative comparison of Z_i between the different systems is therefore not possible. Among the mAb charge variants, the acidic and basic variants have, as expected, the lowest and highest charge values, respectively. Since the behavior of mAb1-mAb3 was studied at constant pH, the parameters $Z_{1,i}$, $Z_{2,i}$ (and $Z_{3,i}$) describing the pH-dependence of Z_i are shown only in the case of mAb4 and mAb5. Given the small pH change of less than one pH unit in the case of mAb4, the pH-dependence was only approximated by a second-degree polynomial and thus only by $Z_{1,i}$, $Z_{2,i}$. The slope of the effective titration curve ($Z_{1,i}$) must always be negative. With parameter values of $Z_{1,i} = -51.07$, $Z_{2,i} = 19.55$, and $Z_{3,i} = -2.96$, the effective model charge of mAb5 follows qualitatively the shape of a titration curve. As shown empirically in [20], in addition to the surface charge density, the thermodynamic parameter Δ_i strongly depends on the size of the protein. In general, large proteins have lower parameter values in Δ_i. The specific adsorber surface area $A_{\mathrm{s},i}$ determined for

Table 6.1: Summary of model parameters. Parameter uncertainty is indicated by the 95% confidence interval.

| Parameter	Unit	mAb1	mAb2	mAb3 · Acidic	Main	Basic	HMWs	LMWs1	LMWs2	HCPs	ProteinA	mAb4 · isoform1	isoform2	isoform3	mAb5
Adsorber		Poros 50 HS	Fractogel EMD SO_3	Capto S ImpAct								Capto S ImpAct			Poros 50 HS
V_c	[mL]	0.98	22.3	1.91								4.7			5.03
L_c	[mm]	50	215	97								100			100
D_{ax}	$[\mathrm{mm}^2\,\mathrm{s}^{-1}]$	0.06	0.10	0.78								0.32			0.61
d_p	$[\mu\mathrm{m}]$	50	65	50								50			50
ε_v	$[-]$	0.53	0.34	0.39								0.38			0.49
ε_p	$[-]$	0.54	0.39	0.87								0.83			0.54
Γ_L	$[\mu\mathrm{mol\,m}^{-2}]$	2.89	1.47	0.6								0.60			2.89
a_i	[nm]	5.5	5.5	5.5	5.5	5.5	7.2	4.1	4.1	5.5	3.2	5.5			5.5
$A_{s,i}$	$[\mathrm{nm}^{-1}]$	0.22 ± 0.001	0.18 ± 0.001				0.75 ± 0.001					0.66 ± 0.004			0.14 ± 0.03
$k_{\mathrm{eff},i}$	$[\mu\mathrm{m\,s}^{-1}]$	1.01 ± 0.03	0.51 ± 0.06	0.6 ± 0.001	0.6 ± 0.001	0.6 ± 0.001	0.51 ± 0.04	0.6 ± 0.003	0.8 ± 0.01	0.67 ± 0.004	0.92 ± 0.01	1.96 ± 0.06	1.96 ± 0.06	1.96 ± 0.06	2.99 ± 0.13
$k^*_{\mathrm{kin},i}$	$[\mathrm{s}^{-1}]$	4.61e7 ± 1.46e4	8.44e7 ± 7.18e7	5.98e6 ± 2.68e5	7.67e7 ± 2.61e5	5.78e7 ± 1.37e6	1.29e6 ± 5.33e4	1.78e4 ± 2.67e2	1.58e4 ± 1.58e2	2.38e5 ± 4.37e3	6.72e5 ± 9.78e3	6.11e5 ± 1.44e4	2.72e5 ± 8.94e3	1.33e4 ± 6.85e2	2.16e6 ± 1.81e4
$Z_i(\mathrm{pH}_{\mathrm{ref}})$	$[-]$	80.45 ± 0.04	111.79 ± 0.22	73.18 ± 0.04	84.47 ± 0.17	84.64 ± 0.27	140.49 ± 3.39	38.92 ± 0.01	33.3 ± 0.11	74.85 ± 0.07	37.96 ± 0.17	110.32 ± 0.53	114.80 ± 0.21	117.04 ± 0.54	94.57 ± 0.03
$Z_{1,i}$	$[-]$	-	-	-	-	-	-	-	-	-	-	-50.97 ± 1.85	-59.05 ± 0.98	-54.24 ± 2.20	-51.07 ± 0.03
$Z_{2,i}$	$[-]$	-	-	-	-	-	-	-	-	-	-	45.64 ± 1.35	49.46 ± 1.67	42.23 ± 1.85	19.55 ± 0.01
$Z_{3,i}$	$[-]$	-	-	-	-	-	-	-	-	-	-	-	-	-	-2.96 ± 0.002
$\log_{10}\Delta_{1,i}(\mathrm{pH}_{\mathrm{ref}})$	$[-]$	-1.90 ± 0.01	-4.04 ± 0.02	-1.19 ± 0.01	-2.18 ± 0.01	-2.00 ± 0.02	-2.72 ± 0.02	-0.03 ± 0.003	0.22 ± 0.003	-1.16 ± 0.01	-0.86 ± 0.01	-3.90 ± 0.02	-4.17 ± 0.01	-4.31 ± 0.02	-3.32 ± 0.001
$\Delta_{1,i}$	$[\mathrm{m}^2\,\mathrm{C}^{-1}]$	-	-	-	-	-	-	-	-	-	-	-	-	-	-90.42 ± 0.09
$Z_{\mathrm{lat},i}$	$[-]$	19.07 ± 0.40	61.87 ± 4.96	25.79 ± 0.13	44.04 ± 0.18	54.69 ± 0.39	35.77 ± 0.30	28.58 ± 0.33	11.60 ± 0.16	59.98 ± 0.30	31.45 ± 0.39	60.72 ± 2.60	70.19 ± 0.04	72.01 ± 2.38	17.70 ± 0.13

Figure 6.2: Salt gradient experiments of mAb1 on Poros 50 HS (a) according to [78], mAb2 on Fractogel EMD SO$_3^-$ (b) according to [40], and mAb3 on Capto S ImpAct (c). Dashed lines represent experimental data while continuous lines indicate simulated data based on the CPA model. The ionic strength or conductivity of the mobile phase is shown in gray. In case of mAb1 and mAb2, model simulations are based on one protein component. Simulations for mAb3 include several product-related and process-related impurities. For the sake of visualization, only the UV sum signal is shown.

Capto S ImpAct is significantly larger than the values determined for Poros 50 HS and Fractogel EMD SO$_3^-$. Since this parameter is related to the skeleton volume of the adsorber system, this difference can be attributed to the large particle porosity of Capto S ImpAct. In case of mAb3 and mAb4, it was assumed that proteins do not differ in $A_{s,i}$. This assumption is reasonable for charge variants and other mAb isoforms, as they are not expected to differ significantly in their steric size. However, for molecular species of the mAb and process-related impurities, this assumption represents a model simplification, as these components can differ in steric size and thus pore accessibility.

6.4.2 Peak Shoulder Formation at High Load Densities

Salt mediated elution behavior of proteins at high column load density was analyzed using data on three strong cation exchange resins, including Poros 50 HS, Fractogel EMD SO$_3^-$, and Capto S ImpAct. An exemplary chromatogram for each adsorber system is shown in Fig. 6.2 along with fitted model curves based on the CPA model. For the sake of visualization, only the UV sum signal is shown. Continuous lines represent fitted model curves while dashed lines indicate experimental data. The slight increase in the simulated conductivity trace during the loading phase can be ascribed to the release of counter-ions described by Eq. (6.22). During protein elution, the decrease in conductivity due to the re-adsorption of counter-ions is hardly noticeable. This can be explained by the low protein concentration in the eluate and the superposition with the salt gradient. In all experiments shown in Fig. 6.2, the chromatography column was loaded beyond protein breakthrough and product elution was performed using a linear salt gradient while keeping the pH of the mobile phase constant. For mAb1 and mAb2, data previously published in [78] and [40] were used as the data could not be explained using the traditional SMA model. According to [78], oscillations in the measured UV signal in Fig. 6.2(a) are caused by flow rate limitations of the chromatography system. For a more detailed summary of all experimental data and model results for mAb1 and mAb2, please refer to Fig. C.1 and Fig. C.2 in the supplementary material.

On all adsorber systems, a comparable elution behavior can be observed that is characterized by a distinct shoulder in the front part of the elution peak. Despite the complex
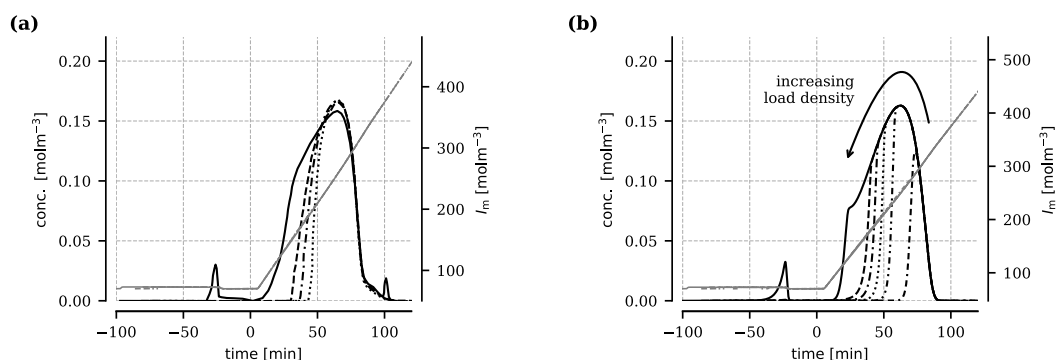
Figure 6.3: Effect of protein load density on the elution profile of mAb2 on Fractogel SO$_3^-$. (a) Experimental data according to [40] at a load density of 72.5 (⋯⋯), 82.8 (–·–), 93.1 (---), and 118.2 g L^{-1} (——). (b) Simulated elution profiles according to the CPA model at a load density of 21.6 (–·–), 55.5 (–··–), 72.5 (⋯⋯), 82.8 (–·–), 93.1 (---), and 118.2 g L^{-1} (——).

elution behavior, the experimental data on all three adsorber systems can be reproduced adequately by the CPA model. As illustrated in Fig. 6.3 for mAb2 on Fractogel EMD SO$_3^-$, the extent of the peak shoulder is strongly affected by the load density and can be observed only for experiments at very high protein load density. Please note that the data shown in Fig. 6.3 were generated at a constant gradient slope. For a better interpretation of the results, the retention time is shown relative to the starting point of the gradient. The effect of the load density on the elution profile is further illustrated based on model simulations for mAb2 in Fig. 6.3(b). According to the CPA model, an increase in the load density initially leads to a shift of the peak maximum towards lower salt concentrations and a strongly compressed peak front. After exceeding a load density of approximately 55 g L^{-1}, the position and height of the peak maximum remains unchanged. Increasing the load density further still leads to a shift of the elution front towards lower salt concentrations. However, the protein concentration in the elution front decreases progressively and the frontal part of the peak becomes more dispersed. This process behavior described by the CPA model is also reflected by the experimental data shown in Fig. 6.3(a). Deviations between model simulations and experimental data in Fig. 6.3 can possibly be ascribed to dispersion effects caused by mass transfer limitations that cannot be fully covered by the applied TDM model. However, as illustrated more closely by the overlay of simulated and experimental chromatograms in Fig. C.2 in the supplementary material, deviations are very small. In general, the elution behavior is adequately captured by the combination of the TDM and the CPA model. Given the good agreement between experiment and simulation and the focus of this work on thermodynamic effects, a transition to the more detailed general rate model was not considered. It is also important to note that simulations shown in Fig. 6.3 are based on one protein component only, as no isoforms are reported in [40] for mAb2. The presence of mAb isoforms or other product-related impurities is also a possible explanation for minor discrepancies, especially in the peak tailing.

6.4.3   Model-Based Analysis of the Formed Shoulder

To provide a possible explanation for the observed elution behavior using the CPA model, Fig. 6.4 shows the simulated axial distribution of adsorbed mAb2 within the chromatography column at the beginning of the linear salt gradient. The black continuous line represents $q_{v,i}$ or Θ as a function of the axial column position. The dashed black line represents the available surface function $B(\Theta)$ given Θ. The gray shading indicates the range $\Theta \in [\Theta_{\text{jam}}, \Theta_{\text{hex}}]$ between the maximum surface coverage of a hexagonal lattice $\Theta_{\text{hex}} = 0.907$ and the jamming coverage $\Theta_{\text{jam}} = 0.547$. Due to the high load density of 72.5 g L^{-1} and favorable load conditions, Fractogel EMD SO_3^- is highly saturated in the upper part of the column with a maximum surface coverage of $\Theta_{\text{max}} \approx 0.658$. Considering a mAb radius of 5.5 nm and a molecular weight of 150 kDa, the predicted value for Θ_{max} corresponds to a saturation capacity of 1.725 mg m^{-2} which is in good agreement with the experimental value of 1.897 mg m^{-2} reported in [166] for a mAb on Fractogel EMD SO_3^-. Given the high surface coverage in the upper part of the column, proteins in the mobile phase have a very small probability of adsorbing by encountering an unoccupied area on the adsorber surface which is indicated by $B(\Theta) \to 0$. In the lower part of the column, on the other hand, the adsorber surface is almost unoccupied. As indicated by $B(\Theta) \to 1$, proteins in the mobile phase have a high probability of encountering an unoccupied area and being adsorbed, provided that the electrostatic conditions are in favor. Increasing the ionic strength at the beginning the salt gradient leads to protein desorption at the top of the column and the formation of a concentration front migrating down the column. Given the high steric hindrance, the velocity of a migration front $w(c^+)$ with concentration c^+ is initially very high and can be close to the migration velocity of an unretained tracer with comparable steric size u_{m}. Once the elution front reaches the unsaturated bottom part of the column, it abruptly decelerates as the ionic strength is still low and favors a re-adsorption of proteins to the unoccupied adsorber surface. Due to the slow migration velocity of the elution front in the bottom part of the column and the steady arrival of proteins from the saturated upper part, the elution front is steadily compressed and concentrated. The maximum concentration that can be achieved in the elution front until it reaches the outlet of the column depends on several factors. In addition to the slope of the salt gradient and the migration velocity of proteins in the saturated part of the column, the length of the unsaturated bottom part plays a decisive role. Although an increase in the protein load density leads generally to a compression and concentration of the elution front, it also leads to a shortening of the unsaturated region. Once a certain load density is exceeded, the concentration of the elution front at the column outlet is no longer limited by the increasing ionic strength, but by the length of the unsaturated region. The elution front has less time or distance to be concentrated which leads to the formation of the observed shoulder. It is important to note that the formation of a shoulder in the peak front is in general also predicted by the SMA model. However, due to the highly simplified stoichiometric description of steric effects in the SMA model, the shoulder is predicted only for infeasible load densities far beyond the DBC of preparative columns. As a consequence, the elution behavior shown in Fig. 6.3 can in general not be reproduced by the SMA model, as already demonstrated by Diedrich et al. [40] and Huuk et al. [78].

While the simulated elution curves in Fig. 6.2(a) and Fig. 6.2(b) based on the CPA model appear similar to the extended SMA models proposed by [78] and [40] from a visual point of view, the proposed mechanistic models differ considerably with respect to the underlying physical mechanism. In [40], the elution behavior of mAb2 shown in Fig. 6.3(a)
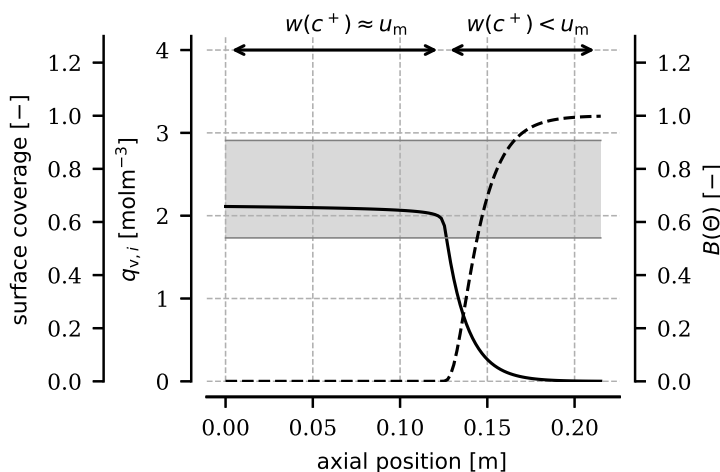
Figure 6.4: Concentration profile $q_{v,i}$ (—) of mAb2 on Fractogel EMD SO_3^- after loading the column with a protein load density of 72.5 g L^{-1}. Gray shading indicates the region between the maximum surface coverage according to random sequential adsorption and hexagonal close packing. The dashed line indicates the available surface function.

was explained by the existence of multiple binding configurations promoted by the properties of Fractogel EMD SO_3^- as a polymer-grafted adsorber system. Adsorbed proteins were thereby assumed to be gradually wrapped by tentacle structures grafted onto the adsorber surface [40]. While the presence of multiple binding configurations cannot be excluded based on existing experimental data, results on Poros 50 HS shown in Fig. 6.2(a) and Fig. C.1 indicate that the analyzed elution behavior is not limited to polymer-grafted adsorber systems, but can also be observed on adsorber systems with normal ligand structure. Furthermore, the behavior seems to be independent of the type of resin backbone as it can be observed on both methacrylate-based adsorbers (Poros 50 HS and Fractogel EMD SO_3^-) and adsorbers based on highly hydrophilic agarose (Capto S ImpAct). In [78], the elution profile in Fig. 6.2(a) was explained by a non-ideal behavior of proteins in the mobile phase. Using an expression for the protein activity coefficient initially introduced by Mollerup [114], the non-ideality was mostly ascribed to the increasing salt concentration during protein elution. While the proposed extension of the SMA model was able to describe the experimental data in Fig. 6.2(a) similar to the CPA model, the hypothesized non-ideal behavior of proteins in the mobile phase is questionable as it usually cannot be clearly reproduced for mAbs or other proteins in the linear adsorption range [19].

6.4.4 Multi-Component Elution Behavior

The foregoing analysis of the observed peak shoulder is based on the assumption that the considered protein system is composed of only one protein species. Although no isoforms of mAb1 and mAb2 are reported in [78] and [40], mAb solutions are commonly complex multi-component systems that do not only contain the protein of interest but product-related and process-related impurities as well. Charge variants of the mAb pose a difficult but common separation problem due to their abundance in the feed material and similar physicochemical properties to the protein of interest. Since they differ only slightly in the

primary sequence or glycosylation pattern, they usually coelute in preparative processes which could also provide a potential explanation for the observed complex peak shape not directly considered in the previous discussion. Due to the different adsorber affinity of the charge variants, a competition for the available adsorber surface area arises in which weaker binding isoforms can be displaced from the adsorber surface by stronger binding isoforms. Given the similarity of charge variants with respect to their steric size, the mutual displacement of these isoforms can likely be considered as a stoichiometric process where one adsorbed protein is exchanged by another protein in the mobile phase. This stoichiometric exchange leads to a change in the composition of the migrating concentration front but not to a significant change in its total concentration. Regardless of its composition, the migrating elution front is decelerated and compressed in the lower unsaturated part of the column as described above. The total protein concentration of the elution front at the end of the column is still dependent on the slope of the gradient and especially the length of the unsaturated part of the column. However, since displacement effects in the upper part of the column cause the lower part to become enriched in weakly binding isoforms, the peak shoulder should be reflected not only in the measured UV absorbance or total protein concentration, but also in the elution profiles of the individual isoforms. To demonstrate the formation of the characteristic peak shoulder for multi-component systems, Fig. 6.5 shows experimental data and model results for mAb3 on Capto S ImpAct. According to analytical data, the protein system contains numerous product-related impurities including charge variants shown in Fig. 6.5(d)-(f) as well as LMWs and HMWs shown in Fig. 6.5(g)-(i). Process-related impurities including HCPs and leached Protein A are reported as well Fig. 6.5(j)-(l). As described in Sec. 6.3.5, HCPs were treated as a single component in the model. This treatment is certainly a significant simplification, as the system is expected to contain a large number of different HCP species varying in size and charge. As a result, discrepancies between model and experiment are more pronounced in the case of HCPs. In general, however, experimental data can again be well reproduced by the model, especially in the case of the charge variants. The experimental data were chosen as they provide a precise analytical resolution of the elution profiles of the individual charge variants. As shown in Fig. 6.5(a)-(c), the measured UV sum signal is again characterized by the previously discussed shoulder in the front part of the elution peak. Only the experiment at lowest load density shown in Fig. 6.5(a) reflects the classical 'shark fin' profile characterized by a compressed peak front and a dispersed back. This behavior is consistent with the results shown in Fig. 6.3. Given the low concentration of HMWs, LMWs, and process-related impurities, it is unlikely that they are responsible for the complex elution behavior. In contrast to mAb1 and mAb2, the measured sum signal is composed of the elution profiles of the individual charge isoforms including one most abundant acidic isoform, a main isoform, and a basic isoform. While the main and basic isoform show a similar elution behavior and coelute in all three experiments, both isoforms differ strongly from the acidic form. With increasing load density from Fig. 6.5(d) to Fig. 6.5(f), the front of the acidic elution profile itself becomes increasingly dispersed reflecting the peak shoulder at the highest protein load density shown in Fig. 6.5(f). The shoulder is formed by the acidic isoform as it shows the lowest affinity to the adsorber surface. At the beginning of the salt gradient, it has the lowest probability of re-adsorbing since it cannot displace the basic or main isoform from the adsorber surface. The main and basic isoform, on the other hand, can displace the acidic isoform from the adsorber surface and are therefore more likely to re-adsorb. As a consequence, the elution profiles of both isoforms are less effected by an increase in the protein load density and follow a

similar behavior in all three experiments. The change in the elution profile of the acidic charge variant from Fig. 6.5(d) to Fig. 6.5(f) shows that the behavior described above is reflected not only in the sum signal, but also in the individual elution profiles of mAb isoforms.

To ensure that the CPA model cannot only describe the elution behavior at very high protein load densities, but the entire linear and nonlinear adsorption range simultaneously, Fig. 6.6 and Fig. 6.7 show data of mAb4 on Capto S ImpAct at different pH values and protein load densities ranging from small pulse injections up to the dynamic binding capacity of the adsorber. In all cases, black and gray dashed lines represent the measured UV and conductivity signal, respectively. Simulated UV signals are indicated by continuous black lines in Fig. 6.6 and Fig. 6.7, while continuous colored lines in Fig. 6.7 represent simulated concentration profiles. For the sake of visualization, measured protein concentrations based on fraction analysis are represented by colored dots. All experiments show good agreement between measured and simulated data indicating that the CPA model can properly reflect the effect of load density on the elution profile ranging from analytical pulse injections up to preparative load densities. Pulse injection experiments shown in Fig. 6.6 were performed at different salt gradient slopes. Measured and simulated elution peaks show no shoulder or split peaks suggesting unexpected elution behavior at higher load densities. Due to the steep gradient slopes considered, no separation of the isoforms is achieved. For the salt gradient experiment at very high load density shown in Fig. 6.7(b), on the other hand, the previously discussed peak shoulder can again be observed. While the isoforms show distinct elution profiles given their individual affinity to the adsorber system and displacement effects, the main isoform follows the same behavior as mAb1 and mAb2. For the remaining preparative experiments, no unexpected elution behavior can be observed. It is worth noting that the salt gradient experiments shown in Fig. 6.7(a) and Fig. 6.7(b) were performed under the same elution conditions but different protein load densities. A comparison of both experiments in Fig. C.3 in the supplementary materials suggests the same behavior as for mAb2 in Fig. 6.3.

6.4.5 pH Gradient Elution

Aside from regulating protein retention by the ionic strength, a regulation by the pH of the mobile phase is common in analytical and preparative chromatography. To compare both elution mechanisms at preparative conditions and verify if the CPA model is capable of describing both mechanisms simultaneously, the model was calibrated and validated using chromatography data of mAb5 on Poros 50HS. Protein elution was performed either by a linear or step-wise increase of the ionic strength at constant pH, or *vice versa*, by a linear or step-wise increase of the pH keeping the ionic strength almost unchanged.

In contrast to salt gradient experiments, the elution mechanism in pH gradients and steps is not primarily based on an electrostatic screening of surface charges by an increase in the ionic strength, but predominantly on a reduction or reversal of the surface charge density itself. Depending on the strength of the adsorber system, the surface charge density of both the protein and the adsorber can be affected.

A comparison between experimental data and model curves is shown in Fig. 6.8(a)-(d) and Fig. 6.8(e)-(h) for the model calibration and validation, respectively. Experimental
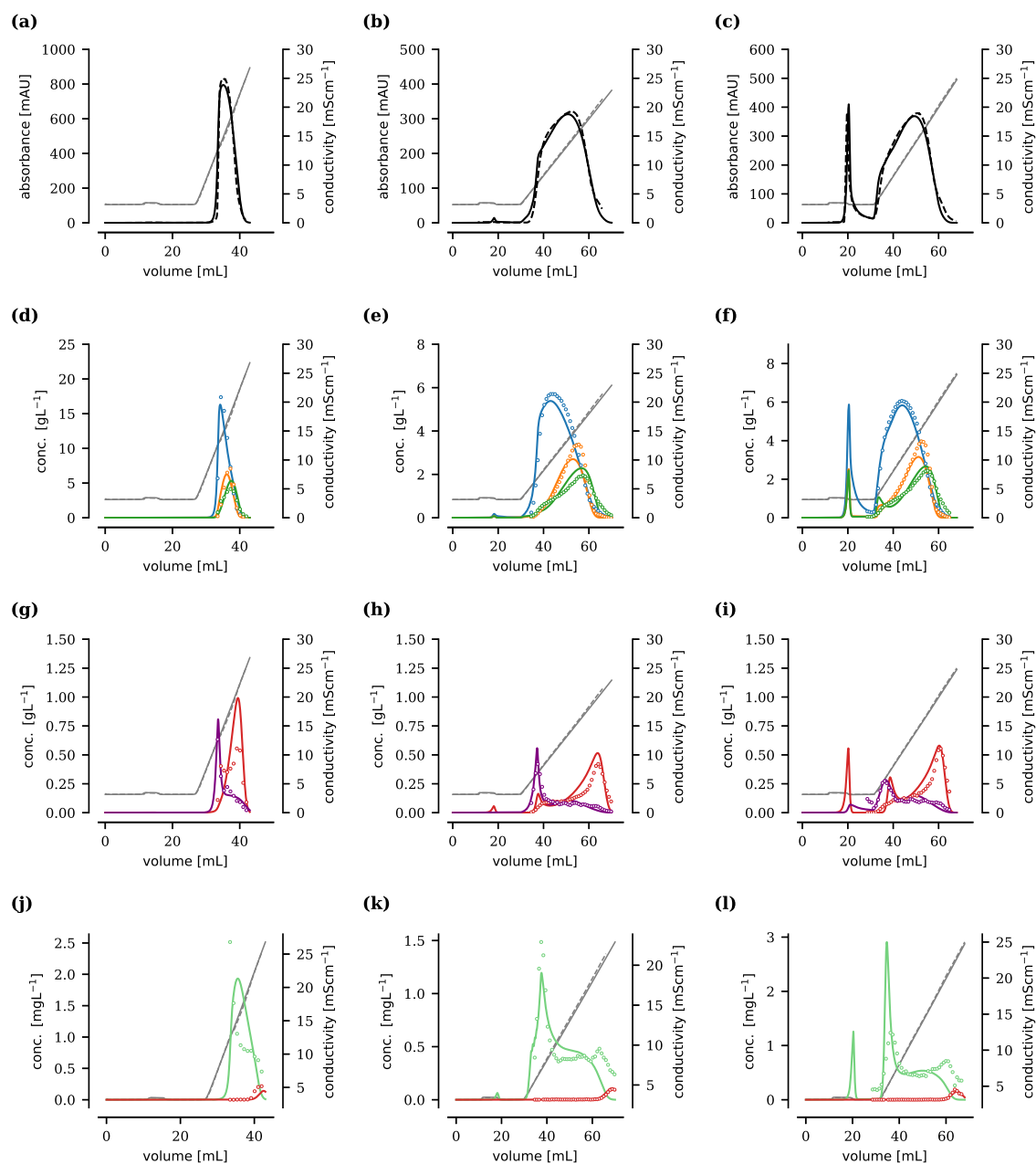
Figure 6.5: Linear salt gradient experiments of mAb3 on Capto S ImpAct. First column: Salt gradient over 10 CV and a load density of 61 g L^{-1}; Second column: Salt gradient over 30 CV and a load density of 98 g L^{-1}; Third column: Salt gradient over 25 CV and a load density of 123 g L^{-1}. (a)-(c): Comparison between measured (- - -) and simulated UV sum signal (——). The conductivity is shown in gray. (d)-(f): Simulated concentration profiles of the acidic isoform (——), main isoform (——), and basic isoform (——) of mAb3 on Capto S ImpAct. Experimental fraction data are represented by colored dots. (g)-(i): Simulated concentration profiles of LMWs (——) and HMWs (——) of mAb3 on Capto S ImpAct. For the LMWs, the sum signal of both LMW species is shown. Experimental fraction data are represented by colored dots. (j)-(l): Simulated concentration profiles of HCPs (——) and leached Protein A (——) on Capto S ImpAct. Experimental fraction data are represented by colored dots.
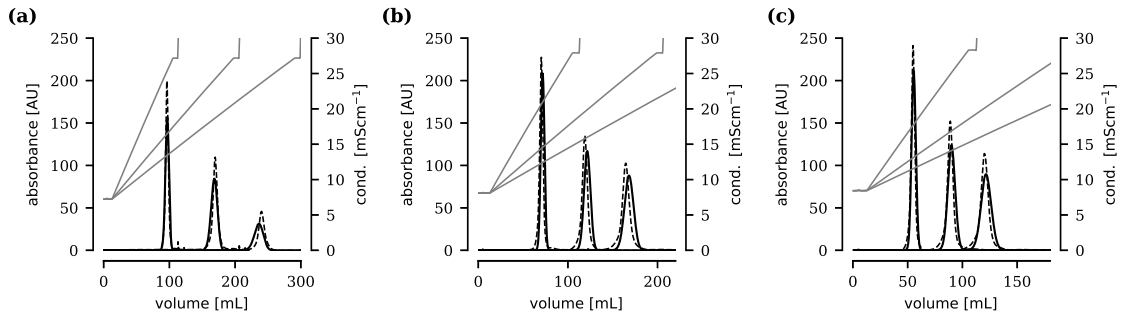
Figure 6.6: Linear salt gradient experiments of mAb4 on Capto S ImpAct at low column load density and relative pH of -0.2 (a), 0 (b), and +0.2 (c). Black and gray dashed lines represent the measured absorbance at 280 nm and the measured measured conductivity signal, respectively. Continuous lines represent model simulations based on the CPA model for three different isoforms of mAb4.
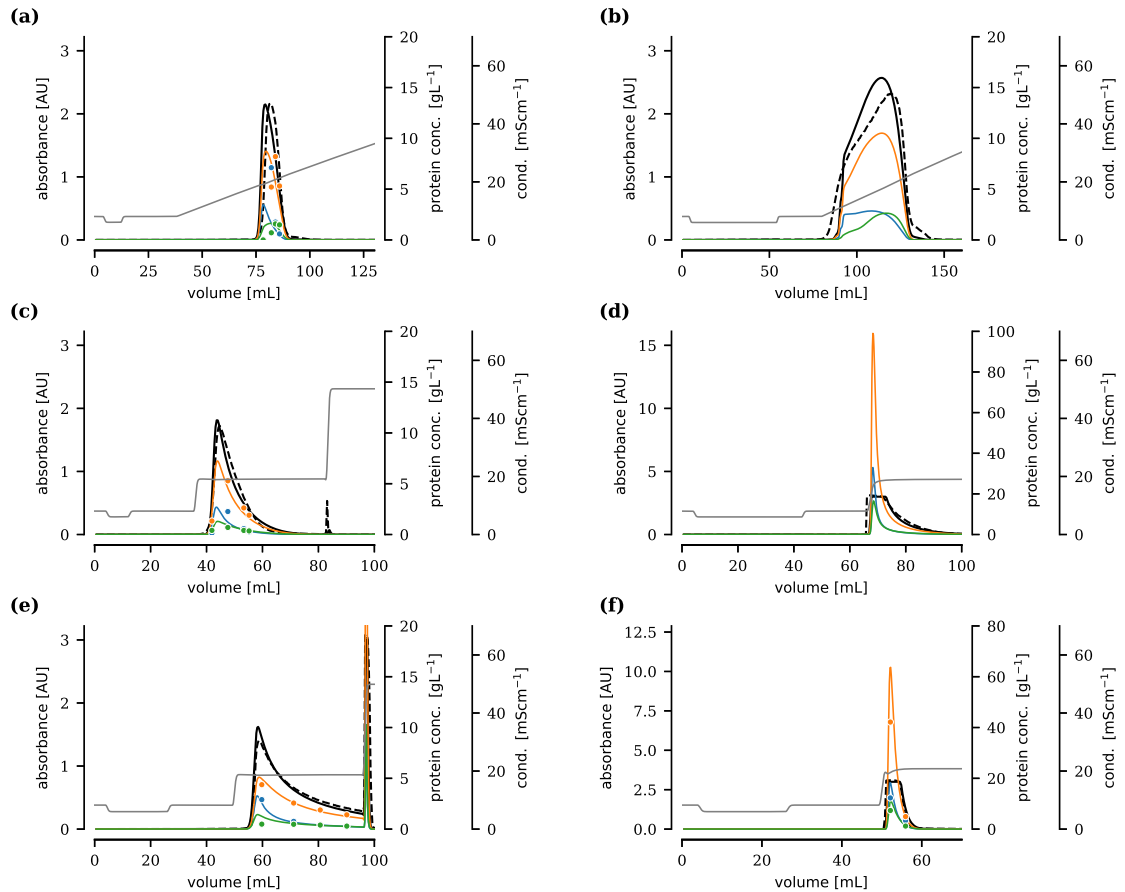

Figure 6.7: Salt elution experiments of mAb4 on Capto S ImpAct at different column load densities and a relative elution pH of 0 (a)-(d), -0.2 (e), and +0.2 (f). Black and gray dashed lines represent the measured UV absorbance and conductivity signal, respectively. Continuous lines represent model simulations based on the CPA model including the UV sum signal (—) as well as the concentration of isoform1 (—), isoform2 (—), and isoform3 (—) of mAb4.
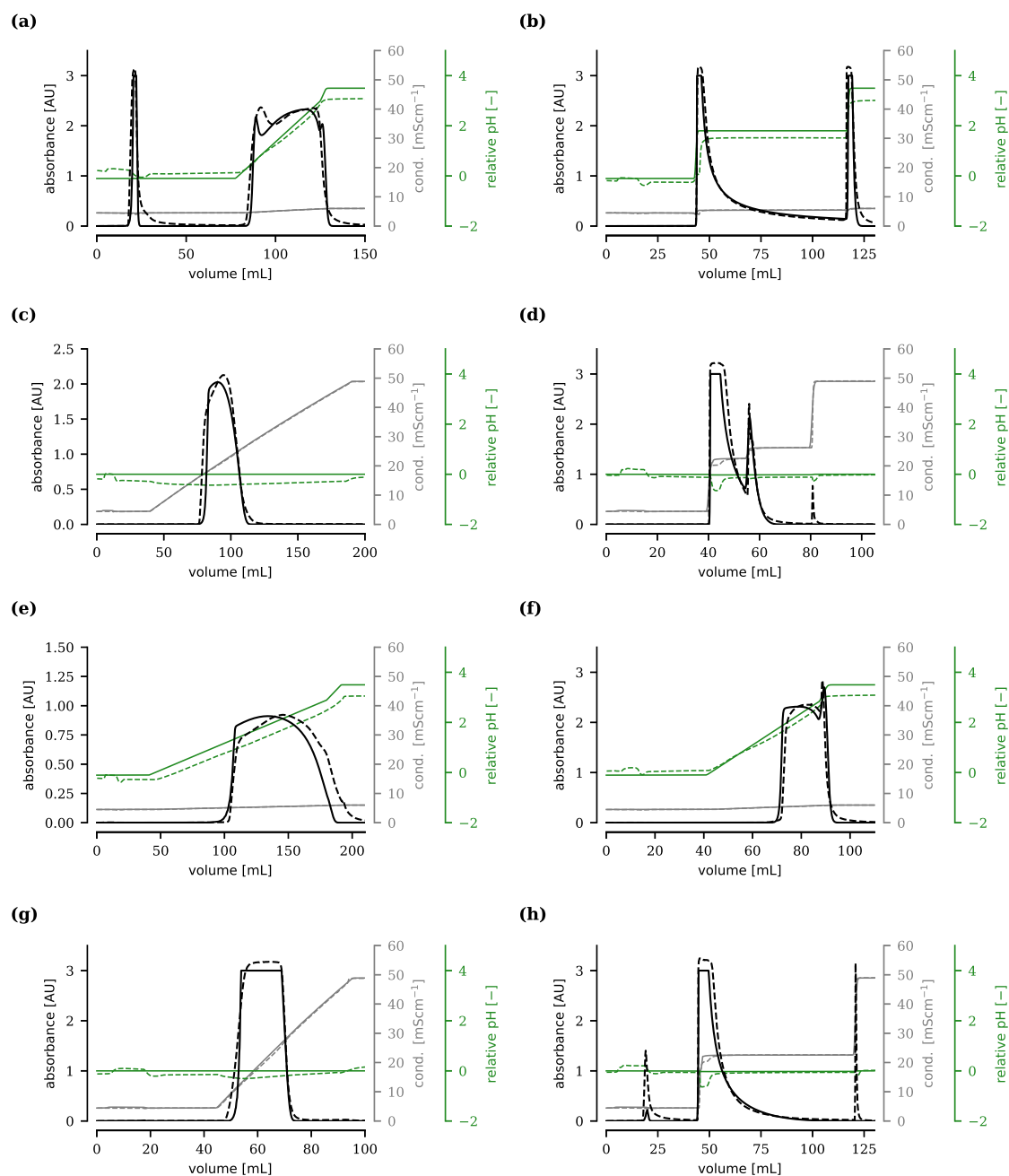
Figure 6.8: Experiments of mAb5 on Poros 50 HS used for the calibration (a)-(d) and validation of the CPA model (e)-(h). Comparison between experimental data (dashed lines) and simulations based on the CPA model (continuous lines). For the sake of visualization, the simulated UV signal was limited to 3 AU. The conductivity and relative pH are shown in gray and green, respectively. Experiments were performed at 130% (a), 80% (b), 60% (c), 80% (d), 80% (e), 60% (f), 100% (g), and 115% (h) of the DBC.

data are represented by dashed lines while continuous lines indicate model results. For the sake of visualization, the simulated UV signal was limited to 3 AU. Experiments in which protein elution was achieved by an increase in pH are shown in Fig. 6.8(a)-(b) and Fig. 6.8(e)-(f). For the experiments shown in Fig. 6.8(c)-(d) and Fig. 6.8(g)-(h), elution was performed by increasing the ionic strength while keeping the pH constant. In case of the ionic strength and pH, solid lines represent theoretical values based on the buffer equilibrium. The increase of the gradient slope at the end of the pH gradient can thereby be ascribed to a decrease in the buffer capacity. Observable deviations between theoretical and measured pH values of up to 0.5 pH units have also been reported in previous studies using the in-line pH electrode of the chromatography system [66; 97]. The discrepancy was mostly attributed to a systematic error of the in-line sensor identified by a drift of the measured pH value over time [97]. Based on the previous reports, deviations between simulated and measured pH values in Fig. 6.8 were not further analyzed. As the experimental UV signal and the conductivity shown in Fig. 6.8 were measured by individual in-line sensors, uncertainties in the measured pH have no effect on other measured process variables. For all calibration and validation experiments shown in Fig. 6.8, a good agreement between model results and experimental data can be observed. Despite the observed complex elution behavior of mAb5 at high column load density, both the shape and position of the elution peaks are adequately described by the CPA model. The sharp increase in the measured and simulated UV signal at the back of the elution peak in Fig. 6.8(f) can be attributed to the decreasing buffer capacity at the end of the pH gradient and a strong decrease in the protein charge for $pH_{rel} > 3.0$. The validation results shown in Fig. 6.8(e)-(h) indicate that the CPA model can explain protein retention over a wide range of column load density, pH, and ionic strength. It is worth noting that experimental data shown in Fig. 6.8(a) and Fig. 6.8(f) were performed under the same elution conditions but different load densities. A comparison of both pH gradient experiments in Fig. 6.9(a) reveals an effect of the load density on the elution profile that is consistent with the observations previously made in Fig. 6.3 for salt gradient experiments. For the sake of visualization, the retention volume in Fig. 6.9 is again shown with respect to the starting point of the pH gradient. As previously described for the salt gradient experiments and further illustrated in Fig. 6.9(b) using the validated CPA model, an increase in the load density initially leads to an increase in the peak height and a shift of the peak maximum towards lower pH values, as expected. However, in accordance with previous observations in Fig. 6.3, the position and height of the peak maximum remains unchanged again after exceeding a load density of approximately 50% of the DBC. A further increase in the load density leads to a significant increase in peak width and the formation of a shoulder in the peak front. The peak height remains unchanged. As the ionic strength was kept very low in the experiment shown in Fig. 6.9 it is very unlikely that the qualitative similar behavior for salt and pH gradients can be ascribed to interactions between proteins and ions as proposed by [78]. By ascribing the observed behavior to a combination of strong steric hindrance in the upper part of the column and protein re-adsorption in the lower part of the column, the CPA model provides an explanation for the observed behavior for both salt and pH gradients.
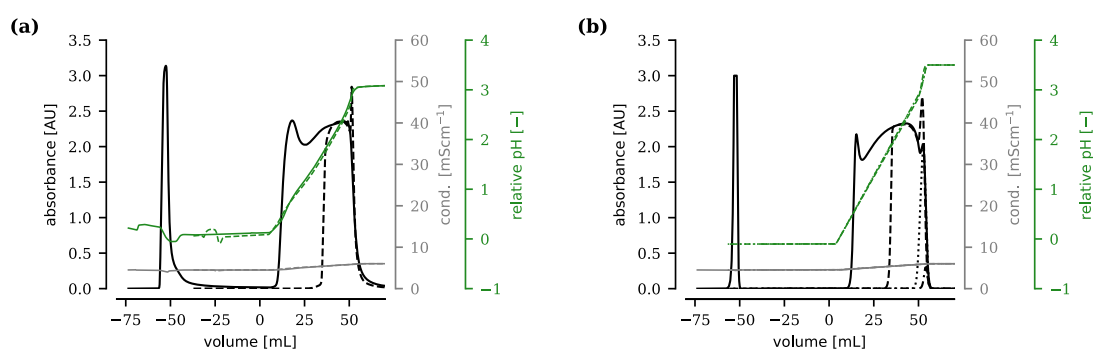
Figure 6.9: Effect of protein load density on the elution profile of mAb5 on Poros 50 HS at a constant pH gradient slope. (a) Experimental data at a load density of 33 (---) and 130% (—) of the dynamic binding capacity. (b) Simulated elution profiles according to the CPA model at a load density of 1 (-··-), 10 (·····), 33 (---), and 130% (—) of the dynamic binding capacity. The retention volume is shown with respect to the starting point of the pH gradient.

6.5   Conclusion

In this work, complex protein retention behavior in preparative chromatography processes was described and analyzed using a previously introduced CPA model. The model was found to be capable of reproducing elution profiles at high protein load densities that cannot be described by the commonly used SMA model. In agreement with reports from the literature, the formation of a characteristic shoulder in the front part of the elution peak was observed for salt gradients and protein load densities close to or beyond the dynamic binding capacity. By considering several mAbs and multiple IEX adsorber systems, it was demonstrated that the reported behavior appears to be independent of the ligand structure and backbone of the adsorber system. Thereby, the formation of the peak shoulder could also be demonstrated for pH gradients. According to the CPA model, the reported complex behavior can be ascribed to a strong compression and concentration of the elution front in the lower unsaturated part of the chromatography column. As the unsaturated part of the column decreases with increasing protein load density, exceeding a critical load density can lead to the formation of the observed peak shoulder.

By using the CPA model for several industrial case studies, it was shown that the model can reproduce the elution behavior of proteins over a wide range of protein load densities, spanning from analytical pulse injections to load densities beyond the dynamic binding capacity. The applicability of the CPA model is not limited to salt gradient or salt step elution experiments, but also includes protein elution controlled by the pH of the mobile phase. The ability of the model to describe complex elution behavior can help to better understand industrial IEX processes and to support the development of these processes in a model-based approach.

Conclusion

This work was devoted to solve important challenges with the use of mechanistic models for the development of preparative ion exchange (IEX) chromatography. Despite the inherent advantages of mechanistic models, their application in an industrial setting is often hindered by insufficient model accuracy or a lack of confidence in mechanistic models on the part of decision-makers.

One key aspect of this work was to increase confidence in the predictive ability of mechanistic chromatography models by developing a strategy to assess the uncertainty of these models in a quantitative manner. Inspired by other research areas, a strategy based on Bayesian inference was introduced and applied in an industry case study (Chapter 3). Within the proposed framework, Monte Carlo techniques like Markov Chain Monte Carlo were used to perform approximate Bayesian inference. Though Monte Carlo techniques can be computationally expensive, they provide reliable information on the residual uncertainty of model parameters as joint probability distributions. In contrast to frequentist approaches used in previous works, the proposed uncertainty assessment does not only provide a lower limit for uncertainty of model parameters, it is also not limited to situations with a symmetric uncertainty interval. Furthermore, the presented uncertainty assessment is not limited to model parameters, but also provides a prediction-based uncertainty assessment of the entire model. Understanding the predictive uncertainty of mechanistic chromatography models is important as they are often used to perform extrapolations beyond the observed range.

Driven by shortcomings of existing mechanistic models like the steric mass action (SMA) model in adequately describing protein retention behavior in IEX chromatography, the main part of this thesis (Chapters 4-6) was dedicated to the development of the colloidal particle adsorption (CPA) model as an alternative adsorption model. The CPA model was first introduced for the linear adsorption range capturing the adsorption equilibrium of proteins onto charged IEX media in the presence of electrostatic double layer interactions. To keep the model computational simple, electrostatic interactions were simulated as a function of the pH value and ionic strength using the linearized Poisson-Boltzmann equation and a simplified colloidal representation of proteins as perfect spheres with uniform surface charge density. The surface charge density was estimated using theoretical

protein titration curves based on molecular structural information. The derived model was found to be capable of describing protein partitioning coefficients over a wide range of ionic strength and pH. By considering the molecular structural differences between a mAb and its post-translational modifications, it was also possible to predict the adsorption behavior of antibody charge variants. While the derivation of the protein surface charge density from theoretical titration curves is beneficial in terms of model calibration, this approach necessitates that the primary structure is known for all proteins. This requirement is usually not met in practice, as many process and product-related impurities are less analyzed than the actual protein of interest. Thus, in the rest of the thesis, the surface charge density was empirically derived from experimental data.

Subsequently, the model was extended to the nonlinear adsorption range by considering steric and electrostatic interactions between adsorbed proteins. A two-dimensional scaled-particle theory was applied to simulate steric interactions. Electrostatic protein-protein interactions were simulated using an approximation of adsorbed proteins as a two-dimensional Yukawa system. Following the general notation, the contribution of steric effects was expressed in terms of an available surface function (ASF). As a measure for the conditional probability by which an adsorbing proteins finds an unoccupied area on the adsorber surface, the ASF physically limits protein adsorption by the available adsorber surface. This is in contrast to the SMA model, where protein adsorption is limited by the ionic capacity of the adsorber system. Both the SMA model and the extended CPA model were compared by simulating adsorption isotherms of a mAb over a wide range of ionic strength and pH. While both adsorption models showed comparable results in the linear adsorption range, they showed significant differences in the nonlinear adsorption range. The comparison indicated that nonlinear adsorption effects can be overestimated considerably by the stoichiometric approach of the SMA model and are in general better represented by the CPA model.

After deriving the CPA model under equilibrium conditions, a kinetic derivation of the model was presented to provide an expression for the rate of adsorption and desorption. Combined with the transport dispersive model as column wide transport model, the kinetic form of the CPA model was used to simulate protein retention behavior in preparative IEX processes. The CPA model was found to be able to describe even complex elution behavior that cannot be described by the traditional SMA model. In agreement with previous reports, the formation of a distinct shoulder in the elution peak was observed at high load densities close to or beyond the dynamic binding capacity of the column. The peak shoulder formation was observed for both salt gradient elution and pH gradient elution. According to the CPA model, the observed behavior can be attributed to a complex interplay between attractive electrostatic protein-adsorber interactions and a steric blockade of the adsorber surface by adsorbed proteins. Shortcomings of the SMA model and other models in describing the observed elution behavior often prevented the use of mechanistic models in the past.

In conclusion, this work contributed to the computational modeling of IEX chromatography by addressing important challenges that often prevent mechanistic models from being used systematically in process development. It was shown that the developed CPA model can overcome shortcomings of existing adsorption theories and explain even complex industrial process behavior. Confidence in the predictive capabilities of mechanistic chromatography models was increased by introducing a strategy for assessing the uncertainty

in model simulations. The approaches and theories developed in this work contribute to a more widespread use of mechanistic models to support process development of IEX chromatography in a scientific but also risk-based manner.

Outlook

Applying mechanistic models to support the development of chromatography processes has gained increasing momentum in recent years. Thanks to the emergence of user-friendly software tools, the barrier to entry for new users has been lowered significantly, making the technology accessible not only to academia but also to industry. Driven by growing regulatory and economic constraints, the use of mechanistic models is expected to continue to increase in the coming years. Several industrial case studies already demonstrate the potential of mechanistic models to support and streamline process optimization, characterization, and scale-up. Thus, it is expected that the evidence of process and product safety that companies provide to regulatory authorities such as the U.S. Food and Drug Administration will in the future no longer be provided by experiments alone, but will increasingly be supported by model simulations. The use of mechanistic models to inform regulatory decisions will present new challenges in the future, especially with respect to the qualification of these models. To date, there is no consensus on how to determine and demonstrate the suitability of a mechanistic chromatography model for an intended use, neither on the part of the industry nor on the part of the regulatory authorities. As the application of mechanistic models is typically guided by experience and internally developed best practices, modeling approaches and qualification standards can vary significantly across the industry. Therefore, a major challenge will be to establish a more unified modeling framework that can help to standardize the development and qualification of mechanistic chromatography models.

A rigorous uncertainty assessment of a model, as described in Chapter 3, will be an important step in demonstrating model qualification. However, while the proposed Bayesian framework provides higher rigor then commonly applied frequentist approaches, applied sampling techniques to perform approximate Bayesian inference can be computationally intensive. Especially if the parameter posterior distribution is not sufficiently constrained due to a large number of unknown model parameters, weak priors, or limited experimental data for model calibration. In this work, only weak priors were used, which contain only little information on the model parameters and constrain the posterior distribution only slightly. While the use of prior knowledge is firmly anchored in the traditional development of chromatography processes, it has not been used extensively in the course of the modeling of such processes. Future studies could focus on the definition of stronger prior

distributions for unknown but physically constrained model parameters. This would help to constrain the parameter posterior distribution, increase the efficiency of Monte Carlo techniques like Markov Chain Monte Carlo, and ultimately simplify the calibration and uncertainty assessment of mechanistic models.

While great progress has been made in understanding and simulating protein adsorption in ion exchange chromatography (IEC), the understanding of protein adsorption in other chromatography modes such as hydrophobic interaction chromatography (HIC) and mixed-mode chromatography (MMC) is still limited. Thus, to date, there are no adsorption models for HIC and MMC that are based on a strictly physical approach. Instead, conceptually simpler stoichiometric models are used that show strong resemblance to the stoichiometric approach used within the steric mass action model for IEC. Despite the widespread use of HIC and MMC processes in modern downstream processing, existing models for HIC and MMC have hardly been used for the simulation of preparative processes. Thus, the validity and general applicability of these models for simulating complex industrial processes is still quite unclear and should be evaluated in future work.

Even though the adsorption theory developed in this work is devoted primarily to IEC, some aspects of this work can also contribute to the computational modeling of other modes of chromatography such as HIC and MMC. While electrostatic interactions are dominant in IEC, they also play a major role in MMC. The developed colloidal particle adsorption model can therefore be used as a starting point for future work to develop more sophisticated adsorption models for MMC. Furthermore, the description of nonlinear adsorption effects by means of the scaled-particle theory is not limited to IEC but can also be applied to describe nonlinear adsorption effects within other modes of chromatography.

Bibliography

1. ADAMCZYK, Z., 2000. Kinetics of diffusion-controlled adsorption of colloid particles and proteins. *Journal of Colloid and Interface Science*, 229, 2 (2000), 477–489. doi: 10.1006/jcis.2000.6993.

2. ADAMCZYK, Z.; SADLEJ, K.; WAJNRYB, E.; NATTICH, M.; EKIEL-JEZEWSKA, M. L.; AND BŁAWZDZIEWICZ, J., 2010. Streaming potential studies of colloid, polyelectrolyte and protein deposition. *Advances in Colloid and Interface Science*, 153, 1-2 (2010), 1–29. doi:10.1016/j.cis.2009.09.004.

3. ADAMCZYK, Z. AND WEROŃSKI, P., 1999. Application of the DLVO theory for particle deposition problems. *Advances in Colloid and Interface Science*, 83, 1 (1999), 137–226. doi:10.1016/S0001-8686(99)00009-3.

4. ASTHAGIRI, D. AND LENHOFF, A. M., 1997. Influence of structural details in modeling electrostatically driven protein adsorption. *Langmuir*, 13, 25 (1997), 6761–6768. doi:10.1021/la970608u.

5. BEHRENS, S. H. AND BORKOVEC, M., 1999. Electric double layer interaction of ionizable surfaces: Charge regulation for arbitrary potentials. *The Journal of Chemical Physics*, 111, 1 (1999), 382–385. doi:10.1063/1.479280.

6. BEHRENS, S. H. AND BORKOVEC, M., 1999. Electrostatic Interaction of Colloidal Surfaces with Variable Charge. *The Journal of Physical Chemistry B*, 103, 15 (1999), 2918–2928. doi:10.1021/jp984099w.

7. BENNER, S. W.; WELSH, J. P.; RAUSCHER, M. A.; AND POLLARD, J. M., 2019. Prediction of lab and manufacturing scale chromatography performance using minicolumns and mechanistic modeling. *Journal of Chromatography A*, 1593 (2019), 54–62. doi:10.1016/j.chroma.2019.01.063.

8. BHAMBURE, R.; ANGELO, J. M.; GILLESPIE, C. M.; PHILLIPS, M.; GRAALFS, H.; AND LENHOFF, A. M., 2017. Ionic strength-dependent changes in tentacular ion exchangers with variable ligand density. II. Functional properties. *Journal of Chromatography A*, 1506 (2017), 55–64. doi:10.1016/j.chroma.2017.05.021.

9. BHAMBURE, R.; GILLESPIE, C. M.; PHILLIPS, M.; GRAALFS, H.; AND LENHOFF, A. M., 2016. Ionic strength-dependent changes in tentacular ion exchangers with variable ligand density. I. Structural properties. *Journal of Chromatography A*, 1463 (2016), 90–101. doi:10.1016/J.CHROMA.2016.08.010.

10. Bhattacharjee, S. and Elimelech, M., 1997. Surface element integration: A novel technique for evaluation of DLVO interaction between a particle and a flat plate. *Journal of Colloid and Interface Science*, 193, 2 (1997), 273–285. doi:10.1006/jcis.1997.5076.

11. Bhattacharjee, S.; Elimelech, M.; and Borkovec, M., 1998. DLVO Interaction between Colloidal Particles: Beyond Derjaguin's Approximation. *Croatica Chemica Acta*, 71, 4 (1998), 883–903.

12. Bishop, C. M., 2006. *Pattern recognition and machine learning*. Springer. ISBN 0387310738.

13. Boardman, N. K. and Partridge, S. M., 1953. Separation of Neutral Proteins on Ion-Exchange Resins. *Nature*, 171, 4344 (1953), 208–210. doi:10.1038/171208a0.

14. Borg, N.; Brodsky, Y.; Moscariello, J.; Vunnum, S.; Vedantham, G.; Westerberg, K.; and Nilsson, B., 2014. Modeling and robust pooling design of a preparative cation-exchange chromatography step for purification of monoclonal antibody monomer from aggregates. *Journal of Chromatography A*, 1359 (2014), 170–181. doi:10.1016/j.chroma.2014.07.041.

15. Borg, N.; Westerberg, K.; Andersson, N.; von Lieres, E.; and Nilsson, B., 2013. Effects of uncertainties in experimental conditions on the estimation of adsorption model parameters in preparative chromatography. *Computers and Chemical Engineering*, (2013). doi:10.1016/j.compchemeng.2013.04.013.

16. Borg, N.; Westerberg, K.; Schnittert, S.; Von Lieres, E.; and Nilsson, B., 2012. Numerical Analysis of Model Parameter Uncertainties as a Result of Experimental Uncertainty - An Example from Preparative Chromatography. (2012). doi:10.3182/20120215-3-AT-3016.00175.

17. Borkovec, M.; Jönsson, B.; and Koper, G. J. M., 2001. Ionization Processes and Proton Binding in Polyprotic Systems: Small Molecules, Proteins, Interfaces, and Polyelectrolytes. In *Surface and Colloid Science*, 99–339. Springer US, Boston, MA. doi:10.1007/978-1-4615-1223-3_2.

18. Brestrich, N.; Hahn, T.; and Hubbuch, J., 2016. Application of spectral deconvolution and inverse mechanistic modelling as a tool for root cause investigation in protein chromatography. *Journal of Chromatography A*, (2016). doi:10.1016/j.chroma.2016.02.011.

19. Briskot, T.; Hahn, T.; Huuk, T.; and Hubbuch, J., 2020. Adsorption of colloidal proteins in ion-exchange chromatography under consideration of charge regulation. *Journal of Chromatography A*, 1611 (2020), 460608. doi:10.1016/j.chroma.2019.460608.

20. Briskot, T.; Hahn, T.; Huuk, T.; and Hubbuch, J., 2021. Protein adsorption on ion exchange adsorbers: A comparison of a stoichiometric and non-stoichiometric modeling approach. *Journal of Chromatography A*, 1653 (2021), 462397. doi:10.1016/j.chroma.2021.462397.

21. BRISKOT, T.; STÜCKLER, F.; WITTKOPP, F.; WILLIAMS, C.; YANG, J.; KONRAD, S.; DONINGER, K.; GRIESBACH, J.; BENNECKE, M.; HEPBILDIKLER, S.; AND HUBBUCH, J., 2019. Prediction uncertainty assessment of chromatography models using Bayesian inference. *Journal of Chromatography A*, 1587 (2019), 101–110. doi: 10.1016/j.chroma.2018.11.076.

22. BROOKS, C. A. AND CRAMER, S. M., 1992. Steric mass-action ion exchange: Displacement profiles and induced salt gradients. *AIChE Journal*, 38, 12 (1992), 1969–1978. doi:10.1002/aic.690381212.

23. BUTT, H.-J.; GRAF, K.; AND KAPPL, M., 2003. *Physics and Chemistry of Interfaces*. Wiley-VCH. ISBN 3527404139. doi:10.1002/3527602313.

24. CARNIE, S. L. AND CHAN, D. Y., 1993. Interaction Free Energy between Plates with Charge Regulation: A Linearized Model. *Journal of Colloid and Interface Science*, 161, 1 (1993), 260–264. doi:10.1006/JCIS.1993.1464.

25. CARTA, G. AND JUNGBAUER, A., 2020. *Protein Chromatography: Process Development and Scale-Up*. John Wiley & Sons, 2nd editio edn. ISBN 978-3-527-82402-1.

26. CASTELLANOS, M. M.; PATHAK, J. A.; LEACH, W.; BISHOP, S. M.; AND COLBY, R. H., 2014. Explaining the non-Newtonian character of aggregating monoclonal antibody solutions using small-angle neutron scattering. *Biophysical Journal*, 107, 2 (2014), 469–476. doi:10.1016/j.bpj.2014.05.015.

27. CHATTERJEE, S.; MOORE, C. M. V.; AND NASR, M. M., 2017. An Overview of the Role of Mathematical Models in Implementation of Quality by Design Paradigm for Drug Development and Manufacture. In *Comprehensive Quality by Design for Pharmaceutical Product Development and Manufacture* (Eds. G. V. REKLAITIS; C. SEYMOUR; AND S. GARCÍA-MUNOZ), 416. Wiley. ISBN 978-0-470-94237-6.

28. CHICZ, R. M. AND REGNIER, F. E., 1989. Single Amino Acid Contributions to Protein Retention in Cation-Exchange Chromatography: Resolution of Genetically Engineered Subtilisin Variants. *Analytical Chemistry*, 61, 18 (1989), 2059–2066. doi: 10.1021/ac00193a012.

29. CLARK, N. J.; ZHANG, H.; KRUEGER, S.; LEE, H. J.; KETCHEM, R. R.; KERWIN, B.; KANAPURAM, S. R.; TREUHEIT, M. J.; MCAULEY, A.; AND CURTIS, J. E., 2013. Small-angle neutron scattering study of a monoclonal antibody using free-energy constraints. *Journal of Physical Chemistry B*, 117, 45 (2013), 14029–14038. doi:10.1021/jp408710r.

30. CLOSE, E. J.; SALM, J. R.; BRACEWELL, D. G.; AND SORENSEN, E., 2014. A model based approach for identifying robust operating conditions for industrial chromatography with process variability. *Chemical Engineering Science*, 116 (2014), 284–295. doi:10.1016/j.ces.2014.03.010.

31. CRAIK, D. J.; FAIRLIE, D. P.; LIRAS, S.; AND PRICE, D., 2013. The Future of Peptide-based Drugs. *Chemical Biology & Drug Design*, 81, 1 (2013), 136–147. doi:10.1111/CBDD.12055.

32. CREASY, A.; BARKER, G.; AND CARTA, G., 2017. Systematic interpolation method predicts protein chromatographic elution with salt gradients, pH gradients and combined salt/pH gradients. *Biotechnology Journal*, 12, 3 (2017), 1600636. doi: 10.1002/biot.201600636.

33. CREASY, A.; BARKER, G.; YAO, Y.; AND CARTA, G., 2015. Systematic interpolation method predicts protein chromatographic elution from batch isotherm data without a detailed mechanistic isotherm model. *Biotechnology Journal*, 10, 9 (2015), 1400–1411. doi:10.1002/biot.201500089.

34. CREASY, A.; RECK, J.; PABST, T.; HUNTER, A.; BARKER, G.; AND CARTA, G., 2019. Systematic Interpolation Method Predicts Antibody Monomer-Dimer Separation by Gradient Elution Chromatography at High Protein Loads. *Biotechnology Journal*, 14, 3 (2019), 1800132. doi:10.1002/biot.201800132.

35. CURLING, J. AND GOTTSCHALK, U., 2007. Process chromatography: Five decades of innovation. *BioPharm International*, 20, 10 (2007).

36. DANCKWERTS, P. V., 1953. Continuous flow systems. Distribution of residence times. *Chemical Engineering Science*, 2, 1 (1953), 1–13. doi:10.1016/0009-2509(96)81811-2.

37. DEGERMAN, M.; WESTERBERG, K.; AND NILSSON, B., 2009. Determining critical process parameters and process robustness in preparative chromatography - A model-based approach. *Chemical Engineering and Technology*, 32, 6 (2009), 903–911. doi: 10.1002/ceat.200900019.

38. DEPHILLIPS, P. AND LENHOFF, A. M., 2000. Pore size distributions of cation-exchange adsorbents determined by inverse size-exclusion chromatography. *Journal of Chromatography A*, 883, 1-2 (2000), 39–54. doi:10.1016/S0021-9673(00)00420-9.

39. DEVAULT, D., 1943. The theory of chromatography. *Journal of the American Chemical Society*, 65, 4 (1943), 532–540. doi:10.1021/ja01244a011.

40. DIEDRICH, J.; HEYMANN, W.; LEWEKE, S.; HUNT, S.; TODD, R.; KUNERT, C.; JOHNSON, W.; AND VON LIERES, E., 2017. Multi-state steric mass action model and case study on complex high loading behavior of mAb on ion exchange tentacle resin. *Journal of Chromatography A*, 1525 (2017), 60–70. doi:10.1016/j.chroma.2017.09.039.

41. DIMASI, J. A.; GRABOWSKI, H. G.; AND HANSEN, R. W., 2016. Innovation in the pharmaceutical industry: New estimates of R&D costs. *Journal of Health Economics*, 47 (2016), 20–33. doi:10.1016/j.jhealeco.2016.01.012.

42. DIMASI, J. A.; HANSEN, R. W.; AND GRABOWSKI, H. G., 2003. The price of innovation: New estimates of drug development costs. *Journal of Health Economics*, 22, 2 (2003), 151–185. doi:10.1016/S0167-6296(02)00126-1.

43. DISMER, F.; PETZOLD, M.; AND HUBBUCH, J., 2008. Effects of ionic strength and mobile phase pH on the binding orientation of lysozyme on different ion-exchange adsorbents. *Journal of Chromatography A*, 1194, 1 (2008), 11–21. doi:10.1016/j. chroma.2007.12.085.

44. DRAGER, R. AND REGNIER, F., 1986. Application of the stoichiometric displacement model of retention to anion-exchange chromatography of nucleic acids. *Journal of Chromatography A*, 359 (1986), 147–155. doi:10.1016/0021-9673(86)80069-3.

45. EDGCOMB, S. P. AND MURPHY, K. P., 2002. Variability in the pKa of Histidine Side-Chains Correlates With Burial Within Proteins. *Proteins: Structure, Function, and Bioinformatics*, 6, July 2001 (2002), 1–6. doi:10.1002/prot.10177.

46. FISHER, R. A., 1922. On the Mathematical Foundations of Theoretical Statistics. *Philosophical Transactions of the Royal Society A: Mathematical, Physical and Engineering Sciences*, 222, 594-604 (1922), 309–368. doi:10.1098/rsta.1922.0009.

47. FOLEY, A. M., 2010. Uncertainty in regional climate modelling: A review. *Progress in Physical Geography*, (2010). doi:10.1177/0309133310375654.

48. FOOD AND DRUG ADMINISTRATION US DEPARTMENT OF HEALTH AND HUMAN SERVICES, 2018. Bioanalytical Method Validation, Guidance for Industry. Technical report. https://www.fda.gov/downloads/drugs/guidances/ucm070107.Pdf.

49. FOREMAN-MACKEY, D.; HOGG, D. W.; LANG, D.; AND GOODMAN, J., 2012. emcee: The MCMC Hammer. (2012). doi:10.1086/670067.

50. FREED, A. S. AND CRAMER, S. M., 2011. Protein-surface interaction maps for ion-exchange chromatography. *Langmuir*, 27, 7 (2011), 3561–3568. doi:10.1021/la104641z.

51. FRÖHLICH, F.; THEIS, F. J.; AND HASENAUER, J., 2014. Uncertainty Analysis for Non-identifiable Dynamical Systems: Profile Likelihoods, Bootstrapping and More. In *Computational Methods in Systems Biology*, 61–72. Springer International Publishing, Cham.

52. GAMA, M. D. S.; SANTOS, M. S.; LIMA, E. R. D. A.; TAVARES, F. W.; AND BARRETO, A. G. B., 2018. A modified Poisson-Boltzmann equation applied to protein adsorption. *Journal of Chromatography A*, 1531 (2018), 74–82. doi:10.1016/j.chroma.2017.11.022.

53. GERONTAS, S.; ASPLUND, M.; HJORTH, R.; AND BRACEWELL, D. G., 2010. Integration of scale-down experimentation and general rate modelling to predict manufacturing scale chromatographic separations. *Journal of Chromatography A*, 1217, 44 (2010), 6917–6926. doi:10.1016/j.chroma.2010.08.063.

54. GISLER, T.; SCHULZ, S. F.; BORKOVEC, M.; STICHER, H.; SCHURTENBERGER, P.; D'AGUANNO, B.; AND KLEIN, R., 1994. Understanding colloidal charge renormalization from surface chemistry: Experiment and theory. *The Journal of Chemical Physics*, 101, 11 (1994), 9924–9936. doi:10.1063/1.467894.

55. GOODMAN, J. AND WEARE, J., 2010. ENSEMBLE SAMPLERS WITH AFFINE INVARIANCE. *COMM. APP. MATH. AND COMP. SCI*, 5, 1 (2010).

56. GOODWIN, J., 2009. *Colloids and Interfaces with Surfactants and Polymers*. Wiley, 2nd editio edn. ISBN 978-0-470-51880-9.

57. GOTTSCHALK, U. (Ed.), 2017. *Process Scale Purification of Antibodies.* John Wiley & Sons, Inc., Hoboken, NJ, USA. ISBN 9781119126942. doi:10.1002/9781119126942.

58. GRAHAM, T., 1861. X. Liquid diffusion applied to analysis. *Philosophical Transactions of the Royal Society of London*, 151 (1861), 183–224. doi:10.1098/rstl.1861.0011.

59. GRAHAME, D. C., 1947. The Electrical Double Layer and the Theory of Electrocapillarity. *Chemical Reviews*, 41, 3 (1947), 441–501. doi:10.1021/CR60130A002.

60. GRIMSLEY, G. R.; SCHOLTZ, J. M.; AND PACE, C. N., 2009. A summary of the measured pK values of the ionizable groups in folded proteins. *Protein Science*, 18, 1 (2009), 247–251. doi:10.1002/pro.19.

61. GRÖNBERG, A., 2018. Ion Exchange Chromatography. In *Biopharmaceutical Processing: Development, Design, and Implementation of Manufacturing Processes* (Eds. G. JAGSCHIES; E. LINDSKOG; K. ŁĄCKI; AND P. GALLIHER), chap. 18, 379–399. Elsevier. ISBN 9780128125526. doi:10.1016/B978-0-08-100623-8.00018-9.

62. GU, T.; TSAI, G.-J.; AND TSAO, G. T., 1990. New approach to a general nonlinear multicomponent chromatography model. *AIChE Journal*, 36, 5 (1990), 784–788. doi:10.1002/aic.690360517.

63. GU, T.; TSAO, G. T.; TSAI, G.-J.; AND LADISCH, M. R., 1990. Displacement effect in multicomponent chromatography. *AIChE Journal*, 36, 8 (1990), 1156–1162. doi:10.1002/aic.690360805.

64. GUÉLAT, B.; DELEGRANGE, L.; VALAX, P.; AND MORBIDELLI, M., 2013. Model-based prediction of monoclonal antibody retention in ion-exchange chromatography. *Journal of Chromatography A*, 1298 (2013), 17–25. doi:10.1016/j.chroma.2013.04.048.

65. GUÉLAT, B.; KHALAF, R.; LATTUADA, M.; COSTIOLI, M.; AND MORBIDELLI, M., 2016. Protein adsorption on ion exchange resins and monoclonal antibody charge variant modulation. *Journal of Chromatography A*, 1447 (2016), 82–91. doi:10.1016/j.chroma.2016.04.018.

66. GUÉLAT, B.; STRÖHLEIN, G.; LATTUADA, M.; DELEGRANGE, L.; VALAX, P.; AND MORBIDELLI, M., 2012. Simulation model for overloaded monoclonal antibody variants separations in ion-exchange chromatography. *Journal of Chromatography A*, 1253 (2012), 32–43. doi:10.1016/j.chroma.2012.06.081.

67. GUÉLAT, B.; STRÖHLEIN, G.; LATTUADA, M.; AND MORBIDELLI, M., 2010. Electrostatic model for protein adsorption in ion-exchange chromatography and application to monoclonal antibodies, lysozyme and chymotrypsinogen A. *Journal of Chromatography A*, 1217, 35 (2010), 5610–5621. doi:10.1016/j.chroma.2010.06.064.

68. GUIOCHON, G.; FELINGER, A.; SHIRAZI, D. G.; AND KATTI, A. M., 2006. *Fundamentals of Preparative Chromatography.* Academic Press, 2 edn. ISBN 9780123705372.

69. HAHN, T.; HUUK, T.; HEUVELINE, V.; AND HUBBUCH, J., 2015. Simulating and Optimizing Preparative Protein Chromatography with ChromX. *Journal of Chemical Education*, 92, 9 (2015), 1497–1502. doi:10.1021/ed500854a.

70. HAHN, T.; HUUK, T.; OSBERGHAUS, A.; DONINGER, K.; NATH, S.; HEPBILDIK-LER, S.; HEUVELINE, V.; AND HUBBUCH, J., 2016. Calibration-free inverse modeling of ion-exchange chromatography in industrial antibody purification. *Engineering in Life Sciences*, 16, 2 (2016), 107–113. doi:10.1002/elsc.201400248.

71. HAHN, T.; SOMMER, A.; OSBERGHAUS, A.; HEUVELINE, V.; AND HUBBUCH, J., 2014. Adjoint-based estimation and optimization for column liquid chromatography models. *Computers and Chemical Engineering*, 64 (2014), 41–54. doi:10.1016/j.compchemeng.2014.01.013.

72. HAKEMEYER, C.; MCKNIGHT, N.; ST. JOHN, R.; MEIER, S.; TREXLER-SCHMIDT, M.; KELLEY, B.; ZETTL, F.; PUSKEILER, R.; KLEINJANS, A.; LIM, F.; AND WURTH, C., 2016. Process characterization and Design Space definition. *Biologicals*, 44, 5 (2016), 306–318. doi:10.1016/j.biologicals.2016.06.004.

73. HANKE, A. T. AND OTTENS, M., 2014. Purifying biopharmaceuticals: Knowledge-based chromatographic process development. *Trends in Biotechnology*, 32, 4 (2014), 210–220. doi:10.1016/j.tibtech.2014.02.001.

74. HARTVIG, R. A.; VAN DE WEERT, M.; ØSTERGAARD, J.; JORGENSEN, L.; AND JENSEN, H., 2011. Protein adsorption at charged surfaces: The role of electrostatic interactions and interfacial charge regulation. *Langmuir*, 27, 6 (2011), 2634–2643. doi:10.1021/la104720n.

75. HIEMENZ, P. C. AND RAJAGOPALAN, R. (Eds.), 1997. *Principles of Colloid and Surface Chemistry, Revised and Expanded.* CRC Press, 3rd editio edn. ISBN 9780824793975.

76. HINRICHSEN, E. L.; FEDER, J.; AND JØSSANG, T., 1986. Geometry of random sequential adsorption. *Journal of Statistical Physics*, 44, 5-6 (1986), 793–827. doi:10.1007/BF01011908.

77. HUNT, S.; LARSEN, T.; AND TODD, R. J., 2017. Modeling Preparative Cation Exchange Chromatography of Monoclonal Antibodies. In *Preparative Chromatography for Separation of Proteins* (Eds. A. STABY; A. S. RATHORE; AND S. AHUJA), 399–427. John Wiley & Sons, Inc., Hoboken, NJ, USA. doi:10.1002/9781119031116.ch13.

78. HUUK, T.; HAHN, T.; DONINGER, K.; GRIESBACH, J.; HEPBILDIKLER, S.; AND HUBBUCH, J., 2017. Modeling of complex antibody elution behavior under high protein load densities in ion exchange chromatography using an asymmetric activity coefficient. *Biotechnology Journal*, 12, 3 (2017), 1600336. doi:10.1002/biot.201600336.

79. HUUK, T. C.; BRISKOT, T.; HAHN, T.; AND HUBBUCH, J., 2016. A versatile noninvasive method for adsorber quantification in batch and column chromatography based on the ionic capacity. *Biotechnology progress*, 32, 3 (2016), 666–677. doi:10.1002/btpr.2228.

80. HUUK, T. C.; HAHN, T.; OSBERGHAUS, A.; AND HUBBUCH, J., 2014. Model-based integrated optimization and evaluation of a multi-step ion exchange chromatography. *Separation and Purification Technology*, 136 (2014), 207–222. doi:10.1016/j.seppur.2014.09.012.

81. International Conference on Harmonization of Technical Requirements for Registration of Pharmaceuticals for Human Use, 2005. ICH Harmonised Tripartite Guideline, Quality Risk Management Q9. Technical report.

82. International Conference on Harmonization of Technical Requirements for Registration of Pharmaceuticals for Human Use, 2008. ICH Harmonised Tripartite Guideline, Pharmaceutical Quality System Q10. Technical report.

83. International Conference on Harmonization of Technical Requirements for Registration of Pharmaceuticals for Human Use, 2009. Pharmaceutical Development Q8(R2). *ICH Harmonised Tripartite Guideline*, (2009).

84. Israelachvili, J., 2011. *Intermolecular and Surface Forces*. Academic Press. ISBN 9780123751829. doi:10.1016/C2009-0-21560-1.

85. Jagschies, G.; Lindskog, E.; Lacki, K.; and Galliher, P. (Eds.), 2017. *Biopharmaceutical Processing: Development, Design, and Implementation of Manufacturing Processes*. Elsevier, 1st editio edn. ISBN 9780081006238.

86. Jakobsson, N.; Degerman, M.; and Nilsson, B., 2005. Optimisation and robustness analysis of a hydrophobic interaction chromatography step. *Journal of Chromatography A*, 1099, 1-2 (2005), 157–166. doi:10.1016/j.chroma.2005.09.009.

87. Jakobsson, N.; Degerman, M.; Stenborg, E.; and Nilsson, B., 2007. Model based robustness analysis of an ion-exchange chromatography step. *Journal of Chromatography A*, 1138, 1-2 (2007), 109–119. doi:10.1016/J.chroma.2006.10.057.

88. Jakobsson, N.; Karlsson, D.; Axelsson, J. P.; Zacchi, G.; and Nilsson, B., 2005. Using computer simulation to assist in the robustness analysis of an ion-exchange chromatography step. *Journal of Chromatography A*, 1063, 1-2 (2005), 99–109. doi:10.1016/j.chroma.2004.11.067.

89. Janson, J.-C., 2011. *Protein purification: principles, high resolution methods, and applications*. John Wiley & Sons, 3rd editio edn.

90. Johnson, C. A.; Wu, P.; and Lenhoff, A. M., 1994. Electrostatic and van der Waals Contributions to Protein Adsorption: 2. Modeling of Ordered Arrays. *Langmuir*, 10, 10 (1994), 3705–3713. doi:10.1021/la00022a052.

91. Joshi, M.; Seidel-Morgenstern, A.; and Kremling, A., 2006. Exploiting the bootstrap method for quantifying parameter confidence intervals in dynamical systems. *Metabolic Engineering*, (2006). doi:10.1016/j.ymben.2006.04.003.

92. Kaltenbrunner, O.; Giaverini, O.; Woehle, D.; and Asenjo, J., 2007. Application of chromatographic theory for process characterization towards validation of an ion-exchange operation. *Biotechnology and Bioengineering*, 98, 1 (2007), 201–210. doi:10.1002/bit.21358.

93. Kesik-Brodacka, M., 2018. Progress in biopharmaceutical development. *Biotechnology and Applied Biochemistry*, 65, 3 (2018), 306–322. doi:10.1002/bab.1617.

94. KHAWLI, L. A.; GOSWAMI, S.; HUTCHINSON, R.; KWONG, Z. W.; YANG, J.; WANG, X.; YAO, Z.; SREEDHARA, A.; CANO, T.; TESAR, D.; NIJEM, I.; ALLISON, D. E.; WONG, P. Y.; KAO, Y. H.; QUAN, C.; JOSHI, A.; HARRIS, R. J.; AND MOTCHNIK, P., 2010. Charge variants in IgG1: Isolation, characterization, in vitro binding properties and pharmacokinetics in rats. *mAbs*, 2, 6 (2010), 613–624. doi: 10.4161/mabs.2.6.13333.

95. KIMERER, L. K.; PABST, T. M.; HUNTER, A. K.; AND CARTA, G., 2019. Chromatographic behavior of bivalent bispecific antibodies on cation exchange columns. I. Experimental observations and phenomenological model. *Journal of Chromatography A*, 1601 (2019), 121–132. doi:10.1016/j.chroma.2019.04.012.

96. KLUTERS, S.; HAFNER, M.; VON HIRSCHHEYDT, T.; AND FRECH, C., 2015. Solvent modulated linear pH gradient elution for the purification of conventional and bispecific antibodies: Modeling and application. *Journal of Chromatography A*, 1418 (2015), 119–129. doi:10.1016/j.chroma.2015.09.053.

97. KLUTERS, S.; WITTKOPP, F.; JÖHNCK, M.; AND FRECH, C., 2016. Application of linear pH gradients for the modeling of ion exchange chromatography: Separation of monoclonal antibody monomer from aggregates. *Journal of Separation Science*, 39, 4 (2016), 663–675. doi:10.1002/jssc.201500994.

98. KOPACIEWICZ, W.; ROUNDS, M.; FAUSNAUGH, J.; AND REGNIER, F., 1983. Retention model for high-performance ion-exchange chromatography. *Journal of Chromatography A*, 266 (1983), 3–21. doi:10.1016/S0021-9673(01)90875-1.

99. KRIGBAUM, W. R. AND KÜGLER, F. R., 1970. Molecular Conformation of Egg-White Lysozyme and Bovine α-Lactalbumin in Solution. *Biochemistry*, 9, 5 (1970), 1216–1223. doi:10.1021/bi00807a024.

100. KUMAR, V.; LEWEKE, S.; VON LIERES, E.; AND RATHORE, A. S., 2015. Mechanistic modeling of ion-exchange process chromatography of charge variants of monoclonal antibody products. *Journal of Chromatography A*, (2015). doi: 10.1016/j.chroma.2015.11.062.

101. KURAMITSU, S. AND HAMAGUCHI, K., 1980. Analysis of the Acid-Base Titration Curve of Hen Lysozyme. *The Journal of Biochemistry*, 87, 4 (1980), 1215–1219.

102. LADIWALA, A.; REGE, K.; BRENEMAN, C. M.; AND CRAMER, S. M., 2005. A priori prediction of adsorption isotherm parameters and chromatographic behavior in ion-exchange systems. *Proceedings of the National Academy of Sciences of the United States of America*, 102, 33 (2005), 11710–11715. doi:10.1073/pnas.0408769102.

103. LAVOISIER, A. AND SCHLAEPPI, J. M., 2015. Early developability screen of therapeutic antibody candidates using Taylor dispersion analysis and UV area imaging detection. *mAbs*, 7, 1 (2015), 77–83. doi:10.4161/19420862.2014.985544.

104. LEBOWITZ, J. L.; HELFAND, E.; AND PSAESTGAAKD, E., 1965. Scaled particle theory of fluid mixtures. *The Journal of Chemical Physics*, 43, 3 (1965), 774–779. doi:10.1063/1.1696842.

105. LESINS, V. AND RUCKENSTEIN, E., 1988. Patch controlled attractive electrostatic interactions between similarly charged proteins and adsorbents. *Colloid & Polymer Science*, 266, 12 (1988), 1187–1190. doi:10.1007/BF01414409.

106. LIU, H.; CAZA-BULSECO, G.; FALDU, D.; CHUMSAE, C.; AND SUN, J., 2008. Heterogeneity of monoclonal antibodies. *Journal of Pharmaceutical Sciences*, 97, 7 (2008), 2426–2447. doi:10.1002/jps.21180.

107. LIU, H. F.; MA, J.; WINTER, C.; AND BAYER, R., 2010. Recovery and purification process development for monoclonal antibody production. *mAbs*, 2, 5 (2010), 480–499. doi:10.4161/mabs.2.5.12645.

108. LORET, C.; CHAUFER, B.; SEBILLE, B.; HANSELIN, M.; BLAIN, Y.; AND LE HIR, A., 1988. Charaterization and hydrodynamic behaviour of modified gelatin: II. Characterization by high performance size exclusion chromatography - comparison with dextrans and proteins. *International Journal of Biological Macromolecules*, 10, 6 (1988), 366–372. doi:10.1016/0141-8130(88)90031-1.

109. LUND, M.; ÅKESSON, T.; AND JÖNSSON, B., 2005. Enhanced protein adsorption due to charge regulation. *Langmuir*, 21, 18 (2005), 8385–8388. doi:10.1021/la050607z.

110. MACKIE, J. S.; MEARES KATCHALSKY, P.; SHAVIT, A.; EISENBERG, N.; KRESSMAN, H.; KITCHENER, R. E.; KRESSMAN, J. A.; LIFSON, J. A.; KATCHALSKY, S.; OOSAWA, A.; IMAI, F.; AND KAGAWA, N., 1955. The diffusion of electrolytes in a cation-exchange resin membrane I. Theoretical. *Proceedings of the Royal Society of London. Series A. Mathematical and Physical Sciences*, 232, 1191 (1955), 498–509. doi:10.1098/rspa.1955.0234.

111. MAREK, W. K.; SAUER, D.; DÜRAUER, A.; JUNGBAUER, A.; PIĄTKOWSKI, W.; AND ANTOS, D., 2018. Prediction tool for loading, isocratic elution, gradient elution and scaling up of ion exchange chromatography of proteins. *Journal of Chromatography A*, 1566 (2018), 89–101. doi:10.1016/J.CHROMA.2018.06.057.

112. MITRAGOTRI, S.; BURKE, P. A.; AND LANGER, R., 2014. Overcoming the challenges in administering biopharmaceuticals: formulation and delivery strategies. *Nature Reviews Drug Discovery 2014 13:9*, 13, 9 (2014), 655–672. doi:10.1038/nrd4363.

113. MOLLERUP, J. M., 2006. Applied thermodynamics: A new frontier for biotechnology. *Fluid Phase Equilibria*, 241, 1-2 (2006), 205–215. doi:10.1016/J.FLUID.2005.12.037.

114. MOLLERUP, J. M., 2008. A review of the thermodynamics of protein association to ligands, protein adsorption, and adsorption isotherms. *Chemical Engineering and Technology*, 31, 6 (2008), 864–874. doi:10.1002/ceat.200800082.

115. MORRISON, C., 2020. Fresh from the biotech pipeline-2019. *Nature biotechnology*, 38, 2 (2020), 126–131. doi:10.1038/s41587-019-0405-7.

116. MURPHY, K. P., 2012. *Machine learning : a probabilistic perspective*. MIT Press. ISBN 9780262018029.

117. NFOR, B. K.; VERHAERT, P. D.; VAN DER WIELEN, L. A.; HUBBUCH, J.; AND OTTENS, M., 2009. Rational and systematic protein purification process development: the next generation. *Trends in Biotechnology*, 27, 12 (2009), 673–679. doi: 10.1016/j.tibtech.2009.09.002.

118. NG, C. K. S.; OSUNA-SANCHEZ, H.; VALÉRY, E.; SØRENSEN, E.; AND BRACEWELL, D. G., 2012. Design of high productivity antibody capture by protein A chromatography using an integrated experimental and modeling approach. *Journal of Chromatography B*, 899 (2012), 116–126. doi:10.1016/j.jchromb.2012.05.010.

119. OBERHOLZER, M. R. AND LENHOFF, A. M., 1999. Protein adsorption isotherms through colloidal energetics. *Langmuir*, 15, 11 (1999), 3905–3914. doi:10.1021/la981199k.

120. OBERHOLZER, M. R.; STANKOVICH, J. M.; CARNIE, S. L.; CHAN, D. Y.; AND LENHOFF, A. M., 1997. 2-D and 3-D interactions in random sequential adsorption of charged particles. *Journal of Colloid and Interface Science*, 194, 1 (1997), 138–153. doi:10.1006/jcis.1997.5095.

121. OHSHIMA, H. AND FURUSAWA, K. (Eds.), 1998. *Electrical Phenomena at Interfaces Fundamentals: Measurements, and Applications.* CRC Press. ISBN 9780824790394.

122. ORELLANA, C. A.; SHENE, C.; AND ASENJO, J. A., 2009. Mathematical modeling of elution curves for a protein mixture in ion exchange chromatography applied to high protein concentration. *Biotechnology and Bioengineering*, 104, 3 (2009), 572–581. doi:10.1002/bit.22422.

123. OSBERGHAUS, A.; DRECHSEL, K.; HANSEN, S.; HEPBILDIKLER, S. K.; NATH, S.; HAINDL, M.; VON LIERES, E.; AND HUBBUCH, J., 2012. Model-integrated process development demonstrated on the optimization of a robotic cation exchange step. *Chemical Engineering Science*, 76 (2012), 129–139. doi:10.1016/j.ces.2012.04.004.

124. OSBERGHAUS, A.; HEPBILDIKLER, S.; NATH, S.; HAINDL, M.; VON LIERES, E.; AND HUBBUCH, J., 2012. Optimizing a chromatographic three component separation: A comparison of mechanistic and empiric modeling approaches. *Journal of Chromatography A*, 1237 (2012), 86–95. doi:10.1016/j.chroma.2012.03.029.

125. PABST, T. M. AND CARTA, G., 2007. pH transitions in cation exchange chromatographic columns containing weak acid groups. *Journal of Chromatography A*, 1142, 1 SPEC. ISS. (2007), 19–31. doi:10.1016/j.chroma.2006.08.066.

126. PACE, C. N.; GRIMSLEY, G. R.; AND SCHOLTZ, J. M., 2009. Protein Ionizable Groups : pK Values and Their Contribution to Protein Stability Measured pK Values in Folded Proteins Perturbation of pK Values. *Journal of Biological Chemistry*, 284, 20 (2009), 13285–13289. doi:10.1074/jbc.R800080200.

127. PARSEGIAN, V. A. AND GINGELL, D., 1972. On the Electrostatic Interaction across a Salt Solution between Two Bodies Bearing Unequal Charges. *Biophysical Journal*, 12, 9 (1972), 1192–1204. doi:10.1016/S0006-3495(72)86155-1.

128. PEREIRA, P. C. AND APOLINARIO, S. W., 2012. Madelung energy of Yukawa lattices. *Physical Review E - Statistical, Nonlinear, and Soft Matter Physics*, 86, 4 (2012), 046702. doi:10.1103/PhysRevE.86.046702.

129. PERSSON, P.; GUSTAVSSON, P. E.; ZACCHI, G.; AND NILSSON, B., 2006. Aspects of estimating parameter dependencies in a detailed chromatography model based on frontal experiments. *Process Biochemistry*, 41, 8 (2006), 1812–1821. doi:10.1016/j.procbio.2006.03.030.

130. PERSSON, P.; KEMPE, H.; ZACCHI, G.; AND NILSSON, B., 2004. A methodology for estimation of mass transfer parameters in a detailed chromatography model based on frontal experiments. *Chemical Engineering Research and Design*, 82, 4 (2004), 517–526. doi:10.1205/026387604323050236.

131. PLATH, F.; RINGLER, P.; GRAFF-MEYER, A.; STAHLBERG, H.; LAUER, M. E.; RUFER, A. C.; GRAEWERT, M. A.; SVERGUN, D.; GELLERMANN, G.; FINKLER, C.; STRACKE, J. O.; KOULOV, A.; AND SCHNAIBLE, V., 2016. Characterization of mAb dimers reveals predominant dimer forms common in therapeutic mAbs. *mAbs*, 8, 5 (2016), 928–940. doi:10.1080/19420862.2016.1168960.

132. RADER, R. A., 2008. (Re)defining biopharmaceutical. *Nature Biotechnology*, 26, 7 (2008), 743–751. doi:10.1038/nbt0708-743.

133. RATHORE, A. S.; LI, X.; BARTKOWSKI, W.; SHARMA, A.; AND LU, Y., 2009. Case study and application of process analytical technology (PAT) towards bioprocessing: Use of tryptophan fluorescence as at-line tool for making pooling decisions for process chromatography. *Biotechnology progress*, 25, 5 (2009), 1433–9. doi:10.1002/btpr.212.

134. RAUE, A.; KREUTZ, C.; MAIWALD, T.; BACHMANN, J.; SCHILLING, M.; KLING-MÜLLER, U.; AND TIMMER, J., 2009. Structural and practical identifiability analysis of partially observed dynamical models by exploiting the profile likelihood. *Bioinformatics*, 25, 15 (2009), 1923–1929. doi:10.1093/bioinformatics/btp358.

135. RAUE, A.; SCHILLING, M.; BACHMANN, J.; MATTESON, A.; SCHELKE, M.; KASCHEK, D.; HUG, S.; KREUTZ, C.; HARMS, B. D.; THEIS, F. J.; KLING-MÜLLER, U.; AND TIMMER, J., 2013. Lessons Learned from Quantitative Dynamical Modeling in Systems Biology. *PLoS ONE*, 8, 9 (2013), e74335. doi:10.1371/journal.pone.0074335.

136. REFAEE, M.; TEZUKA, T.; AKASAKA, K.; AND WILLIAMSON, M., 2003. Pressure-Dependent Changes in the Solution Structure of Hen Egg-White Lysozyme. *J.Mol.Biol.*, 327 (2003), 857. doi:10.2210/PDB1GXV/PDB.

137. REINER, E. S. AND RADKE, C. J., 1991. Electrostatic interactions in colloidal suspensions: Tests of pairwise additivity. *AIChE Journal*, 37, 6 (1991), 805–824. doi:10.1002/aic.690370604.

138. REISS, H.; FRISCH, H. L.; HELFAND, E.; AND LEBOWITZ, J. L., 1960. Aspects of the statistical thermodynamics of real fluids. *The Journal of Chemical Physics*, 32, 1 (1960), 119–124. doi:10.1063/1.1700883.

139. REISS, H.; FRISCH, H. L.; AND LEBOWITZ, J. L., 1959. Statistical mechanics of rigid spheres. *The Journal of Chemical Physics*, 31, 2 (1959), 369–380. doi:10.1063/1.1730361.

140. RISCHAWY, F.; SALEH, D.; HAHN, T.; OELMEIER, S.; SPITZ, J.; AND KLUTERS, S., 2019. Good modeling practice for industrial chromatography: Mechanistic modeling of ion exchange chromatography of a bispecific antibody. *Computers and Chemical Engineering*, 130 (2019), 106532. doi:10.1016/j.compchemeng.2019.106532.

141. ROLANDI, P. A., 2019. The Unreasonable Effectiveness of Equations: Advanced Modeling For Biopharmaceutical Process Development. *Computer Aided Chemical Engineering*, 47 (2019), 137–150. doi:10.1016/B978-0-12-818597-1.50023-0.

142. ROTH, C. M. AND LENHOFF, A. M., 1993. Electrostatic and van der Waals Contributions to Protein Adsorption: Computation of Equilibrium Constants. *Langmuir*, 9, 4 (1993), 962–972. doi:10.1021/la00028a015.

143. ROTH, C. M. AND LENHOFF, A. M., 1995. Electrostatic and van der Waals Contributions to Protein Adsorption: Comparison of Theory and Experiment. *Langmuir*, 11, 9 (1995), 3500–3509. doi:10.1021/la00009a036.

144. ROUNDS, M. A. AND REGNIER, F. E., 1984. Evaluation of a retention model for high-performance ion-exchange chromatography using two different displacing salts. *Journal of Chromatography A*, 283 (1984), 37–45. doi:10.1016/S0021-9673(00)96240-X.

145. ROUSH, D.; ASTHAGIRI, D.; BABI, D. K.; BENNER, S.; BILODEAU, C.; CARTA, G.; ERNST, P.; FEDESCO, M.; FITZGIBBON, S.; FLAMM, M.; GRIESBACH, J.; GROSSKOPF, T.; HANSEN, E. B.; HAHN, T.; HUNT, S.; INSAIDOO, F.; LENHOFF, A.; LIN, J.; MARKE, H.; MARQUES, B.; PAPADAKIS, E.; SCHLEGEL, F.; STABY, A.; STENVANG, M.; SUN, L.; TESSIER, P. M.; TODD, R.; VON LIERES, E.; WELSH, J.; WILLSON, R.; WANG, G.; WUCHERPFENNIG, T.; AND ZAVALOV, O., 2020. Toward in silico CMC: An industrial collaborative approach to model-based process development. *Biotechnology and Bioengineering*, 117, 12 (2020), 3986–4000. doi:10.1002/bit.27520.

146. RUCKENSTEIN, E. AND PRIEVE, D. C., 1973. Rate of deposition of Brownian particles under the action of London and double-layer forces. *Journal of the Chemical Society, Faraday Transactions 2: Molecular and Chemical Physics*, 69, 0 (1973), 1522–1536. doi:10.1039/F29736901522.

147. RUCKENSTEIN, E. AND PRIEVE, D. C., 1976. Adsorption and desorption of particles and their chromatographic separation. *AIChE Journal*, 22, 2 (1976), 276–283. doi:10.1002/aic.690220209.

148. RUSSEL, W. B.; SAVILLE, D. A.; AND SCHOWALTER, W. R., 1989. *Colloidal Dispersions*. Cambridge University Press. ISBN 9780521426008. doi:10.1017/CBO9780511608810.

149. SALEH, D.; WANG, G.; MUELLER, B.; RISCHAWY, F.; KLUTERS, S.; STUDTS, J.; AND HUBBUCH, J., 2020. Cross-scale quality assessment of a mechanistic cation exchange chromatography model. *Biotechnology Progress*, (2020), e3081. doi:10.1002/btpr.3081.

150. SALEH, D.; WANG, G.; MÜLLER, B.; RISCHAWY, F.; KLUTERS, S.; STUDTS, J.; AND HUBBUCH, J., 2020. Straightforward method for calibration of mechanistic cation exchange chromatography models for industrial applications. *Biotechnology Progress*, 36, 4 (2020), e2984. doi:10.1002/btpr.2984.

151. SCHMIDT, M.; HAFNER, M.; AND FRECH, C., 2014. Modeling of salt and pH gradient elution in ion-exchange chromatography. *Journal of Separation Science*, 37, 1-2 (2014), 5–13. doi:10.1002/jssc.201301007.

152. SCHMIDT-TRAUB, H. (Ed.), 2005. *Preparative Chromatography: of Fine Chemicals and Pharmaceutical Agents.* Wiley-VCH. ISBN 9783527306435.

153. SHEN, H. AND FREY, D. D., 2004. Charge regulation in protein ion-exchange chromatography: Development and experimental evaluation of a theory based on hydrogen ion Donnan equilibrium. *Journal of Chromatography A*, 1034, 1-2 (2004), 55–68. doi:10.1016/j.chroma.2004.01.039.

154. SHEN, H. AND FREY, D. D., 2005. Effect of charge regulation on steric mass-action equilibrium for the ion-exchange adsorption of proteins. *Journal of Chromatography A*, 1079, 1-2 SPEC. ISS. (2005), 92–104. doi:10.1016/j.chroma.2005.02.086.

155. SHENE, C.; LUCERO, A.; ANDREWS, B.; AND ASENJO, J., 2006. Mathematical modeling of elution curves for a protein mixture in ion exchange chromatography and for the optimal selection of operational conditions. *Biotechnology and Bioengineering*, 95, 4 (2006), 704–713. doi:10.1002/bit.21019.

156. SHUKLA, A. A.; ETZEL, M. R.; AND GADAM, S. (Eds.), 2006. *Process Scale Bioseparations for the Biopharmaceutical Industry.* CRC Press. ISBN 9780367577841.

157. SINGH, N. AND HERZER, S., 2018. Downstream Processing Technologies/Capturing and Final Purification. In *New Bioprocessing Strategies: Development and Manufacturing of Recombinant Antibodies and Proteins* (Eds. B. KISS; U. GOTTSCHALK; AND M. POHLSCHEIDT), vol. 165, 115–178. Springer. doi:10.1007/10_2017_12.

158. SMILGIES, D. M. AND FOLTA-STOGNIEW, E., 2015. Molecular weight-gyration radius relation of globular proteins: A comparison of light scattering, small-angle X-ray scattering and structure-based data. *Journal of Applied Crystallography*, 48 (2015), 1604–1606. doi:10.1107/S1600576715015551.

159. SPIELMAN, L. A. AND FRIEDLANDER, S., 1974. Role of the electrical double layer in particle deposition by convective diffusion. *Journal of Colloid and Interface Science*, 46, 1 (1974), 22–31. doi:10.1016/0021-9797(74)90021-6.

160. STABY, A.; AHUJA, S.; AND RATHORE, A. S., 2017. Model-Based Preparative Chromatography Process Development in the QbD Paradigm. In *Preparative Chromatography for Separation of Proteins* (Eds. A. STABY; S. AHUJA; AND A. S. RATHORE), 1–10. John Wiley & Sons. ISBN 978-1-119-03110-9.

161. STÅHLBERG, J., 1999. Retention models for ions in chromatography. *Journal of Chromatography A*, 855, 1 (1999), 3–55. doi:10.1016/S0021-9673(99)00176-4.

162. STÅHLBERG, J. AND JÖNSSON, B., 1996. Influence of charge regulation in electrostatic interaction chromatography of proteins. *Analytical Chemistry*, 68, 9 (1996), 1536–1544. doi:10.1021/ac9509972.

163. STÅHLBERG, J.; JÖNSSON, B.; AND HORVÁTH, C., 1991. Theory for Electrostatic Interaction Chromatography of Proteins. *Analytical Chemistry*, 63, 17 (1991), 1867–1874. doi:10.1021/ac00017a036.

164. STÅHLBERG, J.; JÖNSSON, B.; AND HORVÁTH, C., 1992. Combined effect of coulombic and van der Waals interactions in the chromatography of proteins. *Analytical Chemistry*, 64, 4 (1992), 3118–3124. doi:10.1021/ac00048a009.

165. STEINEBACH, F.; ANGARITA, M.; KARST, D. J.; MÜLLER-SPÄTH, T.; AND MOR-BIDELLI, M., 2016. Model based adaptive control of a continuous capture process for monoclonal antibodies production. *Journal of Chromatography A*, 1444 (2016), 50–56. doi:10.1016/j.chroma.2016.03.014.

166. STEINEBACH, F.; COQUEBERT DE NEUVILLE, B.; AND MORBIDELLI, M., 2017. Relating saturation capacity to charge density in strong cation exchangers. *Journal of Chromatography A*, 1507 (2017), 95–103. doi:10.1016/j.chroma.2017.05.054.

167. TALBOT, J., 1997. Molecular thermodynamics of binary mixture adsorption: A scaled particle theory approach. *Journal of Chemical Physics*, 106, 11 (1997), 4696–4706. doi:10.1063/1.473506.

168. TALBOT, J.; JIN, X.; AND WANG, N. H., 1994. New Equations for Multicomponent Adsorption Kinetics. *Langmuir*, 10, 6 (1994), 1663–1666. doi:10.1021/la00018a009.

169. TANG, L.; SUNDARAM, S.; ZHANG, J.; CARLSON, P.; MATATHIA, A.; PAREKH, B.; ZHOU, Q.; AND HSIEH, M. C., 2013. Conformational characterization of the charge variants of a human IgG1 monoclonal antibody using H/D exchange mass spectrometry. *mAbs*, 5, 1 (2013), 114–125. doi:10.4161/mabs.22695.

170. TRAPP, A.; FAUDE, A.; HÖROLD, N.; SCHUBERT, S.; FAUST, S.; GROB, T.; AND SCHMIDT, S., 2018. Multiple functions of caprylic acid-induced impurity precipitation for process intensification in monoclonal antibody purification. *Journal of Biotechnology*, 279 (2018), 13–21. doi:10.1016/j.jbiotec.2018.05.001.

171. TREFALT, G.; BEHRENS, S. H.; AND BORKOVEC, M., 2016. Charge Regulation in the Electrical Double Layer: Ion Adsorption and Surface Interactions. *Langmuir*, 32, 2 (2016), 380–400. doi:10.1021/acs.langmuir.5b03611.

172. TROTTA, R., 2017. Bayesian Methods in Cosmology. (2017).

173. VAN MOURIK, S.; TER BRAAK, C.; STIGTER, H.; AND MOLENAAR, J., 2014. Prediction uncertainty assessment of a systems biology model requires a sample of the full probability distribution of its parameters. *PeerJ*, (2014). doi:10.7717/peerj.433.

174. VANLIER, J.; TIEMANN, C. A.; HILBERS, P. A. J.; AND VAN RIEL, N. A. W., 2012. An integrated strategy for prediction uncertainty analysis. *Bioinformatics*, 28, 8 (2012), 1130–113510. doi:10.1093/bioinformatics/bts088.

175. VÁZQUEZ-REY, M. AND LANG, D. A., 2011. Aggregates in monoclonal antibody manufacturing processes. *Biotechnology and Bioengineering*, 108, 7 (2011), 1494–1508. doi:10.1002/bit.23155.

176. VELAYUDHAN, A. AND HORVÁTH, C., 1988. Preparative chromatography of proteins. Analysis of the multivalent ion-exchange formalism. *Journal of Chromatography A*, (1988). doi:10.1016/S0021-9673(00)94779-4.

177. VERWEY, E. J. W. AND OVERBEEK, J. T. G., 1946. Long distance forces acting between colloidal particles. *Transactions of the Faraday Society*, 42, 0 (1946), B117. doi:10.1039/tf946420b117.

178. Walsh, G., 2010. Biopharmaceutical benchmarks 2010. *Nature Biotechnology*, 28, 9 (2010), 917–924. doi:10.1038/nbt0910-917.

179. Walsh, G., 2018. Biopharmaceutical benchmarks 2018. *Nature Biotechnology*, 36, 12 (2018), 1136–1145. doi:10.1038/nbt.4305.

180. Westerberg, K.; Broberg Hansen, E.; Degerman, M.; Budde Hansen, T.; and Nilsson, B., 2012. Model-based process challenge of an industrial ion-exchange chromatography step. *Chemical Engineering and Technology*, 35, 1 (2012), 183–190. doi:10.1002/ceat.201000560.

181. Wicke, E., 1939. Empirische und theoretische Untersuchungen der Sorptionsgeschwindigkeit von Gasen an porösen Stoffen II. *Kolloid-Zeitschrift*, 86, 3 (1939), 295–313. doi:10.1007/BF01511392.

182. Wiczling, P.; Kubik, Ł.; and Kaliszan, R., 2015. Maximum A Posteriori Bayesian Estimation of Chromatographic Parameters by Limited Number of Experiments. *Analytical Chemistry*, 87, 14 (2015), 7241–7249. doi:10.1021/acs.analchem.5b01195.

183. Wilson, J. N., 1940. A Theory of Chromatography. *Journal of the American Chemical Society*, 62, 6 (1940), 1583–1591. doi:10.1021/ja01863a071.

184. Wittkopp, F.; Peeck, L.; Hafner, M.; and Frech, C., 2018. Modeling and simulation of protein elution in linear pH and salt gradients on weak, strong and mixed cation exchange resins applying an extended Donnan ion exchange model. *Journal of Chromatography A*, (2018). doi:10.1016/j.chroma.2018.02.020.

185. Wldom, B., 1963. Some topics in the theory of fluids. *The Journal of Chemical Physics*, 39, 11 (1963), 2808–2812. doi:10.1063/1.1734110.

186. Wu, Y.; Simons, J.; Hooson, S.; Abraham, D.; and Carta, G., 2013. Protein and virus-like particle adsorption on perfusion chromatography media. *Journal of Chromatography A*, 1297 (2013), 96–105. doi:10.1016/j.chroma.2013.04.062.

187. Xu, A. and Lenhoff, A. M., 2008. A predictive approach to correlating protein adsorption isotherms on ion-exchange media. *Journal of Physical Chemistry B*, 112, 3 (2008), 1028–1040. doi:10.1021/jp0754233.

188. Xu, X. and Lenhoff, A. M., 2009. Binary adsorption of globular proteins on ion-exchange media. *Journal of Chromatography A*, 1216, 34 (2009), 6177–6195. doi:10.1016/j.chroma.2009.06.082.

189. Yamamoto, S.; Nakanishi, K.; Matsuno, R.; and Kamikubo, T., 1983. Ion exchange chromatography of proteins-prediction of elution curves and operating conditions. I. Theoretical considerations. *Biotechnology and Bioengineering*, 25, 6 (1983), 1465–1483. doi:10.1002/bit.260250605.

190. Yao, Y. and Lenhoff, A. M., 2006. Pore size distributions of ion exchangers and relation to protein binding capacity. *Journal of Chromatography A*, 1126, 1-2 (2006), 107–119. doi:10.1016/j.chroma.2006.06.057.

191. YOON, B. J. AND LENHOFF, A. M., 1992. Computation of the electrostatic interaction energy between a protein and a charged surface. *The Journal of Physical Chemistry*, , 4 (1992), 3130–3134. doi:10.1021/j100186a064.

192. YU, D.; MCLEAN, M. D.; HALL, J. C.; AND GHOSH, R., 2008. Purification of monoclonal antibody from tobacco extract using membrane-based bioseparation techniques. *Journal of Membrane Science*, 323, 1 (2008), 159–166. doi:10.1016/j. memsci.2008.06.019.

193. ZHANG, A.; HU, P.; MACGREGOR, P.; XUE, Y.; FAN, H.; SUCHECKI, P.; OL-SZEWSKI, L.; AND LIU, A., 2014. Understanding the conformational impact of chemical modifications on monoclonal antibodies with diverse sequence variation using hydrogen/deuterium exchange mass spectrometry and structural modeling. *Analytical Chemistry*, 86, 7 (2014), 3468–3475. doi:10.1021/ac404130a.

194. ZHANG, L.; SELKER, J.; QU, A.; AND VELAYUDHAN, A., 2001. Numerical estimation of multicomponent adsorption isotherms in preparative chromatography: Implications of experimental error. *Journal of Chromatography A*, (2001). doi:10.1016/S0021-9673(01)01297-3.

# Appendix A: Supplementary Material for Chapter 3
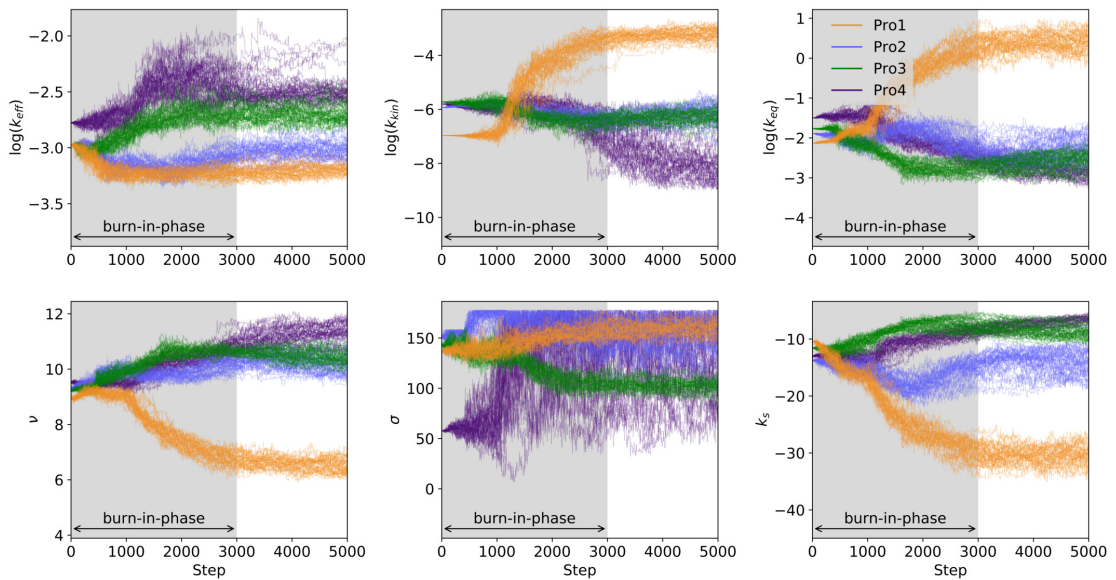
Figure A.1: Parameter traces indicating the parameter values of the 50 walkers at each step in the Markov Chain. The walkers were initialized around the estimated maximum likelihood estimate and evolved over 5000 steps per walker. Samples taken during the initial burn-in-phase were discarded.
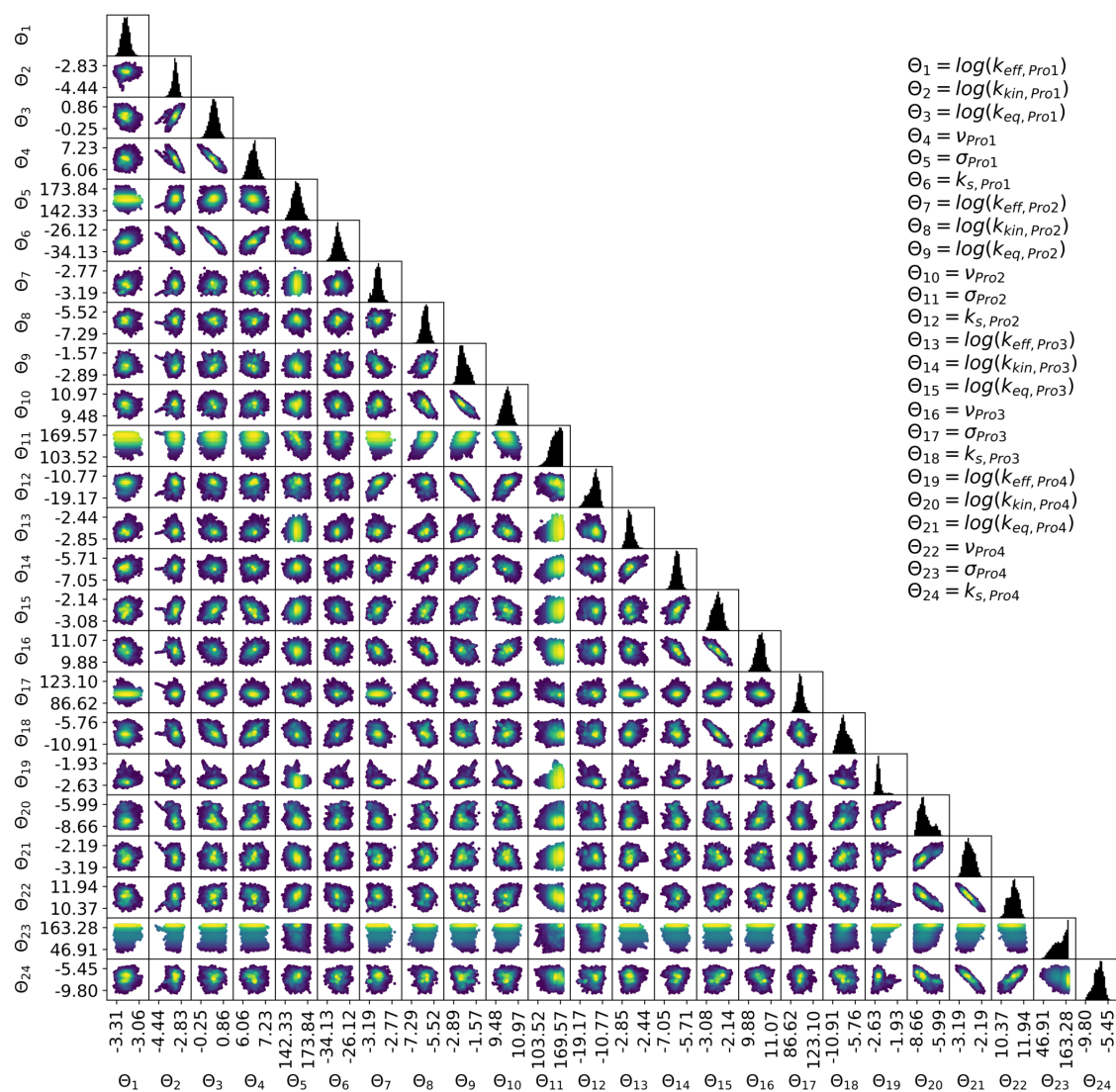
Figure A.2: Parameter posterior distribution. Shown on the diagonal are the marginal distributions of the parameters. Off the diagonal are the joint probability distributions between two parameters. Regions of highest posterior density are shown in yellow.

Appendix B: Supplementary Material for Chapter 5

B.1   System Characterization
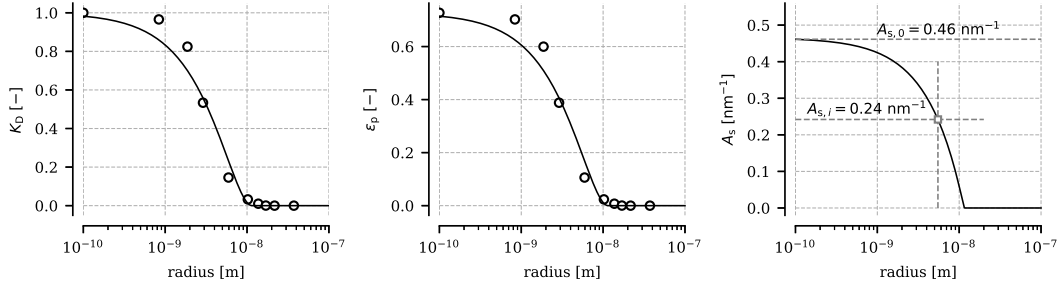
Figure B.1: System parameters of PorosXS. Markers represent experimental retention data of tracer substances of varying molecular size according to [166]. Continuous lines represent fitted pore model data.

B.2   Protein-Protein interaction

In alignment with [128], the two-dimensional adsorption plane is divided in a set of concentric annuli of same thickness D as shown in Fig. B.2. The average number of adsorbed proteins of species i in the k-th annulus is given by

$$n_{k,i} = 2\pi q_i N_A \int_{r_k - \frac{D}{2}}^{r_k + \frac{D}{2}} r dr = 2\pi D r_k q_i N_A, \tag{B.1}$$

whereby $r_k = r_1 + (k-1)D$ represents the average radius of the k-th annulus and r_1 is the average radius of the inner annulus. As shown in Fig. B.2, the number of colloids in the inner annulus corresponds to the number of nearest neighbors, namely 6 in the case of a hexagonal lattice. The average radius of the inner annulus $r_1 = D_{\text{hex}}$ corresponds to the center-to-center distance D_{hex} in a hexagonal lattice. Using Eq. (B.1) and the condition $n_1 = \sum_i n_{1,i} = 6$ for the inner annulus, D is defined by

$$D = \frac{6}{2\pi N_A D_{\text{hex}} \sum_i q_i} = \frac{3\sqrt{3}}{2\pi} D_{\text{hex}}. \tag{B.2}$$
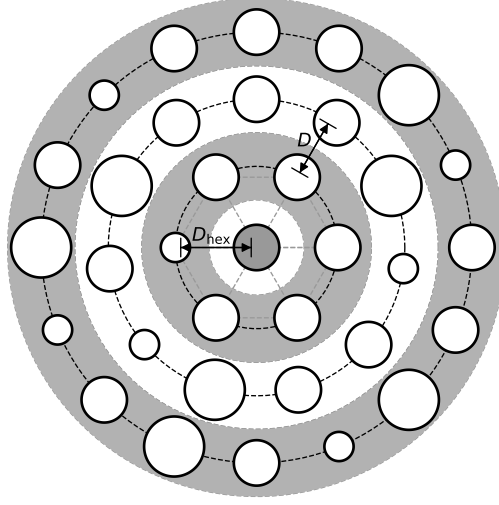
Figure B.2: Schematic representation of the considered protein arrangement within the two-dimensional adsorption layer. Protein centers are assumed to be arranged on evenly spaced concentric circles.

Assuming that proteins within an annulus are evenly distributed over the ring with radius r_k and pairwise additivity of two-body interactions, $u_{\text{lat},i}$ can be approximated by

$$u_{\text{lat},i} \approx \sum_{j=1}^{n} \sum_{k=1}^{\infty} n_{k,j} u_{i,j}(r_k), \tag{B.3}$$

whereby $u_{i,j}$ represents the electrostatic two-body interaction given by the Yukawa potential

$$u_{i,j}(r_k) = \beta_{i,j} \frac{\exp\left(-\kappa r_k\right)}{r_k} \tag{B.4}$$

and

$$\beta_{i,j} = Z_{\text{lat},i} Z_{\text{lat},j} \frac{e^2}{4\pi\varepsilon\varepsilon_0} \frac{\exp\left(\kappa(a_i + a_j)\right)}{(1 + \kappa a_i)(1 + \kappa a_j)}. \tag{B.5}$$

Using Eq. (B.1) and Eq. (B.5), Eq. (B.3) can be rewritten to

$$u_{\text{lat},i} = 2\pi D N_{\text{A}} \sum_{j=1}^{n} q_j \beta_{i,j} \sum_{k=1}^{\infty} \exp\left(-\kappa r_k\right). \tag{B.6}$$

Using the definition of r_k it follows

$$u_{\text{lat},i} = 2\pi D N_{\text{A}} \sum_{j=1}^{n} q_j \beta_{i,j} \exp\left(-\kappa \left(D_{\text{hex}} - D\right)\right) \sum_{k=1}^{\infty} \exp\left(-k\kappa D\right) \tag{B.7}$$

which can be expressed as the closed-form expression

$$u_{\text{lat},i} = 3\sqrt{3} D_{\text{hex}} N_{\text{A}} \frac{\exp\left(-\kappa D_{\text{hex}}\right)}{1 - \exp\left(-\frac{3\sqrt{3}}{2\pi}\kappa D_{\text{hex}}\right)} \sum_{j=1}^{n} q_j \beta_{i,j}, \tag{B.8}$$

whereby D was substituted by Eq. (B.2).

B.3   Linear Gradient Experiments

Experiments were performed with seven proteins varying in molecular weight $M_{\rm w}$ and isoelectric point (pI) as shown in Table B.1.

Table B.1: Proteins used for the linear salt gradient experiments in ascending order of $M_{\rm w}$.

Protein	Oragnism	UniProt	pI [−]	$M_{\rm w}^{\S}$ [kDa]	$a_i^{\dagger}$ [nm]
α-Lactalbumin	Bovine	P00711	4.3	14.2	1.50
Ovalbumin	Chicken	P01012	4.4-4.7	44.3	2.29
Bovine serum albumin	Bovine	P02769	4.7	66.4	2.66
Conalbumin	Chicken	P02789	6.1	77.0	2.79
Amyloglucosidase	Aspergillus niger	Q870G8	3.6	97.0	3.06
Glucose oxidase	Aspergillus niger	P13006	4.2	160.0	3.68
Catalase	Bovine	P00432	5.4	250	4.34

$\S$ according to the manufacturer.
$\dagger$ according to Eq. (B.9).

The protein radius a_i was derived from $M_{\rm w}$ according to the empirical relation

$$\log_{10}\left(\frac{a_i}{1\,{\rm nm}}\right) = a + b\log_{10}\left(\frac{M_{{\rm w},i}}{1\,{\rm kDa}}\right), \tag{B.9}$$

whereby the parameters $a = -0.25$ and $b = 0.37$ have been determined based on light scattering data of globular proteins [158].

Experiments were performed on an Ettan chromatography system equipped with a pump unit P-905, dynamic single chamber mixer M-925 (90 μL mixer volume), UV monitor UV-900 (3 mm optical path length), and a conductivity cell pH/C-900 (all GE Healthcare, Little Chalfont, Buckinghamshire, UK). The strong anion exchanger Q Sepharose FF (GE Healthcare, Uppsala, Sweden) was prepacked by GE Healthcare in a HiTrap column with column volume $V_{\rm c} = 0.962$ mL and column length $L_{\rm c} = 25$ mm. According to the manufacturer, the adsorber surface of Q Sepharose FF is functionalized with a quaternary amine. With reference to [89], the properties of the functional groups are given by $\zeta_{\rm L} = 1$ and $pK_{\rm L} = 12$. The total column porosity and adsorber ionic capacity were determined according to [79] using tracer pulse injections and acid-base titration. Dextran with an average $M_{\rm w}$ of 2000 kDa and sodium chloride were used as non-pore penetrating and fully pore penetrating tracer, respectively. The pore size distribution parameters $r_{\rm p}$ and $s_{\rm p}$ for Q Sepharose FF were determined by inverse size exclusion chromatography as described in Sec. 5.3.1 using sodium chloride, dextran, and all seven proteins at nonbinding conditions as tracer substances. A comparison between the fitted pore model and experimental $K_{\rm D}$ values can be found in Fig. B.3. Based on $r_{\rm p}$ and $s_{\rm p}$, $A_{\rm s,0}$ and $\Gamma_{\rm L} = \Lambda_{\rm IEX}A_{\rm s,0}^{-1}$ were determined. All system parameters are summarized in Tab. B.2.

For all seven proteins, salt gradients were performed at different normalized gradient slopes $G_{\rm H} = \varepsilon(I_{\rm m,B} - I_{\rm m,A})V_{\rm c}/V_{\rm g}$, whereby $V_{\rm g}$ is the duration of the gradient in volume and $I_{\rm m,A}$ and $I_{\rm m,B}$ represent the ionic strength at the beginning and end of the gradient, respectively. A summary of the buffers, pH values, $I_{\rm m,A}$, and $I_{\rm m,B}$ can be found in Table B.3. In all cases, the ionic strength of the buffers was adjusted using sodium chloride. For each
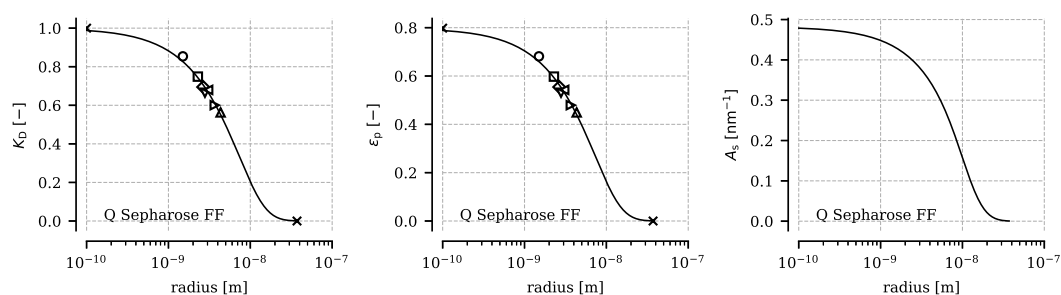
Figure B.3: System parameters of Q Sepharose FF. Markers represent experimental retention data of sodium chloride, dextran (both $\times$), α-Lactalbumin ($\circ$), ovalbumin ($\square$), BSA ($\diamond$), conalbumin ($\triangledown$), amyloglucosidase ($\triangleleft$), glucose oxidase ($\triangleright$), and catalase ($\triangle$) at non-binding conditions. Continuous lines represent fitted pore model data.

Table B.2: System parameters of Q Sepharose FF

System parameter	Unit	Value
Pore size distribution parameter r_{p}	[nm]	17.59
Pore size distribution parameter s_{p}	[−]	0.37
Total accessible surface area $A_{\mathrm{s},0}$	[nm^{-1}]	0.48
Ionic capacity Λ_{IEX}	[M]	1.60
Ligand density $\Gamma_{\mathrm{L}} = \Lambda_{\mathrm{IEX}} A_{\mathrm{s},0}^{-1}$	[μmol m^{-2}]	3.35
Column length L_{c}	[mm]	25
Column volume V_{c}	[mL]	0.96
Void fraction ε	[−]	0.30
Total column porosity ε_{t}	[−]	0.86

experiment, the protein was dissolved in the corresponding equilibration buffer (buffer A) and injected via a 100 μL sample loop. After a wash step over 2 CV of buffer A, the linear salt gradient from buffer A to buffer B was applied. All experiments were performed at a constant flow rate of 0.75 mL min^{-1}. Markers in Fig. B.4 indicate the measured ionic strength at protein elution as a function of G_{H}. Black lines represent fitted model curves based on the CPA model. For Conalbumin and Catalase only data in the range of pH 6.5-8.5 are shown, since both proteins showed non-binding behavior at pH 5.5. This behavior is consistent with the published pI values of both proteins shown in Table B.1. Determined model parameters are summarized in Table B.4 and Table B.5.

Table B.3: Buffers used for the linear gradient experiments at varying pH values. The ionic strength of the buffers was adjusted using sodium chloride.

pH	Buffer system	Ionic strength [M]	
		Buffer A	Buffer B
5.5	Piperazine	0.042	0.344
6.5	Bis-tris	0.010	0.404
7.5	Tris	0.016	0.500
8.5	Tris	0.006	0.512

Table B.4: Model parameters determined for different proteins on Q Sepharose FF using linear salt gradient experiments at low load density: Z_i as a function of the buffer pH.

Protein	Z_i [−]			
	pH 5.5	pH 6.5	pH 7.5	pH 8.5
α-Lactalbumin	-6.21 ± 0.04	-8.71 ± 0.09	-9.38 ± 0.07	$-10.15 \pm 0.0.14$
Ovalbumin	$-14.49 \pm 0.0.25$	-18.98 ± 0.34	-19.18 ± 0.51	-20.35 ± 0.45
Bovine serum albumin	-13.73 ± 0.20	-18.98 ± 0.22	-24.52 ± 0.51	-34.44 ± 0.81
Conalbumin	-	-7.65 ± 0.15	-9.21 ± 0.32	-13.20 ± 0.22
Amyloglucosidase	-44.64 ± 0.15	-51.12 ± 0.13	-53.55 ± 0.13	-59.47 ± 0.19
Glucose oxidase	-42.27 ± 0.52	-53.25 ± 0.69	-57.05 ± 2.35	-62.02 ± 0.90
Catalase	-	-24.56 ± 0.37	-38.96 ± 1.03	-42.10 ± 0.55

Table B.5: Model parameters determined for different proteins on Q Sepharose FF using linear salt gradient experiments at low load density: Δ_i as a function of the buffer pH.

Protein	$\log_{10}(\Delta_i)$ [−]			
	pH 5.5	pH 6.5	pH 7.5	pH 8.5
α-Lactalbumin	-0.59 ± 0.02	-1.05 ± 0.03	-1.22 ± 0.03	-1.33 ± 0.06
Ovalbumin	-1.25 ± 0.08	-1.91 ± 0.09	-1.84 ± 0.14	-2.02 ± 0.12
Bovine serum albumin	-0.49 ± 0.05	-1.00 ± 0.05	-1.76 ± 0.11	-3.28 ± 0.17
Conalbumin	-	0.31 ± 0.04	0.13 ± 0.08	-0.32 ± 0.05
Amyloglucosidase	-3.22 ± 0.02	-3.85 ± 0.02	-4.06 ± 0.02	-4.83 ± 0.03
Glucose oxidase	-2.86 ± 0.09	-3.87 ± 0.11	-4.05 ± 0.37	-4.50 ± 0.14
Catalase	-	-0.45 ± 0.05	-1.56 ± 0.14	-1.57 ± 0.07

Figure B.5(a) shows determined values of Δ_i for all proteins in the pH range 5.5-8.5 as a function of the absolute protein surface charge density. For all proteins, an exponential relationship given by

$$\log_{10}(\Delta_i(\text{pH})) = \log_{10}(\Delta_{0,i}) + \Delta_{1,i}|\sigma_{\text{I},i}(\text{pH})| \tag{B.10}$$
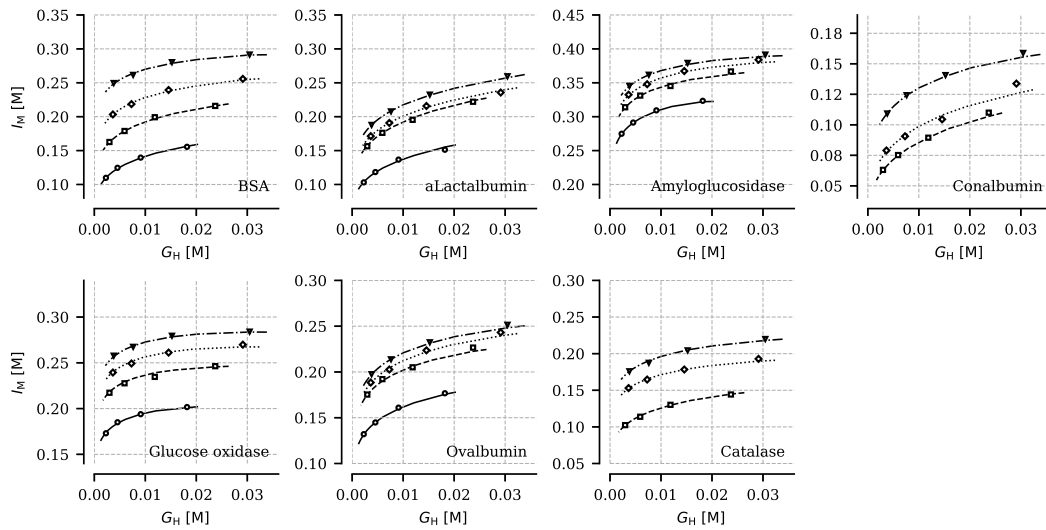

Figure B.4: Elution salt concentration as a function of the normalized gradient slope for seven proteins on Q Sepharose FF. Markers represent experimental data at pH 5.5 (○), 6.5 (□), 7.5 (◇), 8.5 (▽). Black lines represent fitted model curves.

(a)

**(b)**
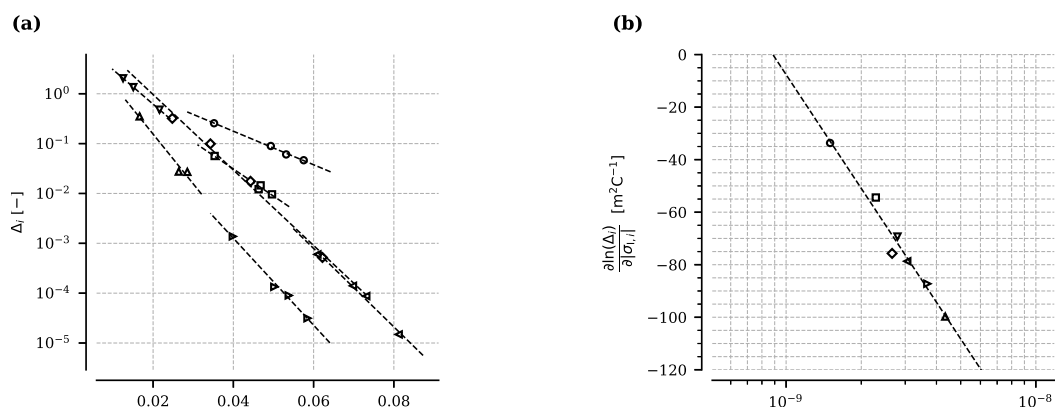
Figure B.5: Dependence of Δ_i on σ_i and a_i. (a) Δ_i as a function of the absolute value of σ_i for α-Lactalbumin ($\circ$), ovalbumin ($\square$), BSA ($\diamond$), conalbumin ($\triangledown$), amyloglucosidase ($\triangleleft$), glucose oxidase ($\triangleright$), and catalase ($\triangle$). Black dashed lines represent fitted curves according to Eq. (B.10). (b) $\Delta_{1,i}$ of Eq. (B.10) as a function of a_i. The dashed line is for visual guidance.

can be observed between Δ_i and $\sigma_{\mathrm{I},i} = eZ_i(4\pi a_i^2)^{-1}$, whereby $\Delta_{0,i}$ represents the intercept at $\sigma_{\mathrm{I},i} = 0$ and $\Delta_{1,i}$ is the slope of the dashed lines shown in Fig. B.5(a). According to Eq. (B.10), the pH dependence of Δ_i is dictated by the effective titration curve $Z_i(\mathrm{pH})$ of the model protein. As shown in Fig. B.5(b), the relationship $\Delta_i(\sigma_i)$ is strongly affected by a_i or $M_{\mathrm{w},i}$ of the protein.

Appendix C: Supplementary Material for Chapter 6

(a)

(c)

(b)
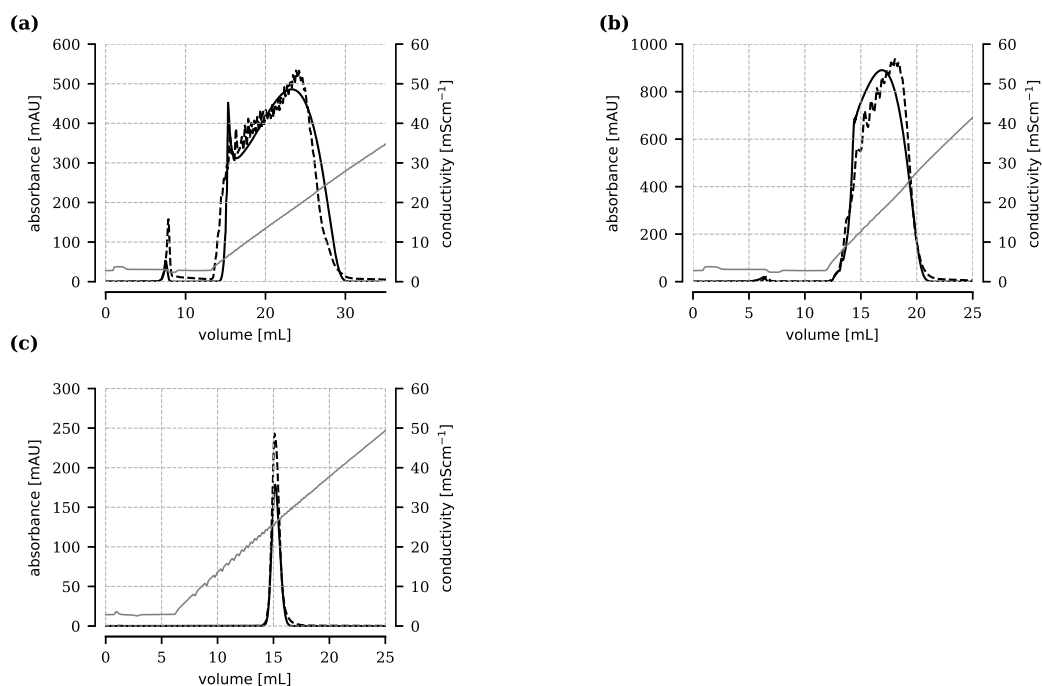
Figure C.1: Salt gradient experiments of mAb1 on Poros 50 HS at different protein load densities including 90 (a), 75 (b), and 2.6 $g\,L^{-1}$ (c). Comparison between experimental data (- - -) according to [78] and simulated data based on the CPA model (——). Black and gray lines represent UV absorbance and the ionic strength, respectively.
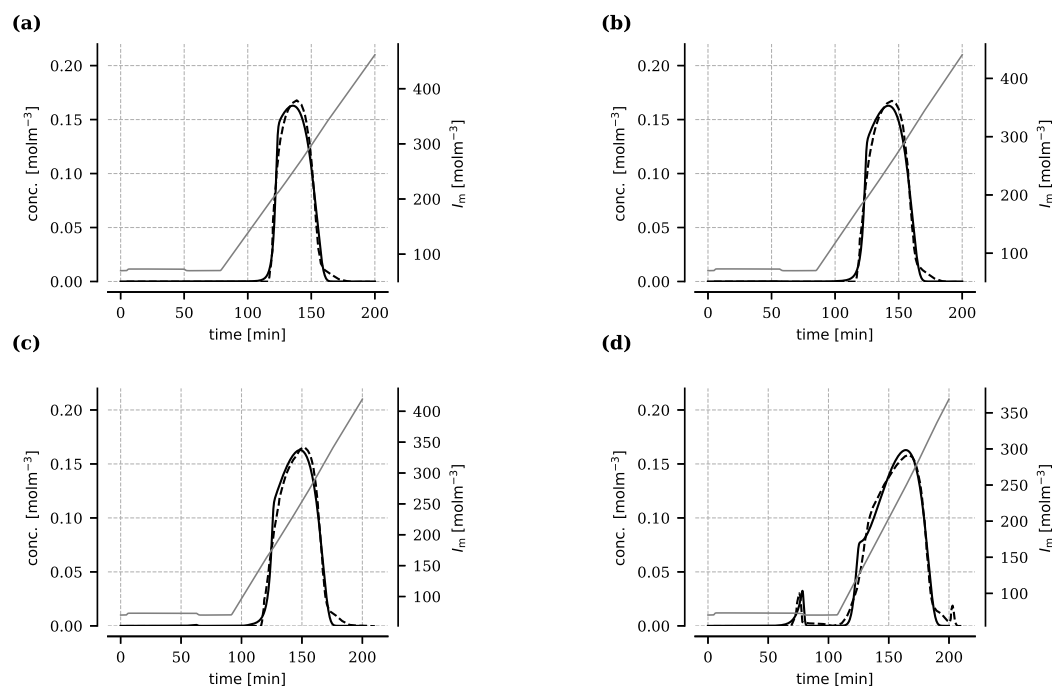
Figure C.2: Salt gradient experiments of mAb2 on Fractogel EMD SO_3^- at different protein load densities including 72.5 (a), 82.8 (b), 93.1 (c), and 118.2 $g\,L^{-1}$ (d). Comparison between experimental data (- - -) according to [40] and simulated data based on the CPA model (——). Black and gray lines represent protein concentration and the ionic strength, respectively.
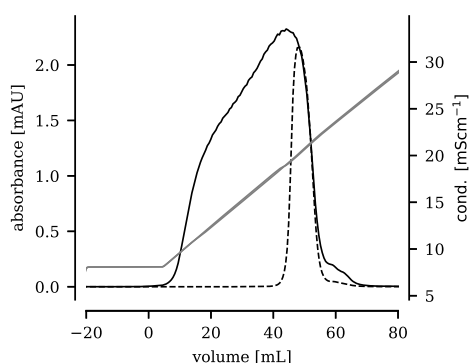

Figure C.3: Salt gradient experiments of mAb4 on Capto S ImpAct performed at a protein load density of 20 (- - -) and 93 $g\,L^{-1}$ (——). The retention volume is shown with respect to the starting point of the salt gradient.